Croissance de nanostructures de composés III-nitrures en épitaxie en phase vapeur d'organo-métalliques : de la croissance auto-assemblée à la croissance sélective

Xiaojun Chen

UNIVERSITÉ DE GRENOBLE

THÈSE

Pour obtenir le grade de

DOCTEUR DE L'UNIVERSITÉ DE GRENOBLE

Spécialité : **Nanophysique**

Arrêté ministériel : **27 Octobre 2008**

Présentée par

Xiaojun CHEN

Thèse dirigée par **Jöel EYMERY** et
Codirigée par **Christophe DURAND**

préparée au sein du laboratoire **Nanophysique et Semi-conducteurs, CNRS/CEA/UJF-Grenoble I**
dans **l'École Doctorale de Physique de Grenoble**

MOVPE growth of III-nitride nanostructures : From self-assembled growth to selective area growth

Thèse soutenue publiquement le **19 Décembre 2011**,
devant le jury composé de :

M. Jean-Christophe HARMAND		
Directeur de Recherche CNRS	Paris	Rapporteur
M. Nicolas GRANDJEAN		
Professeur d'Université EPFL	Lausanne	Rapporteur
M. Jöel CIBERT		
Directeur de Recherche CNRS	Grenoble	Président
Mme. Marie-Antoinette POISSON		
Chercheur Alcatel-Thales III-Vlab	Paris	Examinateur
M. Jöel EYMERY		
Chercheur-Ingénieur CEA	Grenoble	Examinateur
M. Christophe DURAND		
Maître de Conférence	Grenoble	Examinateur

UNIVERSITÉ DE GRENOBLE

Abstract

This work reports the metal-organic vapour phase epitaxy of III-nitride wire- or pyramid-shaped nanostructures and focuses on the growth mechanisms related to these two types of GaN nanostrcutures.

A complete parametric study is presented in order to optimize and to understand the catalyst-free self-assembled GaN nanowire growths. We demonstrate that the silane flux injection is a key-parameter for nanowire growth thanks to the formation of SiN_x passivation layer along the sidewall facets that acts as a mask favoring the vertical growth. A novel silane-free nanowire growth is also proposed in this work using ultra-low precursor flux that favors the formation of vertical facets. Such nanowires exhibit excellent structural and optical properties due to the absence of silicon.

In addition, the polarity is found to play a key-role for GaN nanostructure growth, since the nanostructure shape can be basically determined by the polarity orientation: N-polar nanostructure results in wire, whereas Ga-polar in pyramid. Consequently, the shape wire/pyramid of nanostructure can be chosen depending on the polarity control on sapphire or GaN substrates. This method is applied to get ordered arrays of GaN wires and pyramids using selective area growth on patterned mask. Such nanostructures can be used as template for InGaN/GaN heterostructure growth to get either non-polar multi-quantum wells along the wire sidewalls or InGaN quantum dots at the pyramid apex.

Résumé

Ce travail est consacré à l'épitaxie en phase gazeuse d'organométallique de nanostructures de nitrures en forme de fil et de pyramide, pour lesquelles nous cherchons à comprendre les mécanismes de croissance mis en jeu.

Une étude paramétrique complète est présentée pour optimiser et mieux appréhender la croissance de nanofils GaN auto-assemblés non-catalysés. Nous démontrons notamment que l'injection de silane est un paramètre-clé pour la croissance des nanofils grâce à la formation d'une couche SiN_x de passivation sur les facettes latérales qui joue le rôle d'un masque favorisant ainsi la croissance verticale. Un nouveau procédé de croissance de nanofils sans silane est aussi proposé dans ce travail en utilisant de trs faibles flux de précurseurs qui favorise la formation de facettes verticales. De tels nanofils présentent d'excellentes propriétés structurales et optiques gr âce à l'absence de silicium.

Par ailleurs, nous montrons que la polarité joue un rôle crucial sur la croissance des nanostructures de GaN puisque la forme des nanostructures peut être simplement déterminée par l'orientation de la polarité: une polarité N résulte en fils alors qu'une polarité Ga en pyramides. Par conséquent, la forme fil/pyramide des nanostructures peut être directement choisie en contr ôlant la polarité sur des substrats de saphir ou de GaN. Nous avons justement exploité cette méthode pour obtenir des réseaux ordonnés de fils et de pyramides de GaN en utilisant la croissance sélective à travers un masque nanostructuré par lithographie. De telles nanostructures ont été utilisées pour la croissance d'hétérostructures InGaN/GaN pour obtenir soit des puits quantiques non-polaires sur les flans des nanofils, soit des bo îtes quantiques d'InGaN aux sommets des pyramides.

Contents

Chapter 1

General introduction and targets

Contents

1.1 The interest and brief history of III-nitride semiconductors

The recent advent of III-nitride group has opened a new area in the field of semiconductor materials and devices. The III-nitrides composed of aluminum nitride (AlN), gallium nitride (GaN) and indium nitride (InN), are all direct band gap materials with band gaps (in hexagonal wurtzite structure) ranging from 0.7 eV (α-InN) [1], [2] through 3.4 eV (α -GaN) to 6.2 eV (α -AlN) [3]. Compared to other semiconductors, the III-nitrides could form a complete series of ternary alloys which spans the whole visible spectrum and extends into the infrared and ultraviolet (UV) region, *i.e.* from 1.7 μm to 200 nm as shown in Figure 1.1. These advantage make them ideal candidates for tailored optoelectronic devices, especially visible light emitters in the blue and green regions, which were previously difficult to achieve. Moreover, these materials hold other appealing characteristics including high mobility with high breakdown voltage, the improved mechanical and thermal stability and the ability to work in harsh environments which arises a large enthusiasm in integrating them into various electronic applications.

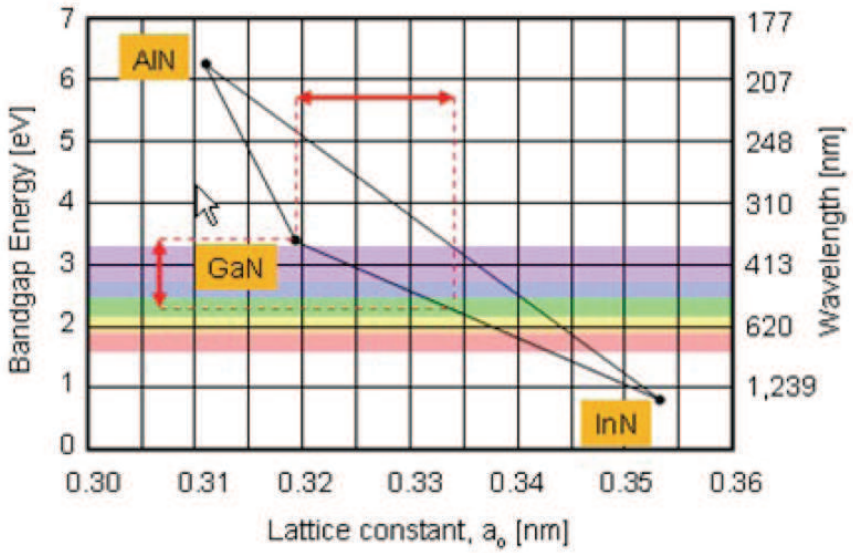

Figure 1.1: Mapping of lattice constant vs. band gap of III-nitride semiconductors.

GaN was first synthesized by Johnson *et al.* in 1932 by passing ammonia through hot Ga [4]. With the technological development of epitaxial growth of high-quality thin films on appropriate substrate materials, the first GaN was epitaxially grown in 1969 by halide vapor phase epitaxy on sapphire [5]. These films were unintentionally n-type doped with electron concentrations ranging from 10^{18} to 10^{20} cm^{-3}. Such high n-type background concentrations made it difficult to achieve p-type doping. After this initial progress made during the 1970s, the pace of research of GaN became slow, because of the lack of high quality epilayers and the lack of success in making p-type GaN. The origin of high background doping was found to be due to O incorporation during the growth [6] instead of N vacancies. It was not until the modern growth techniques of molecular beam epitaxy (MBE) and metal-organic vapor phase epitaxy (MOVPE) were developed to achieve important progress. Strenuous efforts were made to optimize growth conditions and introduce more suitable buffer layers to reduce the n-type background doping levels.

A remarkable progress was made by an insertion of either a low-temperature AlN [7], [8] or a low-temperature GaN buffer layer [9] before the GaN growth. Concerning p-type doping, although the group II element Mg has long been expected to be a good acceptor dopant and significant amounts of Mg could be incorporated into GaN during MOVPE growth, it was impossible to detect positive charge carriers at room temperature. The films turned out to be highly resistive. A rather accidental discovery allowed Amano *et al.* [10] to demonstrate that post-growth low-energy electron beam irradiation activates Mg-doped GaN films and converts them from the as-grown highly resistive state to a p-type conductive state. Nakamura *et al.* [9] have improved the activation of the Mg acceptors in MOVPE grown GaN by thermal annealing in N_2. A hole concentration as high as 3×10^{17} cm^{-3} was achieved with a resistivity of only 2 Ω·cm. These advances led to realizing the first GaN based p-n junction LED in 1993 [11].

Presently, high-brightness nitride-based Light Emitting Diodes (LEDs) mostly comprise InGaN or GaN quantum well (QW) structures as active regions. This breakthrough has paved the way for further rapid research and development of nitride-based devices as compact solid state lamps consisting of high-brightness LEDs and blue laser. Thus, nowadays, III-nitrides have become one of the most promising wide bandgap semiconductors for applications in optoelectronic devices in the blue, green and ultraviolet (UV) wavelengths with continuously increasing efficiency in the last several decades.

1.2 The challenge in the field of III-nitride epilayer growth

Although many hurdles towards efficient devices have been achieved (as dislocation density below 10^8 cm^{-2} and reliable p-type doping) several challenges in III-nitride materials growth required to be well addressed:

- **The high dislocation density in III-nitride heteroepitaxy:** For efficient operation of the devices, the high crystalline growth of the material is essential. In the epitaxial growth, the substrate materials has to be well chosen with appropriate matched crystal lattice constant and thermal expansion coefficient, a good chemical stability in growth environment and the purity of the material avoiding unintentional doping [12]. The substrates mostly used are single crystalline c-sapphire (Al_2O_3), 6H-SiC and (111)-Si. The lattice parameters and the thermal expansion coefficients of sapphire, SiC and Si are all not well-matched to GaN, thus the epitaxial growth generates huge densities of dislocations ($10^8 \sim 10^{11}$ cm^{-2}) [13]. Definitely, for the high crystalline quality, a homoepitaxy growth is the natural solution. Unfortunately, bulk GaN is intrinsically very difficult to grow because of the high vapour pressure of nitrogen at the melting point of GaN which makes them readily available. Moreover, to further push the emission wavelength of III-nitride based high performance LEDs to green, UV even IR region, the InGaN growth with a high In content at low dislocation density level becomes the bottleneck due to the large lattice mismatch between InN and GaN ($\sim 10\%$). To this end, finding ways reducing the dislocation density in III-nitride heteroepitaxy growth has drawn global interests in the materials growth field.

- **The Quantum Confined Stark Effect (QCSE) along c axis growth direction:** At present, GaN devices are mainly grown along the [0001] c-axis of hexagonal GaN, where strong spontaneous and strain induced piezoelectric polarization exists [14] so called QCSE which will be detailed in Chapter 2.1.2. The internal electric field caused by this polarization leads to carrier separation in the active quantum wells and hence reduce the radiative combination probability of the carriers [15]. Furthermore, it has been recently proved that the growth on non-polar plane can also significantly decrease the efficiency drop in LEDs benefiting from the absence of internal electric field [16]. Another way to completely or partially eliminate

the QCSE is to synthesis GaN hexagonal layers oriented along non-polar $[11\bar{2}0]$ a-direction, $[1\bar{1}00]$ m-direction or semipolar $[10\bar{1}1]$, $[11\bar{2}2]$ direction. A lot of pioneering works of non-polar GaN growth have been performed by MOVPE on foreign substrates: $(1\bar{1}02)$ r-sapphire [17], $(11\bar{2}0)$ a-SiC [18], $(1\bar{1}00)$ m-SiC [19] and (100) r-$LiAlO_2$ [20] as well as semi-polar GaN growth on $(1\bar{1}00)$ m-sapphire [21]. However, the GaN films grown on these substrates shows a high density of dislocations and stacking faults [22], [23]. Although free-standing GaN template is also proposed as the substrate for this kind of GaN growth [24], [25], the high cost of such substrate can not be considered for practical applications. In this content, the growth of non-polar or semipolar GaN epilayers on cost-effective substrate and template needs to be developed.

1.3 The peculiarities of III-nitride nanostructures

The size of the nanostructure can reach dimension below the characteristic physical length scale: the exciton Bohr radius, wavelength of light, phonon mean free path, exciton diffusion length. As a result, many physical properties of semiconductors are significantly altered within the confined regime. In addition, their large surface-to-volume ratio allows distinct structural and chemical behavior.

III-nitride nanostructures with various morphologies as quantum dot (QDs) [26], nanowires (NWs) [27], nanopyramids [28], nanorings [29], nanotubes [30], nanoneedles [31], nanopores [32], nanobridges [33] etc. have been widely synthesized and studied in the past decades. We will limit the brief description only on QD, NW and nanopyramid geometry because they will be synthesized and discussed in the scope of this thesis.

- **The peculiarities of III-nitride nanostructures to address the challenge in epilayer growth**

  (1) **To get defect-free III-nitride heteroepitaxy:** Benefiting from the low-scale dimension and large height-to-diameter ratio, the nanostructure mostly NWs is expected to favor elastic-strain relaxation making them virtually free of dislocations in lattice mismatched heteroepitaxy growth. It has been shown in various systems as the GaN

NWs grown on Si substrate [34], the NW based GaN/AlN axial superlattice growth with elastic strain relaxtion [35], the NW based InGaN/GaN/ZnO core-shell growth with green lumnscence [36], the NW based InGaN/GaN axial nanodisc structure emitting white light [37], and the $In_{1-x}GaN_x$ NW growth with a complete In composition turnability on c-sapphire [38]. Apart from the defect-free growth of single NW object, the GaN epilayer initiated from NW array growth using and followed by a coalescence growth has also been demonstrated in both polar [0001] direction on c-sapphire [39] and non-polar [11$\bar{2}$0] direction on r-sapphire [40]. It seems to be a promising way in reducing the dislocation density ($< 10^7$ cm^{-2}) with a rather cheap cost and improving device efficiency compared to commercial epitaxial lateral overgrowth (ELOG) method [13]. Additionally, due to the nearby free surface, it has also been shown that nanostructure system with a pyramidal cap can effectively filter the dislocation [41] and be used to grow LED structure in the long wavelength range [42].

(2) **To be a template for defect-free semi and non-polar heterostructure growth:** Compared to the planar structure grown along the semi or non-polar direction which suffers from high defect density or high cost of GaN substrate, III-nitride nanostructure represents a great opportunity to grow heterostructures with various crystal orientations and the defect-free features. Among which, the GaN NWs and nanopyramids have drawn the most attention. For instance, catalyst-assisted GaN NWs with triangular cross-section could provide semipolar (1$\bar{1}$01) plane for which core-shell LEDs covering the whole visible spectrum range has been demonstrated [43]. The nanopyramid with six inclined semipolar (11$\bar{2}$2) planes could also be used to grow LED structure luminescence at yellow range with internal quantum efficiency as high as 50 % [44].

- **The other peculiarities of III-nitride nanostructures**

(1) III-nitride QD has three dimensional electronic confinement which trap strongly the exciton limiting the non-radiative recombination. Actually, improved efficiencies of the LED have been achieved by incorporation QDs in the quantum well active layer [45] or using QDs in NW structure [46].

(2) III-nitride NW is naturally a good medium for photonic waveguiding applications [47]. Moreover, very high light extraction efficiency could be managed by taking advantage of a lower effective index of the NW array to increase the escape cone for the nanowire/substrate system [48].

(3) The surface-to-volume ratio of the III-nitride NWs is large compared to epilayer or bulk material which makes them a good candidate in gas sensor application [49].

(4) III-nitride NWs allow a carrier confinement in both longitudinal and lateral directions giving the possibility to make a single exciton source [50]. The realization of QD was also recently achieved on tip of the truncated GaN nanopyramids [51].

(5) The sub-micrometer diameter, the possibility to grow axial and core-shell structures and the smooth surface enabled by bottom-up growth approach make the III-nitride nanostructures as promising building blocks for the integration into novel nanoscale 3D devices as LED [52], high electron mobility transistors [53], photovoltaic devices [54], UV-photon detectors [55] and the top-gate in graphene transistors ($<$ 100 nm channel length)[56].

(6) The growth mechanism of III-nitride nanostructures in terms of adatoms diffusion process is different from standard 2D growth. The substrate-surface adatoms exchange, the surface adatoms diffusion and the adatoms direct impinge should be well understood. The material composition (especially InGaN alloys) can vary as a function of interspace and diamater of NWs [57] or the position along the sidewall in the pyramidal-shaped stripe structure [58].

1.4 Motivation and targets

As depicted above, III-nitride nanostructures have various interesting peculiarities and have shown potential applications in nanoscale optoelectronic devices. Among which, the NW geometry stands on the top of the list and deserves a special research effort.

The most common way to fabricate semiconductor NWs is the catalyst-assisted vapor-liquid-solid approach, while the metal contamination has been

proved to harm both the materials optical and structural qualities [59], [60]. Accordingly, the catalyst-free method becomes a particularly attractive issue. In the case of GaN, catalyst-free NWs are currently grown by MBE using N-rich conditions, which spontaneously favor the one-dimensional growth [61], [62], while this method is quite difficult to implement in large volume industry. In contrast, the growth of catalyst-free GaN NWs by MOVPE has shown to be challenging and less extensively addressed, whereas this technique is commonly employed for mass production of compound semiconductors. In this context, only few works requiring specific growth conditions to promote the formation of GaN wire geometry has been reported, such as pulsed precursor mode by Hersee [63], an explicit carrier gas composition ratio of N_2/H_2 Bergbauer [64]. In the lab we have originally developed a method with an *in situ* silane flow injection combined with a low V/III ratio by Koester [65]. The understanding of the influence of the MOVPE growth parameters on the morphology of the NWs and the growth mechanisms involved is a fundamental requirement to ensure high reproducibility and continuously optimization of the growth methods. However, at moment, no systematically work and efforts to address precisely these points in the different MOVPE methods have been performed. Moreover, the complexity of these methods definitely requires a laborious process optimization for the adaptation to other MOVPE reactors and can not be considered as a common approach to grow GaN NWs. Furthermore, the precisely control of the nanostructures growth with controlled position, density and diameter for example by using a pre-patterned mask needs to be also well developed if we want to get homogeneous array of nanostructures with similar optical and electrical properties and consider a easy integration of wafer scale NW assembly for device fabrication.

Thus, the main targets of this PhD work can be divided into five streams:

(1) To systematically study the MOVPE growth parameters' influence on the morphology of the catalyst-free self-assembled GaN NWs growths with *in situ* silane injection. This information could be useful for the deep understanding, reproducibility and further optimization of such kind of growth process.

(2) To study fundamentally the growth mechanisms: the necessity of using silane injection, the related adatoms diffusion path during the NW growth and the pre-requirement for the formation of wire geometry.

(3) To develop a facile and adaptable MOVPE approach to grow catalyst-free GaN NWs with good optical properties in real nanometer scale diameter ($<$ 100 nm).

(4) To initiate the selective area growth of III-nitride nanostructures (NWs and nanopyramids) on patterned mask with a focus on the selectivity homogeneity study.

(5) To grow novel heterostructure (MQW and QD) using as-grown nanostructures as template especially targeting on the nonpolar orientation to eliminate QCSE.

1.5 The organization of the manuscript

The thesis manuscript is divided into six chapters:

Chapter I: The present chapter has given a general introduction with a historical view of the development of III-nitride semiconductors and explanation of the exciting obstacles in view of the planar epitaxial growth for the further materials application. The appealing peculiarities of nanostructure geometry as an alternative approach to address the present challenges in III-nitride growth and some other potential novel applications are also provided. The chapter finishes with the presentation of the motivation and targets of this PhD work.

Chapter II: The second chapter contains an introduction of the general properties of the III-nitride semiconductors. The basic information of the crystalline structure, the band structure and the piezoelectric and spontaneous polarization effect is provided. Then, the state of the art catalyst-assisted, catalyst-free and selective area growth of III-nitride nanostructures, the heterostructures growth and their device applications is summarized with an emphasis on the NW and nanopyramid nanostructures.

Chapter III: The first part of this chapter introduces the physical process involved in the MOVPE growth, the experimental setup of Aixtron machine used in this thesis and the peculiarities of this system regarding the growth control. Then, the standard growth parameters and procedure of the catalyst-free self-assembled growth of GaN NWs with silane injection developed in the lab is briefly introduced. The second part of this chapter deals with the systematic study of growth parameters (growth temperature, precursor flow, V/III ratio, carrier gas flow and reactor chamber pressure) and their impact on the NW morphology (diameter, length and density).

Chapter IV: This chapter first presents the understanding of the presence of *in situ* silane in favor of the NW geometry formation. The underlying mechanism is proposed and approved by the combination of growth experiment and various

characterization methods like Current-Voltage (I-V), Secondary Ion Mass Spectroscopy (SIMS) and Cathode-Luminescence (CL). Then, the adatoms diffusion phenomenon involved in such NW growth is investigated and fitted based on a basic theoretical model. According to this understanding of the growth mechanism, position and length well controlled radial InGaN MQWs along non polar axis is selectively grown on top part of the NWs and the complete n-MQW-p structure is integrated into the fabrication of nano-LED devices. Then, the polarity of the NWs is carefully determined by convergent beam electron diffraction (CBED) measurement and is found to influence the shape selection in GaN nanostructure growth. Finally, a novel approach without silane injection is proposed to get GaN NWs with ultra-fine structural and optical properties. In addition, the growth mechanism is also proposed based on the discussion on the thermodynamic and kinetics of the growth.

Chapter V: The selective area growth of GaN NWs on patterned c-sapphire substrate is presented in the first part of this chapter. The mask patterning process of nanoimprint lithography is detailed. The growth parameter study concerning the improvement of the selectively homogeneity is carefully addressed and the related growth mechanisms are discussed. The structural and optical properties of the as-grown object are characterized by X-ray diffraction (XRD), Transmission Electron Microscopy (TEM) and Cathodo-Luminescence (CL). In the second part, selective area growth of GaN nanopyramids is demonstrated on patterned Ga-polar GaN 2D template. The principle and procedure of the laser interferometry lithography method is introduced. The influence of the growth temperature and reactor pressure on the nanostructure geometry is studied. Based on the facet evolution study for the formation of nanopyramid, the site controlled InGaN QD array is successfully grown on tip of the nanopyramids. The optical property of the QD array is studied by CL mapping and temperature dependent Photo-Luminescence (PL) measurement.

Chapter VI: The most important experimental results and findings for this PhD thesis will be summarized and the important perspective of this work is also proposed.

Chapter 2

Properties of III-nitride semiconductors and the nanostructures grown by MOVPE

The basic requirement for a successful MOVPE synthesis of III-nitride nanostructures is the thorough knowledge of the material properties and of the current state of the art in the growth field. In the first section of this chapter, I will briefly describe the structural and optical properties of the III-nitride materials followed by the specific discussion of crystal polarity and the concepts of spontaneous and piezoelectric polarization. In the second section, the general synthesis method commonly used in MOVPE growth of III-nitride nanostructures will be first explained. Then some typical heterostructures based on III-nitrides will be briefly summarized with a focus on the NW geometry followed by some practical examples of photonic and electronic device applications.

2. PROPERTIES OF III-NITRIDE SEMICONDUCTORS AND THE NANOSTRUCTURES GROWN BY MOVPE

Contents

2.1 Properties of III-nitride semiconductors

2.1.1 Crystalline structure

The III-nitride (GaN, AlN and InN) materials and their ternary alloys exist in two stable crystallographic phases, namely wurzite (α-phase) and zinc-blende (β-phase) as shown in Figure 2.1.

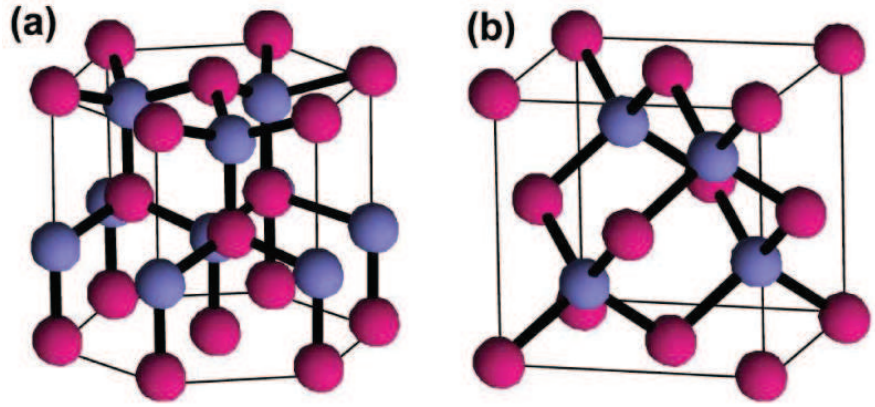

Figure 2.1: (a) Wurtzite and (b) zinc-blende structure of III-nitride. The red and blue spheres indicate III-metals and N atoms respectively.

The thermodynamically stable phase is the wurtzite one, which has a hexagonal structure, space group $P6_3mc$ (C_{6v}^4), and corresponds to two hexagonal lattices shifted by $[00\frac{3}{8}]c$ (Figure 2.1 (a)) composed with group-III metal and nitrogen atoms respectively. These planes are stacked as ABABA... along the direction [0001] which differentiates the cubic crystalline structure (Figure 2.2 (a)).The cubic GaN belongs to $F\bar{4}3m(T_d^2)$ space group and consists of two face-centered cubic structures shifted by $\frac{1}{4}[111]$ with sub-lattices occupied by metal and nitrogen atoms respectively (Figure 2.1 (b)). The cubic phase (111) plane exhibits ABCABC... stacking (Figure 2.2 (b)).

The hexagonal crystal structure of III-nitride is illustrated in more details in Figure 2.3. The atoms are tetrahedrically bonded either centered by metal or nitrogen atoms. The Miller-Bravais indices (hkil) is used to denote the hexagonal system with i=-(h+k). The notation is assigned to the three in-plane base vectors isolated by 120° and the out-of-plane axis c. The edge length a_0 is defined by the basal hexagon along the $[11\bar{2}0]$ axis and the height c_0 of the hexagonal prism along the [0001] axis. The lattice parameters of binary GaN, InN and AlN at 300

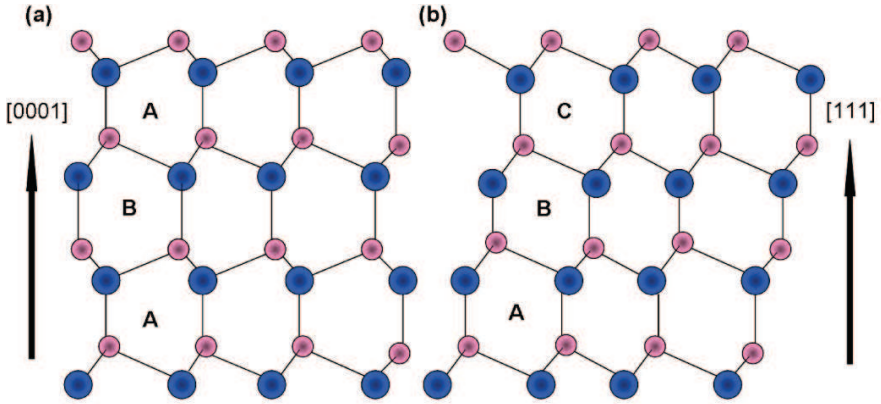

Figure 2.2: Stacking sequence of III-nitride materials for (a)(0001) planes in wurtzite, and (b) (111) planes in zinc-blende. The blue and pink spheres indicate III-metals and N atoms respectively.

K are indicated in Table 2.1. For ternary compounds like $A_xB_{1-x}N$, the lattice parameters is generally deduced from the linear Vegard's law:

$$a_{AB} = (1-x)a_A + xa_B \tag{2.1}$$

Materials	$a_0(\AA)$	$c_0(\AA)$	a_0/c_0
GaN	3.189	5.185	1.626
InN	3.54	5.8	1.615
AlN	3.112	4.98	1.601

Table 2.1: WZ lattice parameters for the III-nitride semiconductors at 300 K.

2.1.2 Crystal polarity

As the hexagonal lattice is not centro-symmetric, the wurtzite structure shows no mirror symmetry with respect to the (0001) plane. As a result, the [0001] and [000$\bar{1}$] directions are not equivalent as illustrated in Figure 2.4. By definition, the arrangement shown in Figure 2.4 (a) is called Ga-polarity and corresponds to the c [0001] vector direction oriented from Ga-atom to N-atom. The mirrored structure is then called N-polar and corresponds to the crystallographic direction [000$\bar{1}$] as shown in Figure 2.4 (b). Polarity is known to determine a large

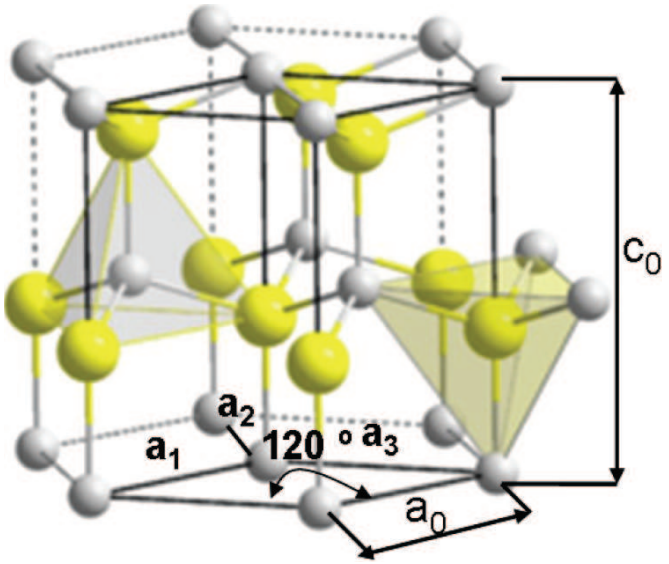

Figure 2.3: Hexagonal structure with representations for the base vectors a_1, a_2, a_3, and the lattice parameters a_0 and c_0. The yellow and white spheres indicates III-metal and N atoms respectively.

number of properties such as impurity [66], [67] and dopant incorporation [68], surface reactivity [69], as well as thermal stability [70]. In addition, opposite polarity of the wurtzite crystal gives a different direction of the internal electric field coming from the spontaneous polarization, which will be introduced later in Chapter 2.1.4. The polarity of the GaN can be usually determined by wet chemical etching using KOH (sensitive to N-polar crystal), the characterization of physical morphology (N-polar surface is normally rough) and by convergent beam electron diffraction.

In the case of the MOVPE growth of GaN on sapphire at low temperature, Ga-polar is usually obtained whatever the substrate preparation. Whereas, for the direct growth at high temperature on sapphire, the surface state of the substrate determines the crystal polarity: N-polar crystal is obtained on nitridated sapphire contrary to Ga-polar crystal growth on bare sapphire substrate [71]. It has been also shown that the crystal polarity can be changed vertically along the growth direction *in situ* by a heavily Mg doping [72].

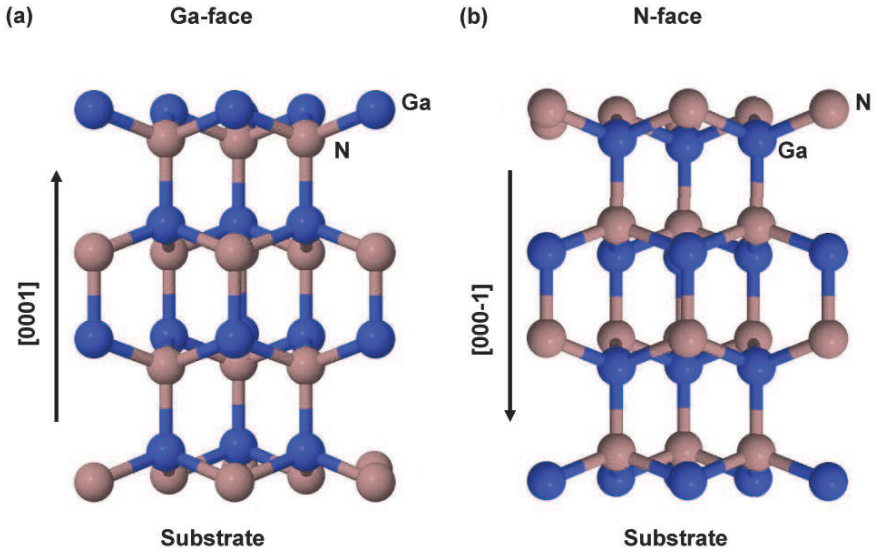

Figure 2.4: Polarity in GaN: (a) Ga-polar along [0001], (b) N-polar along [000$\bar{1}$].

2.1.3 Band structure of III-nitrides

A lot of efforts have been made to investigate the band structure of III-nitride materials using different methods like the all-electron relativistic, full potential, density functional theory in local approximation theory [73], [74], [75].

The calculated band structures of III-nitride are depicted in Figure 2.5. III-nitride semiconductors show a direct bandgap, with valence band maximum and conduction band minimum situated in the center point Γ of the Brillouin zone. The band structure degeneracy in the vicinity of Γ for wurtzite semiconductors

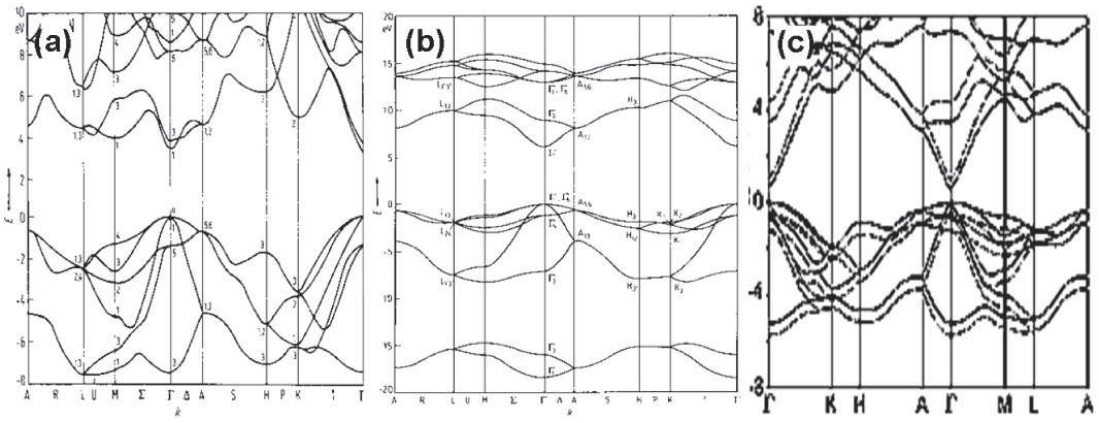

Figure 2.5: Calculated band diagram of (a) GaN, (b) AlN, and (c) InN.

is lifted into heavy hole (A), light hole (B) and spin-orbit, crystal filed splitting hole (C) even in the absence of strain due to the asymmetric nature of wurtzite structure (see Figure 2.6). Generally the uppermost A band has a Γ_9 symmetry and the two other bands B and C lying down have a Γ_7 symmetry as indicated in Figure 2.6. The position and the separation are set by the strength and sign of the spin-orbit coupling. The GaN value of the degeneracy induced by the crystal field and the spin-orbit are respectively ΔCR= 10 meV and ΔSO = 17 meV. The energy difference between the valence band subbands is given by $\Delta E_{AB} = 6$ meV, $\Delta E_{CB} = 37$ meV. The experimental bandgap energies of binary group III-nitrides

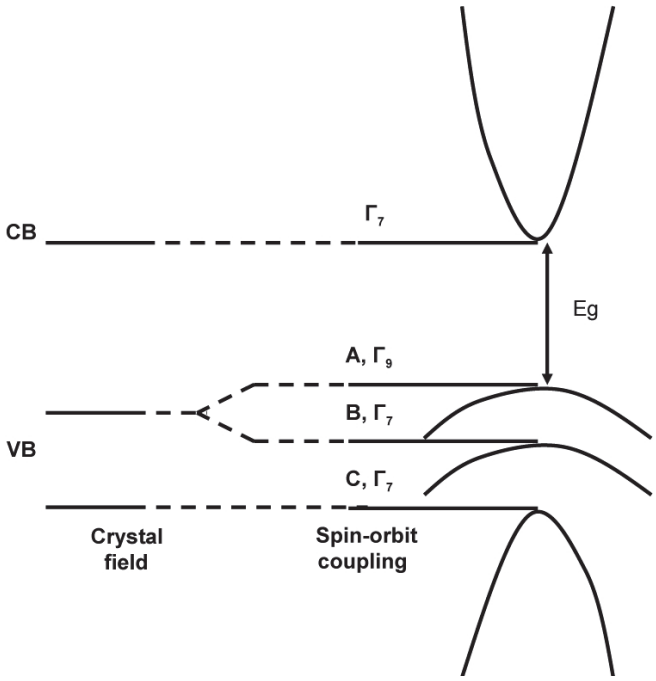

Figure 2.6: Schematic representation of the valence band splitting in wurtzite GaN.

are given in Table 2.2 [3]. For ternary compounds like $In_{1-x}Ga_xN$ or $Al_{1-x}Ga_xN$, the band gap can be approximately calculated by a quadratic equation:

$$E_{AB} = (1-x)E_g(A) + xE_g(b) - x(1-x)b \tag{2.2}$$

in which b is the bowing parameter used to account for the deviation for the linear interpolation from the two binaries materials A and B. The bandgap of the III-nitride semiconductor changes with temperature due to the lattice expansion

	GaN	AlN	InN
E_g(T = 300 K) (eV)	3.39	6.2	0.66
E_g(T = 5 K) (eV)	3.51	6.25	0.62
α (meV/K)	0.909	1.999	0.414
β (K)	830	1429	454

Table 2.2: Band parameters for GaN, AlN and InN.

and the electron photon interaction. Varshni *et al*. have proposed the following equation of the band gap with temperature:

$$E_g(T) = E_g(T=0) - \frac{\alpha T^2}{\beta + T} \tag{2.3}$$

where α and β are constant values accounting for the electron-lattice interaction with typical values for GaN, AlN and InN listed in Table 2.2 [3].

2.1.4 Spontaneous and piezoelectric polarization

A **spontaneous electric polarization ($\mathbf{P}_{\mathrm{sp}}$)** results from the orientation of the anion-cation bond along the polar c axis due to the larger electro-negativity of N atoms than metal atoms. In addition, the application of a strain (from the mismatch epitaxy as in heterostructures) may also lead to a **piezoelectric polarization ($\mathbf{P}_{\mathrm{pz}}$)**.* The internal electrical polarization has a huge effect on the III-nitride heterostructures along the polar c-direction leading to charge depletion or interface charge accumulation across the heterointerface with a fixed charge sheet σ_{pol}. For instance, Figure 2.7 depicts the sign of the polarization vectors and the resulting σ_{pol} in some typical c-oriented III-nitride heterostructures used in electronic devices (light emitting diodes, high electron mobility transistors, photodetectors $\cdots$). The P_{sp} vector always lies as the opposite direction of the +c axis. In $In_{1-x}Ga_xN$/GaN heterostructures the polarization contribution from the piezoelectric polarization is dominant while the spontaneous polarization has a larger influence on $Al_{1-x}Ga_xN$/GaN heterostructures. A detailed quantitative calculation of the electric polarization value can be found in the related references [76], [77].

*The bulk zinc-blende structure has four symmetry equivalent polar <111> axes, which cancel the polarization contribution of each other and is free of electrical polarization.

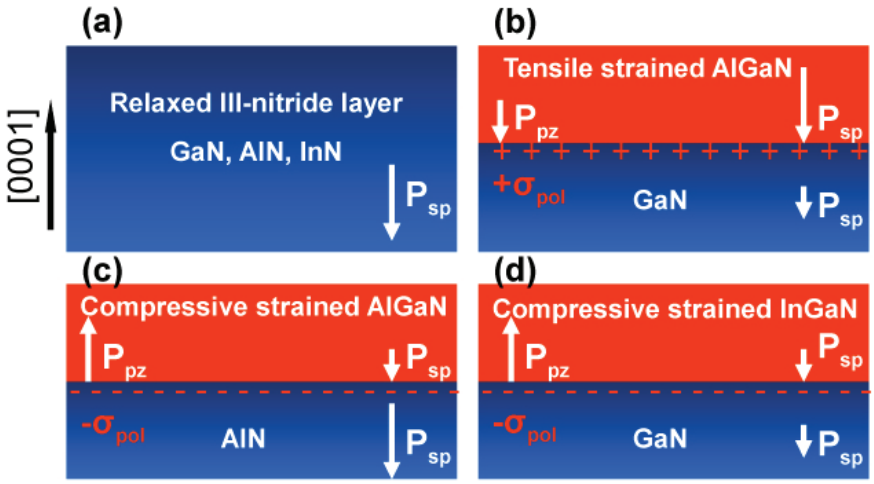

Figure 2.7: Electrical polarization directions and sheet carrier type for III-nitride layers and ternary heterostructures grown along [0001] direction (a) unstrained layers, (b) tensile strained AlGaN on GaN, (c) compressive strained AlGaN on AlN and (d) compressive strained InGaN on GaN.

In this thesis, we focus on the growth of $In_{1-x}Ga_xN$/GaN heterostructures on the facet of the nanostructures and the impact of the electrical polarization will be illustrated on the polar [0001] and non-polar [$1\bar{1}00$] oriented quantum well heterostructures.

- **[0001]-oriented quantum wells:** In this structure, the growth direction is parallel to the total polarization vector P. This total polarization results in the built-in charges with alternating sign at the interfaces, which induces internal electrostatic fields in both quantum barriers and quantum wells as shown in Figure 2.8 (a). Note, the GaN quantum barriers is considered to be fully relaxed with no P_{pz}. The strong internal electrostatic fields within the layers cause a localization of the electron and hole wave functions at both sides of the quantum well as shown in the schematic band diagram of Figure 2.8 (b). Consequently, this carrier separation has two dominant effects. First, the spontaneous interband transition energy will red-shift compared to the flat band condition with only the quantum confinement. This phenomenon called quantum confined stark effect (QCSE) will become more evident if the quantum well thickness is increased. Second, the spatial separation of the electron and hole wave functions will decrease the overlap between them and thus reduce both the oscillation strength and

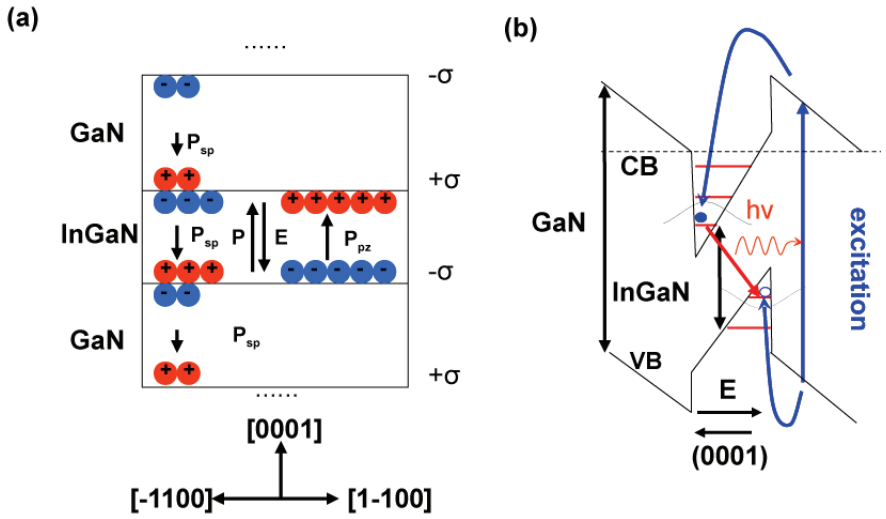

Figure 2.8: Schematic view of (a) the electrical polarization and sheet carrier layer in InGaN/GaN MQW heterostructures grown along [0001] direction and (b) the band diagram of this structure.

transition probability. This effect increases the prolonged radiative recombination decay time. With a longer life time of the carriers, the possibility of the carriers to be captured by the non radiative recombination center is enhanced. Therefore, the QCSE will reduce the internal quantum efficiency ending with a lower output power of the optoelectronic devices.

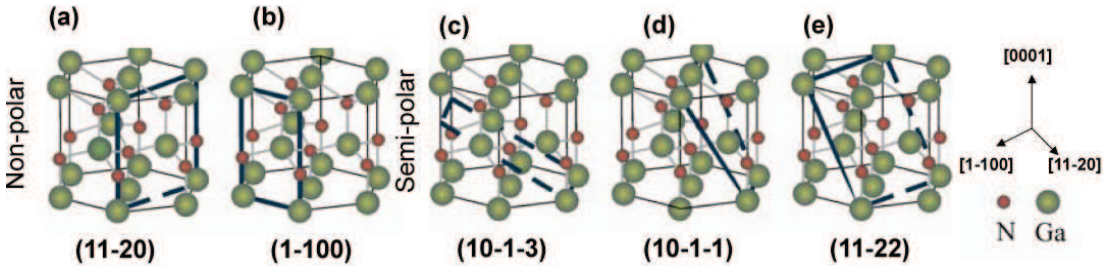

Figure 2.9: Schematic view of (a, b) the non-polar $(11\bar{2}0)$ and $(1\bar{1}00)$ planes and (c-e) the semi-polar $(10\bar{1}\bar{3})$, $(10\bar{1}\bar{1})$ and $(11\bar{2}2)$ planes.

To eliminate the QCSE, one solution is to grow on the semipolar or non-polar planes (see Figure 2.9) [78] as illustrated with the growth along the $[1\bar{1}00]$ axis in the following.

- **$[1\bar{1}00]$-oriented quantum wells:** In this structure, the growth direction

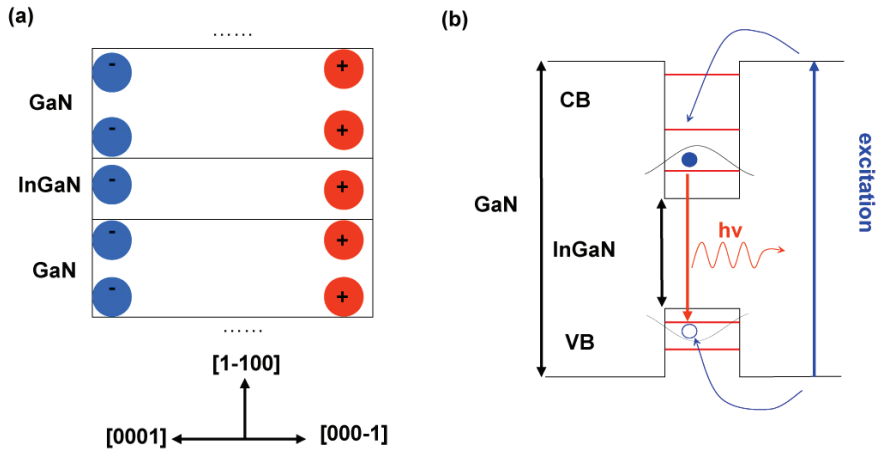

Figure 2.10: Schematic view of (a) the electrical polarization and sheet carrier layer in InGaN/GaN MQW heterostructures grown along [1$\bar{1}$00] direction and of (b) the band diagram of this structure.

is normal to the direction of the total polarization. Therefore, there is no charge accumulation at the interfaces which arises the internal electrostatic fields as shown in Figure 2.10 (a). Then a flat band condition is obtained and transition energy is solely controlled by the quantum confinement effect (see Figure 2.10 (b)). In this situation, the overlap of electron hole wave functions is large enhancing the recombination efficiency and the output power of the devices.

2.2 MOVPE growth of III-nitride nanostructures

2.2.1 Catalyst-assisted growths of NWs

The metal catalyst-assisted growth usually known as vapor-liquid-solid (VLS) growth was initially proposed by Wager *et al*. in 1964 for the formation of whiskers [79]. Basically, this method is driven in the presence of the catalyst that can accelerate the reaction rate. During the III-nitride NW growth, metal particles (Transition or Gold metal pre-deposited on the substrate in the form of thin film layer or metal-nitrate liquid solution) heated in the presence of semiconductor gas precursors acts as a preferential sink to collect material from the surrounding vapor reactants. A eutectic metal particle can then become supersaturated and precipitate the collected material in the NW with a diameter similar to the size of

the initial metal particle. Further growth and extension of the NW occur when an additional material precipitates onto the interface between the metal particle and the NW directly from gas phase or surface and sidewall diffusion. The process is schematically depicted in Figure 2.11.

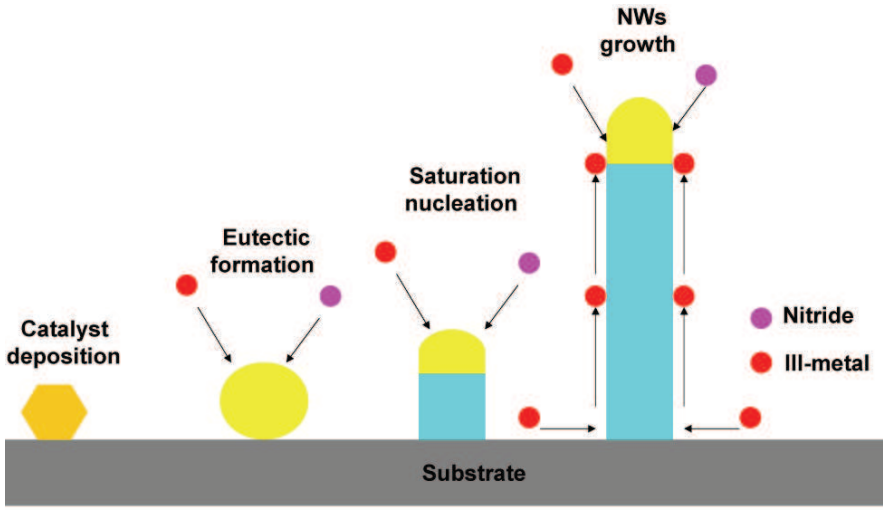

Figure 2.11: The schematic diagram of the catalyst assisted VLS NW growth process.

Initiated in 2000 by Prof. Charles Lieber's group from Harvard University [27], the III-nitride NWs (mostly GaN NWs) has been widely developed and achieved using the VLS approach by CVD [80], [81], [82] and MOVPE methods with growth directions along c [0001], m $[1\bar{1}00]$ and a $[11\bar{2}0]$ as summarized in Table 2.3 and Figure 2.12.

In standard VLS MOVPE growth of GaN NWs, the spatial orientation of the NWs as well as their epitaxial relationships with the substrate are difficult to control. As reported, the epitaxial growth of catalyst GaN NWs can be achieved on γ-$LiAlO_2$ (100), MgO (111) for $[11\bar{2}0]$, [0001] directions respectively [83], on Si (111) for [0001] direction [84], on r-sapphire $(11\bar{2}2)$ substrates for a coexistence of $[11\bar{2}0]$ and $[1\bar{1}00]$ directions with an angle of 30° between the two crystal families [85].* This NW array can be used as a template to obtain high quality non-polar GaN layers with low defect density by coalescence growth [40]. The

*The inclined growth of NWs along $[1\bar{1}00]$ can be completely inhibited resulting in well vertical aligned NWs array by carefully turning the thin film thickness of the pre-deposited Ni catalyst film [86].

catalyst approach allows getting also various III-nitride NW based radial (core-shell) heterostructures which have been proved to be promising future building blocks for the nano-optoelectric devices applications. It is worth to mention that the growth of axial III-nitride heterostructures can not be simply accomplished by the conventional catalyst MOVPE approach, since In and Al precursors suppress the catalytic process due to a formation of stable chemical phases in the droplet. The growth and applications of these radial heterostructures will be introduced in detail later.

In fact, the work dealing with catalysted III-nitride NW MOVPE growth is huge. This thesis will be more focused on the catalyst-free III-nitride nanostructure grwoth method.

Growth Directions	Cross-section Geometry	Notes	Selected References
c [0001]	Hexagonal	Polar axis; Substrate: MgO (1 1 1), Si(1 1 1)	*[83], [87]*
m [$1\bar{1}00$]	Triangular	Nonpolar axis; Substrate: Sapphire ($1\bar{1}02$).	*[87]*
a [$11\bar{2}0$]	Triangular	Nonpolar axis; Substrate: γ-$LiAlO_2$ (100), Sapphire ($1\bar{1}02$), Sapphire (0001).	*[83], [85], [87], [88]*

Table 2.3: The statistic of various catalyst-assisted GaN NWs growth reported in the literature.

2.2.2 Catalyst-free self-assembled (SG) growths of NWs

Although, catalyst assisted MOVPE growth of III-nitride NWs has turned to be an efficient and easy approach, the drawback in terms of degrading the optical and structural properties due to the metal contamination [60] and the difficulty to get well aligned NWs in epitaxy with the substrate, lead to a huge development of epitaxial catalyst-free self-assembled (SG) III-nitride NWs by different growth methods.

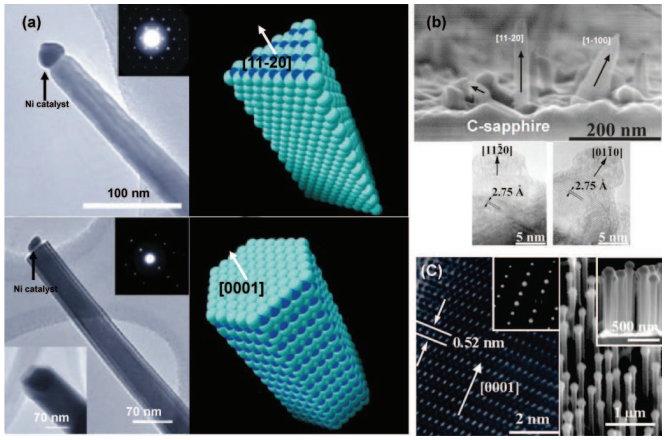

Figure 2.12: TEM and schematic image of along [11$\bar{2}$0] and [0001] direction (a) on (100) γ-$LiAlO_2$ and (111) MgO substrate [83], (b) on (10$\bar{1}$2) r-sapphire substrate [85] and (c) HR-TEM and SEM image of catalyst-assisted GaN NWs grown along [0001] direction on (111) Si substrate [84].

To date, the catalyst-free III-nitride NW growth is mainly achieved by MBE for c-oriented GaN [34], [62], [89], [90], AlN [91], InN [92], [93] and related binary alloys [94]. However, the MBE growth gives a quite low growth rate (100 nm/h) with non-uniformity on large wafer making the potential commercial production difficult. The HVPE has also shown the possibility to get vertical aligned GaN NWs on c-sapphire in catalyst-free approach [95]. The greater achievement in the CVD method is the complete composition tunability for the catalyst-free $In_{1-x}Ga_xN$ ternary alloy NWs synthesis with a band gap from 3.4 to 1.25 eV [38] and these NWs have been utilized to fabricate visible LEDs [96]. However, this approach by using specific precursors tends to be rather difficult and is less addressed. At present, the catalyst-free SG GaN NW growth has been only achieved originally in our group [65] and later on reproduced in CNRS-CREHA [97], the process of which will be detailed later in Chapter 3.3.2.

2.2.3 Catalyst-free selective area growths (SAG)

2.2.3.1 SAG of GaN NWs

The random position, size and density of the catalyst-free SG NWs set a large barrier to integrate the NW arrays directly into the devices. Thus, the catalyst-free approach to get well ordered GaN NWs with epitaxial growth has attracted

considerable attention in the III-nitride research community.

This kind of growth has been recently developed in MBE initiated by Kishino *et al*. [98], [99] and the specific growth mechanism related to both mask geometry and adatoms surface diffusion has also been carefully explored to define three growth regimes regarding the pitch distance [100]. Nevertheless, for MOVPE method, there is still very rare work published yet. In this context, MOVPE SAG of GaN NWs has been explored using a substrate with a pre-patterned dielectric thin layer (SiO_x or SiN_x) as mask with different lithography techniques.

Deb *et al*. [101] have demonstrated in 2005 the SAG growth of GaN NWs on patterned substrates using intermediate porous anodic-aluminum-oxide template (AAO). A 5 μm thick GaN template grown by HVPE on a c-plane sapphire is used as a substrate, followed by a deposition of 80 nm SiO_x thin layer. The patterning process is carried out by first depositing 1 μm thick Al which is then oxidized by anodisation to form a nanoporous oxide layer with a pore diameter between 10 and 15 nm. The pore diameter is further increased to 60 nm by etching in H_3PO_4, and finally the pattern is transferred to the SiO_x layer by SF_6/O_2 reactive ion etching (RIE). For the GaN NW growth, the NH_3 and TMGa are used with a V/III ratio of 1500. The NW growth results as a pyramidal shaped cap with the height and diameter confined by the SiO_x thin film thickness and opening size. The remaining SiO_x layer is finally removed from the sample by means of hydrofluoric acid (HF) to expose the GaN NWs as shown in Figure 2.13 (a).

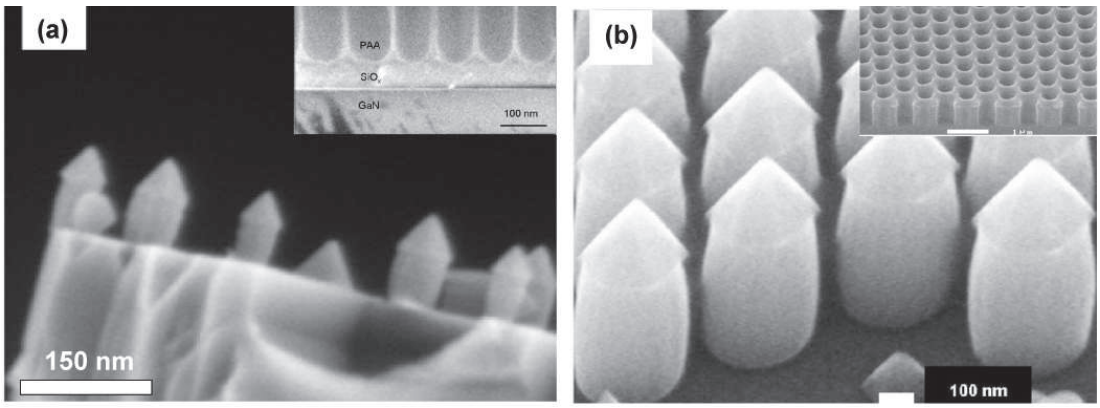

Figure 2.13: Tilted SEM image of confined SAG of GaN on GaN 2D template by MOVPE using (a) self-organized intermediate porous AAO mask [101] and (b) laser interferometry patterned organized SiN_x mask [102].

Using the AAO patterned substrate, Colby *et al.* [41] also managed the MOVPE SAG of pyramid capped GaN NWs with diameter between 60-80 nm and length of 100 nm on the same substrate (GaN/c-sapphire with patterned SiO_x). The dislocation filtering mechanism in GaN NWs was carefully studied by electron transmission microscopy and numerical modeling [41]. It is demonstrated that for a certain window of geometric parameters, the threading dislocation growing within a GaN NW is likely to be excluded either by the strong impinging forces of the nearby free surfaces or filtered by the free surface in the NW especially with larger volume fraction of NW pyramids. As a result, a greater reduction of dislocation density more than a factor of two was observed testifying the defect-free feature of these NWs.

The AAO method has realized the first published 'position and diameter' controlled MOVPE catalyst free growth of GaN NWs. Unfortunately, due to the non-regular formation of the nanoporous within the AAO layer, the position and the diameter of the NWs is not precisely managed, moreover the optical properties of these NWs are not so good showing a strong yellow luminescence.

To overcome this problem, Wang *et al.* [102] have proposed in 2007 the patterning of the SiN_x mask using laser interferometry lithography (LIL) and dry etching. The substrate structure consisted of a 850 nm thick SiN_x mask layer deposited by PECVD on a 600 nm thick planar MOVPE GaN films. The GaN NWs were grown in a low pressure (133 mbar) in a Veeco P75 system with a V/III ratio of 500 at 1060 °C with NH_3 and TMGa (see Figure 2.13 (b)). The growth rate is about 2 μm/h with a growth time adjusted to allow the NWs growth with a length equal to the mask thickness. After growth, the SiN_x mask was completely removed by etching in HF. By this way, the precise location and diameter of NWs are well-controlled by the growth mask patterning and the resulting array has a long range order that is compatible with photonic crystal applications.

Actually, the above depicted methods correspond to confined SAG growth. It means when the nanostructure emerges outside the opening, the lateral growth rate is immediately enhanced resulting in the lost of the NW geometry by coalescence.

To solve this point, Hersee *et al.* [63] demonstrated in 2006 the SAG of GaN NWs using the same substrate (GaN/c-sapphire with patterned SiN_x), lithography method (LIL) and MOVPE growth conditions (pressure, temperature, precursor flow rate and V/III ratio) as in Ref. [102]. But, to avoid the lateral growth of the NWs, the system was switched to the 'pulsed growth mode' where the III and V precursors are provided alternately after a proper filling of the mask holes.

This 'pulsed growth mode' can successfully prevent lateral growth of the NWs after they emerged from the holes as shown in Figure 2.14 (a). The vertical GaN NW growth rate was measured to be 2 μm/h, while the diameter of each NW remarkably remained constant over the entire length of the NWs. In this way, they performed the growth of high quality GaN NWs and uniform arrays in which the position and diameter of each NW is precisely controlled.

The similar MOVPE pulsed mode growth has been further developed to demonstrate the ability of using this NW array for efficient improvement of blue and green LED performance by Prof. Chi-Chung Yang's group from National Taiwan University as shown in Figure 2.14 (b). Tang *et al.* [103] used a more efficient lithography method namely nanoimprint (NI) which can easily vary the geometry of the pattern on SiN_x mask layer with different diameter and pitch distance by using a Si mold design realized by e-beam lithography. This NI lithograph method is also well fitted for wafer scale mass production. The coalescence growth of the NW array was also carried out with different diameter and spacing. A general tendency was observed that the final quality of GaN planar layer is better when the diameter and space distance of the overgrown NW array template is reduced. Based on this method, a high quality GaN planar structure with dislocation density of 10^7 cm^{-2} can be produced which is 2-3 magnitude order lower than ordinary 2-step growth GaN layer. This crystal quality improvement can finally contribute to an increasing internal quantum efficiency by a factor of two in the blue LED structure [39].

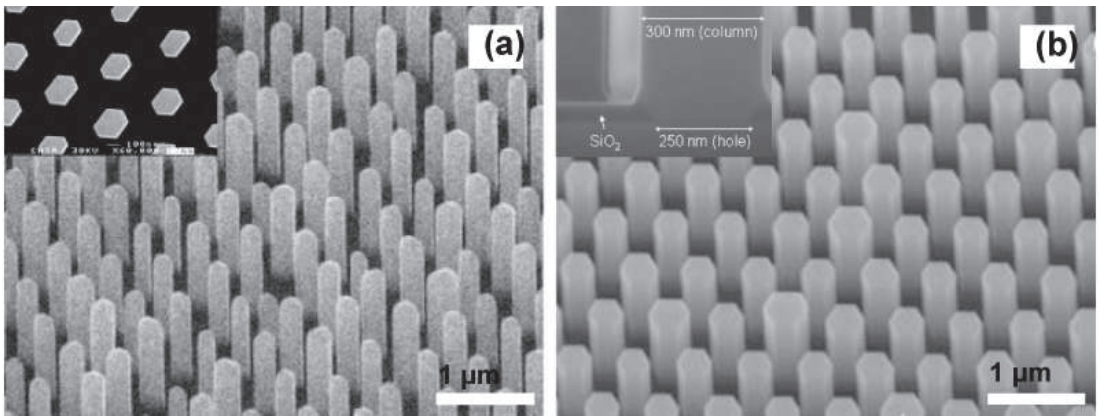

Figure 2.14: Titled SEM image of SAG of GaN NWs on GaN template by MOVPE with pulsed precursor mode reported by (a) Prof. Hersee's group [63] and (b) Prof. Yang's group [84].

However, the using of pulsed mode growth always needs a rigorous MOVPE process optimization depending on different reactor design and atmosphere conditions which definitely represents an obstacle to be considered as a generic approach. Moreover, the necessity of using GaN template and the low growth rate in all the works mentioned above makes the SAG NW growth process both time consuming and expensive.

Bergbauer *et al.* [64] have managed in 2010 to grow well aligned N-face GaN sub-micro wire array directly on c-sapphire substrate with patterned SiO_x mask layer by NI lithography. The statistical variation of the rod diameter is about 100 nm, with an average rod diameter of 400 nm. It has also been shown that the vertical side facets can be realized only by using an optimized H_2/N_2 carrier gas mixture (see Figure 2.15). This ratio and the pattern design have also a huge influence on the rod geometry: the larger H_2/N_2 ratio and smaller pitch distance results in a rod with smaller diameter while the aspect ratio of the rod shows a reverse tendency [104].

The main issue in this topic mainly lies in the understanding of the growth mechanisms. For SAG of GaN wires on c-sapphire, we can observe that the growth homogeneity in terms of size and filling ratio of the opening requires to be well optimized and systematically studied. Moreover the study of growth, structural and optical properties of heterostructures using these wire arrays as templates remains as an open issue and has to be carefully addressed in the future. These points are also the interest of this PhD thesis.

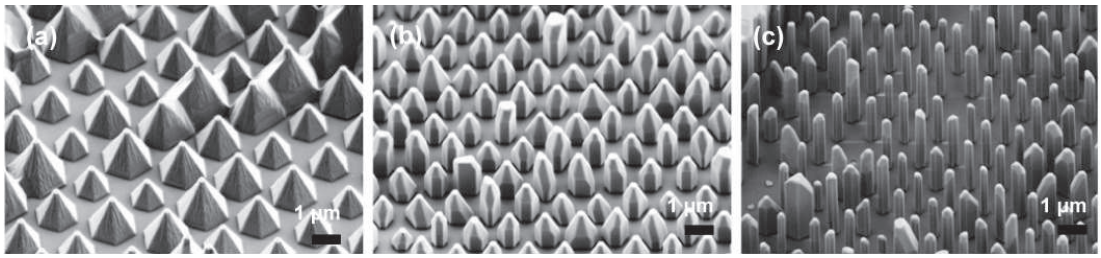

Figure 2.15: Titled SEM image of SAG of GaN nanostructures on c-sapphire with (a) pyramidal shape under pure N_2 carrier gas, (b) pyramidal-capped wire shape under N_2/H_2 ratio 2:1 and (c) wire shape under N_2/H_2 ratio 1:2 [64].

2.2.3.2 SAG of GaN pyramids

The MOVPE SAG of GaN pyramids can be achieved using c-oriented GaN template on which a patterned dielectric (SiO_x or SiN_x) thin layer is used as mask. Contrary to the MOVPE SAG to get III-nitride NW geometry, the synthesis of this hexagonal pyramidal-shaped structure with six inclined facets tends to be much easier to manage. This kind of growth was demonstrated first time by Bidnyk *et al*. in 1998 for room temperature laser under strong excitation power [105]. Later on this structure have continuously being reported in the literature by different groups mainly serving as template for InGaN/GaN MQW heterostructure growth. It has the advantage of fully relaxed biaxial strain in the upper part of the pyramids giving high crystalline quality evidenced by the 7 meV red-shift of the PL position compared to the underneath tempelate [106] and the semipolar orientation with six $\{10\bar{1}1\}$ semi-polar facets (61.8 ° to (0001) plane [32], which will be introduced later in Chapter 2.3.2). The patterning process was at the

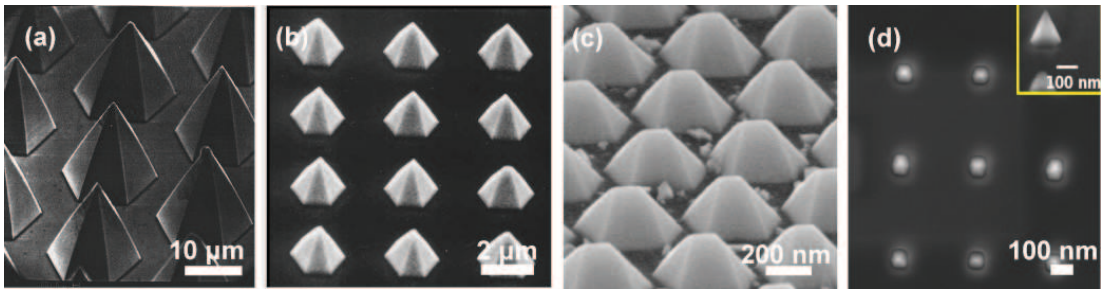

Figure 2.16: SEM image of SAG of GaN nanopyramids on GaN template with different size from micrometer scale to nanometer scale (a) 10 μm [106], (b) 2 μm [107], (c) 200 nm [28] and (d) 100 nm [108].

time always performed by standard optical UV lithography. Owing to the limitation of the lithography resolution, the typical base diameter of the pyramidal structures was in the range of several μm with a pitch distance at the same order resulting in a low pyramids array density ($< 10^5$ cm^{-2}) [54], [106], [107]. The sub-μm diameter pyramids array may allow efficient dislocation filtering and elastic strain relaxation. To address this point, a large area closely spaced GaN pyramid array (wafer scale 2" c-sapphire substrate) with higher density (10^9 cm^{-2}) and smaller diameter (200 nm) has been recently realized with a surface patterning using NI lithography method [28]. 'Nano' pyramids (< 100 nm) are also reported by SAG using e-beam lithography [103]. The diameter evolution of the SAG GaN pyramid from sub-μm to nm scale reported in literature has been shown in

Figure 2.16.

Beyond the great efforts to realize the close packed GaN pyramids with smaller diameter, lots of work have also been made to understand more fundamental issues like the facet evolution, shape formation and *in situ* impurity incorporation from mask diffusion. The facet evolution and formation process for submicro sized GaN pyramids have been determined by SEM observation at different growth stages. First, a truncated pyramid is formed with both top c-plan and six inclined $\{10\bar{1}1\}$ planes and ends up with pyramidal shape with a sharp tip due to the fast growth rate along [0001] compared to that of $[10\bar{1}1]$.

It has been proposed that the pyramidal-shaped sharp tip is caused by the low strain state in the interface of the homoepitaxy process [109]. If there exists biaxial strain in the interface, for example, the GaN structure grown on AlN or directly on c-sapphire, it will form truncated pyramidal shape or hexagonal prismatic shape with a flat c-plane surface respectively even under the same growth conditions. This phenomenon is explained by the author taking into account the strain dependent Ehrlich-Schwoebel barriers across different planes. Later on, it has been further demonstrated that even on the homoepitaxial growth, the GaN structure can be turned from pyramid to hexagonal prism under a pulsed growth mode created by flow modulation [110] and this result was reproduced with strip patterned mask geometry to get flat c-plane and vertical a-plane shaped structure for GaN epitaxy lateral overgrowth on micrometer sized circular opening [111]. The CL measurements on single pyramid object reveal a gradual 2-4 nm red-shift of NBE emission position from apices to base of the pyramid depending on the object diameter. This could evidence the Si and O impurity incorporation into the crystal lattice from the dielectric mask through surface diffusion with an estimation value of 10^8 cm^{-3} from finite element calculation [112].

It is worthwhile to note that, till now, the homoepitaxy SAG of hexagonal pyramidal shaped GaN structure in the nanoscale range with circular patterning mask geometry is not reported. More efforts are thus needed to study in detail the facet evolution for the growth of this nanoscale SAG GaN pyramids on GaN template.

2.2.4 MOVPE III-nitride nanostructures based heterostructures growth for device applications

2.2.4.1 NW based heterostructures

The MOVPE synthesis of III-nitride NWs introduced in last part showed high crystalline quality compared to the 2D growth due to the effective relaxation of strain avoiding the creation of dislocations. These objects become excellent template to grow coaxial (mainly radial) heterostructures like $In_{1-x}Ga_xN$/GaN or $Al_{1-x}Ga_xN$/GaN with successful doping and composition modulation with larger lattice mismatches than in traditional planar structures.

LED:

A core/multishell III-nitride nanoNW radial heterostructures has been used to fabricate the nano LED by Qian *et al*. from Prof. Charles Lieber's group at Harvard University [43]. This Core/multishell nanoNWs were prepared by catalyst-assisted MOVPE giving a triangular shaped n-GaN core and $In_{1-x}Ga_xN$ /GaN/p-$Al_{1-x}Ga_xN$/p-GaN shells as shown in Figure 2.17 (a). Current versus voltage characteristics (Figure 2.17 (b)) shows typical p-n diode current rectification with a sharp onset at around 3.5 V in forward bias. Normalized EL (Figure 2.17 (c) and (d)) of this nano LED exhibits distinct spectral peaks varying from 367 to 577 nm with In compositions of about 1 to 35 % in the quantum well layer accomplished by reducing the growth temperature. In addition, devices exhibit dominant emission from the free NW ends (Figure 2.17 (e)).

Although this work has pioneered the fabrication of III-nitride LEDs based on NW geometry and shows the possibility to cover the green gap, this demonstration is based on single NWs, which basically do not meet the commercial product requirements.

Lee *et al*. in Prof. Gyu-Chul Yi's group from National Seoul University fabricated ZnO/n-GaN/$In_{1-x}Ga_xN$/p-GaN nanoarchitecture LED microarrays consisting of position-controlled GaN/ZnO coaxial nanotube heterostructures as shown in Figure 2.18 (a) [52]. This technique uses ZnO nanotube arrays as template. Then a Si-doped n-GaN, three periods GaN/ $In_{0.24}Ga_{0.76}N$ MQW were grown to achieve the green emission from nanoarchitecture LED microarrays. Subsequently, a Mg-doped p-GaN layer was deposited on top of the last GaN quantum barrier using a commercial nitride MOVPE system (Figure 2.18 (b)). The I-V curve exhibited typical rectifying behavior with a turn-on voltage of 3 V and a leakage current of 5×10^4 A at -4 V. Above the turn on voltage, the current in-

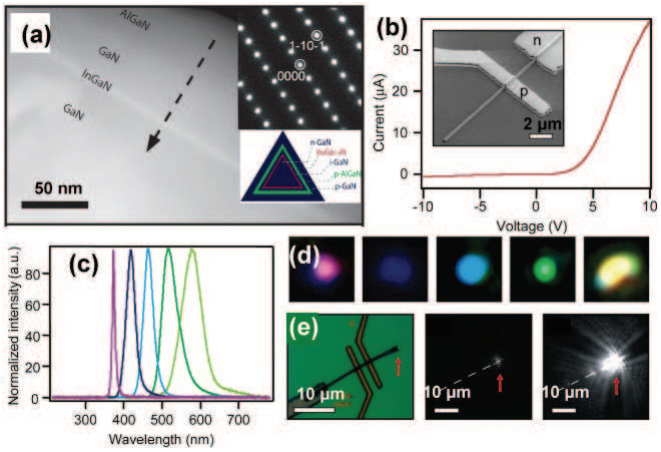

Figure 2.17: (a) Dark-field TEM image of a cross-sectional GaN/In1-xGaxN/GaN/AlGaN NW, (b) SEM image of the connected NW device with n and p metal pads and the corresponding I-V curve,(c) Normalized EL spectra of five representative NWs with different In content, (d) Optical microscopy images collected from around p-contact of NW LEDs in forward bias showing different colors, and (e) From left to right : optical microscopy image of NW LEDs with metal contact and the EL image recorded in a forward bias of 9 V and 11 V respectively.

crease very fast and at 100 mA most of the single nanoarchitecture emitting light at green range.

This kind of structure has made a great progress for the III-nitride NW based LED although the inconvenient lies in the switch between the two MOVPE reactors for ZnO and GaN growths. Such strategy using ZnO nanostructures was chosen due to the easy approach getting catalyst-free ZnO NWs by MOVPE.

Very recently, this group in collaboration with SAMSUNG demonstrated the synthesis of MOVPE SAG core-shell/axial III-nitride NWs for full visible spectrum tuneable LED [113]. This time GaN NWs are used instead of ZnO nanotubes as the core template to make a real homoepitaxy, but unfortunately the growth condition are not detailed. The basic strategy for epitaxial growth of multifaceted GaN nanostructures and fabrication of color-tunable LEDs is shown in Figure 2.19 (a). The GaN NW arrays were grown on n-GaN/c-sapphire substrates using SAG catalyst-free MOVPE. After the growth of GaN NW arrays, $In_{1-x}Ga_xN$/GaN MQW layers were heteroepitaxially grown over the entire surface of each GaN NW array (Figure 2.19 (b)). Subsequently, Mg-doped p-GaN was epitaxially coated on the NW with the MQW to form an overlayer film (inset

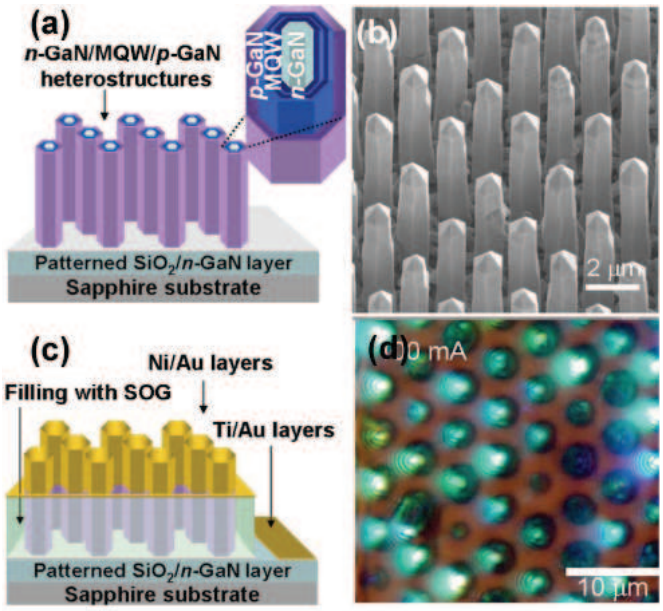

Figure 2.18: (a) Schematic and (b) SEM images for GaN/In1-xGaxN/GaN/ZnO p-n homojunction coaxial nanoarchitecture heterostructure arrays, (c) Schematic for nanoarchitecture LED microarrays with ohmic metal contact and (d) Photography of light emissions from nanoarchitecture LED microarrays with 100 mA inject current.

of Figure 2.19 (b)). The HR-TEM analysis showed that the MQWs are formed on both the topmost and upright sidewall areas of the NW, respectively. A significantly difference in the QW and QB thicknesses and In composition in QW was observed (Figure 2.19 (c)). This anisotropically deposition of the MQW on the GaN NWs is believed to play a critical role in the color turnability of the NW embedded LEDs: a blue-shift of the EL spectrum position by increasing the forward voltage as shown in Figure 2.19 (d). Furthermore, by integrating three zones on single chip with different p-electrode area, a multicolor (red, blue, green) single inorganic LED chip was first time demonstrated with the same injection current of 20 mA (Figure 2.19 (e) and (f)).

Laser:

Optically pumped lasing operation of single GaN NWs with $(In_{1-x}Ga_xN/n\text{-}GaN)_n$ (n= 3, 13, 26) MQW (thickness 1-3 nm) core-shell heterostructures at room temperature has also been demonstrated by Qian *et al.* in Prof. Charles Lieber's group from Harvard University [114]. The MQW NWs structure design

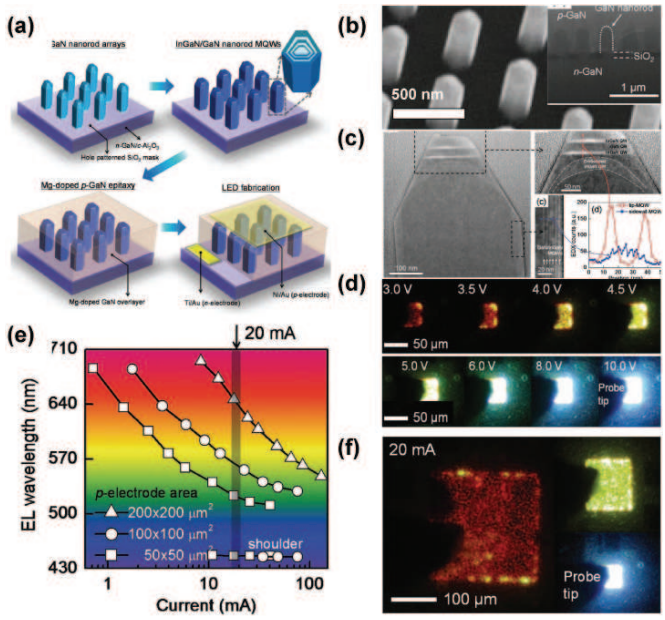

Figure 2.19: (a) Fabrication process of GaN NW embedded LEDs, (b) tilted SEM and inset the cross-section TEM image of GaN NW array, (c) cross-section TEM image of GaN NW with $In_{1-x}Ga_xN$ MQW structure, (d) visible-color-turntable GaN NW LEDs under different forward bias and (f) visible-color-turntable GaN NW LEDs under same current flow with different p-contact area.

(Figure 2.20 (a)) consists of a triangular shaped GaN NW core, which behaviors as the primary part of the optical cavity, and epitaxial $In_{1-x}Ga_xN$/GaN MQW shells, which serve as the composition-tunable gain medium. Dark-field cross-section STEM revealed the MQW structure growths along the $(1\bar{1}01)$ facets, but not along the third facet of the triangle, *i.e.* $(000\bar{1})$ facet where the growth rate is very small (Figure 2.20 (b) and (c)).

The light emission recorded by optical microscopy from single NWs shows a wave guiding effect with enhanced luminescence intensity from the end part of the object as shown in Figure 2.20 (d). Figure 2.20 (e) is normalized photoluminescence spectra acquired from four representative 26×MQW NW structures with increasing In concentration from 5-23 %. It evidences a lasing behavior with peak maxima at 383, 420, 452 and 478 nm, spanning a substantial portion of the ultraviolet to visible region of the electromagnetic spectrum. The threshold power densities for these four MQW NW lasers are all below 700 kW/cm^2. It is also found that the threshold ratio of the lasing decreases with the increase

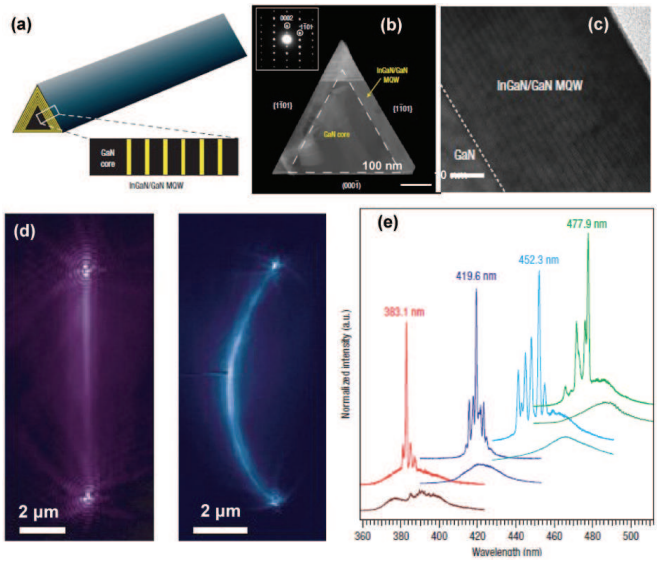

Figure 2.20: (a) Schematic and (b), (c) cross-section TEM images of 26×GaN/$In_{1-x}Ga_xN$ MQW grown on GaN NWs, (d) recorded PL image (false color) of GaN NWs with 26×MQW structures of different In content and (e) normalized PL spectra collected from GaN NWs with 26×MQW structures with increasing In content pumped pumped at 250 and 700 kWcm^{-2}.

of the MQW pairs. The electrically pumped lasing of III-nitride NWs is not yet reported in the literature.

HEMT:

Li *et al*. in Prof. Charles Lieber's group from Harvard University demonstrated HEMT heterostructures based on a GaN/AlN/ $Al_{1-x}Ga_xN$ core/shell NWs [53]. GaN NWs are first grown along the a-direction with catalyst-assisted MOVPE and have a triangular cross-section with non equivalent facet planes (see the indexation in Figure 2.21 (a) and (b) the TEM image of the structure), then an AlN (1.8 nm thick) and $Al_{1-x}Ga_xN$ shell is deposited around the NWs.

The NW horizontal HEMT device is fabricated with ZrO_2 dielectrics and metal top gates showing excellent gate coupling with near ideal sub-threshold slopes of 68 mV/dec and an on/off current ratio of 10^7. Transport measurements demonstrate the existence of electron gas in the undoped GaN/AlN/$Al_{1-x}Ga_xN$ NW heterostructures and also yield an intrinsic electron mobility of 3100 cm^2/Vs and 21000 cm^2/Vs at room temperature and 5 K, respectively (see Figure 2.21 (c) and (d)).

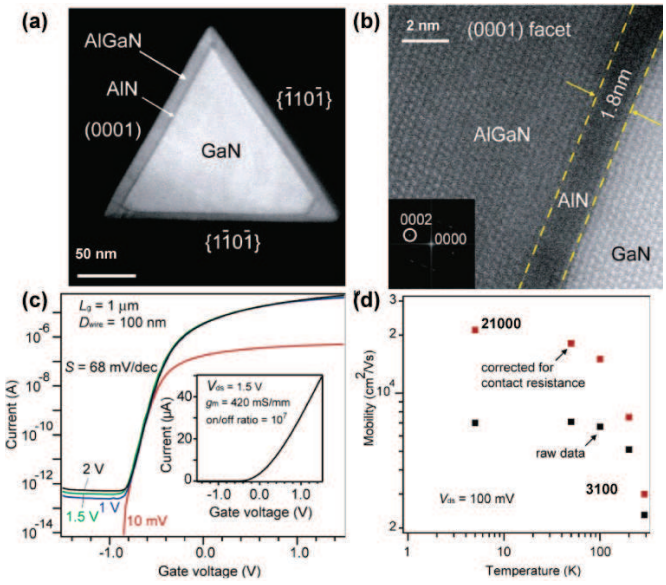

Figure 2.21: (a) Cross-section TEM of a triangular NW with the GaN core and the AlN/AlGaN shells, (b) HR-TEM image shows the 1.8 nm thick AlN layer, (c) I_{ds}-V_{gs} curves recorded at different V_{ds} value on the same core-shell NW. Inset: linear scale I_{ds}-V_{gs} data recorded at V_{ds} = 1.5 V and (d) measured (black symbols) and intrinsic (red symbols) electron mobility of the core-shell NW at different temperatures.

Photovoltaic device:

The core/shell n-GaN/$In_{1-x}Ga_xN$/p-GaN NW based heterostructures offer potential applications in photovoltaic applications as demonstrated by Dong *et al.* in Prof. Charles Lieber's group from Harvard University [54]. A key advantage of the core/shell architecture is that the p-i-n interface extends along the entire length of the NW with carrier separation in the radial direction. In this geometry, photo-generated carriers can reach the p-i-n junction with high efficiency since diffusion lengths are relatively short.

In this work, the a-axis oriented n-GaN core NWs is first grown by catalyst-assisted MOVPE method. Then $In_{1-x}Ga_xN$ shell is deposited where the variation of indium mole fraction was used to control the active layer band gap with a tunable emission from 556 to 371 nm. Finally the structure was terminated by a p-GaN layer (Figure 2.22 (a)). The Simulated one-sun AM 1.5 G illumination yielded open-circuit voltages (V_{oc}) from 1.0 to 2.0 V and short-circuit current densities (J_{sc}) from 0.39 to 0.059 mA/cm^2 (Figure 2.22 (c)) as In composition is

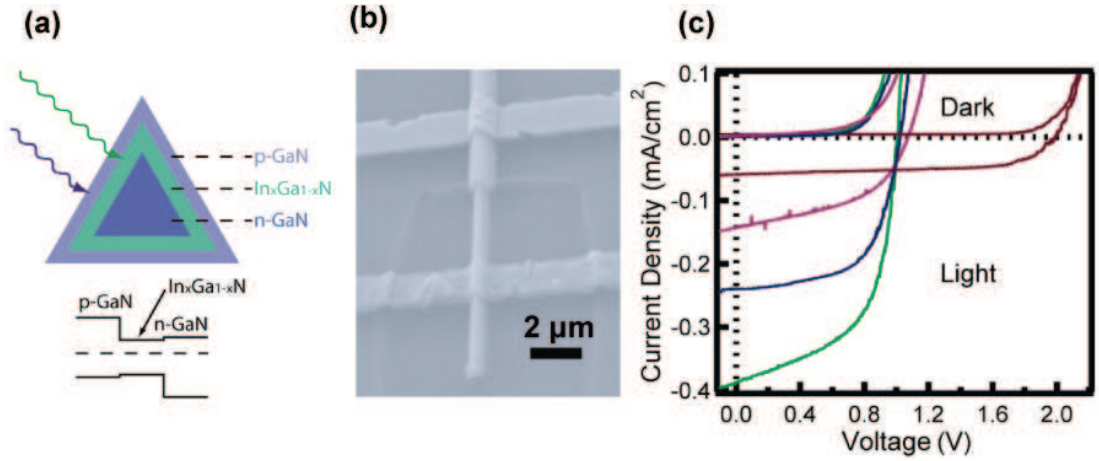

Figure 2.22: (a) Schematic of n-GaN/$In_{1-x}Ga_xN$/p-GaN core-shell NWs and corresponding band diagram, (b) SEM image of the connected core-shell NW device with n and p metal pads and (c) I-V curve for NWs with different indium contents with and without illumination.

decreased from 0.27 to 0 and a maximum efficiency of about 0.19 %. Although the low efficiency, this work report the first demonstration of III-nitride nansotructrue device for photovoltaic applications.

2.2.4.2 Pyramids based heterostructures

The MOVPE SAG of GaN pyramids has been well developed for decades as presented before. The site control feature and the six inclined semipolar facets have thus attained continuous research interests for $In_{1-x}Ga_xN$/GaN heterostructures overgrowth in order to obtain lighting emitter sources. It has been demonstrated that $In_{1-x}Ga_xN$ QD in association with QW structures can be deposited on the tip and sidewall facets of the GaN micropyramid respectively. However, for nano-sized GaN pyramids with a diameter below 300 nm, there is no clear evidence of the existence of the QD structures at the pyramid tip. This particular point will be later addressed in this PhD.

In the literature, Péerez-Solòrzano *et al.* [107] deposited five periods of 5 nm $In_{1-x}Ga_xN$ thin layer capped by a 10 nm GaN barrier layer on the facet of the GaN pyramid with a base diameter of 2 μm with a pitch distance of 5 μm. Two regions of different confinement were identified with CL with the emission around 2.03 eV located at the pyramid tip and the other contribution at 2.35 eV originating from the side wall surface see Figure 2.23 (a). The relaxation

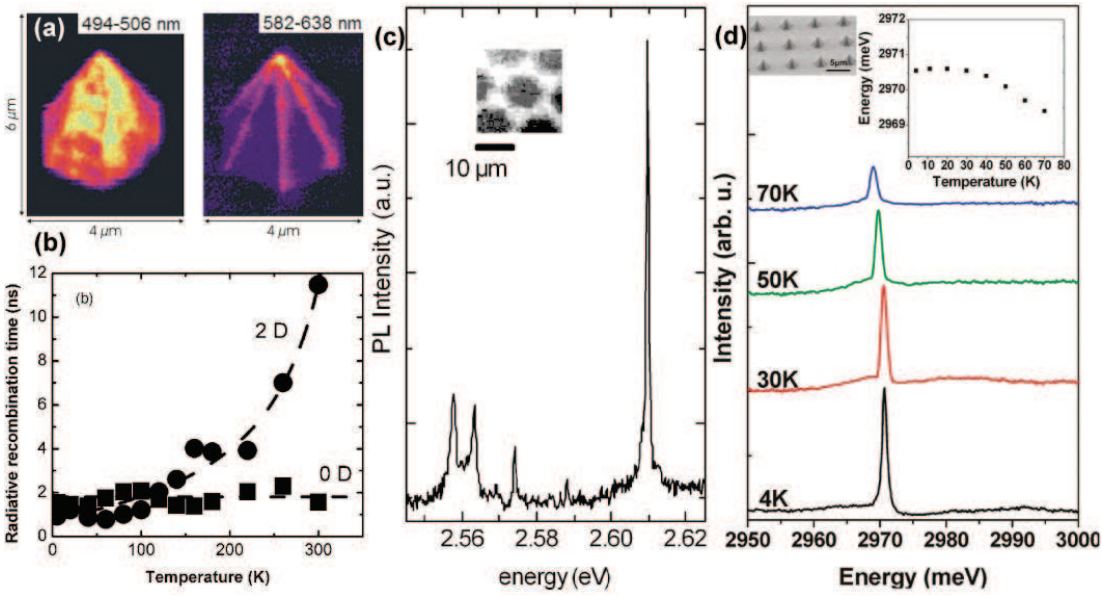

Figure 2.23: (a) CL mapping of single GaN pyramid with $In_{1-x}Ga_xN$ QD in the $\sim$ 500 nm and $\sim$ 640 nm range [107], (b) radiative decay time as a function of temperature for the QW (500 nm) and QD (640 nm) emission in (a) [107], (c) 4 K spatially resolved PL exhibits sharp lines corresponding to $In_{1-x}Ga_xN$ QDs emission [115] and (d) Temperature-dependent μPL measurements of a selected $In_{1-x}Ga_xN$ QD on the top of the truncated GaN pyramid as shown in the left inset SEM image. The right side inset is a plot of the peak energies as a function of the temperature [51].

and recombination mechanisms of the two peaks were studied by temperature dependent time resolved PL. The results (Figure 2.23 (b)) present a constant temperature behavior of the radiative decay time as 1.5 ns for 2.03 eV emission confirming the zero dimensional confinement character (QD), whereas the gradual increase of the decay time with a value exceeding 10 ns indicated a typical behavior for two dimensional QW emission for the 2.35 eV peak.

Edwards *et al.* [115] have also managed to grow the $In_{1-x}Ga_xN$ QDs structure on the tip of GaN pyramids array with 8 μm in height and base edges of 5 μm (repeated in a hexagonal array with a 10 μm pitch). The low temperature PL spectra showed spatially resolved peaks with a linewidth down to 650 μeV which is a standard signal from the QDs emission as presented in Figure 2.23 (c).

Recently, the single exciton emission from $In_{1-x}Ga_xN$ QDs on GaN micro pyramid arrays has been first time reported [51]. The formation of single QDs

is evidenced by showing single sub-meV emission lines in PL spectra on single object and the temperature stabilization intensity as shown in Figure 2.23 (d). In addition, the growth mechanism of this kind of QDs was first time discussed. It was believed to be a typical S-K mode with transitions from layer by layer growth to island growth on a microscopic c-plane area on top of the micropyramid. This is evidenced by the authors with the observation that the formation probability is significantly increased on pyramids with a notably small c-plane truncated apex.

The density of the site controlled $In_{1-x}Ga_xN$ QDs grown on GaN micropyramid by MOVPE is roughly 10^6 cm^{-2} which is about six orders of magnitude lower than that of self organized III-nitride QDs synthesized by MOVPE [116]. This ultra low density strongly limits this kind of SAG QD in frontier line quantum light emitter device applications because of the low power output with few emitting sources. Naturally, one straightforward and easy solution comes up by employing the closely packed nanoscale sized GaN pyramids as template. Moreover, growing on the nanoscale offers more specific features, for example limited gradients in the ambient at the growing surface due to the decreased diffusion path along the sidewall facet (In has higher surface diffusivity compared to Ga [117]) and notably reduced temperature variations across the growth surface (In incorporation is higher at lower temperature).

Thus, the object is expected to give a more homogenous emission wavelength compared to the normally observed rainbow colored emission (namely with a red-shift of the emission position from bottom to top along the inclined facet) on multi-faceted GaN microstructures in which the MQW structure is deposited [58]. In this context, Liu *et al.* have made the first attempt [28]. Single period $In_{1-x}Ga_xN$/GaN QW was deposited on the facets of dense arrays of SAG GaN nanopyramids with a diameter of 300 nm spaced by a period of 460 nm in hexagonal geometry grown on (0001) GaN using SiO_x as mask patterned by NIL. The RT CL spectra and mapping (Figure 2.24 (a) and (b)) indicated that the three main contribution locating at 375 nm, 425 nm and 525 nm coming from the GaN template, the MQW on sidewall facets and the deep level defect band respectively. No obviously isolated emission from the pyramids top assigned to the QDs luminescence was detected. Later on, the efficient green luminescence with IQE exceeding 40 % probed by PL was realized on $In_{1-x}Ga_xN$/GaN MQW structures on GaN nanopyramids with a diameter of 250 nm and pitch distance of 450 nm by Kim *et al.* [44]. In this work, the TEM characterization has been made on the nanopyramids in the cross section geometry as shown in Figure 2.24 (c), a clear MQW structure on the facets can be observed with a QW thickness

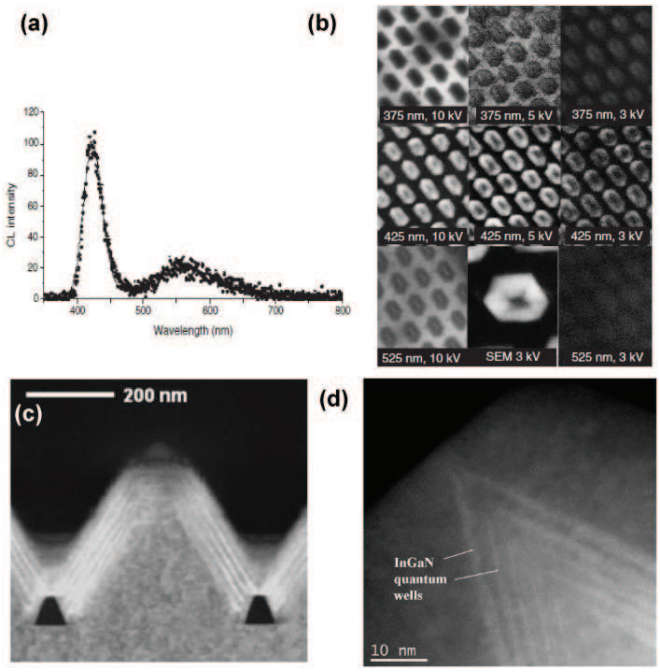

Figure 2.24: (a) A CL spectra measured on the GaN nanopyramid facet [28], (b) RT monochromatic CL mapping at different wavelength and beam voltage [28], (c) and (d) cross-section TEM image of GaN nanopyramid with $In_{1-x}Ga_xN$ MQW showing no singnal of QD structure from [44] and [108].

of 4 nm, whereas there is no formation of QDs on top. The similar observation has been recently reported by Goh *et al.* [108], the deposition of five periods $In_{1-x}Ga_xN$/GaN MQW on GaN nanopyramids of 80 nm diameter resulted in a homogeneous overgrowth of thin layer on the facet rather than the QD structures on the tip as shown in Figure 2.24 (d).

Chapter 3

MOVPE process of III-nitride semiconductors: A case study of self-assembled (SG) growth of GaN NWs

The continuous development of semiconductor microelectronic industry has broug ht tremendous improvements in our daily life in the last decades. Today, metal-organic vapor phase epitaxy (MOVPE) also known as metal-organic chemical vapor deposition (MOCVD) has become most common techniques in industry for the commercial epitaxial growth of semiconductor materials. MOVPE can produce semiconductor compounds with purity equaling or exceeding all other techniques and superlattice structures with extremely abrupt compositional variations. In this chapter, we will first summarize the fundamental growth processes, the basic principles occurring in the MOVPE system and the precursor sources used in III-nitride growth. Then, a short introduction will cover the particularities of the Aixtron close coupled showerhead (CCS) system which is used for this PhD work including the system setup and some considerations about the growth rate control. Finally, after a general description of the original catalyst-free MOVPE GaN NW synthesis previously developed in the laboratory, a systematic study will be given to discuss the MOVPE process parameters' influence on this kind of NW growths.

3. MOVPE PROCESS OF III-NITRIDE SEMICONDUCTORS: A CASE STUDY OF SELF-ASSEMBLED (SG) GROWTH OF GAN NWS

Contents

3.1 Overview of the MOPVE growth

The crystal growth named epitaxy is the process for preparing a crystal material on a single crystal wafer called substrate with certain crystal orientation in between. The crystal material and the substrate can be the same crystal (homoepitaxy) or two different crystal (heteroepitaxy) with a similar lattice parameter according to the specific availability and requirement. Epitaxy can allow the formation of extremely high quality materials, with structural and optical properties, controllable at atomic scale. The MOVPE growth processes are highly complex with numerous empirical growth parameters.

3.1.1 The fundamental physical processes during MOVPE crystal growth

Before giving a simple overview of MOVPE growth principles, we will introduce first the fundamental processes occurring during MOVPE crystal growth (thermodynamics and kinetics). Generally speaking, thermodynamic determines the driving force for the overall growth process and kinetic defines the rates for which the various steps occur. Hydrodynamics and mass transport which are intimately linked, control the rate of transport of material to the growing solid/vapor interface. The rates of the chemical reactions occurring during growth, either homogeneously in the gas phase or heterogeneously at the growing interface, also play a role. The rates of the heterogeneous processes depend on the details of the surface structure, such as the reconstruction and step structure. Each of these factors will dominate some aspects of the overall growth process.

The principle of MOVPE process is schematically shown in Figure 3.1. Atoms that you want to incorporate into the crystal are combined with complex organic molecules in carrier gas and pass over a hot wafer rotated with certain speed put in the reactor. The heat breaks up the molecules and deposits the desired atoms on the surface with a number of reactions involving both homogeneous and heterogeneous pyrolysis as well as physical processes. Finally the exhaust gas and particles will be pumped away from the reactor passing the filter and a scrubbing system for purification. By varying the organic molecules in the gas, you can change the properties and composition of the deposited crystal. It offers the possibility to grow high crystal quality layer with fine uniformity on the very large surfaces and perfectly aligned structure with the substrate in a reproducible and safe manner.

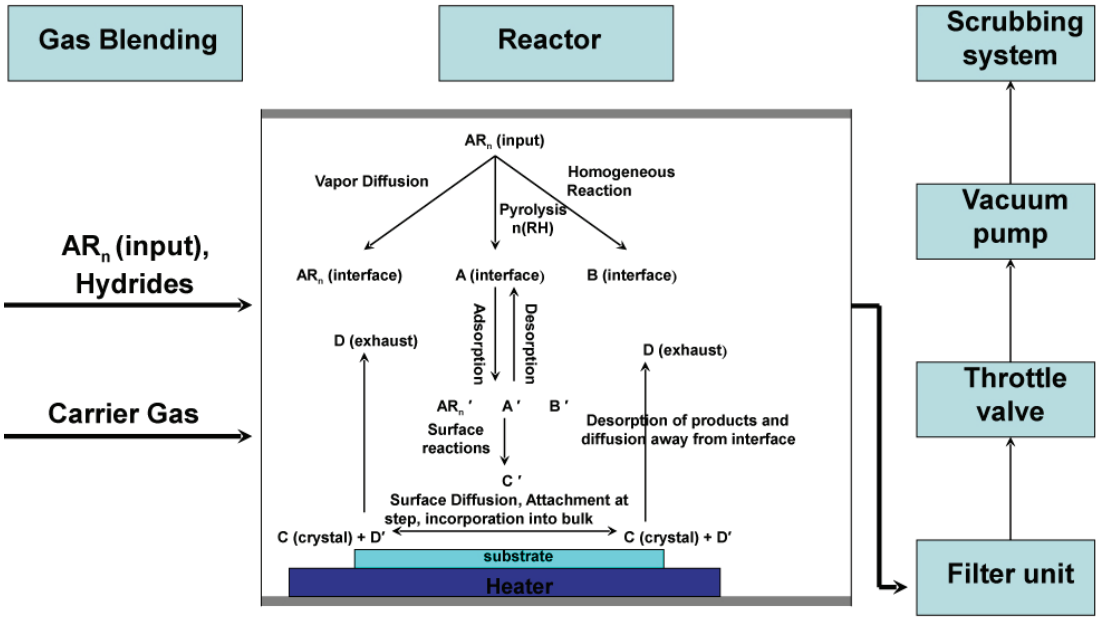

Figure 3.1: The overview of the MOVPE process.

3.1.2 The different growth regime of MOVPE

The dependence of a macroscopic quantities such as the growth rate versus external parameters like substrate temperature gave the first insights into the overall growth mechanism. For example, Reep *et. al.* [118] have examined the MOVPE growth rate of GaAs with increasing of the temperature, which allows a general categorization of the MOVPE growth into three different regimes as shown in Figure 3.2.

(I) **Kinetically limited regime:** In this regime, the growth rate is limited by the reaction rates, which are temperature dependent. Especially, the growth rate is generally governed by the desorption kinetics of CH_3. The growth rate increases with temperature in the following form:

$$V_{growth} \propto exp\frac{-\Delta E}{RT} \tag{3.1}$$

where ΔE is the Arrhenius activation energy, R is the ideal gas constant and T is the temperature.

(II) **Mass transport limited regime:** In this case, the reactions are not limited by kinetics but by the gas phase transport that limits the flux of input

precursors. The gas phase diffusion is a nearly temperature independent process in the simple case of diffusion through a mass transport boundary layer. The group III flux is expressed as follows:

$$J_{III} = \frac{D(P^*_{III} - P^i_{III})}{RT\delta_0} \tag{3.2}$$

where D is the diffusion coefficient, R is the ideal gas constant, P^*_{III} is the input partial pressure of the group III source, P^i_{III} is the group III partial pressure at the interface and δ_0 is the thickness of the boundary layer defined as the distance from the precursor concentration maximum in gas phase to growing surface. In typical case of III-arsenide or III-nitride growth, $P^*_V \gg P^*_{III}$, thus the growth rate is independent of group V flow rate, and becomes proportional to group III flux J as:

$$V_{growth} \propto J \tag{3.3}$$

This formula gives a direct explanation that in this regime, the straightforward way to increase the growth rate is the increase of the input III precursor flux in the gas phase.

(III) **Thermodynamically limited regime:** The further increase of the temperature results in a decrease of the growth rate. In this regime, evaporation of deposited crystal, etching, surface desorption and strong parasitic reactions together with the pre-deposition on the hot wall of the reactor will become dominant and consequently decrease the growth rate.

For GaN MOVPE growth, standard growth occurs at around 1040 °C which corresponds to an overlap of regime II and III. As depicted above, it shall be mostly mass transport limited with a combination of significant desorption and especially etching effects. Thus, the growth rate becomes as mass transport growth rate minus the desorption/etching rate. Particularly, the etching rate is mostly controlled by temperature, pressure and atmosphere of the reactor. In general, the H_2 causes a much higher etching rate than NH_3 or N_2. In addition, there are more parasitic reactions with higher pressure and higher temperature in the Al-content growth which can also reduce the growth rate in this regime.

3.1.3 The source molecules for III-nitride MOVPE growth

(1) **Group III molecules:** There are mainly two types of organometallic molecu les generally used in III-nitride MOVPE growth: the trimethyl (TM) ($3CH_3$)

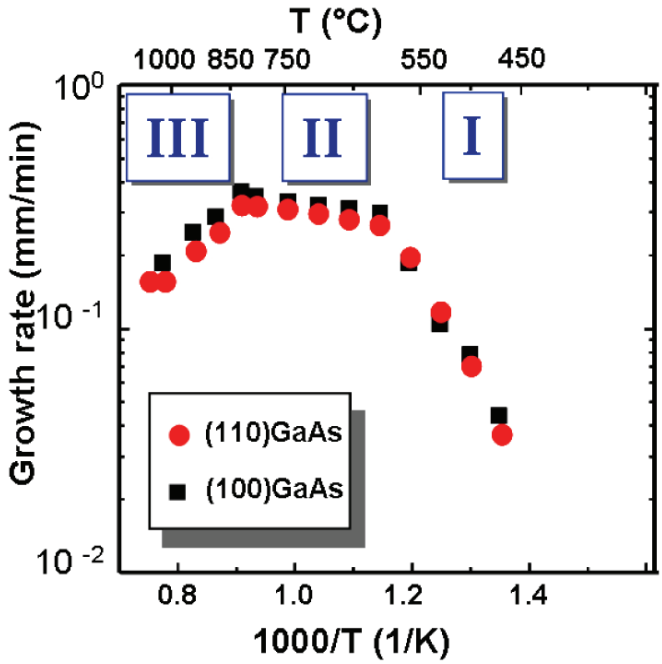

Figure 3.2: Growth rate versus reciprocal temperature for epitaxial growth of GaAs on (110) and (100) GaAs substrate.

and triethyl (TE) ($3CH_2CH_3$) alkyls linked to the metallic atom (Ga, Al, In) as schematically shown in Figure 3.3. The TM sources are frequently used because of their higher vapor pressures (see Table 3.1) and greater stability. Thus, they can be stored for very long periods at room temperature and less likely to be involved in parasitic reactions. However, in lower pressure MOVPE process, the use of TE alkyls significantly reduces the incorporation of carbon concentrations since they pyrolyze without producing the CH_3 radicals which are attributed to be the main source of carbon in the epitaxial layers. In this work, TM sources serves as III-precursors for NWs growth, whereas for the InGaN/GaN heterostructures growth at lower temperature and pressure, the TE sources are used as Ga precursor.

(2) **Group V molecules:** Ammonia (NH_3) is typically used as the nitrogen (N) source for III-nitride MOVPE growth. Due to the high volatility of nitrogen combined with the high growth temperature in GaN MOVPE growth,* it is rather difficult to produce the required high quality minority carrier devices with a low N-vacancy level, which could lead to a high residual n dopant

*It is because of both large bond strength in GaN and high stability of NH_3.

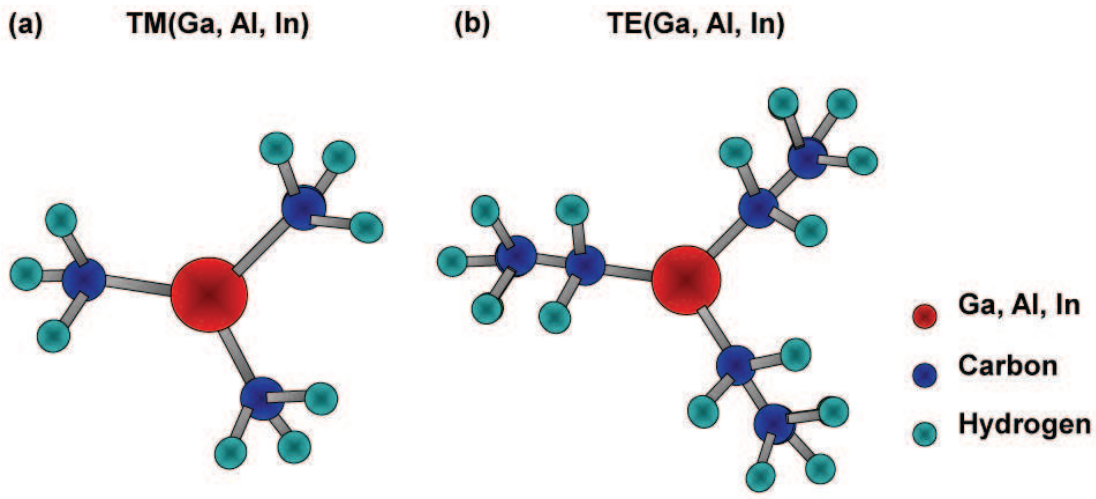

Figure 3.3: Schematic of precursor molecules used for MOVPE growth of III-nitride semiconductors: (a) TM(Ga, Al, In) and (b) TE(Ga, Al, In)

concentration in the as-grown intrinsic GaN materials [119]. A high partial pressure of NH_3 (large V/III ratio) during the growth is always required to reduce the N vacancy concentration in 2D growth.

(3) **N and p-type dopant molecules:** Si serves as the n-type dopant in III-nitride growth. The source of Si in commercial MOVPE system is silane. At room temperature, silane is a pyrophoric gas and must be handled very carefully to avoid spontaneous combustion in air. Mg has been proven to be the effective p-type dopant in III-nitride growth, although the activation energy is as high as 200 meV. Such activation energy generally requires a thermal annealing under pure nitrogen flow to activate the acceptor center. For Mg precursor, Bis(cyclopentadienyl)magnesium (Cp_2Mg) is mostly used. The other problem for the p type doping is the memory effect, which is probably due to adsorption of these precursors (Cp_2Mg) on the wall or quartz of the reactor. This makes the abrupt changes in p-type doping level impossible and special attention should be paid for the run to run reproducibility after the p-type doping process. For example, a bake of the reactor under hydrogen is necessary before the next growth.

Precursor	Melting point (°C)	Boiling Point (°C)	Vapor Pressure	
			a	b, K
TMGa	-15.8	55.8	8.07	1.703
TMAl	15.4	127	8.224	2134.83
TMIn	88.4	133.8	10.52	3.014
TEGa	-82.3	143	8.083	2.162
TEAl	-52.5	186	10.784	3.625
TEIn	-32	184	8.93	2815

Table 3.1: Melting and boiling point of Group III organometallic precursors. a and b are constant values for the calculation of saturated vapor pressure for the precursor depending on temperature as expressed in Equation 3.4.

3.2 The peculiarities of the Aixtron close coupled showerhead (CCS) MOVPE system

3.2.1 The setup of Aixtron CCS MOVPE system

In this PhD work, the Aixtron 3×2" CCS MOVPE system is used to grow the III-nitride nanostructures as shown in Figure 3.4. The MOVPE system can be divided into four major parts, *i.e.*, (1) the gas handling system consisting of alkyl (MO) and hydride (HYD) sources, necessary gases and all instruments used to control the gas flows and mixtures; (2) the reaction chamber, where the pyrolysis reaction and deposition occur; (3) the heating and temperature control system; and (4) the exhaust, pumping and pressure control system.

3.2.1.1 Gas handling system

Gas handling system mainly includes the sources (precursors and other necessary gases), and the gas mixing system. The purpose of the gas handling system is to deliver into the growth chamber precisely metered amounts of reactants without transients due to the changes of pressure or gas flows .

The sources used in our Aixtron CCS MOVPE system are the precursors of group-III, group-V, dopants, and the carrier gases (nitrogen (N_2) and hydrogen (H_2)). Extra purifiers are used for further reduction of oxygen and other contaminants in the highly purified gases of NH_3, N_2 and H_2. TMGa, TEGa, TMAl, and

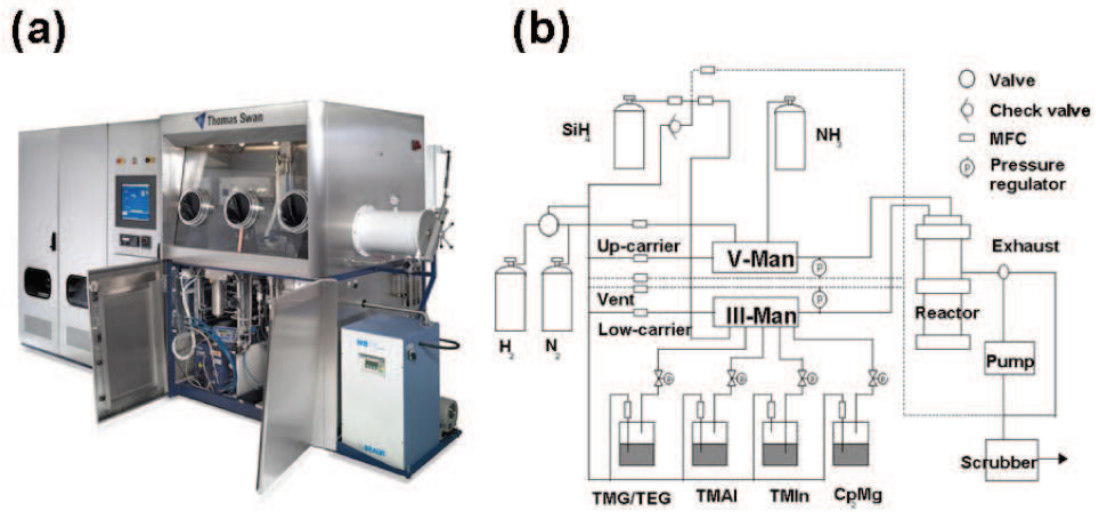

Figure 3.4: (a) A photography and (b) a schematic of the Aixtron 3×2" CCS MOVPE system.

TMIn are used as the group-III precursors of gallium (Ga), aluminum (Al), and indium (In), respectively. High-purified NH_3 is used as the group-V precursor of nitrogen (N). Cp_2Mg, and 1000 particles per million (ppm) SiH_4 diluted in H_2 are used as the p and n-type dopant precursors respectively. High purified H_2 (99.999 %) is generally used as the carrier gas to grow GaN 2D template, for the substrate and reactor bake step, and as the carrier and pushing gas for MO sources. High purified N_2 (99.999 %) is employed as the carrier gas for the growth of GaN nanostructures on GaN 2D template, InGaN heterostructures and to activate p-type dopants.

In order to precisely control the reaction, the amounts of reactants delivered to the chamber have to be precisely controlled by the gas handling system. The mass flow controller (MFC) can accurately and reliably measure and control the molar flow rates of gases. Therefore, for gas phase sources such as NH_3, SiH_4, N_2 and H_2, which are stored in pressurized cylinders, the MFC can be solely used to control the molar mass flow rates precisely. For solid or liquid phase sources such as MO precursors (stored in the stainless-steel cylinders called bubblers), the exact amount of materials is controlled with the MFC as well as the pressure controller and temperature controllers (thermal bath of the bubbler). The MO source carrier gas flows into the bubbler to transport metalorganic precursor vapors. After that, the MO push gas dilutes the mixture of carrier gas and metalorganic precursor to avoid the precipitating and contaminating the gas line.

More H_2 or N_2 will be flowed though the MO run line to further dilute the MO precursors and take the mixture into the reactor. Figure 3.5 shows the gas flow schematic of one MO precursor. The saturated vapor pressure of MO precursor

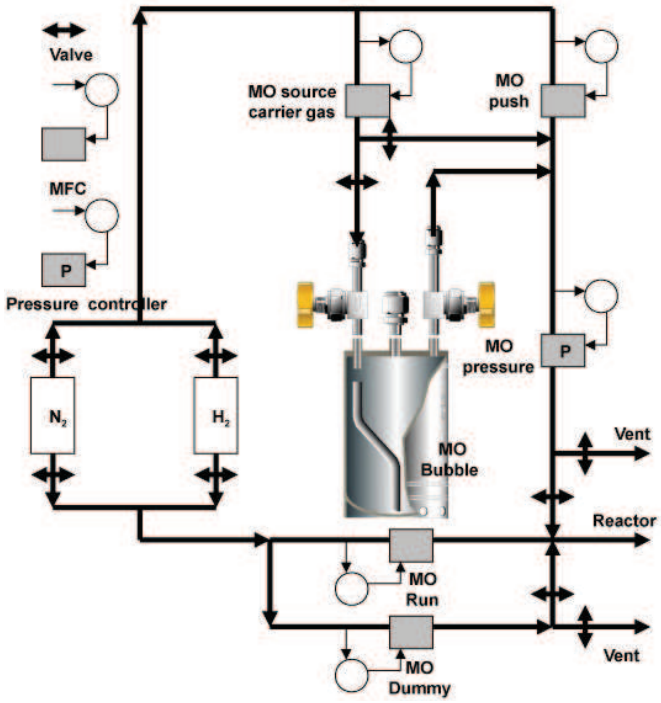

Figure 3.5: Gas flow schematic of the MO bubbler source.

depends on temperature following the relation:

$$\lg P_{vapor,MO} = a - \frac{b}{T} \tag{3.4}$$

where $P_{vapor,MO}$ is the saturated vapor pressure of the MO source in unit of mmHg (or Torr), T is MO source temperature in unit of Kelvin, a and b are constants as listed in Table 3.1 for common MO precursors. A controlled amount of MO precursor can be transported by controlling the exact amount of carrier gas flow with MFC through the bubbler using the ideal gas equation. The molar MO precursor flow can be expressed as:

$$F_{M,MO} = \frac{P_{vapor,MO}}{RT} F_{V,MO} = 0.0446 \frac{mmol}{cm^3} \frac{P_{vapor,MO}}{P_{total}} F_{V,total} \tag{3.5}$$

where $F_{M,MO}$ is the molar flow rate of the MO precursor (given in moles per minute), $F_{V,MO}$ is the volume flow rate of the MO precursor (given in standard

cubic centimeter per minute (sccm)), P_{total} is the total pressure of the gas mixture. $F_{V,total}$ is the total volume flow rate of the gas mixture (given in sccm). In most cases, the partial pressure of the MO precursors is much smaller than the partial pressure of the carrier gas. Hence, two approximations can be made

$$P_{total} \approx P_{vapor,carrier} \tag{3.6}$$

$$F_{V,total} \approx F_{V,carrier} \tag{3.7}$$

where, $P_{vapor,carrier}$ is the partial pressure of the carrier gas which is regulated by the pressure controller (PC) and $F_{V,carrier}$ is the volume flow rate of the MO source carrier gas flow (given in sccm). Therefore, the molar flow rate of the MO precursors can be reduced or increased in the following ways:

- **Change of MO source volume flow rate (MO source carrier gas flow)**

  The MO molar flow rate is increasing with increasing of the source carrier gas flow. This is the regular way to change the mole flow rate. However due to the limitation of the MFC, the molar flow rate has a lower and upper limit.

- **Change of MO source carrier gas pressure**

  The MO molar flow rate is increasing with decreasing of the source carrier gas pressure. In practice, the pressures of bubblers are at least 300 mbar above that of growth chamber.

- **Change of thermal bath temperature**

  The MO molar flow rate is increasing with increasing of the thermal bath temperature. The temperature will change the saturated vapor pressure of MO precursors. Generally, this temperature should be kept constant. It is in practice not possible to change the bubbler temperature during the growth due to transients.

- **Hardware modification**

  This could be done by either put a double dilution to further reduce the volume flow rate or directly change the MFC of the MO source carrier gas flow rate to reach the required range.

The other important parts of the gas handling system includes: 1) The reactor atmosphere switching time shall be minimized by adding enough carrier gas to the MO Run line to lead to a fast delivery of reactants through the gas line to the growth chamber. This is essential to get the sharp surface especially in heterostructures growth; 2) The flow rate of the MO run line shall be adjusted automatically to keep the total injection flow rate constant. Hence, the injection gas velocities and the reactor pressure are stable during the growth even when the flow rates of precursors are frequently changed. This is particularly important for complex structures in which specific sharp doping profile, abrupt interfaces and alternatively grown of thin multilayers with different composition are needed.

3.2.1.2 Reactor

The reaction chamber of the Aixtron CCS MOVPE system is a vertical-geometry close coupled showerhead reactor as shown in Figure 3.6. The main body of the reactor is made of stainless steel. There is a quartz liner in between the metallic reactor wall and the susceptor, which can protect the reactor wall from aggressive reactants. The substrates are positioned and held on a circular horizontal disk called susceptor (with three rounded 2" indentations) which is made of graphite and covered with 100 μm thick SiC thin layer to avoid NH_3 etching.

Thus, it allows to be heated up to over 1200 °C due to the high materials melting point. During growth, the showerhead lid is mechanically locked and sealed by vacuum established between two O-ring seals (can be pumped < 1 mbar).

In horizontal reactor geometry the precursor arrives horizontally with respect to the substrate surface and may create flow vortices responsible of concentration gradients along the susceptor. In the CCS technology, reagents (MO and Hydride) are introduced vertically into the reactor through the showerhead surface over the entire area of deposition and the vertical geometry is therefor used to improve uniformity of doping, composition and thickness on the whole wafer. The showerhead is close to the substrates (11 mm in III-nitride growth in this work) and is constructed to enable precursors to be separated right up to the point where they are injected onto the substrates through a multiplicity of small tubes to create a very uniform distribution of reagent gases. This geometry also completely separates the MO and Hydride molecules until they reach the chamber avoiding pre-reaction during the gas transport. Moreover, due to the vertical geometry, the gases that react near or on the substrate do not re-mix with the

inlet gas flow, so that the chemical concentration boundary conditions in gas phase can be precisely controlled with very little hysteresis or memory effects. Therefore, the uniformity of growth rate, doping and composition can be well achieved by this design.

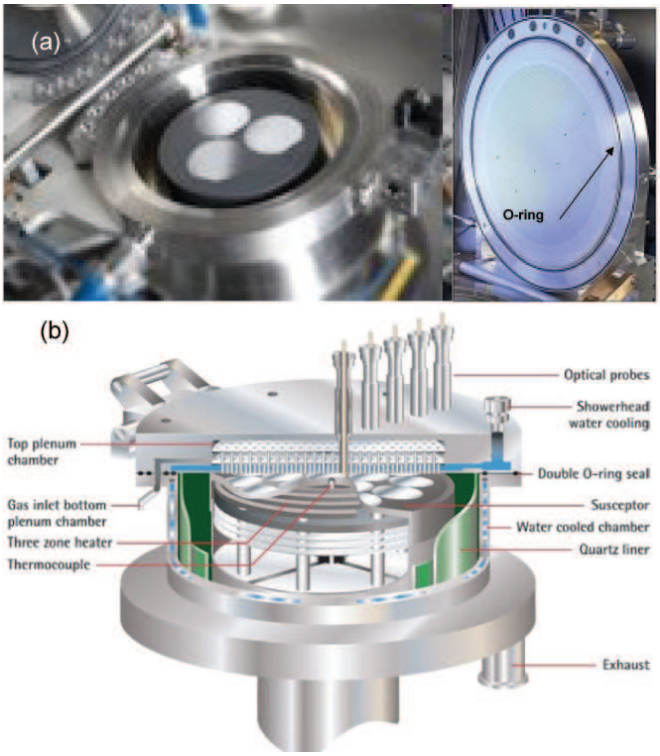

Figure 3.6: (a) A photography, and (b) a detailed schematic of the Aixtron 3×2" CCS MOVPE reaction chamber.

The showerhead and the reactor wall are cooled (or heated) by a water flow provided by an external circulation chiller system with a controlled warm temperature of 50 °C. This will keep the showerhead surface at a relatively low temperature as 150 °C even the growth temperature is above 1000 °C. The cold showerhead surface can eliminate the reagent adsorption/condensation and undesired parasitic reaction directly after the injection into the reactor which is especially important for AlGaN and GaN growths at high pressure and temperature .

Additionally, small windows are opened on top of the showerhead. An optical interferometry system is positioned on one window in order to measure *in situ* the surface morphology and the growth rate. The other windows can be used to

trace the substrate surface temperature in different zone during calibration runs by inserting temperature pyrometer probes.

3.2.1.3 Heating and temperature control system

The system is heated by a three zone heater located inside of the susceptor support and below the susceptor. The heater consists of three sets of coils made of Tungsten Rhenium (Zone A, B and C respectively as shown in Figure 3.7). Each Zone has its own power supplier and can be controlled separately to get a homogeneous temperature distribution across the susceptor surface. This point is important to guarantee a uniform growth regarding the layer thickness,* doping concentration and In incorporation during InGaN quantum well deposition. A thermocouple is mounted under the heater to measure the temperature. As the thermocouple does not directly measure the temperature of the susceptor surface, three windows for pyrometers probes are installed on top of the reaction chamber (as shown in Figure 3.6) in order to measure the real surface temperature. Then, the current power of the three different zones will be balanced to minimize the substrate temperature gradient (Normally the Zone C power is kept constant at 80 % and the power of Zone A and Zone B are adjusted in this work.). The susceptor is always rotated (50 round/min in our growth) during the process to further improve the temperature homogeneity and avoid the SiC coating crack induced by the temperature gradient.

3.2.1.4 Exhaust and low pressure control system

The pumping and low-pressure control system (or vacuum system) is connected to the reaction chamber through an outlet at the bottom. The vacuum system basically consists of three parts, *i.e.*, (1) a rotary pump, (2) two stage gas exhaust particle filters and (3) a throttle valve. The reaction chamber pressure is controlled by adjusting the position of the throttle valve flap with a MKS pressure controller unit.

The exhaust effluent leaving the reactor consists of hot gases and particles. They must be trapped before reaching atmosphere to protect the environment and the system components. The particles are trapped by the two-stage particle filters. The toxic parts in the exhaust gases are then absorbed in the Toxic Gas

*The temperature variation could even change the chemical boundary thickness uniformity, pre-reaction rate and induce local flow vortices above the substrate surface.

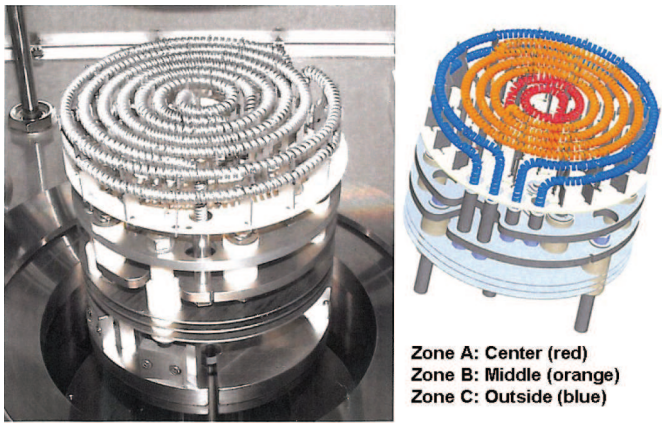

Figure 3.7: A photography (left) and a schematic (right) of the heater coils system

Absorber unit (scrubbing system) before they are released into the environment.

3.2.2 The growth rate control in Aixtron CCS MOVPE system for GaN growth

As depicted in section 3.1, the MOVPE growth of high quality GaN crystal at high temperature ($\sim$ 1000 °C) is limited by the mass transport limited region where the growth rate is therefore governed by in the simple case of diffusion through a mass transport boundary layer with nearly temperature independent:

$$V_{growth} \propto D\frac{C_{MO}^{Max} - C_{MO}^{Surf}}{RT\delta_0} \tag{3.8}$$

where D is the diffusion coefficient, R is the ideal gas constant, T is the growth temperature, C_{MO}^{Max} and C_{MO}^{Surf} is the maximum mass fraction concentration of the MO precursors in the gas phase (in MOVPE GaN growth, the active precursor for III atoms is MMGa as a by product of TMGa after thermal decomposition). At the susceptor surface, this concentration is always zero because of the depletion as shown in Figure 3.8. δ_0 is the thickness of the chemical boundary layer: the distance from the precursor concentration maximum in gas phase to growing surface, as schematically defined in Figure 3.9. There are two straightforward ways to modify the GaN MOVPE growth rate in this regime. First, we could change the C_{MO}^{Max} in the gas phase which has a proportional behavior with the growth rate. This can be easily managed through turning the imputing MO

precursor carrier gas flow by the methods as discussed in last section. Another solution is to modify the δ_0 thickness which has a reverse relationship with the growth rate. In the Aixtron CCS MOVPE system, the thickness of chemical boundary is related to process parameters mainly by carrier gas flow rate and composition (ratio between N_2/H_2) under thumb rules:

$$\delta_0 \propto F^{\frac{1}{2}} \tag{3.9}$$

$$\delta_0 \propto \rho^{-\frac{1}{2}} \tag{3.10}$$

where F is the carrier gas flow and ρ is the carrier gas density, for example in the two kind of carrier gas used in this work the density of N_2 is about twelve time larger than that of H_2. It means, the MOVPE growth rate of GaN can be increased either by decreasing the carrier gas flow or increasing its density.

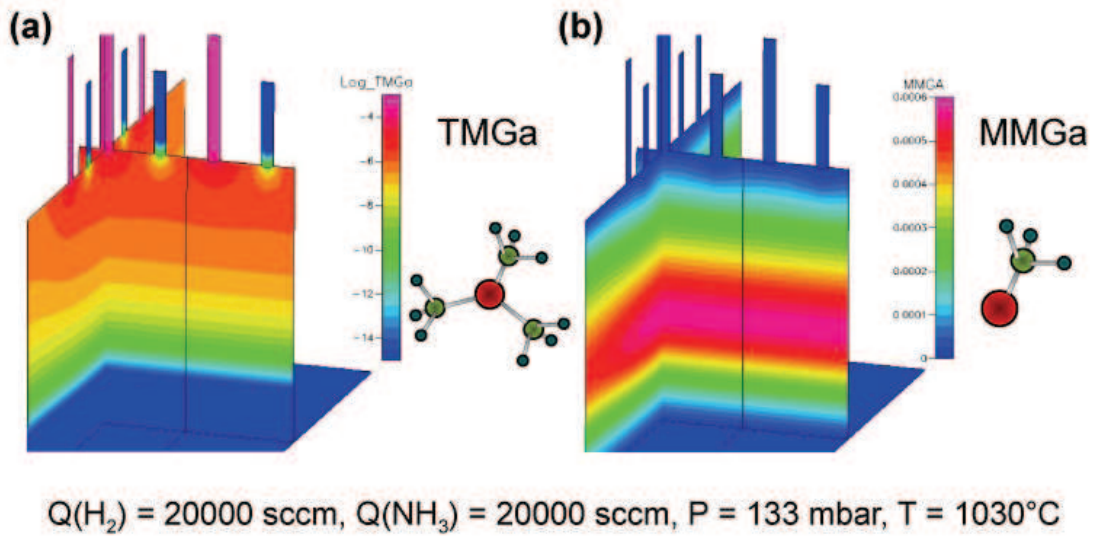

Figure 3.8: The simulated concentration distribution of (a) TMGa (mass fraction in logarithmic scale) and (b) MMGa (mass fraction in linear scale) in gas phase of Aixtron CCS MOVPE System at the indicated growth conditions. [from www.aixtron.com]

Although the other growth parameters do not have a direct influence on C_{MO}^{Max} and δ_0 in this regime. They could contribute to the variation of the growth rate in other ways like gas phase pre-reactions, which may form GaN nanoclusters and consume the MO precursor thus reducing the growth rate. In this context, two main factors should be considered: one is the reactor pressure and another is

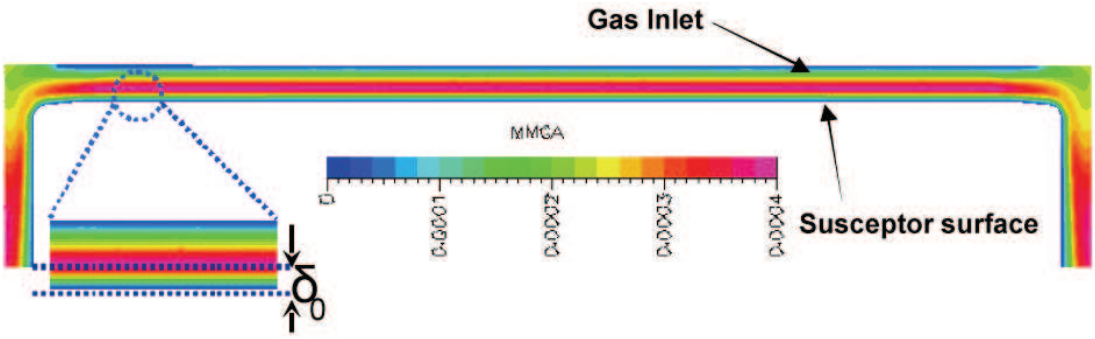

Figure 3.9: The schematically definition of chemical boundary thickness in MOVPE growth in terms of the MMGa mass fraction concentration distribution. [from www.aixtron.com]

the height of the susceptor (chamber gap height) that can be adjusted in specific for Aixtron CCS MOVPE system. As shown in Figure 3.10, the increasing of the reactor pressure will reduce the GaN growth rate due to the enhanced parasitic reaction in gas phase. This is because of the reduced efficiency of TMGa precursor at higher partial pressure due to the enhanced reaction kinetics and nano-cluster formation [120].* However, the reducing of the chamber gap could give a hotter showerhead surface and results in a faster growth rate [121].

3.3 Systematic study of the MOVPE parameters' influence on self-assembled (SG) GaN NWs growth

3.3.1 General description of the MOVPE SG GaN NWs growth

The MOVPE SG GaN NWs are grown on c-sapphire substrates (Kyocera with a miscut of 0.3°) of R$\bar{3}$c space group. The usual growth direction of GaN on c-sapphire is [0001] with an in-plane rotation of 30° of the unit lattice with respect to c-sapphire as shown in Figure 3.11 [122]. This rotation reduces the lattice mismatch to 13.9 %. The detrimental effects of performing GaN growth on such

*It is due to the reduced mean free path length and higher collision probability of molecules at elevated pressures.

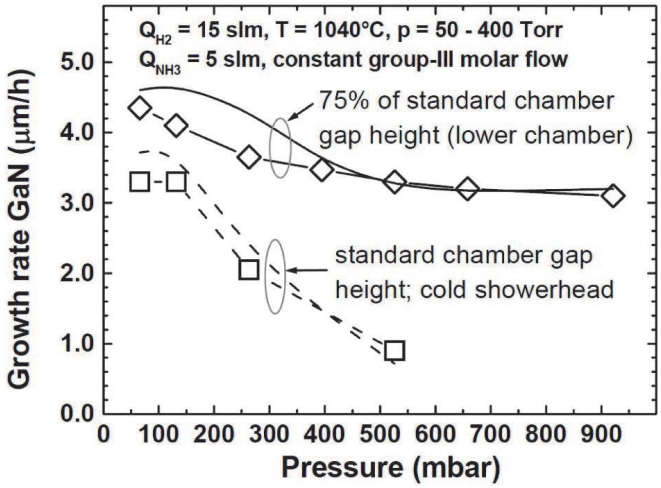

Figure 3.10: Growth rate as a function of pressure with two different chamber gap heights [121].

substrate with large lattice mismatch are usually managed by sophisticated processing like surface nitridation and low temperature buffer layers deposition in 2D growth to get low dislocation density and flat surface.

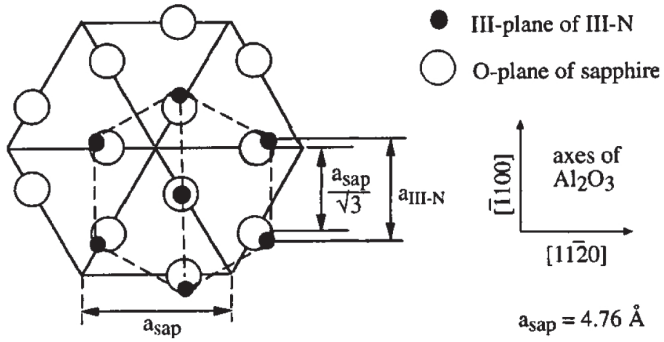

Figure 3.11: Schematic representation of in-plane atomic arrangement in the case of (0001) GaN film grown on c-sapphire substrates.

The MOVPE growth of SG GaN NWs was originally developed by former PhD student Dr. Robert Koester in the lab and can be summarized into three main steps (please see detailed growth parameters in PhD thesis of Dr. Robert Koester.).

(1) **Surface preparation**

- Surface cleaning: bake of c-sapphire substrate to remove dust and contaminations;
- Standard c-sapphire surface nitridation using NH_3 to form very thin AlN layer;
- *In situ* SiN_x layer deposition using silane and NH_3;
- Annealing of SiN_x layer with NH_3 to favor the formation of hexagonal prismatic shaped GaN nucleation seeds.

(2) **Seeds nucleation**

- Nucleation of GaN seeds with TMGa and NH_3.

(3) **NWs growth**

- Growth of GaN NWs by TMGa and NH_3 with *in situ* silane injection.

The c-sapphire surface nitridation step combined with the SiN_x annealing ensures the formation of a prismatic hexagonal nucleation disc with flat top surface directly grown at high temperature which is rather important to get the GaN NWs geometry. The *in situ* deposition of very thin SiN_x ($\sim$ 1.5 nm) is probably not continuous. It allows forming spontaneously small openings *i.e.* confined site for seeds nucleation. Low gas phase V/III ratio, high atmosphere pressure and *in situ* silane injection were proved to be critical for maintaining the NWs geometry with a height/diameter aspect ratio ($>$ 10). A typical as-grown GaN NW sample is shown in Figure 3.12 exhibiting an epitaxial growth with the substrate. These NWs have a diameter ranging from 300 nm to several μm with a height variation between several μm to tens of μm with no obvious tapering effect [65].

3.3.2 Process parameters study of MOVPE SG GaN NWs

The process parameters of the III-nitride 2D MOVPE growth has been widely studied [123], [124], [125]. These studies have turned out to be critical for the desired structure growth with controlled morphology and thickness, a further optimization of the crystal quality and the fundamental understanding of the growth mechanism. In the case of MOVPE SG GaN NW growth, we have succeed to achieve such structure with high crystalline and optical properties. A complete

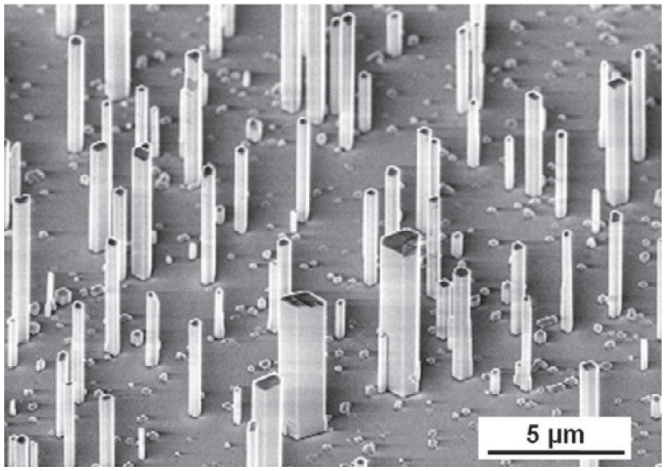

Figure 3.12: A typical 45°-tilted SEM image of an array of as-grown MOVPE SG GaN NWs on c-sapphire substrates [65]

process parameters study is now necessary to improve the control of the NW morphology in terms of nucleation density, size and vertical growth rate. Moreover, for practical purpose, MOVPE technique is known to be a complex process involving various critical parameters. Thus, the aim of this systematic study is also to set some reference points to improve the control and the reliability of the NW growth process.

For the simplicity and clarity of the study, the MOVPE process parameters (growth temperature, percussor flow, V/III ratio, carrier gas flow and reactor pressure) have been varied independently only during Step II and III for seed nucleation and NW growth stage. The total gas flow provided to the reactor is kept constant by balancing the carrier gas flow in the MO and HYD feed lines (except in the study of the carrier gas flow influence) and the molar flow ratio between TMGa and silane is fixed at 676.

3.3.2.1 The growth temperature

To evaluate the effect of the growth temperature on the SG MOVPE NW growth technique, a series of growths varying the reactor temperature from 850 to 1050 °C with a step of 50 °C was carried out as shown in Figure 3.13. This temperature range is chosen to be in the mass transport limited regime with no dependence of the growth rate on the growth temperature itself. It can be observed that the morphology (diameter (D) and length (L)) and the density (ρ) of the NWs array

have a large deviation at different temperatures, a quantitative statistic for the D, L and ρ of single NWs in each growth are plotted in Figure 3.14 as a function of the growth temperature.

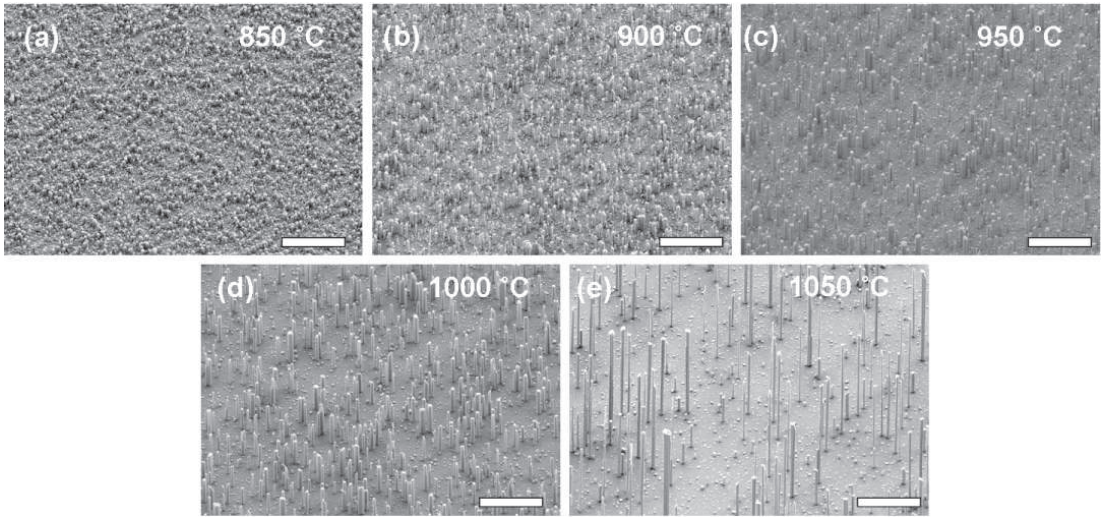

Figure 3.13: Typical 45°-titled SEM images with different NWs growth temperatures (a) 850 °C, (b) 900 °C, (c) 950 °C, (d) 1000 °C, and (e) 1050 °C respectivly. The scale bars are 10 μm.

With increasing the growth temperature, the NW average diameter gradually increases from 291 to 535 nm as observed in Figure 3.14 (a). This tendency can be understood from the reduced species diffusion length at lower temperature. It could result in the smaller NW seed diameter due to the limited lateral diffusion length of the atoms before incorporating into the crystal lattice. In contrast, the NW density exhibits a reverse behavior with temperature compared to the NWs diameter: a decrease by a factor of 50 becomes evident when the temperature is increased from 850 to 1050 °C as shown in Figure 3.14 (b). This may also be attributed to the larger adatoms diffusion length at higher temperature that reduces the nucleation site density.

In addition, as mentioned, in this temperature range (850 to 1050 °C), the growth rate is limited by mass transport. This means the total amount of deposited material (volume V) of the NW array remains constant in each growth. To verify this point, we first deduce the V value supposing that NWs are cylinder: $V = \rho\pi(\frac{D}{2})^2 L$ using D, L and ρ values extracted from the SEM image of the growth at 850 °C. Based on the mass transport limited assumption (constant V), the NW length for the other growths can be calculated from the V, the measured

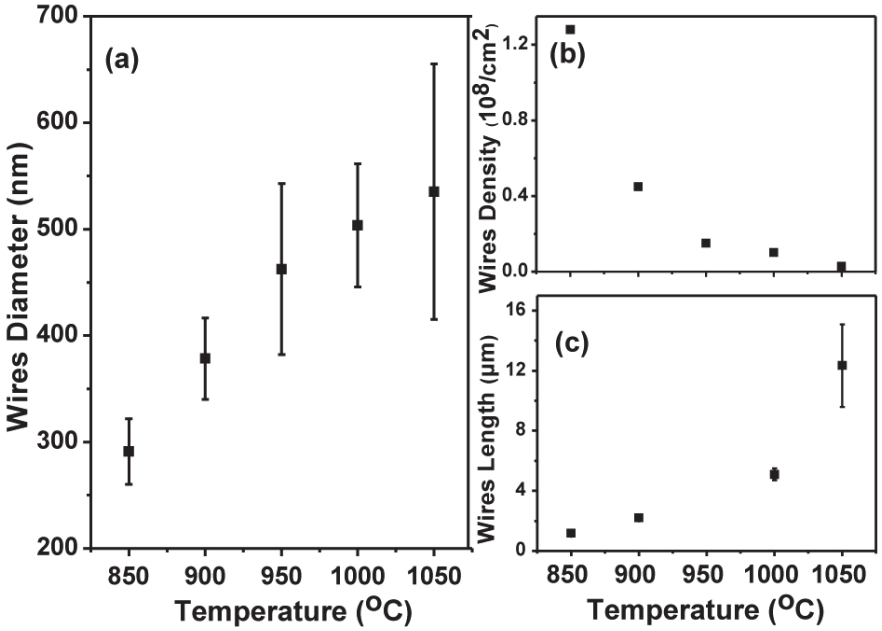

Figure 3.14: The statistic of growth temperature in MOVPE SG GaN NW growth as a function of (a) Diameter, (b) Density and (c) Length.

D and the measured ρ values.

x (°C)	$(L_x)_{calculated}$ (nm)	$(L_x)_{measured}$ (nm)
900	2010	2202
950	4089	4102
1000	5156	5090
1050	16743	12339

Table 3.2: Calculated and measured values of the NW lengths for growths at different temperatures.

As a result, the calculated NW length (L) is given in Table 3.2 for the growth at different temperature in comparison with the measured values extracted from the SEM observation. As expected, there is a good match between these two values indicating the accuracy of the mass transport limited assumption, except for the growth at 1050 °C, for which the measured length 12.3 μm is much smaller than the calculated value 16.7 μm. This result can be partially attributed to the fact that the NW length has been already beyond the adatoms diffusion length along the NW sidewall ($\sim$ 7.7 μm in this growth condition which will be deduced

in Chapter 4.1.2.2). Thus, some species can not contribute to the crystal growth and result in a reduced growth rate. This point concerning the adatoms NW sidewall surface diffusion will be discussed more in detail in Chapter 4.1.2.2.

3.3.2.2 The V/III ratio and the amount of precursors flow

The V/III ratio corresponds to the molar ratio of group V (NH_3) and group III (TMGa) precursor flow. As discussed in Chapter 3.1.2, the GaN 2D growth is always performed with high V/III ratio over 1000 due to the high volatility of the N atoms during MOVPE process. For one-dimensional GaN NW growth the lateral growth rate ($V_{<1\bar{1}00>}$) must be smaller than the vertical growth rate ($V_{[0001]}$). Previous study has concluded that once the GaN hexagonal nucleation seeds are formed, a low V/III ratio favors a higher growth rate along the [0001] axis whereas a larger growth rate along [10$\bar{1}$0] axis is obtained for high V/III ratio (see Figure 3.15) [126].

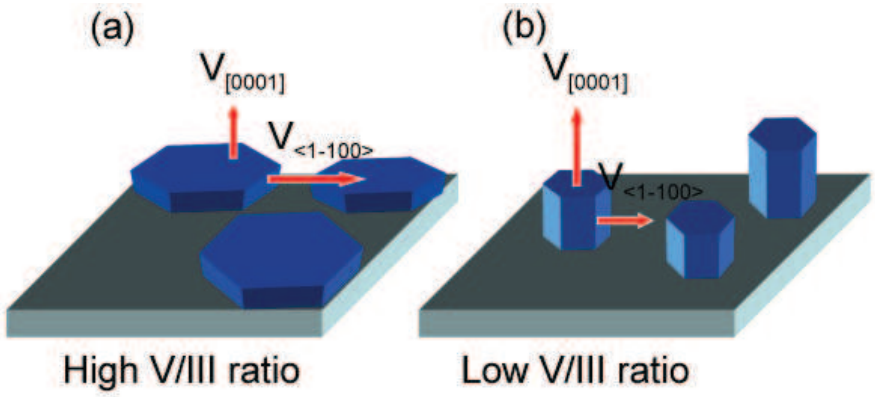

Figure 3.15: A schematic showing the different relationship of the growth rate along c and m axis at (a) high and (b) low V/III ratio. The longer the red arrow is, the larger the growth rate.

In order to have more understanding about this point, a series of three experiments have been carried out at the same V/III ratio fixed at 16 (the typical value for the SG MOVPE NWs growth) with various V and III precursor flows as shown in Figure 3.16 for (a) (50 sccm NH_3, 60 sccm TMGa), (b) (75 sccm NH_3, 90 sccm TMGa) and (c) (100 sccm NH_3, 120 sccm TMGa). It is observed that the GaN NW diameter differs in each growth whereas the V/III ratio is the same. With increasing of precursor flow, the average NW diameter is increased from 503 to 680 nm as shown in Figure 3.17 (a). This gives an indication that

the quantity of precursors flow is probably also a key parameter to control the NW diameter for low V/III ratio conditions.

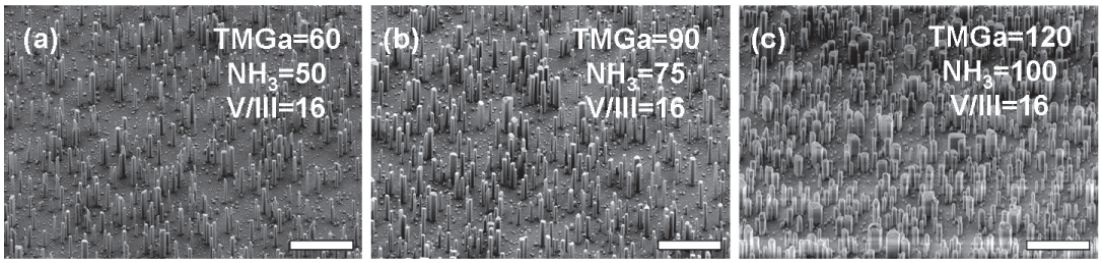

Figure 3.16: 45°-titled SEM image of the as grown SG GaN NWs array with different precursor flow (a) TMGa = 60 sccm, NH_3 = 50 sccm, (b) TMGa = 90 sccm, NH_3 = 70 sccm and (c) TMGa = 120 sccm, NH_3 = 100 sccm. The V/III ratio is the same as 16 for all the growth. The scale bars are 10 μm.

To further investigate the influence of the quantity of precursor flow and the V/III ratio on the NW diameter, series of growths with different TMGa flow (30, 60 and 90 sccm) and NH_3 flow (50, 200 and 400 sccm) were performed as shown in Figure 3.18. The precursor flow and V/III ratio are indicated in each SEM image for clarity (NH_3 flux increases from left to right, TMGa flux increases from top to bottom). As a result, an opposite observation between the NW diameter and the V/III ratio is observed. In Figure 3.19 (a), at the fixed TMGa flux in each case (30, 60 and 90 sccm respectively), with the increasing of the NH_3 flux from 50 to 400 sccm (an increase of the V/III ratio), the NW diameter becomes larger. However, in Figure 3.19 (b), if we plot the data by keeping the NH_3 flux constant (50, 200 and 400 sccm respectively) with the increase of the TMGa flux from 30 to 90 sccm (a decrease of the V/III ratio), the NW diameter becomes larger.

This controversy result further confirms that the V/III ratio is not the only factor that affects the NW diameter for low V/III ratio (in our study < 500). However, if we solely link the NW diameter to the precursor flow, a consistent conclusion about the NW diameter control can be deduced in both situations: the NW diameter becomes larger with higher precursor flow. We can finally conclude that the NW diameter is also controlled by the precursors flow and not only by the V/III ratio in the NW growth regime.

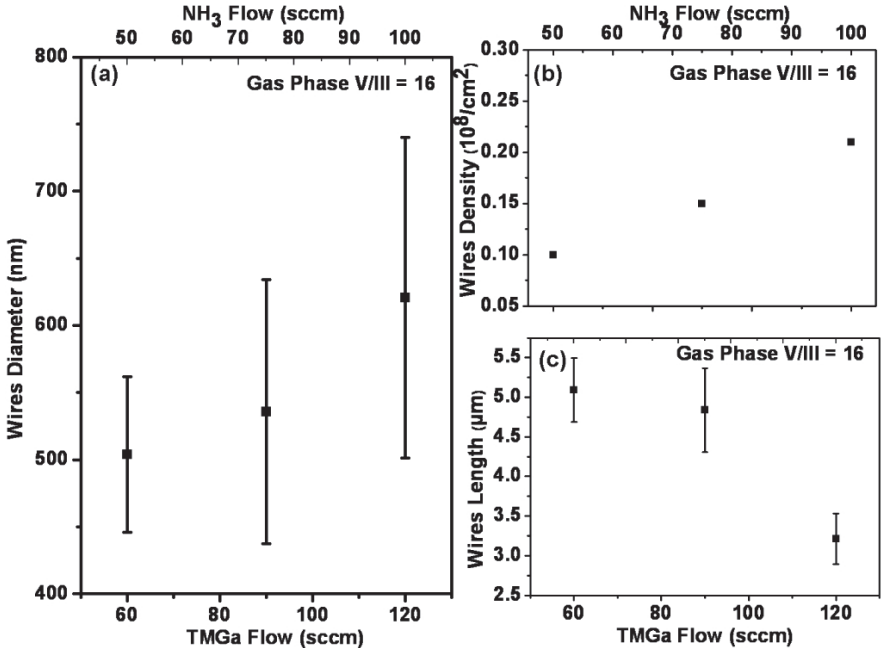

Figure 3.17: The statistic of TMGa flow in MOVPE SG GaN NW growth as a function of (a) Diameter, (b) Density and (c) Length.

3.3.2.3 Carrier gas flow

The carrier gas flow transports the precursors into the reactor chamber and determines the GaN growth rate in the mass transport limited regime following the thumb rules as depicted in Equation 3.8, 3.9 and 3.10 for 2D growth. Its influence on the NWs growth has been demonstrated using four different N_2 carrier gas flow rate (500, 1000, 2000 and 4000 sccm) as shown in Figure 3.20.

An obvious increase of the NW diameter from 360 to 760 nm is observed, when the carrier gas flow is gradually decreased from 4000 to 500 sccm (see Figure 3.21 (a)). This could be explained by the fact that the 'effective' TMGa/silane mole flow ratio in the reactor atmosphere is increased for lower carrier gas flow growth even this value is intentionally kept constant in the input gas flow. A higher growth rate (higher TMGa concentration) is expected with lower carrier gas flow due to the reduction of the chemical boundary thickness δ_0 as indicated in Equation 3.8. This gives a higher TMGa/silane mole ratio in growths with lower carrier gas and leads to a larger NW diameter (see Chapter 4.1.2.1).

The volume of the NWs for the growth with different carrier gas flow, normalized with respect to the growth using 4000 sccm carrier gas, is listed in Table 3.3

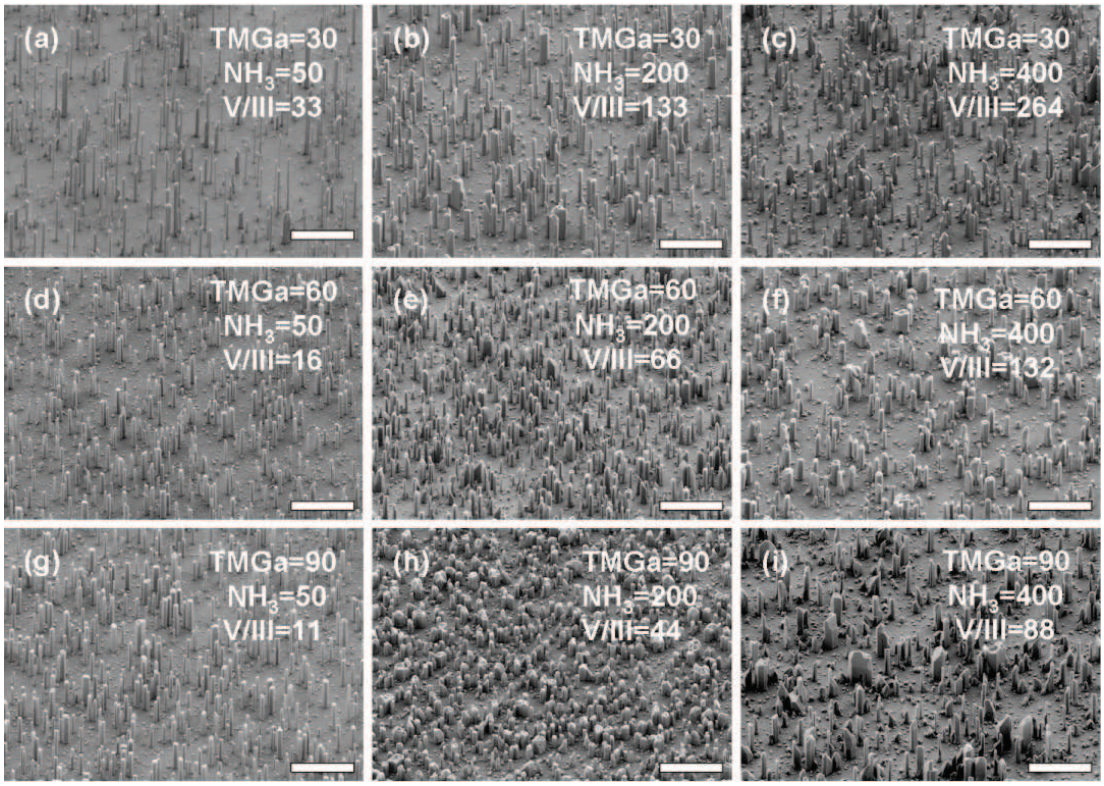

Figure 3.18: 45°-titled SEM image of the as-grown SG GaN NWs array with different precursor flows. The precursor flow of TMGa and NH_3 is indicated in each image for clarity. The scale bars are 10 μm.

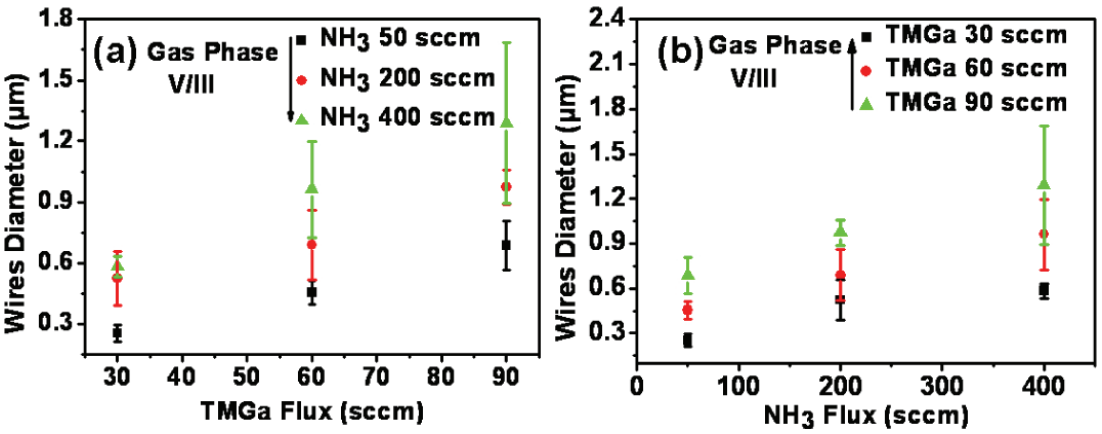

Figure 3.19: The plot of SG GaN NW diameter as a function of (a) TMGa flow and (b) NH_3 flow with different V/III ratios.

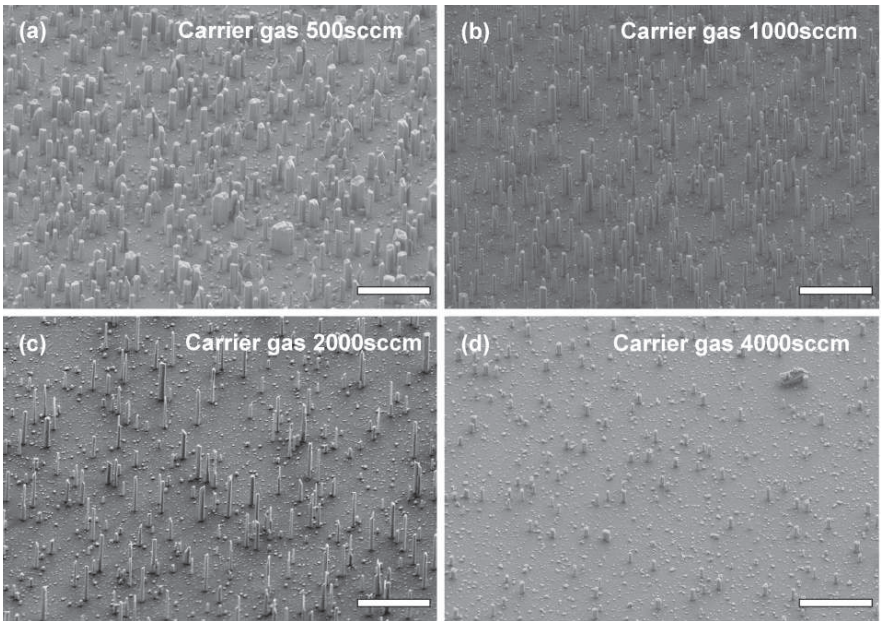

Figure 3.20: The MOVPE SG GaN NW growth with carrier gas flow of (a) 500 sccm, (b) 1000 sccm, (c) 2000 sccm and (d) 4000 sccm with the other growth parameters and process the same. The scale bars are 10 μm.

for a cylindrical shape assumption. These measured values are compared with the calculated ones from Equation 3.8 and 3.9, which define the growth rate (the volume) of the GaN 2D deposition in mass transport limited regime regarding carrier gas flow rate. Surprisingly, there is a large difference between these two values. The quantity of the incorporated materials increases significantly when the carrier gas flow becomes smaller. This indicates that the carrier gas has probably other dominative effect on the growth except than just changing the chemical boundary thickness. Actually, with increasing of the carrier gas flow, the dwell time of the precursor in the reactor chamber could be largely decreased. We suspect that this precursor dwell time plays a key-rule in the MOVPE NW growth. For instance, if there is a decrease of the dwell time, the precursor arriving between the NW either in gas phase or on substrate surface could be desorbed and be pumped away from the reactor instead of having enough time to diffuse around and contribute to the NW growth. This could in principle decrease the growth rate of NW growth with larger carrier gas flow.

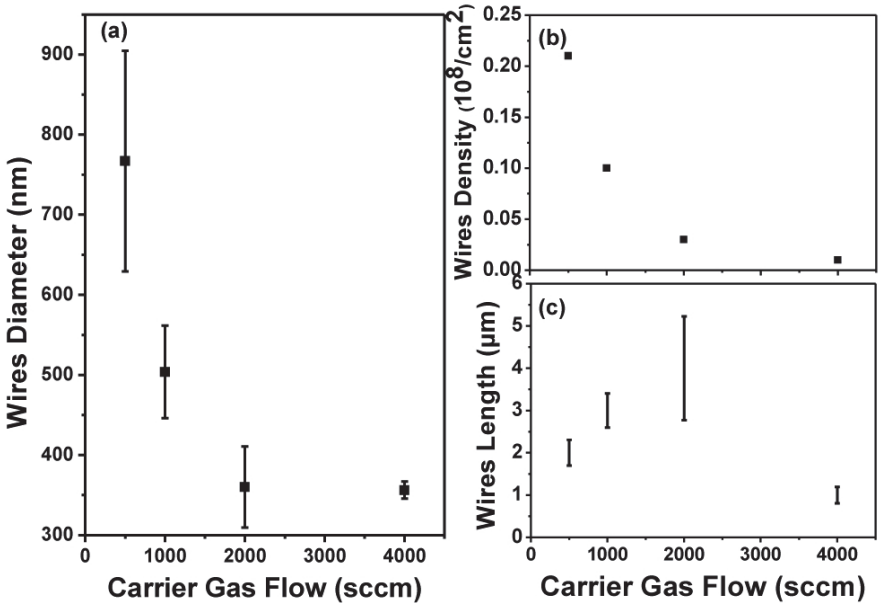

Figure 3.21: The statistic of carrier gas flow in MOVPE SG GaN NW growth as a function of (a) Diameter, (b) Density and (c) Length.

x sccm	$(V_x/V_{4000})_{calculated}$	$(V_x/V_{4000})_{measured}$
500	$2\sqrt{2}$	243.57
1000	2	31.58
2000	$\sqrt{2}$	10.36
4000	1	1

Table 3.3: Normalized volume ratio of the deposited materials in the case of 2D growth calculated from Equation 3.8 and 3.9 and measured values for NWs with different carrier gas flows. The normalization is performed with respect to the growth with 4000 sccm carrier gas flow.

3.3.2.4 The reactor pressure

The reactor pressure is also a fundamental parameter governing the MOVPE process, especially for the pre-reactions of precursors in the gas phase. As depicted in Chapter 3.2.2, at lower reactor pressure, the pre-reaction in the gas phase is largely reduced and results in a higher growth rate for GaN 2D growth.

In order to evaluate the effect of the reactor pressure on the NW growth, we have carried out three experiments with different reactor pressure, as shown in

Figure 3.22 (a) 400, (b) 600, and (c) 800 mbar respectively. It can be observed that with decreasing of the reactor pressure, the NWs diameter is sharply increased.* We believe that this diameter increase is due to larger providing of TMGa precursors (It can be induced by a decrease of the pre-reaction in gas phase) at the frontier of the substrate surface at lower pressure that locally increases the 'effective' TMGa/silane mole ratio.). Meanwhile, the increase of the 'effective' TMGa precursor flow also results in the higher NWs density. And for the growth at 400 mbar, a coalescence of the island is even observed due to the high nucleation density in combination with the larger diameter.

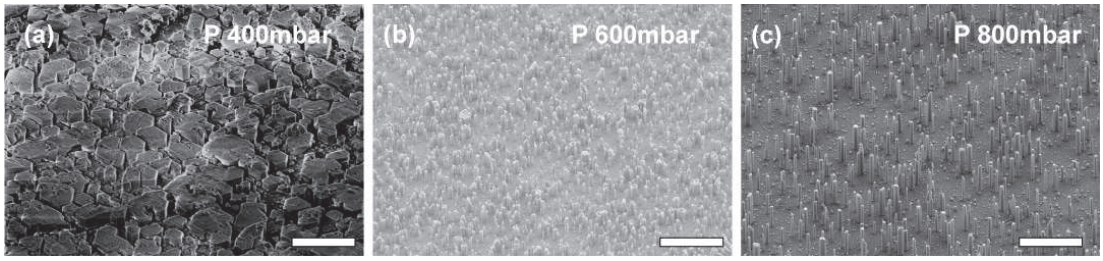

Figure 3.22: 45°-tilted SEM image of the as-grown SG GaN NWs array with different reactor pressures of (a) 400 mbar, (b) 600 mbar and (c) 800 mbar. The scale bars are 10 μm.

3.4 Conclusions

In this chapter, we have first briefly presented the basic physical process, the growth regime, the properties of the III-nitride precursor molecules and the Aixtron CCS system setup for MOVPE method. It is shown that the growth rate control for Aixtron CCS system in mass transport regime is mainly governed by two factors: 1) the chemical boundary thickness which is related to the III-precursor flow rate and the carrier gas composition and 2) the reactor pressure which determines the precursor pre-reaction rate in gas phase.

Then, the influence of the process parameter (temperature, V/III ratio, precursors flow rate, carrier gas flow rate and pressure) on the morphology of the catalyst-free self-assembled GaN NW growth with low V/III ratio and *in situ*

*Actually for the growth with pressure of 400 mbar, the NW geometry can no longer be obtained and the structure appears to be hexagonal prismatic column with a low length/diameter aspect ratio (< 1).

silane injection regarding density, diameter and length was systematically studied and interpreted. The result is summarized in Table 3.4. In particular, it was pointed out that, apart from the V/III ratio, the real precursor flow and mole ratio between TMGa/silane also have a large impact on the NW diameter determination: an increase of these values gives NWs with smaller diameter. For this point, the detailed mechanism concerning the silane injection to favor the NW formation will be further studied and illustrated in chapter IV.

	Temperature	V/III	Precursors flow rate		Carrier gas flow rate	Pressure
			III	V		
Density	↓	+	↑	↑	↓	↓
Diameter	↑	+	↑	↑	↓	↓
Length	↑	+	↓	+	first ↑, then ↓	↑

Table 3.4: The summary of the influence of the process parameters on the NW morphology with the growth condition of low V/III ratio and silane injection. ↑ means increasing with increasing, ↓ means increasing with decreasing and + means no obvious dependence.

Chapter 4

Catalyst-free MOVPE self-assembled growth of GaN NWs: from growth mechamism study with *in situ* silane injection to a new method with low precursor flow injection

This chapter deals with the in-depth investigation of the growth mechanism of the catalyst-free self-assembled GaN NWs method already depicted in Chapter 3. The role of the *in situ* silane flux injection promoting the formation of NW geometry will be first enlightened by addressing the effect of silane flux on the NW diameter and length. The atoms diffusion process during the NW growth will be studied by a systematic measurement of the NW diameter and length variation as a function of the growth time. The use of this *in situ* silane flux method for the NWs growth finally turns out to be great promise for making NW-based optoelectronic devices. In the second part of this chapter, the polarity of the GaN NWs characterized by CBED method shows the N-polarity of Si doped NW and is found to be closely related to the shape of the as-grown GaN structures. Finally, a novel approach without silane injection will be presented combining polarity control and low precursor flow will be presented. Such method allows to

grow Ga-polar GaN NW exhibiting high quality optical and structural properties, due to the absence of heavily Si-doping.

Contents

4.1 MOVPE self-assembled growth of GaN NW with *in situ* silane injection: from growth mechanisms to applications

4.1.1 Introduction

One of the critical issues in the physics of NWs for developing versatile functional high performance devices is the understanding of NW formation mechanisms. The growth behavior of NWs is also interesting from the viewpoint of fundamental physics as an example of one-dimensional growth of nanocrystals. In general, apart from the common VLS method introduced in Chapter 2.2.1, there exist some other well recognized NW growth mechanisms like vapor-solid-solid [127], [128], vapor-solid [129], oxide-assisted [130], solution-liquid-solid [131], and growth from threading dislocations [132], [133]. By carefully analyzing the growth rates as a function of diameter and NW spacing, three main phenomena have been proposed as: (1) solid-phase diffusion of reactant adatoms on substrate and sidewall surface [100], [134], (2) gas-phase diffusion of species [135] and (3) the Gibbs-Thomason (GS) effect [136] caused by the finite curvature of the NW surface. Several models to take into account all these effects for NW growth [137], [138], [139] are also reported.

In these studies, it has been found that in NW VLS growth, the length normally increases with the diameter if the GS effect dominates the growth (*i.e.* with the reduction of the supersaturation in the metal droplet with decreasing of diameter) whereas the length and the diameter generally decrease for adatoms diffusion induced (DI) growth. In the SAG growth with patterned mask, the inter NW distance will influence the growth rate by both substrate and gas phase diffusion. For example, the competition of attracting reactants between two neighboring NWs will become significant and reduce the growth rate for small adjacent NW distance [100].

For the MOVPE SG of GaN NWs discussed in this PhD thesis, the necessity of silane injection to favor the formation of one dimensional NW geometry has been already demonstrated [65]. However, the role of the silane flux played in the NW growth has not been clarified up to now. The growth mechanism of heterostructures overgrowth based on NW templates needs also to be understood. These two important points will be addressed in this section.

4.1.2 The growth mechanisms of SG GaN NWs with *in situ* silane injection

4.1.2.1 Surface passivation effect of SiN_x layer

The effect of different silane flux

To demonstrate that in our method the additional injection of silane flux in the GaN NW growth stage is essential to get the NW geometry and to quantify its effect, a series of MOVPE SG GaN NW growth is first carried out with different silane flow rate during the NW growth while keeping the other parameters similar to those given in Chapter 3.3.2. Figure 4.1 presents typical 45°-tilted SEM images of the as-grown GaN structure array with (a) 0, (b) 50, (c) 100, (d) 150, (e) 200, (f) 300 and (g) 400 nmol/min silane flux, respectively. These vertical GaN structures present well c-oriented epitaxy with the c-sapphire substrate. It can be observed that the lateral growth rate of the GaN structure is strongly reduced in parallel with a strong enhancement of the vertical extension with increasing of silane flux. For example, the growth using no silane injection (Figure 4.1 (a)) and with 400 nmol/min silane flux (Figure 4.1 (g)) turns the shape from planar hexagonal disc to sharp NWs. We also deduced from these experiments that the critical threshold value of the injection silane flux to achieve GaN NWs * in our growth condition is about 150 nmol/min. The quantitative variation of the NW diameter and length with increasing injection silane flux is given in Figure 4.1 (h) and (j). Values are obtained by counting at least 50 single objects for each point. The increase of silane flux from 0 to 400 nmol/min drastically reduces the diameter of the GaN structure from 2.8 μm to 225 nm whereas the vertical growth rate is multiplied by a factor of 16 (with a value of about 112.72 μm/h). In addition, an anti-tapering effect (larger diameter in the top part of the NWs than in the bottom part) becomes noticeable when the silane flux is larger than 150 nmol/min as shown in Figure 4.1 (h). This effect could result in a degradation of the crystalline quality of the GaN NWs with the appearance of hollows and cracks at the NW sidewall surface (see Figure 4.1 (g)).

As introduced in Chapter 3.1.4, the silane is normally used as precursor for Si doping in the n-type III-nitride MOVPE growth. In order to have an idea of the role played by the silane flux to get the NW geometry, the Si profile inside a NW has been determined using dual-beam time-of-flight secondary ion mass spectrometry (TOF-SIMS) from ION-TOF GmbH (Munster, Germany) in the

*with a length/diameter aspect ratio larger than 10

4. CATALYST-FREE MOVPE SELF-ASSEMBLED GROWTH OF GAN NWS: FROM GROWTH MECHAMISM STUDY WITH *IN SITU* SILANE INJECTION TO A NEW METHOD WITH LOW PRECURSOR FLOW INJECTION

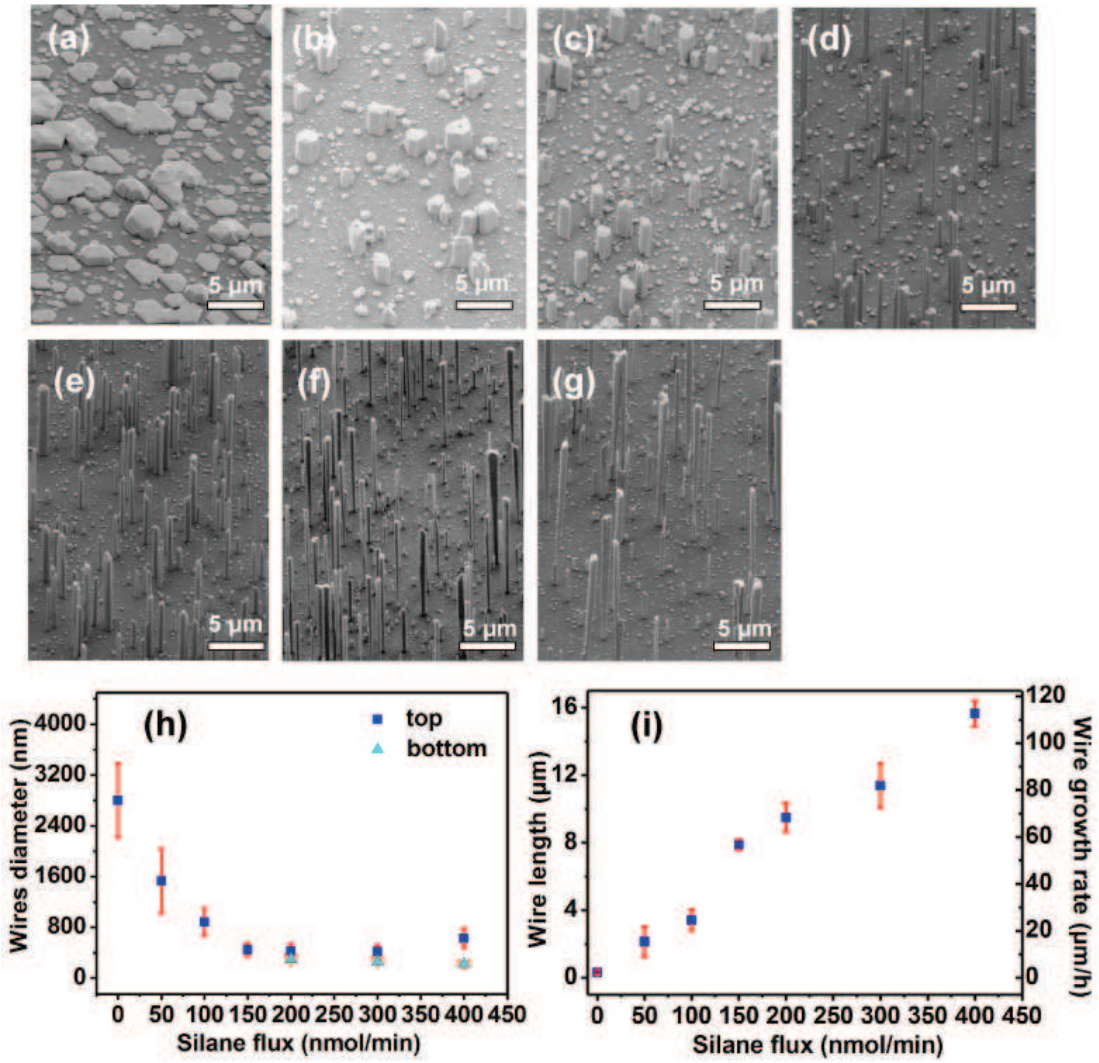

Figure 4.1: 45°-titled SEM images of the as-grown GaN structures with injection silane flux of (a) 0 nmol/min, (b) 50 nmol/min, (c) 100 nmol/min, (d) 150 nmol/min, (e) 200 nmol/min, (f) 300 nmol/min and (g) 400 nmol/min for MOVPE SG GaN NW growth method as depicted in Chapter 3.2.2. Statistics of the (h) diameter and (i) length and growth rate of the GaN structures as a function of different injection silane flux.

case of the 200 nmol/min silane flux sample (The experiment has been performed by J.P. Barnes, CEA/LETI.).

The TOF-SIMS 3-D mapping of Si atom distribution inside GaN NWs

Figure 4.2 (a) gives schematically a drawing of the SIMS measurement method to analyze dispersed GaN NWs. For SIMS measurement, a pulsed operated bismuth ion gun (Bi^+) with energy of 25 keV is used as analysis beam to obtain TOF spectra by sputtering the sample surface and producing secondary ions emitted from the first monolayer on the sample surface. These secondary ions are then focused and accelerated with the same kinetic energy for analysis. The travel time of these ions in the analyzer is proportional to the square root of the masses and this information could be directly used to determine the element. A 500 eV oxygen beam is also used for depth profiling as abrasion beam. The depth resolution and lateral resolution are estimated to be 2 nm and 200 nm respectively. The visualization of the structure is achieved by combining the 3-D position of the scanned Bi^+ ion beam with the time of flight data recorded at each pixel. This 4-D data cube (x, y, z, δt) allows to get accurate depth profiles from different parts of the NWs.

The NWs are detached from the c-sapphire substrate by sonication in isopropanol and then dispersed on Ge substrate (during the dispersion process, the Ge substrate is placed on a hot plate to evaporate the isopropanol easily). In this measurement, the scanning area on the NWs surface is along X direction 7.14 μm and Y direction 3 μm with an in-depth Z abrasion sputtering time with O^+ ion beam of about 750 s. Figure 4.2 (b) shows the TOF-SIMS spectra of the Si^+ counts as a function of the sputter time. As introduced before, the sputter time corresponds to the in-depth abrasion and this figure shows that there is an accumulation of Si^+ atoms at the surface of the GaN NWs. To have a more visible representation of this Si^+ accumulation, Figure 4.2 (c) presents the Si^+ mapping along Y-Z (left) and X-Z (right) directions respectively. The 'bright colour' stands for an appearance of the recorded Si^+ signal. It can be observed that the concentration of the Si^+ dopant atoms is much higher at the edge compared to the inner core of the NWs in both X and Y direction. Due to the complex quantification protocols of this TOF method, it is not possible to quantify easily this Si^+ atom accumulation from this raw data. In forthcoming experiments, we will use intentionally doped Si:GaN layers with known dopant concentration and thickness to quantify composition and thickness. NWs will be dispersed on this layer to make simultaneous measurements and therefore enhance the quantification accuracy.

4. CATALYST-FREE MOVPE SELF-ASSEMBLED GROWTH OF GAN NWS: FROM GROWTH MECHAMISM STUDY WITH *IN SITU* SILANE INJECTION TO A NEW METHOD WITH LOW PRECURSOR FLOW INJECTION

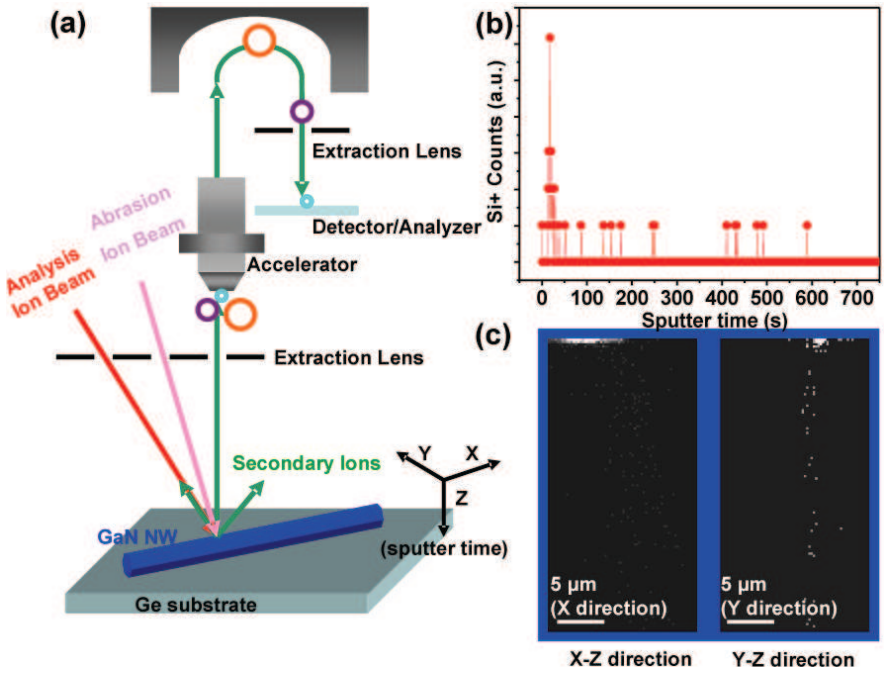

Figure 4.2: (a) The schematic drawing of the working principle of TOF-SIMS, (b) the Si^+ atoms counted as a function of the sputter time and (c) the Si^+ atoms mapping in the single GaN NW along X (left) and Y (right) direction.

In the literature, the dopant incorporation and distribution into semiconductor NWs has been measured using atom probe tomography on VLS Ge NWs with Phosphor doping [140] and indirectly determined on VLS Si NWs with Boron doping by capacitance-voltage measurements [141]. It has been demonstrated in these two systems that an under-doped core can be surrounded by a heavily-doped shell resulting in a radially inhomogeneous dopant distribution. This effect is believed to be induced by the differences in precursor decomposition rates between the vapor-liquid (V-L) catalyst and vapor-solid (V-S) NW surface. The same type of dopant segregation may apply to the asymmetry of Si incorporation in between the GaN NW core and surface in our sample. However, in our catalyst-free method, there is no obvious thermodynamic driving force reflecting the difference in underlying reaction kinetics for the dopant incorporation on c and m plane surface that may explain the surrounding shell dopant accumulation effect.

Actually, beside the n-dopant precursor, the silane is also used to deposit a thin SiN_x in combination with NH_3 for reducing the threading dislocation density

in GaN 2D growths [142]. This *in situ* SiN_x layer deposition method is also used in our SG GaN NW growth method to define the NW nucleation site as depicted in Chapter 3.3.1. Thus, another possibility for the causing of Si atom accumulation on the NW surface could be attributed to an *in situ* deposition of thin SiN_x layer surrounding the NW. It is well known that SiN_x materials are used as dielectric layers in microelectronic industry for their insulator property. Therefore, there shall be a very low current flow though the dielectric layers under operation conditions until the irreversible dielectric breakdown phenomenon happens giving a low resistive conduction path. Thus, in practice, a SiN_x layer surrounding the NWs should induce a transport barrier that should be measured by I-V electrical measurement on the single GaN NWs.

The I-V measurement of the GaN NWs

As grown GaN NWs (with n-i-n structure) were detached from the growth substrate by sonication in ethanol, and then dispersed on a patterned Si/SiO_2 substrate. The contacts to the NW extremities have been fabricated by e-beam lithography and a standard Ti/Al metallization has been performed for n-GaN ohmic contact (see the inset of Figure 4.3) [143] (in collaboration with M. Therychera CNRS/IEF). Figure 4.3 shows the I-V measurements on one typical single GaN NWs. The first I-V measurement on the NW exhibits a very low current with the increasing of bias voltage until 6 V. Beyond 6 V, an abrupt jump of the current flow happens and induces a soft breakdown. Afterwards, the I-V curves are very stable for several cycles with an ohmic behavior. The current for voltage less than 6 V was largely increased compared to the first run.* We can suppose from these measurements with the SIMS results that the Si atoms accumulation at the NW surface may certainly form a SiN_x dielectric layer at the m-plane surface rather than a heavily n-type doped shell structure.

Little Si^+ atom signal inside the core of the NWs is still observed in the TOF-SIMS measurement. These Si^+ atoms shall be partially assigned to the n-type dopant incorporated into the crystal lattice. The further question which arising now is: does the silane flux still induce an apparent n-type doping in our NW growth apart from as the precursor for SiN_x deposition? In fact, the n-type doping will induce a blue shift of the semiconductor NBE luminescence peak position. The shift arises because the Fermi energy (E_f) lies in the conduction band for heavy n-type doping. The filled states can therefore block thermal or optical excitation. Consequently, the measured band gap determined from the onset of

*Similar soft breakdown behavior has been observed in four other NWs measurements.

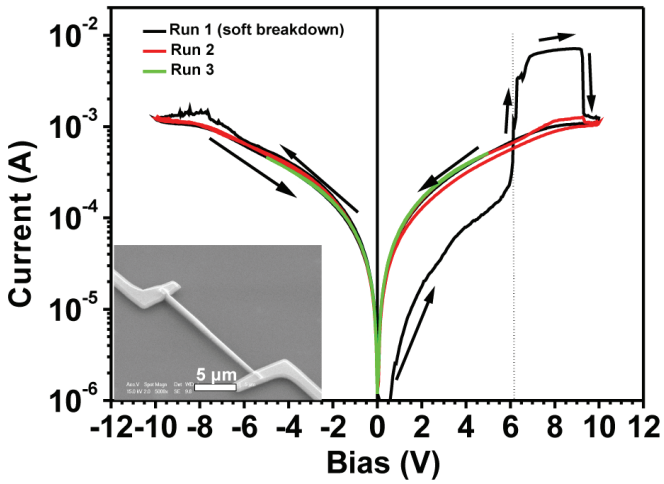

Figure 4.3: The I-V curves of the single GaN NWs (n-i-n structure). The inset is the SEM image showing the as-measured GaN NW device with ohmic metal contact.

interband absorption moves to higher energy: the higher the doping level is, the more the peak will be shifted. In addition, a broadening of the FWHM should be also observed with the increasing of the doping level because of the band filling effect. These assumptions have been tested systematically in the following by CL measurements.

The CL measurement on the GaN NWs

The optical properties of the GaN NWs with different silane flux from 100 to 400 nmol/min were studied by cathodoluminescence measurements at 5 K (in collaboration with A.L. Benvencove, CEA/LETI and experiments performed in CNRS/Néel Institute.). The NWs were dispersed on a conductive silicon substrate to avoid the charging effect from the insulation substrate. Single NWs were excited by an electron beam with a voltage of 30 keV and 1 nA current. Typical low temperature CL spectra with normalization to the maximum of the NBE peak emission intensity for NWs with different silane flux are presented in Figure 4.4 (a). As expected, we observe in Figure 4.4 (b) a gradual blue-shift (compared to the intrinsic GaN NBE emission for 3.47 eV at 5 K) of the NBE emission peak from 3.483 to 3.541 eV and the FWHM broadening from 115.5 to 172.0 meV with the increasing of the silane injection flux. This means that the GaN NWs are n-type doped and proves that some incorporated Si atom in the NW core detected by TOF-SIMS are responsible of n-type dopant.

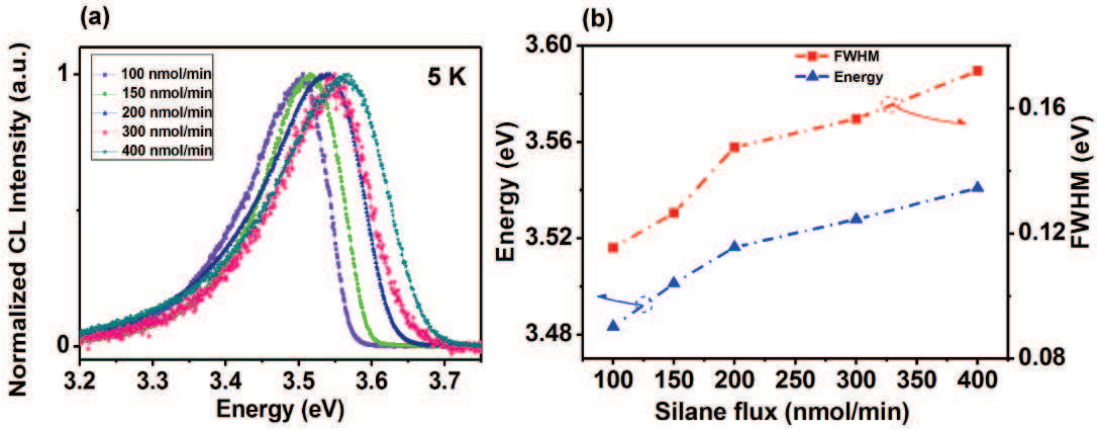

Figure 4.4: (a) CL spectrum of single GaN NWs grown with different silane flux at 5 K and (b) the NBE emission peak position and the FWHM plotted with different silane flux.

Mechanism for the surface passivated growth of GaN NWs

After noticing that a thin SiN_x layer is formed around NW sidewalls with the *in situ* silane injection. We will propose a growth mechanism explaining the role of SiN_x layer to favor the NW geometry.

We believe that the NW formation is divided into three steps as schematically shown in Figure 4.5:

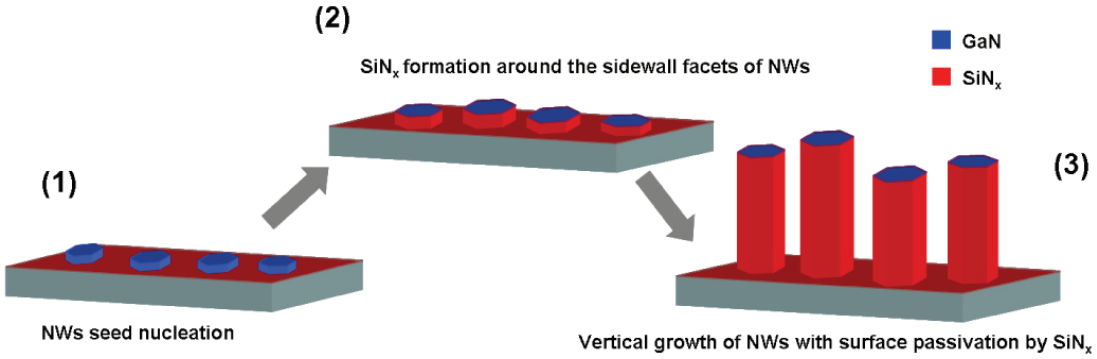

Figure 4.5: Schematic drawing of the GaN NW growth process with (1) seed nucleation, (2) SiN_x formation around the sidewall facets and (3) vertical growth with surface passivation by SiN_x.

(1) **GaN NW nucleation process:** In this stage, the GaN hexagonal-shaped discs nucleate from the openings or defects in non-continuous thin SiN_x layer that has been first *in situ* deposited on nitridated c-sapphire substrates.

(2) **SiN_x formation on GaN NW sidewall surfaces and initial diameter determination:** After the nucleation step, the silane flux is injected into the reactor in combination with TMGa and NH_3 precursors. We can suppose that most of the Si atoms may diffuse along the surface and are then accumulated on the outmost sidewall facets of the NWs. Few Si atoms can still be incorporated into the NW core leading to the residual n-type doping as confirmed by CL measurements. During this stage, the diameter of the NWs will continue to laterally expand. With the increasing of time, the Si concentration at the sidewall surface is increased to a threshold for which a thin SiN_x layer can be formed and plays the role of passivation layer. The diameter of the NWs is finally fixed at this stage. Obviously, with a higher silane flux, more Si atoms are provided to the reactor resulting in a reduction of the time to reach the threshold value to form this SiN_x shell. Consequently this reduction will ultimately reduce the NW diameter. This hypothesis is consistent with the observation shown in Figure 4.1 (b) indicating that the larger silane flux results in smaller NW diameter. Moreover, the decrease of the effective mole ratio of TMGa/silane leads to a decrease of the NW diameter, which is in agreement with the result discussed in Chapter 3.3.3.

(3) **GaN NW surface passivation by SiN_x layer and vertical extension at fixed diameter:** In the next stage, the lateral growth will be inhibited due to the lower sticking coefficient of the Ga species on SiN_x dielectric materials well-known in selective growths. In other words, the species adsorbed on the SiN_x layer will diffuse to top facet of the NWs (or desorbed) and contribute mainly to the vertical growth due to the surface passivation effect. Afterwards, during the NW growth, SiN_x layer on the sidewall facets of the NWs will form again as the self-passivation layer leading to vertical extension with maintained diameter.

4.1.2.2 The adatoms diffusion process

The ability to manipulate the NW properties during growth and to fabricate devices based on controlled doping and heterostructures requires critical information concerning the growth mechanism especially the adatoms diffusion which

is strongly related to the kinetic aspect of the crystal growth [144]. It has been widely admitted that the adatoms incorporation can be mainly divided into three parts arising from: (1) direct impingement on the top facet, (2) NW sidewall diffusion and (3) the adatoms exchange from the substrate [145]. These individual contributions to the NW growth rate $\frac{\partial l}{\partial t}$ are noted in following of this thesis as K_{top}, K_{sw} and K_{sub} respectively. The NW sidewall diffusion itself can be further divided into two streams: the direct collection from the sidewall impinging flux ($K_{sw,dir}$) and the indirect sidewall flux from the substrate scattering for re-emission and transport to the top of the NWs ($K_{sw,indir}$) [146]. Figure 4.6 schematically illustrates the above mentioned different adatoms diffusion paths that have to be taken into account in the growth mechanism.

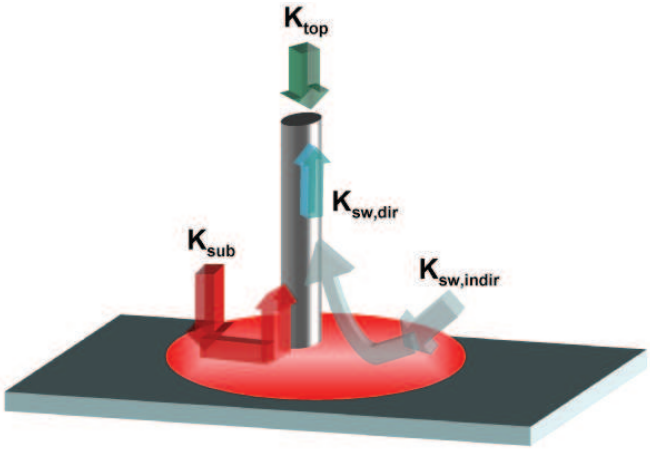

Figure 4.6: Schematic illustration of the different adatoms diffusion paths contributing to the NW growth called K_{top}, K_{sub}, $K_{sw,dir}$ and $K_{sw,indir}$ respectively (see description in the text).

The adatoms diffusion paths from top surface (K_{top}) and direct sidewall diffusion (K_{sw}) always exists and contributes largely to the NW growth, whereas the contribution from the substrate diffusion (K_{sub}) may only occur with certain growth conditions. In this content, the approach of utilizing NW elongation rate with time to determine K_{sub} has been discussed in early studies by Ruth and Hirth for growth of NWs [147]. They considered a reactant adatoms gradient across the NW sidewalls and substrate with accounting for different diffusion lengths on both surfaces. After solving the continuity equation on the substrate surface to determine the boundary condition at the NW base and using a moving frame of reference at the NW tip, they were able to solve the continuity equation at the

NW sidewalls and to obtain a NW elongation rate to identify the regimes in which the NW elongation arises nonlinearly with time depending on the power of K_{sub} as depicted in Figure 4.7. The key parameter in this model is β which indicates the direction and strength of adatoms exchange between the substrate and the NW. For example, if $0 < \beta < 1$, K_{sub} is negligible compared to the other adatoms diffusion paths and in contrary case when $\beta > 1$, K_{sub} becomes dominant.

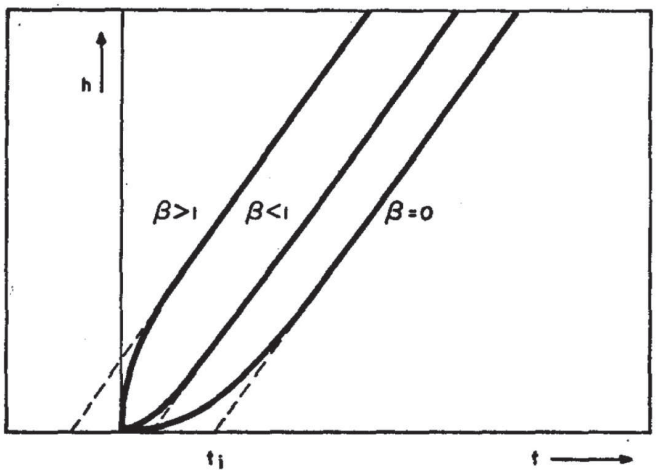

Figure 4.7: Schematic plot of NW length as a function of the growth time presents different regimes with low ($0 < \beta < 1$) and high ($\beta > 1$) substrate-NW adatoms exchange [147].

To get the important paths governing the NW growth and especially to determine whether the contribution from K_{sub} exists or not, we studied a series of samples with different growth time from 200 to 2000 s with a silane flow of 150 nmol/min (see Figure 4.8 (a)-(h) presenting the 45°-titled SEM images of these growths). The plot of GaN NW diameter and length as a function of the growth time is shown in Figure 4.8 (i). It can be seen that with increasing growth time, the NW diameter remains almost constant (as expected from the surface passivation effect) and two regimes for the NW length can be set apart. A first one with an exponential increase at short growth time (< 500 s) and a second one where NW length increases linearly with time (> 500 s). The shape of the NW elongation curve in our experiment matches well the trends corresponding to the $0 < \beta < 1$ regime in Figure 4.7, which indicates a weak contribution of K_{sub} in our GaN NW growth. To further confirm this point, we have fitted our experimental data with the expression of growth time (t) as a function of the NW length (l)

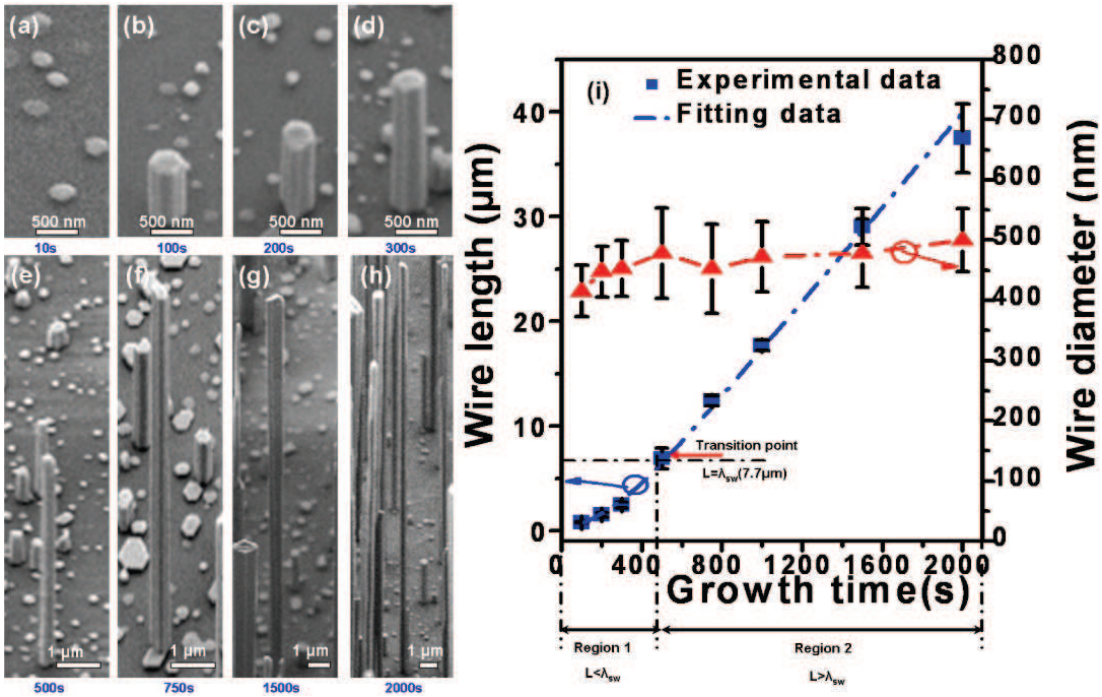

Figure 4.8: The 45°-tilted SEM images of as grown GaN NWs with a Silane flow of 150 nmol/min at different growth time (a) 10 s, (b) 100 s, (c) 200 s, (d) 300 s, (e) 500 s, (f) 750 s, (g) 1500 s and (h) 2000 s. The experimental data of NWs diameter and length at different growth time from 10 s to 2000 s is plotted in (i) with the fitted curve of the NWs length with the model proposed in the text [147].

within the model developed by Ruth and Hirth [147] as:

$$t = \frac{V_L \lambda_{NW}}{\sqrt{2}(V_L^2 - I^2)} ln \left[\frac{(\beta + \frac{I}{V_L}) \cosh(\frac{\sqrt{2}l}{\lambda_{NW}}) + (1 + \frac{\beta}{V_L}) \sinh(\frac{\sqrt{2}l}{\lambda_{NW}})}{(\beta + \frac{I}{V_L})} \right] - \frac{Il}{V_L^2 - I^2} \tag{4.1}$$

where V_L is the linear growth rate at large growth time regime, λ_{NW} is the diffusion length of the adatoms on the sidewall facet of the NW and I is the growth rate induced by the direct impinging flow. The fitted curve matches well with the experimental result with β=0.1 that assumes a very low substrate to NW adatoms diffusion K_{sub}, V_L=18.5 nm/s which is determined experimentally form the slope of l(t) in Figure 4.8 (i) at long growth time, I = 4 nm/s and λ_{NW}= 7.5 μm, which is in good agreement with the 7.7 μm value extracted from the exponential-linear transition length in Figure 4.8 (i).

Moreover, if the substrate adatoms diffusion contribution K_{sub} can be ne-

glected, the NW can be assumed to grow by transport of material to the top surface (without a change in Diameter D) by the three diffusion mechanisms defined as K_{top}, $K_{sw,dir}$ and $K_{sw,indir}$. Each of these contributions gives a growth rate proportional to the flux of impinging reactant precursor on the respective collection area divided by the top surface deposition area as:

$$\frac{\partial l}{\partial t} = A\frac{(Collection\ area)_{K_{top}}}{(Deposition\ area)_{Top\ surface}} + B\frac{(Collection\ area)_{K_{sw,dir}}}{(Deposition\ area)_{Top\ surface}} + C\frac{(Collection\ area)_{K_{sw,indir}}}{(Deposition\ area)_{Top\ surface}}, \quad (4.2)$$

where A, B and C is defined as the growth rate for the three different flux equivalent to the deposition rate of a planar layer of GaN on (0001) surface respectively. Then, the l(t) curve with its exponential and linear parts can actually be modeled by a NW cylindrical shape with fixed diameter D with the following instantaneous growth rates on the top surface from:

(1) **Direct growth rate on the top surface K_{top}**

$$\left(\frac{\partial l}{\partial t}\right)_{top} = A\frac{\pi(\frac{D}{2})^2}{\pi(\frac{D}{2})^2} = A \quad (4.3)$$

(2) **Direct sidewall collection and flux transport $K_{sw,dir}$**

$$\left(\frac{\partial l}{\partial t}\right)_{sw,dir} = B\frac{\pi D min[l,\lambda_{NW}]}{\pi(\frac{D}{2})^2} = B\frac{4min[l,\lambda_{NW}]}{D} \quad (4.4)$$

(3) **Indirect sidewall collection of flux after re-emission from the SiN_x thin layer deposited on c-sapphire and transport to the top surface (see detailed calculation in Ref [146].**

$$\left(\frac{\partial l}{\partial t}\right)_{sw,indir} = C\frac{2min[l,\lambda_{NW}]}{D} \quad (4.5)$$

The addition of the three incorporation mechanisms gives the NW total growth rate:

$$\frac{\partial l}{\partial t} = A + B\frac{4min[l,\lambda_{NW}]}{D} + C\frac{2min[l,\lambda_{NW}]}{D} \quad (4.6)$$

Since the diameter D ($\sim$ 450 nm) and λ_{NW} (7.7 μm) are constant during the growth, it can be deduced from Equation 4.6 that the NW length elongation

with time is exponential when l is smaller than λ_{NW} and increases linearly with time once the l exceeds the λ_{NW}, as experimentally observed in Figure 4.8 (i).

We have established a simple model to describe the adatom diffusion process in SG GaN NW growth on the study of the longer NWs in each growth. Nevertheless, a careful look into the Figure 4.1 (d)-(g) also shows the presence of shorter NWs in between these studied longer ones. How to explain the origin of the strong difference in the growth rate for these NWs within the same run? In order to investigate this phenomena, a precise counting of the appearance frequency of the NW length was made taking into account also shooter NWs.

Figure 4.9 presents the statistics of the NW frequency as a function of NW length for growths with different silane flux from 100 to 400 nmol/min. Interestingly,, the appearance of two families of NWs with different length becomes more and more evident with the increasing of the silane flux. In other words, the larger the growth rate of the first family is (with larger silane flux), the slower the growth rate of the second family tends to be.

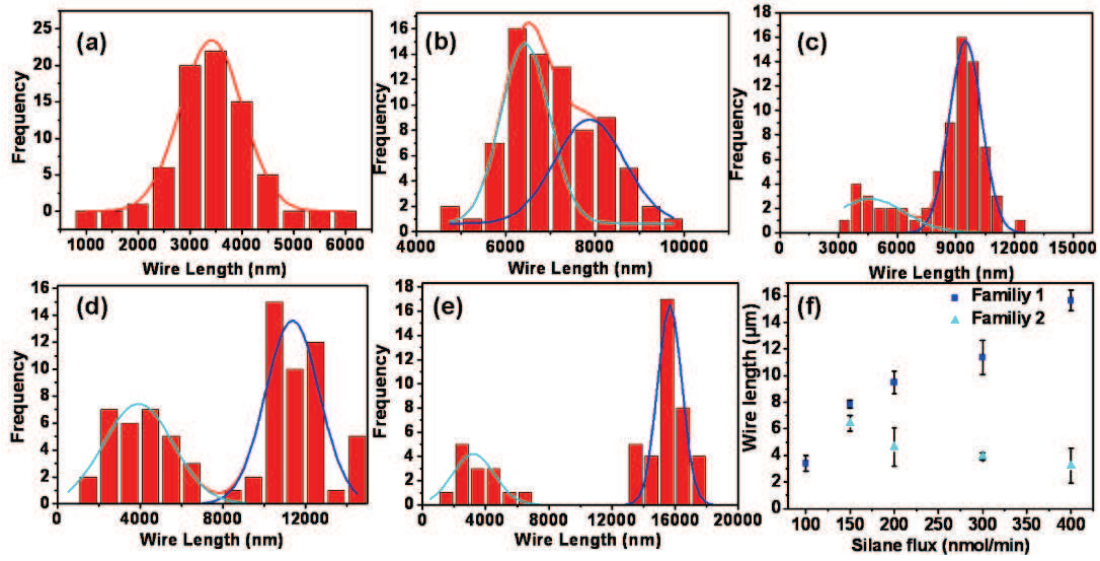

Figure 4.9: The NW diameter plotted as a function of the NW length from experiments with different silane flux (other growth conditions and growth time are constant): (a) 100 nmol/min, (b) 150 nmol/min, (c) 200 nmol/min, (d) 300 nmol/min, (e) 400 nmol/min and (f) the statistic plot of the average NWs length for the two families with different silane flux.

It is generally believed that the nucleation of the NWs does not appear at the same time. Normally with the increasing of growth time, the density of

NWs will increase which means some NWs appear later than the others [62]. Consequently, the first nucleated NW seeds become the sink that change the chemical potential and attract more easily molecular species. In our growth, with reactant are coming mainly from gas phase (in terms of direct top facet impinging and sidewall surface diffusion). As depicted in Figure 4.10 the NWs are divided into two families: the first family nucleated earlier grows faster than the second family which appears later. Moreover, if the growth rate of the first family is increased which means even less precursors will be provided to the surface owing to the enhanced upstream absorption, the second family shall grow at a lower speed.

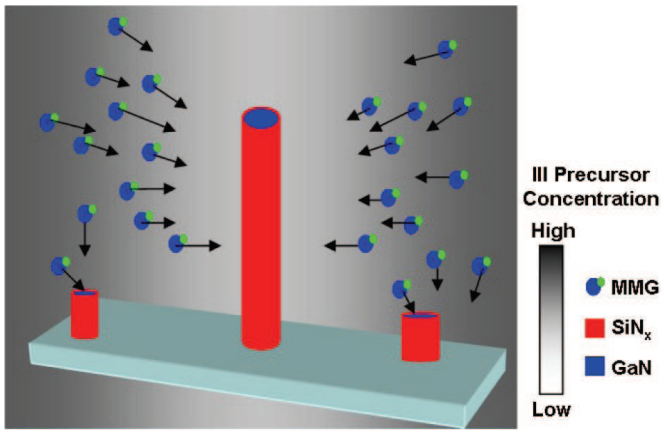

Figure 4.10: Schematic drawing shows the dominant sink effect for the NW growth from direct gas phase transport.

This interpretation is consistent with the result we observed from Figure 4.9 and could be another indication of the accuracy of the proposed adatoms diffusion process in our NW growth.

4.1.2.3 Summary of the growth mechanism

To summarize, the growth model of catalyst-free SG GaN NW using *in situ* silane injection is schematically presented in Figure 4.11. The main paths for the adatoms diffusion contributing to the NW growth are determined to be the direct impinging from top facet (K_{top}) and the sidewall facet ($K_{sw,dir}$). In regime 1 (Figure 4.11 (a)), the length of the NW is smaller than the NW sidewall diffusion length λ_{NW}, thus the NW elongation follows a sub-linear exponential extension because of the gradually increasing collection surface area for the K_{sw} diffusion.

After the transition point where l is equal to λ_{NW} (Figure 4.11 (b)), the NW length will increase linearly with a constant growth rate due to the fixed sidewall collecting area defined as regime 2 (Figure 4.11 (c)). The adatoms sidewall diffusion process contributing to the NW growth appears only on the topmost part of the NW for which the distance to the top facet is below λ_{NW}. The other precursors arrives at the bottom part of the NW will be desorbed and probably be either evaporated away from the reactor chamber or responsible for the other nucleation and growth of NW on the substrate. This is due to both the limited diffusion length which is not long enough to arrive to the NW top facet and the SiN_x surface passivation inhibiting the incorporation into crystal lattice. For clarity, the related regime 1, the transition point and the regime 2 are also indicated in Figure 4.8 (i).

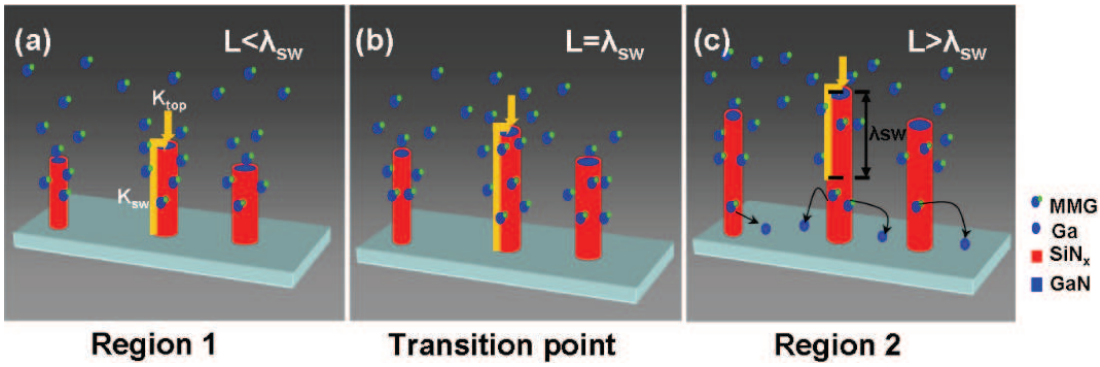

Figure 4.11: Schematic drawing of the three distinguished NW growth regime regarding the adatoms diffusion process from K_{top} and K_{sw} (a) $l < \lambda_{NW}$, (b) $l = \lambda_{NW}$ and (c) $l > \lambda_{NW}$.

4.1.3 The controllable InGaN/GaN MQW radial heterostructures growth

It has been demonstrated in last part that a thin SiN_x layer covers the sidewall of the GaN NWs serving as surface passivation layer. Due to the high selectivity of InGaN growth on this dielectric layer, it is rather impossible to deposit InGaN/GaN radial heterostructures on the NW sidewall. Nevertheless, Koester *et al.* have shown that, beyond a certain length of n-GaN NW, the GaN growth can maintain the NW geometry even if the silane flow is switch off [65]. It results a u-GaN part supposed to be free of surface covered SiN_x layer (u means

unintentionally doped) and is suitable for the InGaN/GaN radial heterostructures growth. Thus, by stopping the *in situ* silane flow after the initial n-GaN NW growth, the InGaN/GaN radial MQW heterostructures can be grown with controllable position along the NW with tuneable length.

To illustrate this point, we grow a series of GaN NW with initial n-GaN using the *in situ* silane flow during 300 s followed by an u-GaN growth (without silane flow) for 0, 100, 200 and 400 s, respectively. These NWs were then used as template for the growth of five periods InGaN/GaN MQW heterostructure. The QW and the QB growth conditions are summarized in Table 4.1:

	Temperature (°C)	Pressure (mbar)	TEGa (μmol/min)	TMIn (μmol/min)	NH_3 (sccm)	Time (s)
QW	750	400	3.64	8.11	500	20
QB	900	400	14.57	0	500	150

Table 4.1: The detailed growth conditions for InGaN/GaN MQW heterostructures growth.

Figure 4.12 (a) shows typical cross section SEM images of the as-grown GaN NWs with radial InGaN/GaN MQW heterostructures for different u-GaN growth time. It can be observed that for u-GaN growth time of 0 s, there is almost no coating of InGaN/GaN MQW on the sidewall facets of the NWs except the deposition of non-continuous small crystal grains. Whereas, in the case of GaN NWs with longer u-GaN growth time, the GaN NW length increases linearly with an increase of the InGaN/GaN MQW coating length at the top. Figure 4.12 (b) gives statistics of the GaN NW length as a function of the InGaN/GaN MQW coating length with different u-GaN growth time. Interestingly, this two lengths are proportional with a slope of 0.97. The linear fit gives also a initial n-GaN NWs length of 7.75 μm, as expected for 300 s of growth. We can thus deduce that the InGaN/GaN MQW are only deposited on the u-GaN part located at the the upper part NWs on the n-GaN part with SiN_x, only some small grains can be grown due to the surface passivation. The structures is schematically shown in Figure 4.12 (c) to summarize the observations.

TOF-SIMS measurements were carried out on single GaN NWs coated with InGaN/GaN MQW with a 200 s grown u-GaN part to characterize the distribution of Si^+ and In^+ ions. Figure 4.13 (a) shows the optical microscopy image of the as-measured single NW lying on the Si substrate, (b) and (c) correspond to

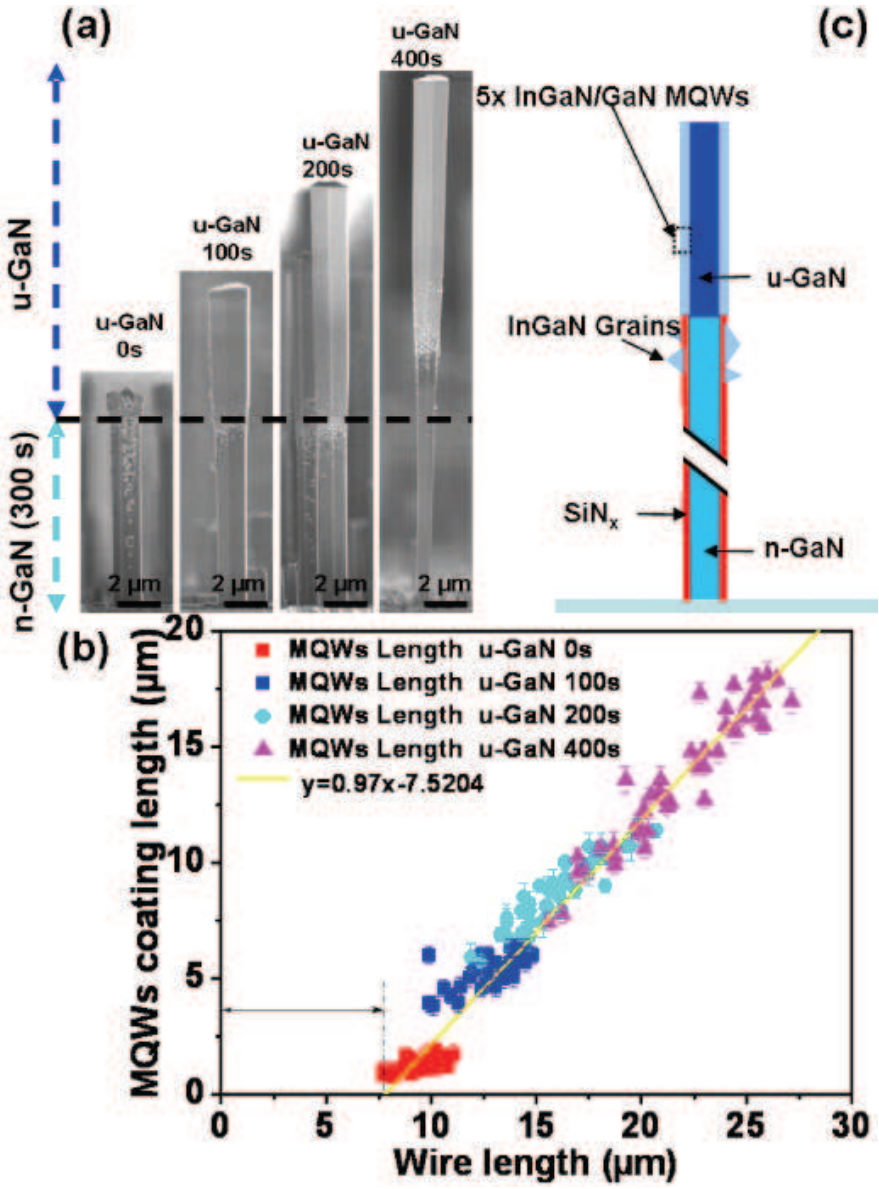

Figure 4.12: (a) Cross-section SEM images of as-grown single GaN NWs with InGaN/GaN MQW heterostructures of different u-GaN growth times (from left to right 0 s, 100 s, 200 s and 400 s). (b) Plot of the complete NW length as a function of the InGaN/GaN MQW coating length for different u-GaN growth time. The yellow line corresponds to linear fit. (c) Schematic drawing of the selective coating of InGaN/GaN MQW heterostructures on top of the NWs with u-GaN.

the top-view SIMS mapping of the Si^+ and In^+ ions along the in plane direction (X-Y). The Si^+ signal is an indication of the n-GaN part whereas the signal of In^+ only comes from the InGaN/GaN MQW coating. It can be clearly observed that the signal of Si^+ and In^+ ion come from well-separated part in the NWs located on bottom and top part of the NW respectively, as indicated by the red dashed line. It confirms that there is no InGaN/GaN MQW deposition on the n-GaN part coated with SiN_x shell. Thus, it proves that the position and the coating length of the InGaN/GaN MQW heterostructure can be directly turned by the duration of silane flow addition.

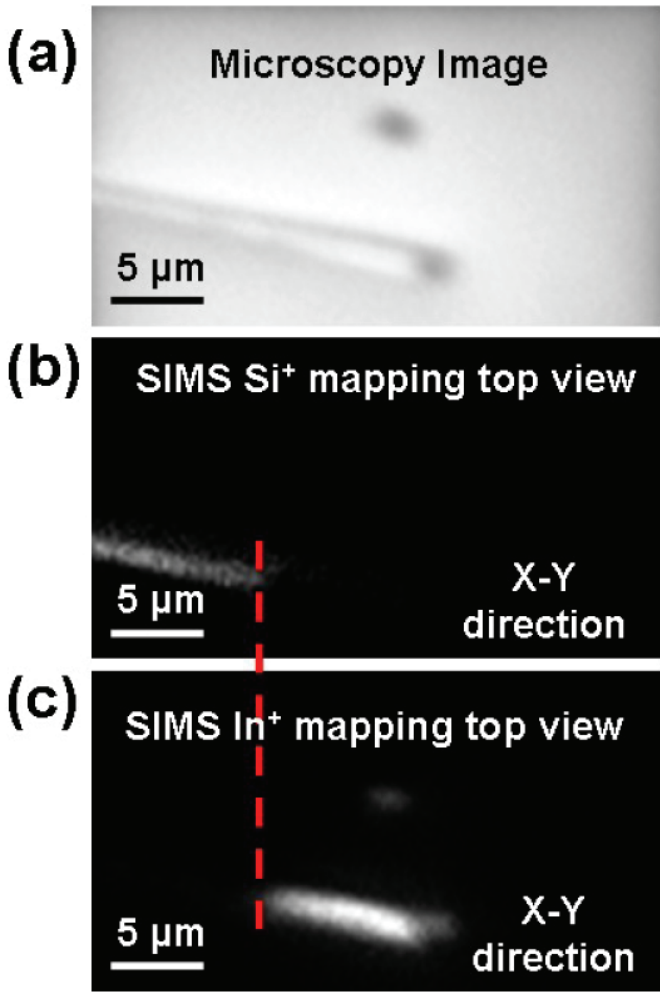

Figure 4.13: (a) Optical microscopy image of a single GaN NW on Ge substrate with a coating of InGaN/GaN heterostructures at the upper top. Top-view TOF SIMS mapping images of (b) Si^+ and (c) In^+ ions in the plane (X-Y) direction.

The InGaN/GaN MQW heterostructures were then investigated by high resolution scanning transmission electron microscopy (HR-STEM) to confirm the core-shell radial coating. NW cross-sections orthogonal to the length direction have been prepared with focused ion beam (FIB) setup and samples have been handled by micromanipulators. Microscopy experiments were performed using a Cs probe-corrected FEI Titan operated at 300 kV (Experiments performed by C. Bougerol CNRS/I. L. Néel). In Figure 4.14 (a) and (b), cross-sectional high-angle angular dark-field (HAADF) images of two heterostructures corresponding to the 20 and 80 s quantum well growth time are shown (for 80 s QW growth the other MQW growth parameters are the same as listed in Table 4.1). The NWs have an irregular hexagon shape and exhibit no defect indicating the good structural quality of the heterostructures. In the HAADF image, the dark (resp. bright) contrast corresponds to the GaN (resp. InGaN shell). The thickness can be measured in Figure 4.14 (a) and (b): the 20 and 80 s InGaN growth time gives respectively 1.0 ($\pm$ 0.1) nm and 5.2 ($\pm$ 0.5) nm for the QW thickness. Images exhibit sharp GaN/InGaN interfaces, although the interface transition from GaN to InGaN is more diffuse due to the temperature ramps during the GaN QB deposition.

Figure 4.14 (c) is a multi-beam high-resolution image for Figure 4.14 (b) sample taken along the $[11\bar{2}0]$ zone-axis with g vector of $[1\bar{1}00]$ of the MQW showing bright stripes as indicated by black arrows. This observation is very similar to the distribution of stacking faults (SFs) along the [0001] direction that is commonly observed in the literature for planar growth [148]. These SFs originate at the first InGaN well and are associated to Frank dislocations with $\frac{1}{6}[2\bar{2}03]$ Burgers vector, which relaxes misfit strain along the c-direction. The $\frac{1}{2}[0001]$ lateral shift in the (0001) planes adjacent to the SFs produces a cubic-like insertion inside the hexagonal phase. In core-shell NWs, high resolution TEM measurements confirm (see Figure 4.14 (d)) that the same SFs are present. The first interface of the MQW contains misfit dislocations that may be detrimental to the optical properties, as checked by the low emission of single well insertion. Further material optimization (out of the scope of this thesis) is required to decrease the SF density and to understand its influence on the optical properties (The current work of PhD student D. Salomon in the lab).

The TEM observations have proved that the InGaN/GaN heterostructures are core-shell coated on the u-GaN part of the GaN NWs. The SFs associated to Frank dislocations with $\frac{1}{6}[2\bar{2}03]$ Burgers vector are present due to the strain relaxation, as commonly observed in the non-polar m-plane 2D MQW growths.

4. CATALYST-FREE MOVPE SELF-ASSEMBLED GROWTH OF GAN NWS: FROM GROWTH MECHAMISM STUDY WITH *IN SITU* SILANE INJECTION TO A NEW METHOD WITH LOW PRECURSOR FLOW INJECTION

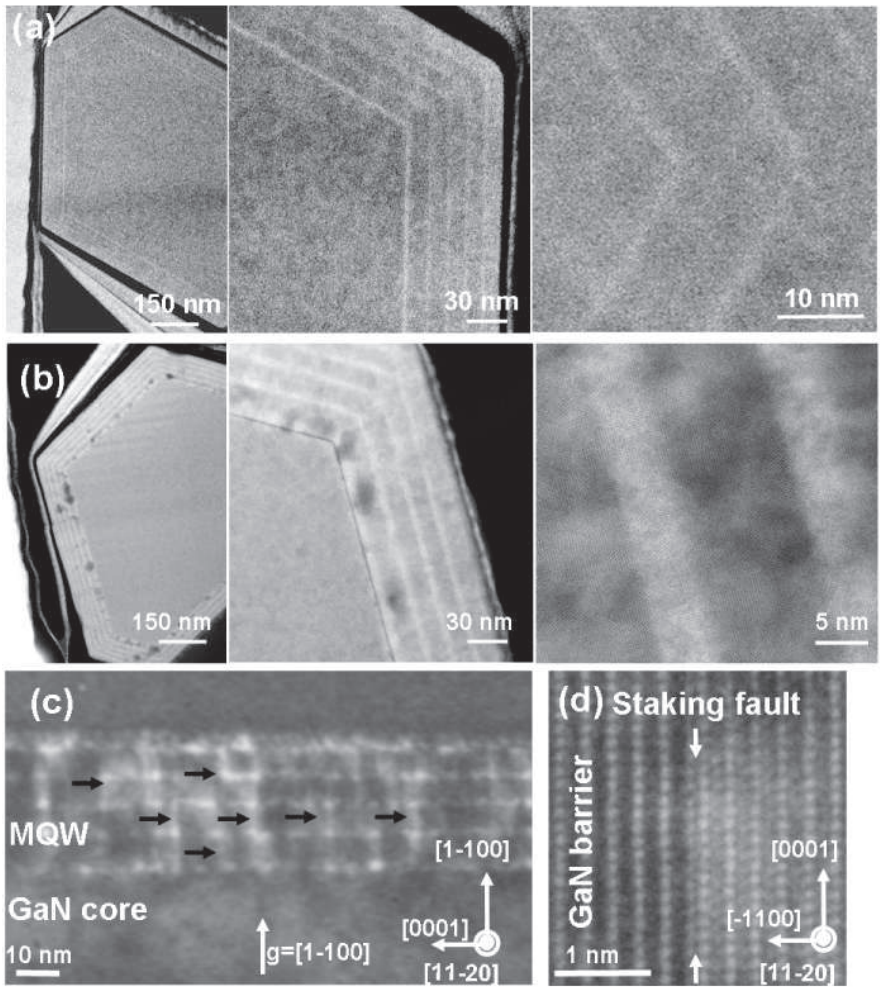

Figure 4.14: High angle annular dark field (HAADF) STEM images of 20-80 s InGaN well growth time NWs prepared by FIB. The NW cross-section is orthogonal to the length direction and shows irregular hexagon shape with m-plane facets (*i.e.* $(1\bar{1}00)$ planes). These images give InGaN well-GaN barrier thicknesses about (a) 1.0-7.5 and (b) 5.2-11.6 nm. (c) Low magnification dark field TEM image taken with g=$[1\bar{1}00]$ showing bright defects originating from the first QW and propagating across the QWs (sample (b)). (d) High resolution TEM image taken along the zone axis $[11\bar{2}0]$ showing that the defects presenting $\frac{1}{2}[0001]$ lateral shift in the (0001) planes evidenced in Figures (c) correspond to stacking faults (SFs) associated to Frank dislocations with $\frac{1}{6}[2\bar{2}03]$ Burgers vector.

4.1.4 Integration in single NW device applicaitons

Single semiconductor NWs with core-shell heterostructure has been demonstrated to be promising building blocks for electronic device applications [54], [149]. However, the main difficulty of integration of this core-shell NWs into device fabrication is the metal contacting for carrier injection. For example, an additional processing step of selective etching of the shell materials is generally required to connect the core part. This definitely increases the process complexity and possibly induces damage. Interestingly, benefiting from the partial coverage of the radial InGaN/GaN heterostructures, which are selectively grown on u-GaN part, the n-GaN part can be easily contacted when the thin SiN_x layer is removed, as shown in Figure 4.15 (a).

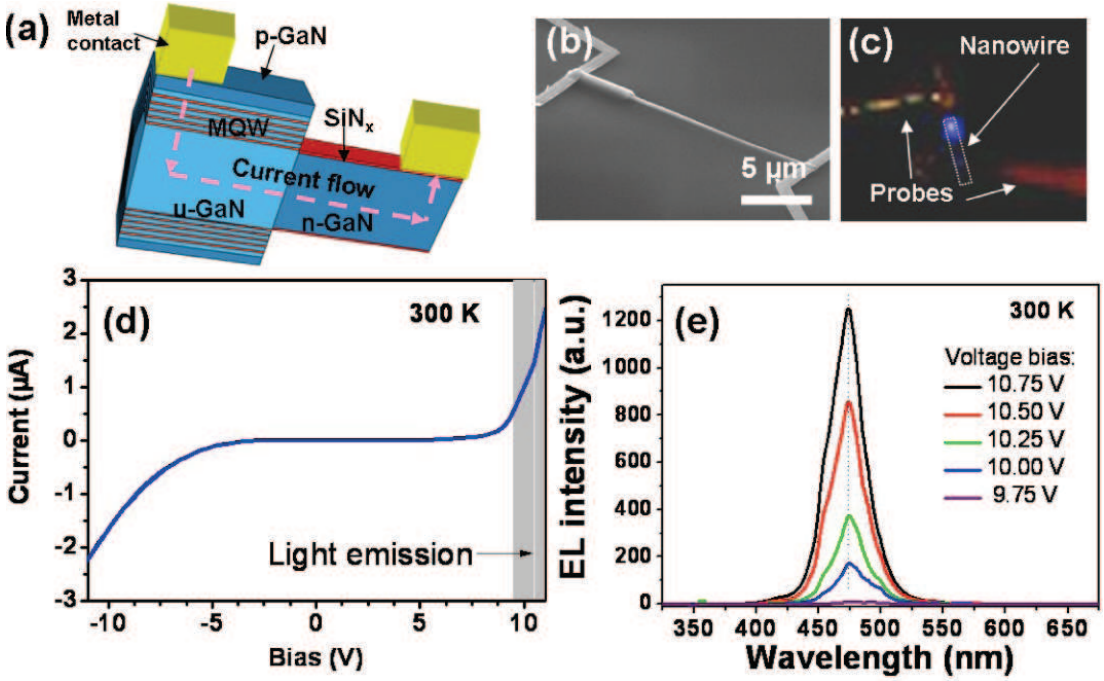

Figure 4.15: (a) Schematic of the core-shell LED structured GaN NWs (n-GaN/InGaN MQW/p-GaN) and the metal contact for the device fabrication. Note that the MQW and p-GaN is selectively coated only on u-GaN part on top of the NWs (b) SEM view of an electroluminescent single NW device with: (c) its related optical microscopy image showing blue-light emission, (d) Current/tension characteristics at 300 K, (e) Electromuminescence intensity as a function of the applied voltage at 300 K.

Single-NW horizontal devices have been fabricated in collaboration with IEF laboratory to demonstrate the electroluminescence properties and the easy device integration of these InGaN/GaN MQW heterostructures. A radial p-GaN shell grown at 920 °C in N_2 is added on the MQW using Cp_2Mg as a precursor source with an annealing step performed at 750 °C during 20 min to activate Mg-dopants. NWs are then dispersed on Si/SiO_2 substrate after sonication in ethanol. The n-p metal contact is obtained by the deposition of metal contacts (Ti/Al/Ti/Au) defined by e-beam lithography and dry etching at both ends of single NWs (see in Figure 4.15 (a) the schematic and (b) the optical microscopy image). Current-voltage (I-V) characteristics measured at room temperature and in ambient air show typical n-p diode behaviour with sharp current increase at around 9 V in forward bias (see Figure 4.15 (c)). As shown in Figure 4.16 (d), the single-NW devices yield significant electroluminescence for positive bias (> 9.75 V) in the blue wavelength region at 473 nm (2.62 eV) with a FWHM of 40 nm (250 meV) without any defect band. The light intensity exponentially increases with the voltage bias (up to 12 V). The electroluminescence comes from the upper part of the single NWs close to p-contact in the region of MQW deposition (see in Figure 4.15 (c)).

4.2 Shape selection induced by crystal polarity

4.2.1 Introduction

Up to now, we have been succeeded to understand the growth mechanism of catalyst-free SG GaN NWs grown by MOVPE under *in situ* silane flux. However, the substrate used in our growth is c-sapphire which is nonconductive and and represent a barrier for the direct integration of the NWs assembly for device fabrication. In this context, conducting substrates as GaN templates are usually preferred for direct integration of NW array-based photonic devices [57]. Nevertheless, in the last decade most of MOVPE GaN nanostructures grown on GaN templates exhibit pyramidal shapes [115], [150] rather than NW geometry as discussed in chapter 2.2.

The substrate polarity is known to impact the growth kinetics and shapes of polar materials with hexagonal symmetry [151],[152]. In the case of NW growth, this point has been recently evidenced for ZnO NWs, which are grown on Zn-polar, but not on O-polar ZnO surfaces [153]. But up to now, no systematic studies have been dedicated to understand the influence of the substrate polarity

on the shape of GaN nanostructures.

4.2.2 Polarity study of self-assembled GaN NWs

C-oriented GaN nanostructures were firstly grown on c-sapphire substrates using SG and SAG approaches (the detailed growth condition of SAG will be depicted in Chapter 5.1.3). In the SG approach, the standard growth condition and process is used as depicted in Chapter 3.3.2. A surface nitridation was performed after hydrogen annealing which gives usually N-polar two dimensional GaN layers [71]. In the SAG approach, a thicker Si_3N_4 layer ($\sim$ 5 nm), which was *ex situ* deposited and patterned by nanoimprint, acts as a mask for selective growth. The detailed information about the patterning method will be introduced later on in Chapter 5.1.2. Identical growth conditions were used for both methods except for the SAG growth where the *in situ* silane flow was not introduced into the reactor during the NW growth stage.

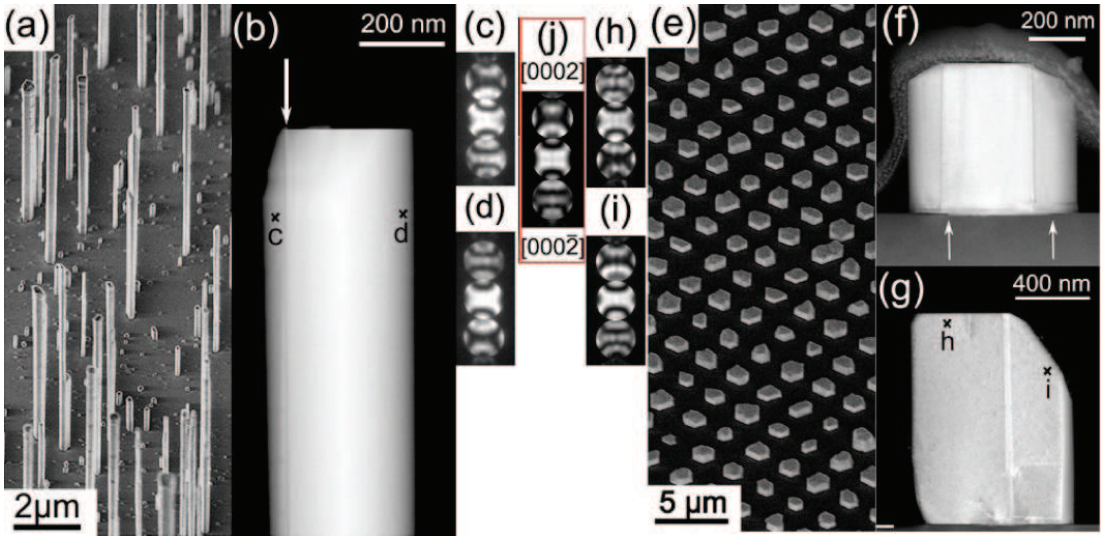

Figure 4.16: Self-assembled growth (SG) of GaN NWs on c-sapphire. (a) 45°-tilted SEM view and (b) STEM image of a single NW. Selective area growth (SAG) of a NW seed array: (e) 45°-tilted SEM view and (f, g) STEM images of single seeds. Experimental CBED patterns of the points marked c, d and h, i in (b) and (g) are given in (c), (d) and (h), (i) respectively. As a reference, the simulated CBED pattern for 110 nm thickness is given in (j). CBED patterns show Ga-polarity of the domains with inclined facets (c and i), and N-polarity of the ones with horizontal facets (d and h).

Figure 4.16 presents the SG and SAG of GaN nanostructures grown on c-sapphire substrates. Figure 4.16 (a) shows a 45°-tilted SEM image of as-grown SG GaN NWs. These NWs grow vertically along the c-axis in epitaxy with the substrate. Figure 4.16(b) shows a STEM image of a representative NW where two different regions separated by an inversion domain boundary (IDB, indicated by the white arrow) are observed: one with a flat top facet and the other with an inclined top facet at the NW edge. CBED patterns collected for these two domains are shown in Figure 4.16 (c) and (d) respectively. By comparing the contrast inside the experimental disks with the simulation [Figure 4.16 (j)], it is deduced that the small domain on the left side of the IDB with an inclined facet has a [0001] growth direction (Ga-polarity), whereas the main domain on the right side with a flat top surface exhibits a $[000\bar{1}]$ growth direction (N-polarity) in agreement with the nitridated surface preparation. This behavior tends to show that N-polar crystals favor the NW geometry formation with vertical sidewalls, while Ga-polar crystals present inclined facets that may limit the vertical extension and in some extent may lead to the formation of pyramidal geometry. The longitudinal change of polarity can not occur spontaneously during the crystal growth, however this can be achieved with a precursors addition like heavily Mg-incorporation [154]. The polarity of GaN crystal is probably imposed by the nucleation seeds, which are related to the surface state, *i.e.* to the thin in situ deposited SiN_x layer or to the thin AlN layer formed during the sapphire surface nitridation.

To verify this assumption, we performed SAG on patterned c-sapphire substrates using a thicker Si_3N_4 layer to have an efficient mask with controlled dimensions and to identify its influence on the crystal polarity. Short growth duration ($\sim$ 200 s) was chosen for SAG to obtain only the GaN-NW nucleation seed array [see Figure 4.16 (e)]. Three areas are observed by STEM on the typical as-grown seed shown in Figure 4.16 (f): a central part with a flat top surface surrounded by two crystals with inclined facets. The size of the central part is around 400 nm (*i.e.* the diameter of the patterned holes). Two vertical IDBs are located close to the mask edge opening (indicated by white arrows in Figure 4.16 (f)). An ion-milled seed [Figure 4.16 (g)] was analyzed by CBED showing that the flat top crystal is N-polar [Figure 4.16 (h)] while the inclined facet crystal is Ga-polar [Figure 4.16 (i)]. It confirms the co-existence of opposite polarities in GaN crystals correlated to the nature of the surfaces: Ga-polar crystal is preferentially formed on SiN_x mask and N-polar crystal on AlN/c-sapphire surface, as depicted in Figure 4.17.

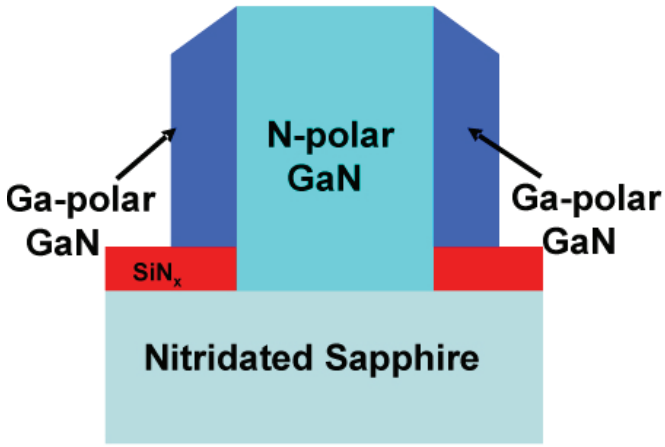

Figure 4.17: Schematic drawing of the co-existence of opposite crystal polarities in single GaN macrostructures grown on patterned c-sapphire substrate with Si_3N_4 as mask layer.

4.2.3 Homoepitaxial growth on freestanding GaN substrate

4.2.3.1 The growth process

Based on these results concerning the shape dependence on the polarity, we chose to control in a straightforward way the polarity variants by using suited GaN substrates. Self-assembled GaN nanostructures were grown on both N- and Ga-polar c-GaN freestanding substrates using the standard SG process. 45°-tilted SEM images of as-grown samples on N-polar and Ga-polar surfaces are shown in Figure 4.18 (a) and (f) respectively showing the huge impact of the substrate polarity on the crystal growth shapes. The nanostructure polarities were checked by CBED taking into account the simulation references given in Figure 4.18 (k)-(l) corresponding to the observed area thicknesses [Figure 4.18 (b) and (g)]: the growth on N-polar GaN exhibit N-polar NW-shaped nanostructures [Figure 4.18 (c)-(e)], whereas the growth on Ga-polar GaN exhibits Ga-polar pyramidal shape nanostructures [Figure 4.18 (h)-(j)]. As expected, the polarity is conserved between the substrate and the nanostructures as schematically shown in Figure 4.19 (a) and (c). In the case of growth on N-polar GaN and as mentioned for SG on sapphire, some Ga-polar crystals are observed due to nucleation on the SiN_x layer.

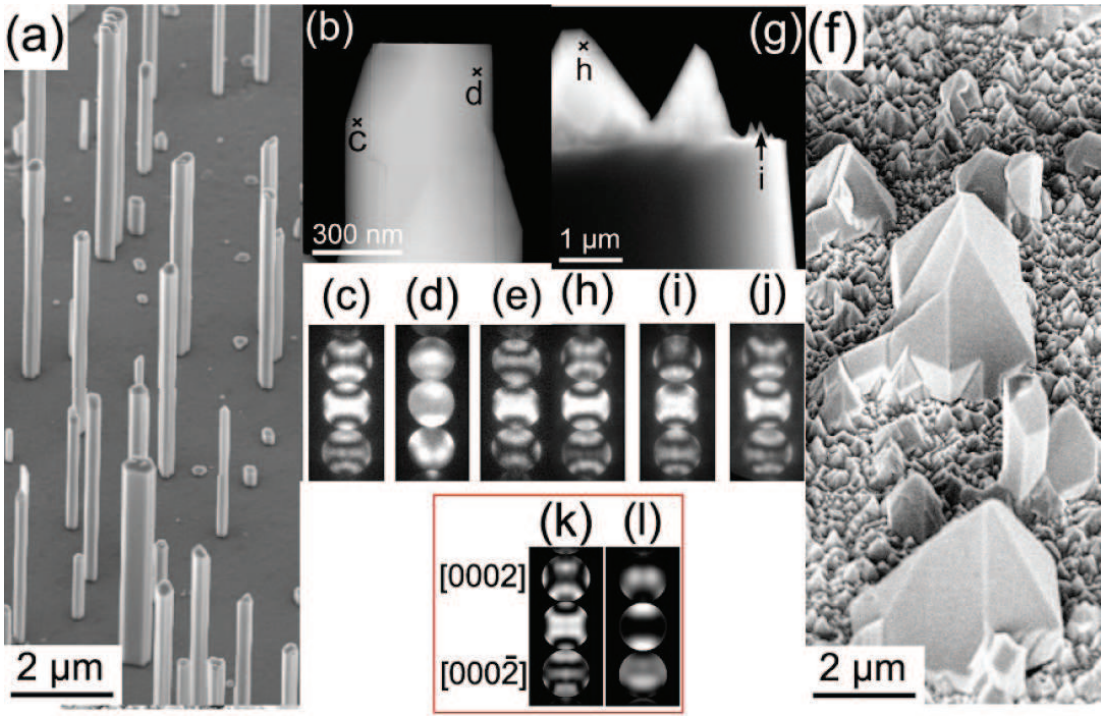

Figure 4.18: Self-assembled growth of GaN NWs on N-polar GaN: (a) 45°-tilted SEM view, (b) STEM image of a single NW. Experimental CBED patterns showing (c) Ga polarity of the domain with an inclined facet (marked c), (d) N polarity of the one with a horizontal facet (marked d), and (e) N polarity of the GaN substrate. Self-assembled growth of GaN pyramids on Ga-polar GaN: (f) 45°-tilted SEM view, (g) STEM image. Experimental CBED patterns showing Ga polarity of (h) big pyramids, (i) small pyramids, and (j) the GaN substrate. As references, the simulated CBED patterns for 110 nm and 60 nm thicknesses are given in (k) and (l) respectively.

4.2.3.2 The kinetic Wulff's plots

The kinetic Wulff's plots (ν-plot) giving the growth velocities along different orientations are usually used to describe the MOVPE growth features to take into account non equilibrium phenomena. Recently, the GaN non-equilibrium shapes obtained by MOVPE have been measured or calculated for different growth conditions on polar, semipolar and nonpolar surfaces [155]. The anisotropy of the growth rate along <0001> coming from the crystal polarity has been pointed out without mentioning the influence of the substrate polarity. Our present results allow obtaining the schematic representation of the ν-plot considering the substrate polarity effect (see Figure 4.19 (b) and (d) where the measured growth velocity values are noted by dots). For N-polar GaN, cusps along $[000\bar{1}]$ and $<10\bar{1}0>$ are in agreement with literature, and the relative observed velocities lead to c-oriented NWs with {10-10}-sidewalls. For Ga-polar GaN, the [0001] and $<10\bar{1}0>$ cusps are not observed, but rather the $<10\bar{1}n>$ giving the pyramidal shape (n=1, 3 ... depending on local growth conditions).

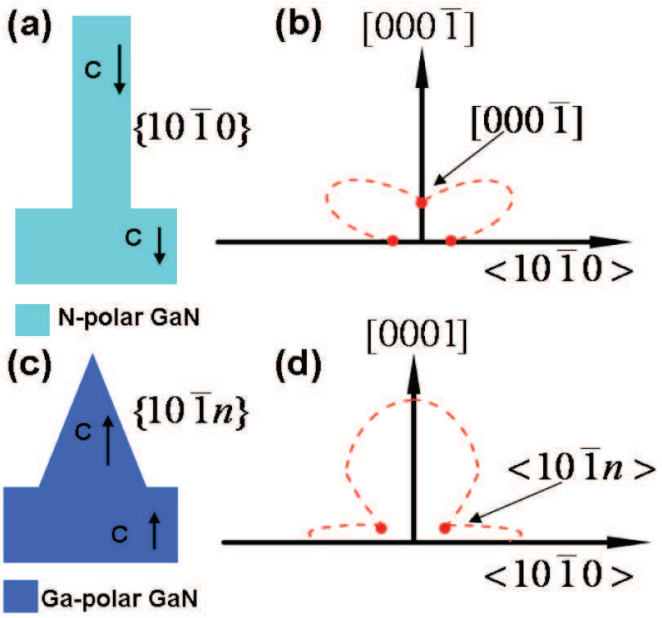

Figure 4.19: Schematics of the GaN nanostructure shape selection for growths on (a) N-polar and (c) Ga-polar GaN. The corresponding kinetic Wulff's plots mapping on the $(11\bar{2}0)$ plane are given in (b) and (d): dots correspond to observed planes and dotted lines are extrapolated velocity values.

4.2.3.3 The optical properties

Optical properties of as-grown pyramidal and NW-shaped nanostructures were measured at room temperature by photoluminescence (PL) excited with a 244 nm laser beam using the same experimental conditions (see Figure 4.20 (a)). The optical property of the as-grown GaN NWs is better than the pyramidal shaped nanostructures without a defect-related yellow band (YB) luminescence. In order to rule out the signal coming from the substrate, μ-PL was also made on single GaN NWs at room temperature (see Figure 4.20 (b)). The spectrum shows a good near band edge emission peak at 351 nm without YB indicating the high crystal quality of the NWs.

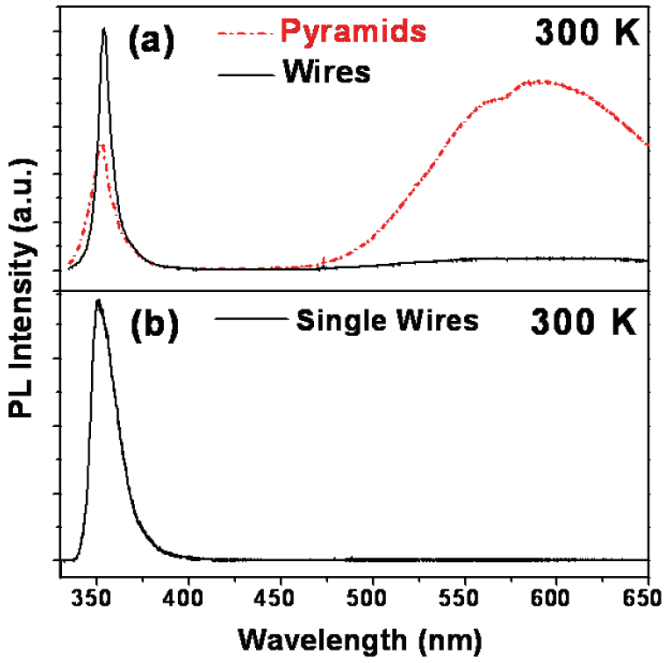

Figure 4.20: Room temperature (300 K) photoluminescence (PL) spectra of (a) as-grown pyramids and NWs on GaN freestanding substrates having respectively the Ga- and N-polarities and (b) Micro-PL of a single NW dispersed on a Si substrate.

4.2.3.4 Conclusions

In this part, a direct relationship is established between the shape and the polarity of GaN nanostructures grown by MOVPE under specific growth conditions (as

low V/III ratio and addition of silane flow). It is shown that the shape of the GaN nanostructures can be directly tuned depending on the polarity of GaN substrates in the case of homoepitaxy, *i .e.* the Ga-face polarity results in pyramids, whereas N-face polarity in hexagonal prisms or NWs. Finally, the optical properties of N-polar NWs will be demonstrated by photoluminescence spectroscopy validating our approach to get high quality catalyst-free GaN NWs.

4.3 Self-assembled low precursor flow growth without *in situ* silane injection

4.3.1 Introduction

We have shown that the additional silane flow allows to grow cataylyst-free GaN NW by MOCVD thanks to the SiN_x passivation layer formation on m-plane facets.

This method produce efficiently GaN NW which can be used for single NW device fabrication, as mention in Chapter 4.4.4. Nevertheless, the high residual n-dopant concentration induced by the high silane injection will definitely degrade the optical properties of the materials. Also, the mixture of polarity in single GaN NWs can induce more free carriers trapping in the IDB, which may degrade the luminescence homogeneity [156] and the N-polar GaN NWs is believed to have higher impurities incorporation [67]. In addition, another limitation may come from the typical diameter of the catalyst-free GaN NWs grown by MOVPE, which is generally around several hundreds of nanometer. This value is much larger than those synthesized by catalyst-assisted MOVPE [27], [80] or catalyst-free MBE (in the 30-100 nm range) [34], [157]. It obviously hinders some appealing advantages of the NW such as the elastic strain relaxation for large lattice-mismatch heterostructures [158] and the use of quantum dot confinement in light emitters [50]. Furthermore, the reported linewidth of the photoluminescence (PL) near band edge (NBE) emission for GaN NWs grown by MOVPE is about several hundred meV at 5 K [159], *i. e.* about two orders of magnitude larger than high-quality GaN NWs grown by MBE [160], [161].

Thus, in this thesis, there was a strong motivation to develop a facile way to grow nanoscale GaN NWs without silane to improve potical properties. In addition, we have also shown that the N-polarity is required to grow NW with silane injection. We are also interested to develop the growth of Ga-polar NW.

In this section, we present a new catalyst-free route without *in situ* silane injection to obtain by MOVPE nanoscale GaN NWs on c-sapphire exhibiting a high-optical quality with single Ga-polarity. This approach can be applied to all kind of MOVPE reactors, since the process is simply based on the use of bare c-sapphire substrates - without nitridation process and buffer layer deposition - and on the decrease of precursor flow compared to the standard GaN NW growth, keeping the same V/III ratio ($\sim$ 25). Such growths produce pencil-shaped NWs with a stem diameter less than 200 nm and a $\sim$ 5 nm pyramidal tapered top. Excellent optical properties, comparable to the best reported MBE GaN NWs, have been measured by μPL at 5 K indicating a high-crystalline quality as confirmed by high resolution TEM and X-ray diffraction.

4.3.2 Growth process and mechanisms

In a first step, the c-sapphire substrate is baked in situ under H_2 (8000 sccm, 100 mbar) at 1100 °C for 20 min. Then, the reactor temperature and pressure are directly set to the NW growth conditions at 1000 °C and 100 mbar without any surface nitridation. The NW growth is performed by injecting simultaneously 3.38 μmol/min of TMGa and 89 μmol/min of NH_3 under N_2 carrier gas flow (2000 sccm, 100 mbar) for 30 min. The nominal V/III ratio is equal to 26 (*i.e.* an usual value for the NW growth), but note that the injected precursor quantity is at least two orders of magnitude lower than in standard planar [162] and NW [63], [65], [64] GaN MOVPE growths.

Figure 4.21 (a) shows a 45°-tilted scanning electron microscopy (SEM) image of the as-grown GaN NW assembly. They grow perpendicularly to the substrate and their average density is about 1.3×10^3 cm^{-2}. This very small value can be explained by the unusual low precursor flows that may decrease the seed nucleation probability. As shown by the detailed views in the inset of Figure 4.21 (a), GaN NWs have a pencil shape composed of a stem with vertical sidewall facets of typical diameter around 100-200 nm and a pyramidal top terminated by inclined facets. The growth rate is very low (about 4 μm/h) compared to the growth under silane that may reach 150 μm/h [65]. As reported before in Chapter 4.2.2, the geometry of wurtzite GaN nanostructures in MOVPE growth can be governed by the crystal polarity [163]. It is therefore highly probable that the pyramidal shape of the NW top results from the Ga-polar growth induced by the nucleation on non-nitridated c-sapphire surface, in agreement with Reference [71].

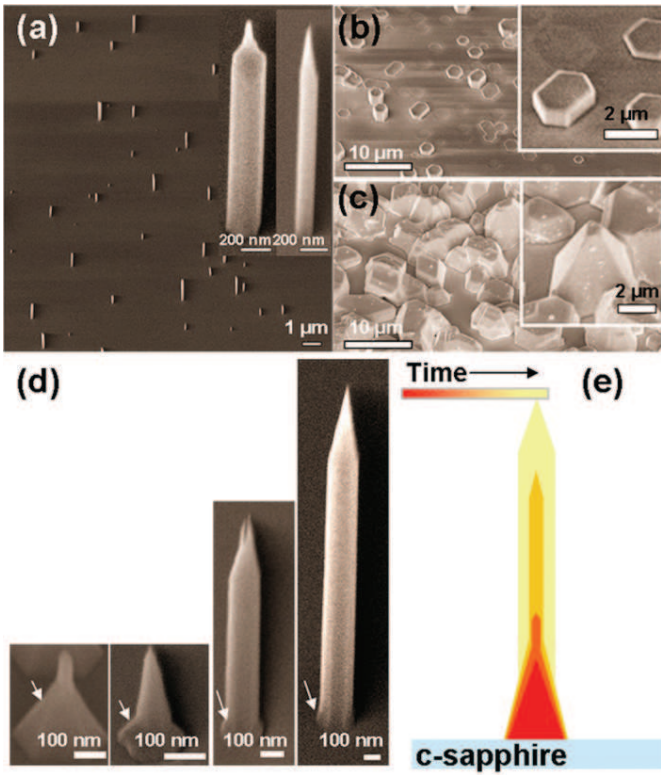

Figure 4.21: (a) 45°-tilted SEM image of GaN NWs grown on a non-nitridated c-sapphire surface at low precursor flows (see details in the text). Comparison with similar growths on (b) nitridated sapphire surface (same flows) and (c) non-nitridated surface, but with larger precursor flows. (d) Shape evolution of the GaN NW as a function of time and (e) schematics.

To check this point, a similar growth has been performed by adding a surface nitridation step using NH_3 treatment (2000 sccm, 1050 °C, 100 mbar) for 90 sec before the NW growth to force the N-polar crystal c-orientation [71]. As shown in Figure 4.21 (b), hexagonal prismatic nanostructures with large diameter (1-2 μm) are observed, confirming that the Ga-polar crystal growth orientation is required within our conditions to form nanoscale pencil-shaped GaN NWs. In order to further investigate the growth mechanism and in particular the morphology evolution, SEM observations were performed at different stages of the NW synthesis (see Figure 4.21 (d)). Interestingly, at the early stage of the growth, a pyramid is first formed and followed by a distinctive NW nucleation on its top. Afterwards, NWs undergo a relatively fast vertical extension for longer growth durations with a limited lateral growth maintaining the NW geometry with a pyramidal top. In

addition, inclined facets are always observed at the base of the NWs (marked by the white arrows in Figure 4.21 (d)) as a signature of the initial pyramid seed formation. To summarize these observations, the NW growth evolution is schematically depicted in Figure 4.21 (e).

4.3.3 The structural properties

For HRTEM measurements, the NWs have been scraped off from the as-grown sample and dispersed onto copper grids covered by amorphous carbon film. Observations along the $[11\bar{2}0]$GaN zone-axis at the NW tip and sidewall are shown in Figure 4.22 (a) and (b). The corresponding selective area electron diffraction (SAED) patterns (see Figure 4.22 (c)) confirm the NW wurtzite crystal structure and the c-axis growth direction ([0002]). The NW presents in Figure 4.22 (a) a perfect crystalline quality without showing any structural defects like threading dislocations and stacking faults. It is worth to mention that the measured 0.52 nm c-interplanar distance corresponds to a fully strain relaxed crystal (see Figure 4.22 (b)). The tapering is explained by the change of facet orientations on the NW sidewalls: vertical $\{10\bar{1}0\}$ planes alternate with inclined $\{10\bar{1}1\}$ planes as indexed by the SAED patterns and the angle measurements (151 ° between these two planes). This facet evolution supposes a small difference between surface energies that is also consistent with the transition between pyramidal seeds with the six $\{10\bar{1}1\}$ plane [164] and NWs as discussed in Figure 4.21 (d). It has been checked that this small energy difference and the resulting shape transition are directly related to the low precursor flow growth and kinetics. Indeed, by employing a higher precursor flow (TMGa: 135.22 μmol/min and NH_3: 2232 μmol/min) and keeping constant the other growth parameters, we observe in Figure 4.21 (c) truncated pyramidal nanostructures without the appearance of vertical $\{10\bar{1}0\}$ facets. This result is in agreement with the theoretical calculation of equilibrium shapes in GaN nanostructure grown along the Ga-polar c-direction [155].

The epitaxial relationships of the NWs with the sapphire substrate and the occurrence of other phases have been studied by XRD with the European Synchrotron Research Facility (ESRF, Grenoble, France) at the energy of 10.30 keV (0.1204 nm). Extended reflectivity has been measured along the [00L] direction of the c-sapphire with a very high counting range. As shown in Figure 4.23 (a) drawn in L reciprocal lattice units (r.l.u.) of sapphire ($R\bar{3}c$, c = 1.2991 nm), the c-GaN planes (see (004) and (002) Bragg peaks) grow along the c-axis of sapphire

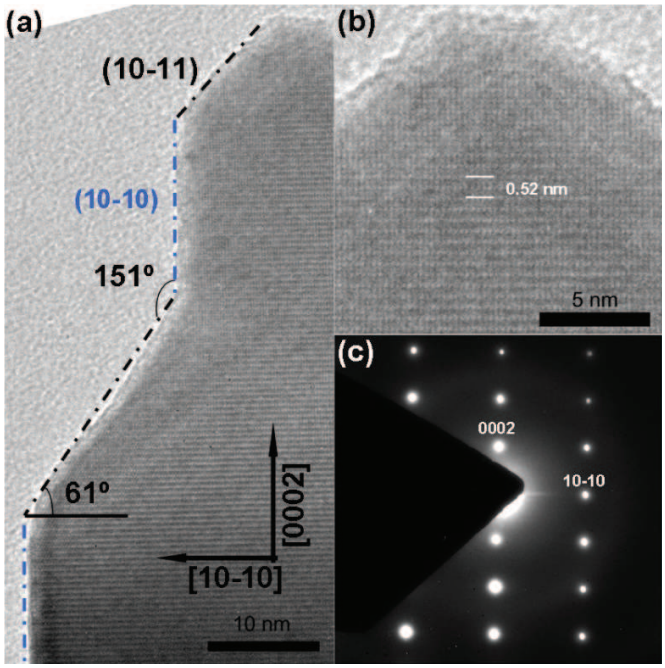

Figure 4.22: High resolution transmission electron microscopy of GaN NWs along the $[11\bar{2}0]_{GaN}$ zone-axis at (a) sidewall and (b) tip positions with corresponding selective area electron diffraction pattern (c).

(see (0012) and (006) peaks).* The c lattice parameter of relaxed GaN (0.5188 nm) can be directly retrieved from this measurement confirming HRTEM local measurement. The oscillations at small L-values indicate the deposition of a 2.9 ± 0.1 nm thick layer on the sapphire consistent with a flat overgrowth between 3D objects. Grazing incidence X-ray diffraction (GIXRD) has been performed at very small grazing incidence (0.03°) to evidence that c-axis GaN growth is truly coming from the NWs. In-plane (H00), (0K0), (HH0) scans have been measured with respect to the sapphire reference to analyze the epitaxial relationships (see for example the (0K0)-scan reported in Figure 4.23 (b)). We observe that the majority GaN phase corresponds to the usual 30° rotation of the GaN around the sapphire c-axis (generally noted $[1\bar{1}00]_{GaN} \parallel [1\bar{2}10]_{Sapphire}$ and $[0001]_{GaN} \parallel [0001]_{Sapphire}$) with an in-plane twist disorientation of about 2°. Complementary

*A small amount of (110) and (100) GaN well-crystallized phases can be also indexed as well as a broad contribution centered at L ∽ 5 r.l.u. This signal is attributed to large objects of very small density, which were not observed in more conventional growth method using silane injection (see Reference [65]).

crystal truncation rods (CTRs) have been also measured by varying the grazing incidence in the 0.03-0.30 range to verify the signature of NW-specific diffraction features [165]. These measurements allow estimating also the tilt to be around 2°.

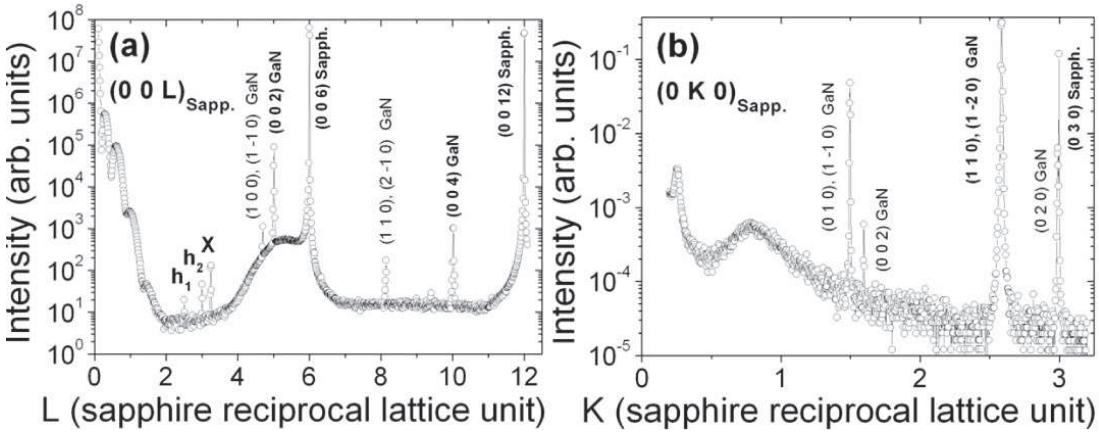

Figure 4.23: X-ray diffraction measurements of GaN NWs grown on c-sapphire performed at the European synchrotron radiation facility (wavelength 0.12037 nm). Peak indexation are performed in agreement with the usual bulk lattice parameters. (a) Scan along the [00L] direction of the sapphire substrate. h1, h2 correspond respectively to second order (002) GaN and (006) Sapphire harmonics. Peak X may be indexed by a sapphire reflection tail or by a Ga crystalline phase. (b) In-plane grazing incidence X-ray diffraction measurements at 0.03° along the [0K0] sapphire direction.

4.3.4 The optical properties

The optical properties of single GaN NWs have been studied by μPL at low temperature (5 K) using a 244 nm frequency-doubled continuous wave Ar^+ laser excitation source focused to $\sim$ 2 μm diameter spot (in collaboration with B. Gayral and D. Sam-Giao, CEA/INAC). Benefiting from the low density of the GaN NWs assembly, PL spectra were obtained on as-grown single NWs without any dispersion step that could modify the intrinsic NW optical properties [161]. Figure 4.24 shows a typical PL spectrum of single standing GaN NWs that exhibits only one intense sharp peak centered at $\sim$ 3.47 eV assigned to the NBE emission from GaN while no important contribution from deep defect bands is observed. The inset of Figure 4.24 gives a detailed view of the NBE emission. The

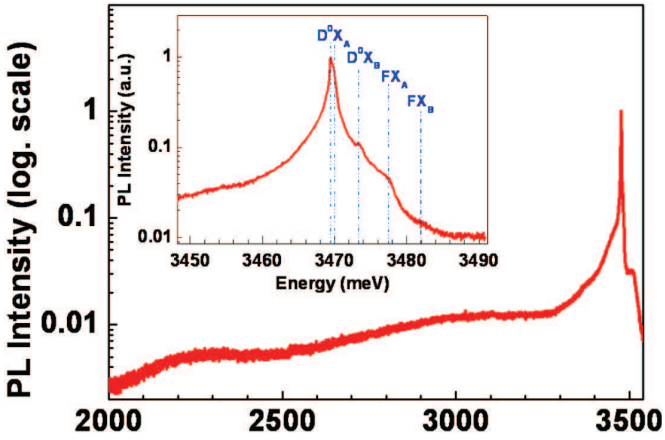

Figure 4.24: Typical low temperature (5 K) micro-photoluminescence measurement of single GaN NWs. The peak full width at half maximum of this near band edge emission is about 0.95 meV. Donor bound exciton recombinations (D^0X_A and D^0X_B) and free A and B exciton (FX_A and FX_B) are indicated. Intensities are in arbitrary units and in log scale, the inset shows a magnification of the main peak.

dominant contribution, related to donor bound exciton recombination (D^0X_A) is located at 3.470 eV and has a fullwidth at half maximum of only 0.95 meV. This peak is actually composed of two contributions with linewidth 320 μeV and 720 μeV, tentatively ascribed to exciton bound to various donor species. While the displayed spectrum corresponds to the narrowest linewidth that was probed, the typical linewidth for the D^0X_A peak on this sample range between 1 and 3 meV. These peak widths are remarkable for NWs grown by MOVPE and are comparable to what can be obtained by MBE [161]. At higher energies, three shoulders respectively at 3.473, 3.477 and 3.482 eV can be ascribed to the donor bound exciton with a B-type hole (D^0X_B), the free A and B exciton (FX_A and FX_B). Note also that the emission around 3.41-3.42 eV associated to exciton bound to stacking faults, which is commonly observed in MBE GaN NWs is not observed in this sample. The fact that donor bound exciton recombination dominates the 5 K PL with a narrow 0.95 meV linewidth at the fully relaxed position value (3.470 eV) confirms the excellent NW crystalline quality and homogeneity.

4.3.5 The growth mechanisms

Actually, the low flow of the precursors decreased the Damkohler number $D_a = k\frac{\delta}{D}$ where k is the average rate constant of the heterogeneous surface reaction, δ is

the boundary layer thickness (fixed by carrier gas) and D is the diffusion constant [166]. This dimensionless number corresponds to the ratio between the chemical reaction and the mass transfer rates. At low-flow conditions (decreasing mainly k and keeping D almost constant), the system may become more reaction-rate rather than kinetically limited. The system should therefore reach more easily the theoretical equilibrium shapes predicted for GaN nanostructure grown along the Ga-polar c-direction in favor of m-planes exhibiting low surface energy [155].

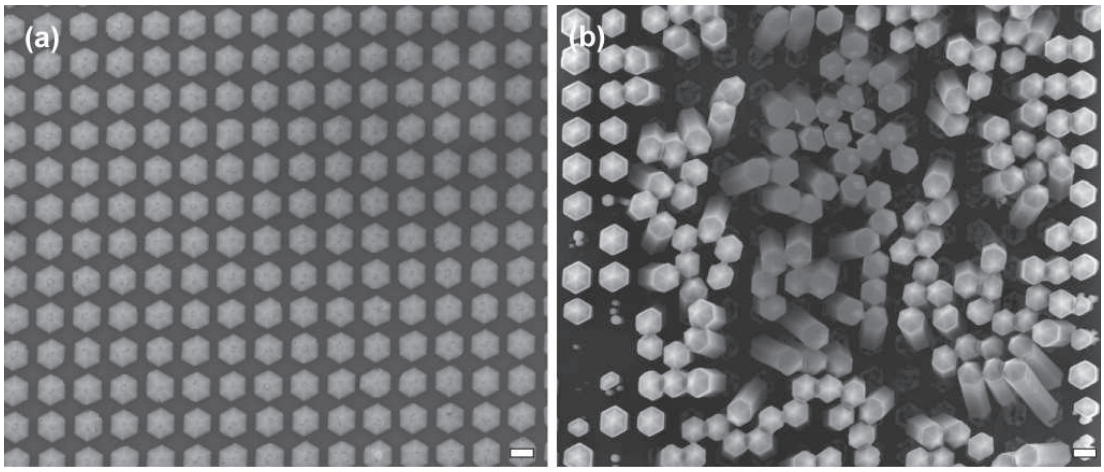

Figure 4.25: Top-view of SAG Ga-polar nanostructures on GaN patterned surface with different growth temperature: (a) pyramids at 1040 °C and (b) wires at 1150 . The scale bars are 200 nm.

Another way to decrease D_a is to increase the growth temperature T to benefit from a faster increase of D than k. This proposal has been checked with high temperature growth ($\sim$ 1150 °C) where pyramidal like structures transform to wires with m-plane facets. A patterned substrate of a GaN layer grown on c-sapphire has been first realized by laser interferometry lithography. This layer is Ga-polar due to the standard planar growth conditions. The detailed patterning process and polarity measurement by CBED will be discussed in Chapter 5.2. Then, a 450 s SAG has been performed with 135.22 μm/min TMGa, 2232 μm/min NH_3 under N_2 (without silane injection). As shown in Figure 4.25 (a), hexagonal pyramids with $<1\bar{1}01>$ facets can be observed at the growth temperature of 1040 °C. At much higher temperature ($\sim$ 1150 °C) as shown in Figure 4.25 (b), we observe the growth of wires with m-plane facets and pyramids at the top. In this case, it is supposed that the diffusion coefficient D is increased with temperature

faster than the surface reaction rate leading to a decrease of the D_a number and therefore to the limitation of the growth by reaction rate (thermodynamic) considerations rather than mass-transport (kinetics). These results are also in agreement with experimental measurements reported in Ref. [167].

4.3.6 The growth of radial MQW heterostructures

We have then performed the InGaN/GaN MQW heterostructures growth using this pencil-shaped μ-GaN NWs as template. The growth parameters of the MQW deposition are the same as used in Chapter 4.1.3. Figure 4.26 (a) presents a typical 45°-tilted SEM image of the as-grown sample. It can be observed that the InGaN/GaN MQW heterostructures cover all the sidewall surface of the u-GaN NWs from top to bottom as schematically shown in Figure 4.26 (b). This is consistent with the observation in chapter 4.1.3 that the MQWs coating can cover all the u-GaN part. It also further confirms that the selectively partial coverage of the MQWs on top u-GaN part but not on n-GaN part at the bottom is due to the SiN_x passivation layer rather than the specific adatoms diffusion process itself. Optical and structural measurements are currently underway to further characterize the core-sell heterostructures.

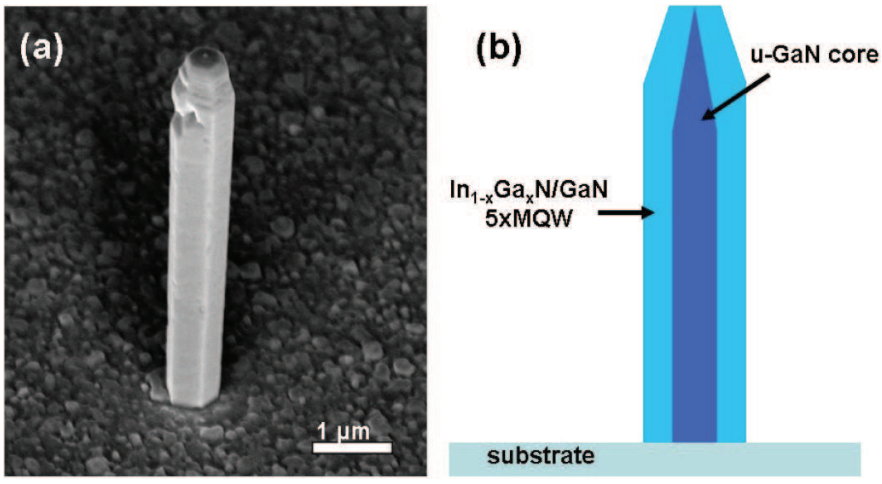

Figure 4.26: (a) 45°-tilted SEM image of the as-grown pencil-shaped single GaN NWs with radial InGaN/GaN MQW heterostructures and (b) the schematic drawing showing the complete coverage of the MQW on the sidewall facets of the NWs.

4.4 Conclusions

In this chapter, firstly, the mechanism related to the necessity of using *in situ* silane flow to grow catalyst-free self-assembled GaN NW by MOVPE was investigated. It has been proved that the NW sidewall surface passivation induced by the formation of a thin SiN_x dielectric layer is responsible for the limited lateral growth rate to favor the wire geometry. The constant NW diameter during the growth due to this surface passivation phenomenon has also enabled the study of the adatoms diffusion path in the NW growth. It has been clarified that the adatoms incorporated into the NW mainly comes from direct gas phase impinging and sidewall surface diffusion with little contribution from substrate to NW diffusion. This fundamental growth mechanism understanding was also expanded to applications for the position and length controlled growth of InGaN/GaN radial MQW heterostructures on top part of the NW. In addition, this radial n-MQW-p heterostructure has also been demonstrated to be easily integrated into single NW LED device fabrication benefiting from the uncovered nature of n-GaN part at the NW base.

Secondly, it has been shown that the shape of GaN nanostructures is linked with crystal polarity: the N-polar leads to wire shape, whereas the Ga-polar leads to pyramidal shape. This property gives a novel approach to grow GaN NW on N-face GaN templates in the case of epitaxial NW growths.

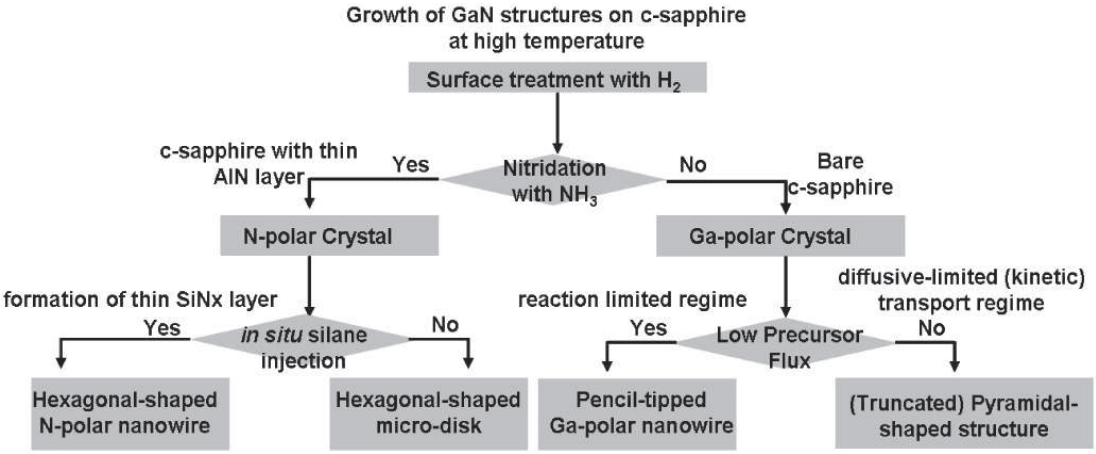

Figure 4.27: Chart flow of the main step and specific growth condition to grow N or Ga-polar GaN NWs on c-sapphire substrate.

Thirdly, we have demonstrated the MOVPE growth of catalyst-free Ga-polar GaN NWs with 100-200 nm diameters capped with a pencil shaped tip ($\sim$ 5 nm diameter) on bare c-sapphire substrates by using both low V/III ratio and V-III precursor flows without *in situ* silane flux. The growth mechanism is explained due to the favor of reaction-limited mechanisms rather than diffusive-limited (kinetic) transport in this growth condition. Their excellent optical emission properties with a 1-3 meV photoluminescence NBE linewidth at 5 K and negligible deep defect band emission show that they are made of relaxed homogeneous material with few point defects.

It is worth to note that both N-polar and Ga-polar GaN NW can be grown on c-sapphire substrate with a carefully polarity control through the surface treatment (nitridated c-sapphire leads to N-polar crystal and bare c-sapphire gives Ga-polar) and specific growth conditions (N-polar NW needs the *in situ* silane flow and Ga-polar NW has to be grown with low flow rate) as depicted in Figure 4.27.

4. CATALYST-FREE MOVPE SELF-ASSEMBLED GROWTH OF GAN NWS: FROM GROWTH MECHAMISM STUDY WITH *IN SITU* SILANE INJECTION TO A NEW METHOD WITH LOW PRECURSOR FLOW INJECTION

Chapter 5

Selective area growth of GaN nanostructures

This chapter deals with the selective area growth (SAG) using Si_3N_4 mask of (1) GaN NWs on full 2" c-sapphire substrates patterned by nanoimprint lithography and (2) GaN nanopyramids on Ga-polar GaN template patterned by laser interferometry lithography. It will be pointed out particularly that the shape selection between SAG GaN NWs and nanopyramids is controlled by the crystal polarity of the substrate surface as observed in Chapter 4.2. In the case of SAG growths on sapphire, the emphasis will be put on the studies of the growth homogeneity and selectivity in both seeds nucleation period and NWs growth stage. The optical properties of these SAG GaN nanostructures studied by low temperature CL will be correlated with the structural properties measured by TEM and XRD. In the case of SAG growths on GaN template, the effect of different MOVPE growth parameters on the geometry of the nanopyramids is analyzed. After a study of the nanopyramids facet evolution as a function of the growth time, it will be shown that InGaN QDs can be positioned on tip of a pyramid array with high density ($\sim 10^9$ cm^{-2}).

Contents

5.1 SAG of GaN NWs on c-sapphire

5.1.1 Introduction

In the previous chapters, we have already detailed the catalyst-free self-assembled GaN NWs growth by MOVPE suffering from a low control of size and density. In the literature, significant efforts have already been made to control the growth of GaN compound nanostructures in terms of size, position and density to get homogeneous structural and optical properties as introduced in Chapter 2.2.3.

Indeed, as discussed in Chapter 4.2, nitridated sapphire surface favours the growth of N-polar GaN crystals and such polarity is particularly interesting to promote the growth of hexagonal GaN NWs. This motivates us to develop the SAG of GaN nanostructures directly on c-sapphire that gives the opportunity to grow well organized c-oriented hexagonal GaN NWs. Moreover, the study and control of homogeneity of the nucleation selectivity of SAG GaN NWs on c-sapphire substrate remains an open question to be addressed. In addition, some more fundamental issues like the structural and optical properties of SAG GaN nanostructures grown on sapphire have to be carefully studied especially due to the large lattice mismatch between sapphire and GaN as well as the use of a relatively thicker dielectric layer than for self-assembled GaN NWs growth.

In this part, we will present the SAG of c-oriented GaN NWs directly on patterned c-sapphire substrates. The patterning is obtained by nanoimprint lithography (NIL), which exhibits relevant advantages with reported other nanoscale patterning methods (for example electron beam lithography) with no charge effect coming from insulating materials and full wafer surface patterning at low cost and time-consumption. The first part of this section will detail how the nanostructure shape of GaN nucleation seeds and the SAG nucleation homogeneity are related to the growth temperature. Then it will be shown that hexagonal prismatic-shaped GaN SAG nanostructures can be managed with a high homogeneity by a two-step temperature growth process combined with an annealing procedure. Next, it will be further demonstrated that this high nucleation homogeneity can be maintained during the NWs growth by a pulsed TMGa and silane flow method. Finally, thanks to the use of sapphire substrate without any intermediate GaN template layer, the optical properties of single GaN hexagonal nanostructures will be studied with respect to the structural properties to understand the influence of the nanostructure size and compared to the self-assembled grown GaN NWs. In addition, the optical properties of SAG GaN NWs grown under pulsed precursor

mode are also compared to those of NWs with a continuous precursor growth.

5.1.2 Surface patterning by nanoimprint lithography

The patterning of 2" c-sapphire substrates was carried out by NIL using a silicon mold with a uniform square array of circular pillars named 'picot' (diameter: 350 nm and pitch 1 μm) [168] (in collaboration with S. Landis and B. Martin, CEA/LETI). Figure 5.1 shows schematically the three main steps to prepare the patterned substrates.

(1) A 5 nm-thick Si_3N_4 dielectric mask is deposited by plasma enhanced chemical vapour deposition at 300 °C. Hexamethyldisilazane (HMDS) is then spin coated to promote the adhesion of the imprint resist (see in Figure 5.1 (a)).

(2) A 225 nm-thick resist (NEB22 from Sumitomo) is spread and soft-baked at 110 °C for 1 minute. The imprint process is done at 110 °C using a contact-force of 10 kN in a EVG 520HE nanoimprint equipment (see in Figure 5.2 (a) the SEM image of the resist layer just after the imprint). The residual resist layer at the bottom of the holes is removed by a short oxygen plasma treatment (O_2 100 sccm, pressure 133 mbar, power 100 w and time 45 s) to reach the Si_3N_4 surface (see Figure 5.1 (c) and Figure 5.2 (b)).

(3) The Si_3N_4 mask is etched by using SF_6 plasma (SF_6 15 sccm, pressure 26.6 mbar, power 50 w and time 30 s) followed by resist stripping by Acetone to obtain a uniform patterning on the whole 2" wafers with a regular array of circular holes of 400 nm in diameter spaced by 1.1 μm (see in Figure 5.1 (c) and (d) the AFM image of the patterned substrate after resist stripping).

The choice of the circular shape of the openings is motivated by simplicity arguments in order to avoid taking into account the anisotropy of the pattern shape and orientation and its possible influence on the growth in terms of facet evolution.

5.1.3 The homogeneity of seed nucleation selectivity

The growth of nucleation seeds was performed at high pressure (800 mbar) using a carrier gas flow of 8000 sccm of N_2 . Before growth, an *in situ* pre-treatment of the patterned sapphires was done at high temperature ($\sim$ 1200 °C) using two steps: first a bake under H_2 atmosphere during 20 min to clean the surface followed by a

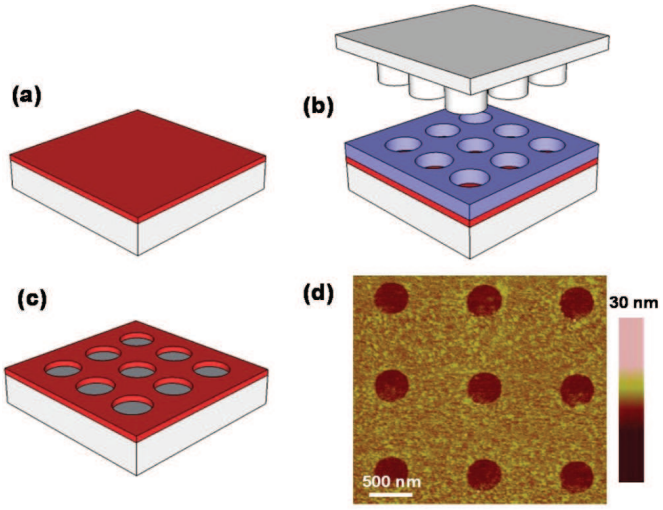

Figure 5.1: (a)-(c) Schematic of the nanoimprint patterning process on c-sapphire substrate. (d) Typical AFM image of the patterned Si_3N_4 mask: array of 400 nm holes spaced by 1.1 μm.

surface nitridation using ammonia flow (200 sccm) for 400 s. For GaN deposition, TMGa and NH_3 were used as precursors for the III and V materials. The V/III molar ratio was set to 16 corresponding to an injection flux of 135 μmol/min and 2.230 mmol/min for TMGa and NH_3. The growth temperature has been set between 900 and 1040 °C to study the influence of growth temperature on the SAG seed nucleation selectivity homogeneity.

5.1.3.1 Single-step temperature growth

SAG on patterned sapphires was performed at 900, 950, 1000 and 1040 °C and Figure 5.3 (a) and (d) shows the corresponding 45 °-tilted SEM images. At 900 °C (see Figure 5.3 (a)), GaN crystals are irregular in shape and size and are strongly disoriented with respect to the c-sapphire substrate. By increasing the temperature to 950 °C (see Figure 5.3 b)), the orientation along the c-axis is improved, but the shape is still irregular. From 1000 to 1040 °C (see Figure 5.3 (c) and (d)), we observe more regular hexagonal shapes composed of flat <0001> horizontal planes on top (*i.e.* prisms) and six $<1\bar{1}00>$ vertical side facets. Despite the significant improvement of the crystalline quality and orientation with increasing growth temperature, the homogeneity of the nucleation in the mask openings is strongly degraded since only a few openings are filled for 1040 °C growth. Ac-

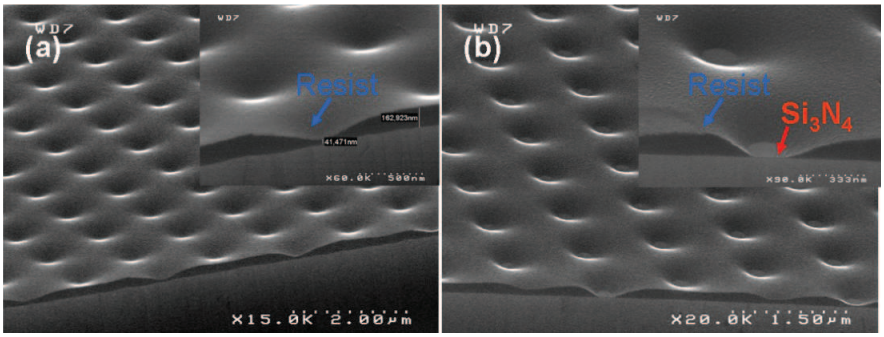

Figure 5.2: Tilted SEM image of the pattern substrate with resist (a) just after the imprint process (b) after the O_2 plasma treatment to exposure the Si_3N_4 layer beneath the opening.

tually, the percentage of opening fillings noticeably decreases from nearly 85 % at 900-950 °C, to 60 % at 1000 °C and to about 20 % at 1040 °C. The SAG of GaN nanostructures on patterned sapphire substrates is therefore highly sensitive to the growth temperature in terms of crystal shape and homogeneity of nucleation selectivity: the formation of regular hexagonal nanostructures is obtained at high temperature with poor selectivity efficiency, while the opposite trends are observed for lower temperatures.

5.1.3.2 Two-step temperature growth

To combine high homogeneity of nucleation selectivity and high crystal quality of GaN nanostructures grown on sapphire, a two-step temperature process has been developed. The initial nucleation step is first made at 950 °C for 200 s with TMGa and ammonia sources to get a high homogeneity of the GaN nucleation seeds. The TMGa source is then stopped and the temperature is ramped from 950 to 1040 °C in 200 s under ammonia flow. Finally, the TMGa supply is restarted for 350 s at higher temperature (1040 °C) to grow high quality GaN crystals. The other growth parameters (pressure, flows of carrier gas and precursors) remain the same as written in Chapter 5.1.3.1. Figure 5.4 (a)-(c) shows the 45 °-tilted SEM measurements after each step of the growth. The evolution of GaN crystal shape is schematically illustrated in Figure 5.4 (d).

As observed in Figure 5.4 (a), GaN growths at 950 °C result in c-oriented crystals with mostly an irregular truncated pyramidal shape (see the inset) with a filling percentage of mask openings around 85 %. The average diameter of the GaN nanostructures is about 500 nm that means there is already a lateral

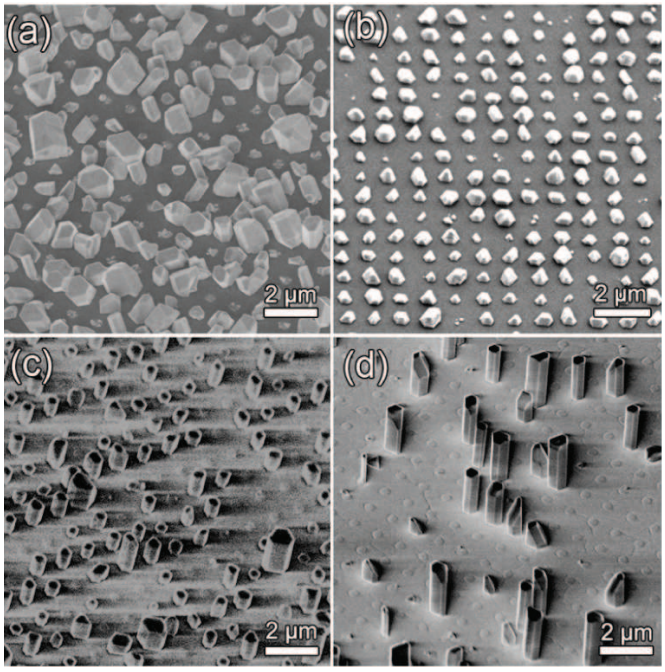

Figure 5.3: 45°-tilted SEM images of the SAG for a single-step temperature process at (a) 900 °C, (b) 950 °C, (c) 1000 °C and (d) 1040 °C.

overgrowth outside the 400 nm openings. The temperature ramping under ammonia changes the crystal shape from irregular truncated pyramids to well-shaped hexagons as shown in the inset of Figure 5.4 (b) while keeping the homogeneity of nucleation selectivity. This anisotropic shape evolution of GaN nanostructures may be explained first by a mass transport driven by Ga diffusion to reach the energetically stable facets, *i.e.* the $(1\bar{1}00)$ planes at high temperature for growth on pre-nitridated sapphire substrates, which gives rise to the facets of the hexagons [169].

In addition, the isotropic size reduction of the hexagonal nanostructures compared to the initial truncated pyramids in both lateral and vertical directions is also observed and could be explained by a decomposition of GaN at high temperature induced by H_2 etching coming from the NH_3 decomposition. The duration of the step is thus critical to avoid the complete vanishing of GaN seeds. Notice, the exact value of this duration should be optimized as a function of MOCVD setup. In the third step, the restart of the GaN growth maintains the previous hexagonal shape (see Figure 5.4 (c) and the inset). The typical diameter of hexagonal nanostructures after a supplementary growth duration of 350 s is

about 500-700 nm in the lateral dimension with a 0.6-1 aspect ratio. The increase in size distribution of the GaN nanostructures with the growth time is probably due to the uncontrolled lateral overgrowth on the mask and to the initial size distribution of the nucleation seeds.

To sum up the multi-step temperature growth approach, the first step allows to get high homogeneity of nucleation selectivity of the seeds, the annealing step at ramped temperature induces the formation of hexagonal islands with uniform size (400 ± 20 nm) and the third step leads to hexagonal prismatic nanostructure growth.

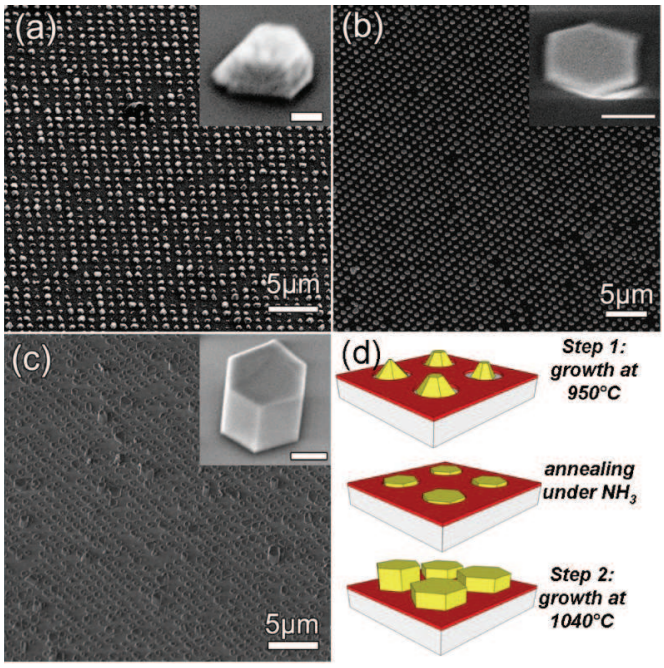

Figure 5.4: 45°-tilted SEM images of the major stages of the two-step temperature process for the GaN SAG on c-sapphire: (a) after 200 s GaN deposition at 950 °C, (b) after 200 s temperature ramping from 950 to 1040 °C under ammonia, (c) after 350 s GaN deposition at 1040 °C. The insets of each image give an enlarged view of typical single objects in the openings (the inset scale bars are 200 nm). (d) Schematic describing the shape evolution of GaN nanostructures during this two-step temperature growth method.

5.1.3.3 Shape evolution versus growth temperature

In the last decade, the relationship between the crystal shape of GaN nanostructures and the growth parameters, especially the temperature has been mainly investigated by using the Wulff's plot (γ-plot) which deals with the anisotropy of the surface energy. It has been found in molecular beam epitaxy SAG that the equilibrium geometry of GaN nanostructures may change from pyramid to hexagon by decreasing the growth temperature [170].

In the case of MOVPE SAG process, Tanaka *et al.* [171] have reported the modification of SAG stripe morphologies from trapezoidal to rectangular cross-section with an increase of growth temperature from 850 to 1040 °C on pre-nitridated sapphire substrates. The kinetic influence in terms of kinetic Wulff's plot (ν-plot) must also be taken into account in a real MOVPE growth condition [147], [155]. For instance, as mentioned several times in this thesis that it has been found that the GaN crystal polarity strongly influences the growth rate of different crystal facets at high temperature leading to hexagonal N-polar wires [163]. In conclusion, the observed shape evolution of the GaN nanostructures from pyramidal shape at low temperature to hexagonal prismatic shape at high temperature can be understood by a combination of the influences of temperature-related facet energy anisotropy and kinetics. Further experiments to quantify this behaviour in details should be addressed in the future.

5.1.3.4 Selectivity versus growth temperature

The MOVPE growth rate is in general determined by the competition between deposition from the vapour phase transport and desorption phenomena (evaporation, H_2 etching ...). In our growth temperature range (above 950 °C), the transport of species in the vapour phase can be considered as constant (transport regime), whereas the desorption rate increases with the growth temperature (desorption regime). Additionally, the desorption of N atoms should be higher than in the standard two-dimensional GaN growths because of the low V/III ratio used to avoid the lateral growth, when a high ammonia partial pressure is generally required above 1040 °C to limit N-desorption [172]. In the case of SAG, the effective diffusion length of the reactive species on the mask (called the migration length) is a third effect that may contribute significantly to the growth rate [173], [174]. The migration length is usually strongly dependent on the growth temperature [175], [176]. At high temperature, ammonia molecules are immediately decomposed to adduct in the gas phase [172], and therefore, mainly Ga

species are involved in the mask migration process. By increasing temperature, the migration length of the Ga species is decreased due to the significant reduction of the residence time of Ga species on the mask, which reduces the amount of supplied materials for incorporation [176]. Thus, the combination of deposition, desorption and migration contributions leads to a reduction of the nanostructure growth rate when the growth temperature is increased in the 900-1040 °C range.

Furthermore, we can suspect that the nucleation of GaN crystals does not occur exactly at the same time in all openings due to the different surface states in terms of chemistry and structure: residues of resist, different diffusion barriers, surface defects, efficiency of nitridation (with respect to polarity control). The seeds, which appear first, will serve as 'sink' to collect the contiguous growth species. It then creates an adatom concentration gradient on the nearby surface that may lead to a diffusion network [134]. For 1040 °C growth, less material is provided compared to the growths at lower temperature. Therefore, the quantity of provided material is not large enough to compensate the desorption effect in the mask openings, except for some sites benefiting from the 'sink' effect that may locally increase the growth rate. It finally gives a poor homogeneity of nucleation selectivity of SAG growth at high temperature. In the case of growths at lower temperature (900 and 950 °C), although the 'sink' effect still exists, the growth rate is high enough to fill most of the mask openings, which leads to a higher homogeneity of nucleation selectivity.

For two-step temperature growth, the GaN seeds nucleate in most of the mask holes due to the low temperature process (950 °C) giving a high homogeneity of nucleation selectivity. After the annealing step under ammonia, the homogeneity of nucleation selectivity is maintained with a reduction of the size distribution of the nanostructure growth. Thanks to the high homogeneity of nucleation selectivity and size uniformity after the ammonia annealing, the 'sink' effect corresponding to a local gradient of incoming species is strongly reduced at high temperature (1040 °C), and SAG of GaN hexagonal prisms with high homogeneity of nucleation selectivity can be obtained.

5.1.4 The study of NWs growth selectivity homogeneity

By using the two-step temperature nucleation growth method, we have successfully managed to grow the nucleation seeds with a high selectivity homogeneity in the hexagonal prismatic shape. Following on, in order to get ordered GaN NWs array we turn the growth condition to favor the NW formation by introducing

an additional 200 nmol/min *in situ* silane flow just after the step of annealing under NH_3.

Figure 5.5 (a) presents the 45°-tilted SEM image of the typical as-grown NW array with a growth time of 500 s. It can be observed that the NW selectivity homogeneity defined as filling factor in the mask opening is as low as 5 %. As it has been studied in Chapter 4.1.2.2, the main adatoms diffusion path for the NW growth is the top and sidewall gas phase diffusion. As a result, the first nucleated NWs serves as 'sink' and attract most of the precursors. Notably, it also has been shown in this thesis that this so-called 'sink' phenomenon becomes more evident in the growth either with higher growth rate (see the discussion of Figure 4.9) or with a relatively large desorption rate (see the discussion of Figure 5.3). Thus, we believe that by choosing carefully the growth regime with appropriate growth rate and by enhancing the adatoms diffusion to compensate the 'sink' effect, the SAG GaN NWs selectivity homogeneity shall be effectively increased.

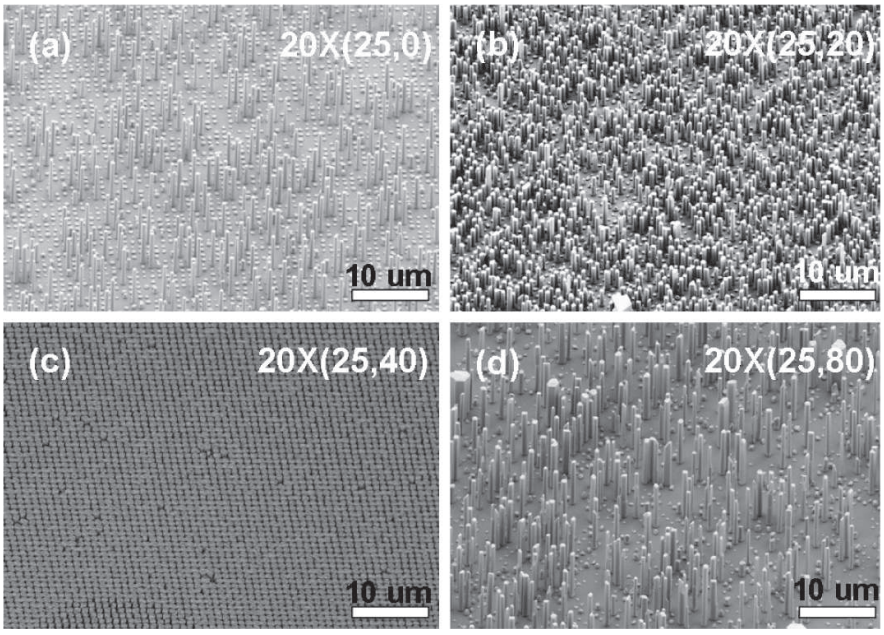

Figure 5.5: 45°-tilted SEM image of SAG GaN NW array with (a) continuous gas flow growth mode and pulsed precursor growth mod with an interval of TMGa and silane flux supply of (b) 10 s, (c) 20 s and (d) 40 s respectively.

The precursor flow modulation growth method (named also pulsed precursor growth mode) has been reported in the literature to be an effective method to reduce the growth rate along the c-axis and to improve the surface flattening by

enhancing the precursor adatoms surface diffusion in GaN [169] and AlGaN [177] 2D growths. In this content, we propose to use a pulsed precursor growth mode to eliminate the 'sink' effect and get a high NWs selectivity homogeneity. In the pulsed precursor growth mode, we continuously inject NH_3 into the reactor whereas TMGa and silane flows are interpreted for t_1 of 20, 40 and 80 s for every 25 s as depicted in Figure 5.6. The choice of supplying TMGa alternately but continuously providing NH_3 in our NW growth is motivated by the reduction of the GaN desorption at high temperature and avoid the formation of large amount of Nitrogen vacancy degrading the optical properties. In addition, the number of growth cycles is fixed as 20, which ensures the same total amount of TMGa precursor provided to the reactor in each growth.

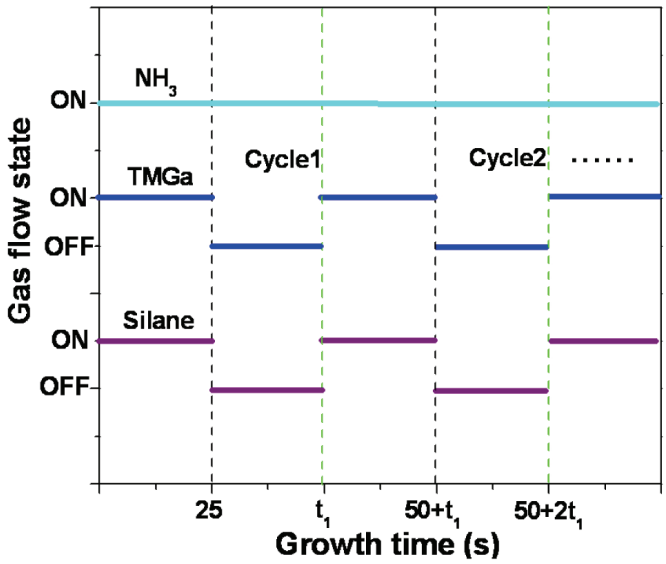

Figure 5.6: The time chart diagram of the gas flow (TMGa, NH_3 and silane) open state as a function of growth time in pulsed precursor mode SAG GaN NW growth.

Figure 5.5 (b)-(d) shows the 45 °-titled SEM images of the pulsed growth of SAG GaN NWs arrays with an interval supply of TMGa and silane flux of 20, 40 and 80 s respectively. It can be observed that with the increasing of t_1, the selectivity homogeneity of NWs growth improves gradually from 25 % (Figure 5.5 (b) with t_1 20 s) to nearly 100 % (Figure 5.5 (c) with t_1 40 s). Whereas, a further increase of t_1 80 s reduces this selectivity homogeneity to less than 5 % (Figure 5.5 (d)). Interestingly, it can be found that the value of selectivity homogeneity increases with a decrease of the NWs length. It indicates

that the selectivity homogeneity of NWs growth is very sensitive to the NWs growth rate. As discussed before, it could be attributed to the reduction of the 'sink' effect. With increasing of the interval time, the provided precursors has more time to diffuse and contributes to the more uniform materials distribution across the whole surface resulting in more homogeneous growths. However, if the interval time is too long, the high temperature desorption of GaN will become effective, the growth will be canceled in some openings and the 'sink' effect will be increased again. As a result, the final NW selectivity homogeneity is sharply reduced. For this point, if we look closely into Figure 5.5 (d), for the openings without NWs growth, the pre-deposited nucleation seeds disappearance could be certainly assigned to this desorption phenomenon.

5.1.5 The structural properties of SAG nucleation seeds

Standard XRD measurements in the symmetric Θ-2Θ geometry have been performed to investigate the crystallographic phases of the as-grown nucleation seeds obtained by the two-step growth process. As shown in Figure 5.7, three Bragg peaks can be indexed with the (006) α-Al_2O_3 reflection ($R\bar{3}c$, c =1.2991 nm), the (002) and the (004) wurtzite GaN reflections ($P6_3mc$, c = 0.5188 nm). It indicates c-axis oriented growth of nanostructures on c-sapphire without significant other secondary phases.

To characterize the epitaxial relationships and the local structural properties, TEM measurements were performed on as-grown samples prepared by standard polishing and ion-milling processes. Figure 5.8 (a) and (b) depicts cross-section dark-field TEM images taken in a two-beam condition with g-vectors along <0002> and <$1\bar{1}00$> to image screw and edge dislocations having <0002> and <$11\bar{2}0$> Burgers vectors. In the TEM images, a lateral overgrowth of the nanostructures outside the mask openings (see the limits indicated by the two black arrows in Figure 5.8 (a)) can be observed since the 550 nm nanostructure size is larger than the 400 nm mask opening. This overgrown part has been proved to be Ga-polar crystal in contrary to the N-polar crystal part within the opening as discussed in Chapter 4.2.2.

In the central part, we observe fringes in TEM images (Figure 5.8 (a)) coming from the large GaN/sapphire lattice mismatch and also misfit dislocations at the interface due to the strain relaxation. Threading dislocations (TD) are rarely observed: only two TDs with screw type are for instance visible in Figure 5.8 (a) (see white arrows) and no edge-type TD is observed in Figure 5.8 (b). On

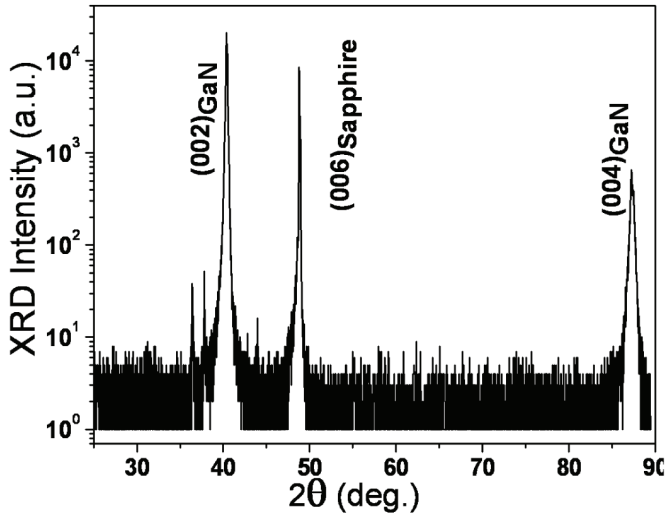

Figure 5.7: X-ray diffraction spectrum (standard Θ-2Θ geometry, $\lambda = 0.17902$ nm) of as-grown GaN nanostructure arrays obtained with the two-step temperature growth method described in the text.

the contrary, in the lateral overgrowth part, a better crystal quality is observed with a low strain (absence of fringe) and no dislocation is observed. Only a few stacking faults have been observed in Figure 5.8 (b) indicated by the white dashed retangular. It has been recently published that GaN nanorods grown on c-sapphire can present a high TD density [64]. These observations are attributed to the use of a thicker dioxide mask (100 nm) [64], and our work evidences that a very thin mask (5 nm) significantly improve the crystalline quality of the SAG GaN nanostructure on sapphire. SAED pattern taken in the central interface area with the beam parallel to the $<11\bar{2}0>$ direction of the GaN crystal is given in Figure 5.8 (c). The pattern indexation (black and white arrows denoting GaN and sapphire respectively) confirms the usual in-plane epitaxial relationship between GaN and sapphire ($[1\bar{1}00]_{GaN} \| [11\bar{2}0]_{Sappire}$) with a measured lattice mismatch of about 16.0 % along the $[10\bar{1}0]$ direction, in agreement with the 16.09 % bulk value.

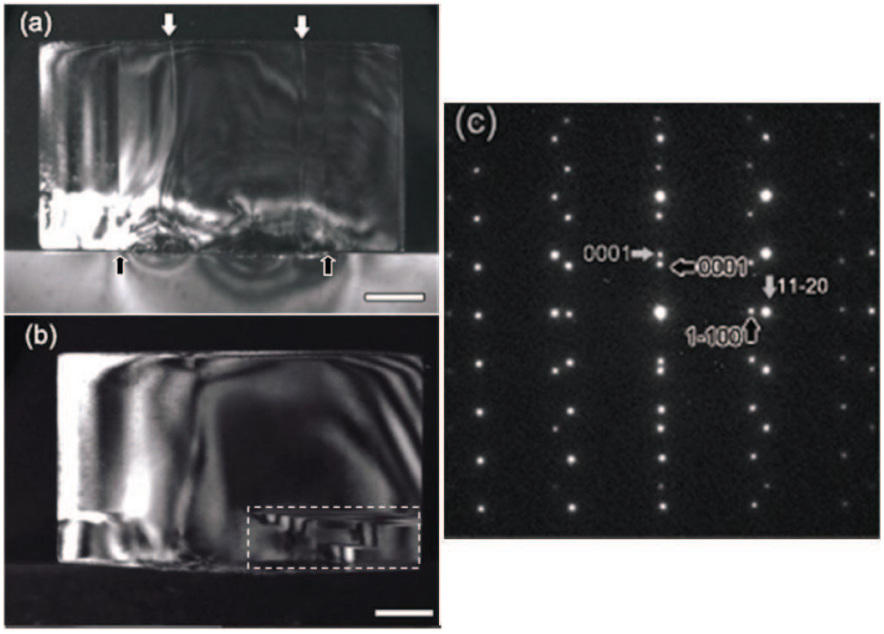

Figure 5.8: (a) and (b) Cross-section dark field TEM images of 500 nm GaN hexagonal nanostructures with <0002> and <10$\bar{1}$0> g-vectors, respectively. White arrows in (a) denote threading dislocations (TDs) and black arrows the mask limits. White dashed rectangular in (b) denotes the stacking faults (SFs). The scale bars are 100 nm. (c) Electron diffraction pattern taken at the GaN/Sapphire interface with a beam direction parallel to $[11\bar{2}0]_{GaN}$. The spots indexed with white and black arrows correspond to sapphire and GaN, respectively.

5.1.6 The optical properties

5.1.6.1 Optical properties of single SAG nucleation seeds

CL measurements in area-scanning mode were carried out at 5 K on single nanostructures to study the optical properties. Figure 5.9 shows the CL spectra taken in a top view of single nanostructures (grown with the two-step temperature method) having 250, 500 and 1300 nm diameters and relatively the same size in height. The spectra are normalized to the intensity maximum. Figure 5.10 gives the SEM image and the corresponding CL mappings measured at 3.46 and 2.26 eV in the top and cross-section views. In these images, darker area corresponds to larger emission intensity.

CL spectra exhibit two main contributions: the near band edge (NBE) emission of GaN in the UV region ($\sim$ 3.4 eV) and the yellow band (YB) emission at

$\sim$ 2.2 eV in the visible wavelength range, which is generally assigned to crystal defects like Ga vacancies and O complexes [178]. The relative intensity ratio between YB and NBE contributions strongly depends on the diameter of single nanostructures: it increases with the decrease of the nanostructure size as observed in Figure 5.9 (a). To understand this behavior, CL mappings were performed to localize the spatial emission of the NBE and YB wavelengths in the nanostructures. Figure 5.10 (a) shows the top view SEM image of the nanostructure arrays. The corresponding CL mapping images of the NBE and YB emissions at 3.46 and 2.26 eV are shown in Figure 5.10 (b) and (c) respectively. We can deduce from these measurements that the NBE emission mostly comes from the border part of the nanostructures, especially for the ones with size larger than 400 nm. On the contrary, the luminescence of the YB emission is more or less uniformly distributed whatever the nanostructure size. This observation is confirmed in Figure 5.10 (e) and (f) by CL mappings at 3.46 and 2.26 eV on 550 nm ion-milled sample in cross-section (the dashed line indicates the contour of the single nanostructure). This is consistent with the fact that the NBE emission is more sensitive to carrier diffusion than the YB emission, and the side part of the nanostructures is of much higher structural quality than the central part (see TEM results above). In addition, the central part is N-polar crystal which often leads to a more rough surface morphology with hexagonal hillocks [179] and higher O incorporation as well as higher background electron concentrations [180] than the Ga-polar crystal in the border part. This leads to a relative poor crystal quality of the central part and ends up with lower NBE emission intensity [181]. The size dependence of the optical properties can be also attributed to the fact that crystals with larger size have larger volume ratio between the side and the central part of the nanostructures leading to much stronger NBE emission. This result is in favour of the use of small diameter openings for optoelectronic applications.

In addition, we observe a variation of the NBE peak position of the nanostructures with different diameters as shown in Figure 5.9 (b). The peak shift can be assigned to two opposite effects: a blue-shift due to compressive strain induced by the lattice mismatch [182] and a red-shift induced by silicon doping [183]. Such unintentional Si doping, which is mostly located at the bottom part of the nanostructures, may come from the Si_3N_4 dielectric mask through a surface diffusion process as already reported in SAG pyramids [112]. Depending on the concentration, Si doping may induce a gradual red-shift up to $\sim$ 40 meV due to band gap renormalization [112], [183]. For nanostructures with diameter

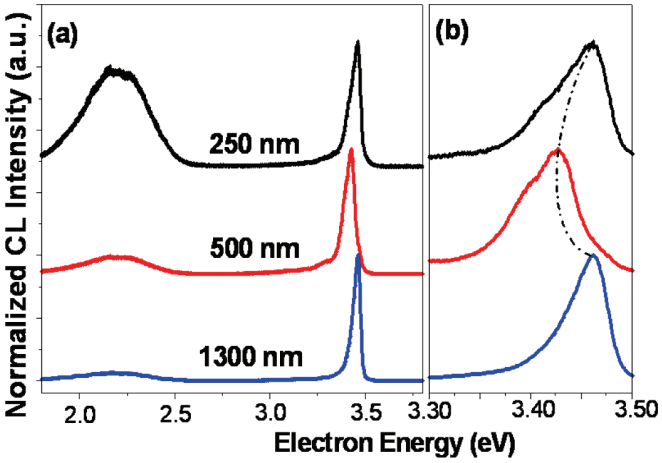

Figure 5.9: (a) Normalized cathodoluminescence spectra at 5 K for single GaN nanostructures with 250 nm, 500 nm and 1300 nm diameters and (b) enlarged view corresponding to the near band edge emission contribution.

equal to 1300 nm, the NBE emission is principally related to the strain-relaxed lateral overgrowth. Thus, the NBE peak position located at 3.46 eV corresponds to the value of the fully relaxed GaN 2D layers at 5 K [184]. For nanostructures with a diameter close to 500 nm, the NBE emission is mostly attributed to the strain relaxed lateral overgrowth on the mask and the NBE redshift of 35 meV can be mainly assigned to the Si incorporation from the mask surface diffusion. For nanostructures equal to 250 nm, the NBE emission comes from the crystals grown in direct epitaxy with the sapphire since the nanostructures size is smaller than the mask openings. Thus, the compressive stain must be also taken into account in addition to the Si incorporation effect. The 28 meV blue-shift of the NBE peak position compared to that of the nanostructure with 500 nm size can be assigned to this compressive strain. Moreover, the peak profiles of the NBE emission for nanostructures with a diameter of 500 and 250 nm are consistent with the Si doping assumption: the shape of the NBE emission is typical of Si-doped GaN, featuring a sharp cut-off at high energy and a low energy tail [183], [185]. From the observed FWHM of 60 meV, the doping level can be estimated in the 10^{19} cm^{-3} range [186].

5.1.6.2 The optical properties of single SAG NWs

CL measurements in area scan mode were carried out at 300 K with 30 kV and 1 nA current on single SAG NWs. Two types of samples were studied: Type

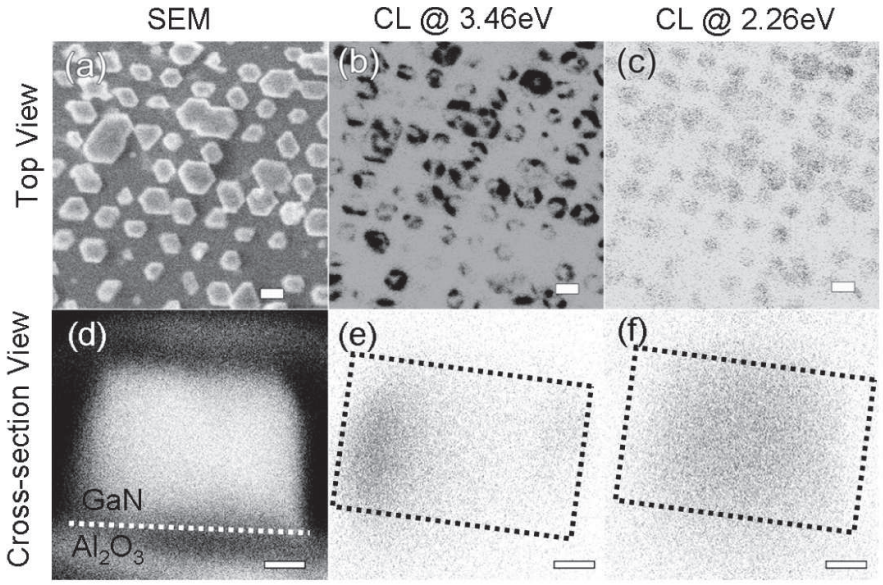

Figure 5.10: (a) Top view SEM image of an array of GaN nanostructures grown by the two-step temperature method described in the text. Cathodoluminescence (CL) mappings at 5 K of the area shown in (a) at (b) 3.46 eV and (c) 2.26 eV respectively corresponding to the near band edge (NBE) and yellow band (YB) emissions. (d) Cross-section SEM image of a single GaN hexagonal prismatic nanostructure prepared by ion-milling. (e) and (f) correspond to CL mappings at 5 K of the nanostructure shown in (d) at 3.46 eV and 2.26 eV respectively. The dashed rectangles in (e) and (f) show the contour of the single object. Scale bars are 500 nm in (a)-(c) and 100 nm in (d)-(f).

A grown under continuous precursor mode as shown in Figure 5.5 (a) and Type B grown under pulsed precursor mode labeled as shown in Figure 5.5 (d). The NWs were detached from the c-sapphire substrate by sonification in isopropanol and then dispersed on a conduction silicon substrate to avoid the charging effect from the insulation substrate.*

Figure 5.11 (a) shows the area scan CL spectra taken along the NW sample A from point 1 to 11. The point 1 is supposed to be at the top part of the

*For the CL measurements performed along single NWs, we prefer to use area scan mode instead of spot scan mode to have a more average value with integrated information. To get comparable results of the peak intensity, it is required to excite the same amount of materials volume in each data acquiring. Thus, the scan area of the beam on the surface is as 400 × 400 nm^2 and 700 × 600 nm^2 respectively for sample A and B along X-Y direction.

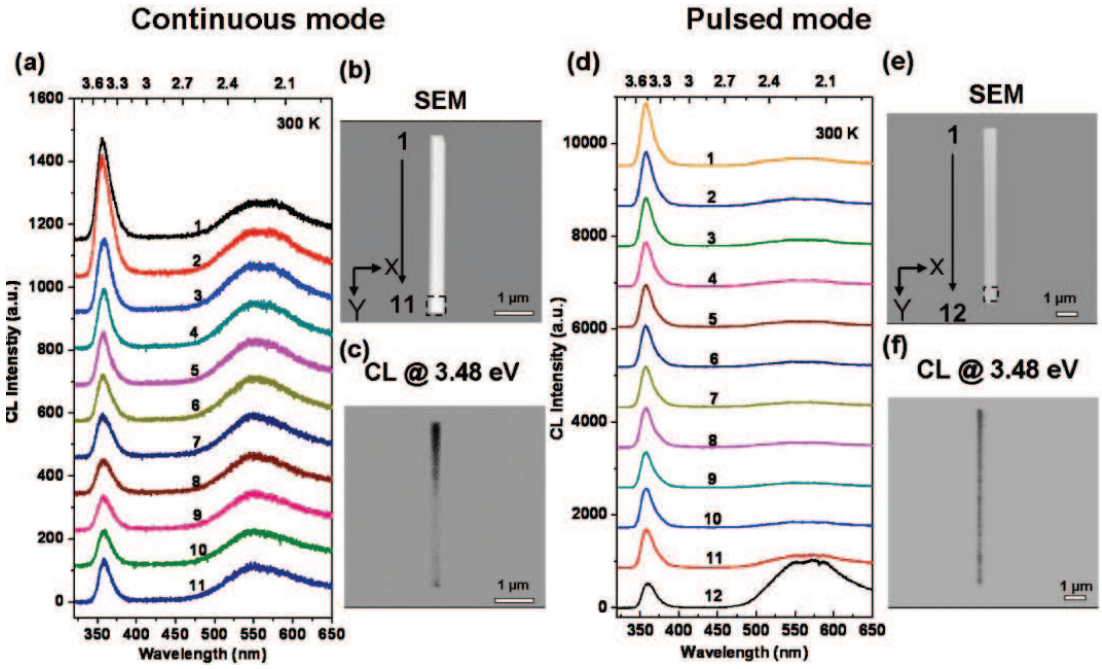

Figure 5.11: The 300 K area scan CL spectra acquired along the SAG GaN NWs, the SEM image and the CL mapping at NBE emission (3.48 eV) of (a), (b), (c) continuous precursor growth mode and (d), (e), (f) pulsed precursor growth mode.

NW due to the presence of the inclined facets on the right side related to the termination of Ga-polar crystal. All CL spectra exhibit two main contributions: the near band edge (NBE) emission of GaN in the UV region ($\sim$ 3.45 eV) and the yellow band (YB) emission at $\sim$ 2.2 eV in the visible wavelength range. The intensity of the NBE emission is gradually decreased from top to bottom (point 1 to 11) confirmed by the CL mapping at 3.48 eV (see Figure 5.11 (c)) (the darker area presents a higher emission intensity), whereas the YB emission intensity is homogeneous along the NW. The same CL measurements has been performed on sample B. In this case, the point 1 is also supposed to be the top part due to the slight anti-tapering of the NW diameter. As shown in Figure 5.11 (d), the GaN NBE emission maintains similar intensity from top to bottom part as further confirmed in the CL mapping at 3.48 eV presented in Figure 5.11 (f). However, the YB emission is only visible at the bottom part of the NW and becomes negligible in intensity for the rest of the NW. Moreover, if we compare the NBE emission intensity of both samples with a normalization to the excited

materials volume, the intensity for sample B is still much larger than sample A showing a better optical properties.

The SAG GaN NW growth is performed with a low NH_3 flow of 50 sccm which is about 50 times less than standard 2D growth under pure N_2 carrier gas. This growth condition which avoids etching will definitely induce more oxygen, carbon impurity incorporation and higher nitrogen vacancy due to volatile of NH_3. This could lead to the presence of relatively strong YB luminescence and nonradiative recombination centers in the materials and quench the NBE emission intensity [178], [187]. For sample B, during the interruption of TMGa precursor, the system is still supplied with NH_3. This so-called annealing step can increase the partial pressure of NH_3 and reduce the impurity incorporation and the formation of point defects. As a result, it will limit the YB emission and give much better NBE emission properties in terms of better homogeneity and higher intensity. The YB emission from the bottom part shall be assigned to the structural defects like threading dislocations as observed in Chapter 5.1.5. The issue why the NBE emission on the upper part of the sample A is much stronger than the other part has to be further studied in the future.

5.2 SAG of GaN nanopyramids on GaN template

5.2.1 Introduction

In this section, after a brief introduction of the laser interferometry patterning process, we will first detail the growth parameter study (temperature and pressure) and the facet evolution during the selective area growth (SAG) of GaN nanopyramids on GaN template. It will be demonstrated by CBED measurement that the Ga-polarity is conserved between the 2D layer and the as-grown GaN nanostructures leading to a pyramidal-shape. Finally, it will be demonstrated that InGaN QD ($\sim$ 5 nm in diamater) with well controlled position and quite high density (10^9 cm^{-2}) can be grown on the tip of nanopyramids.

5.2.2 Surface patterning by laser interferometry lithography (LIL)

The LIL surface patterning process has been preformed in collaboration with O. Lartigue and B. Martin, CEA/LETI and can be summarized as follows:

(1) A 2.5 μm-thich GaN temeplate is grown on c-sapphire substrate.

(2) A 5 nm-thick Si_3N_4 dielectric mask is deposited on the template by plasma enhanced chemical vapour deposition at 300 °C.

(3) The patterning of the substrate surface is prepared by LIL. This technique generates patterns on the photoresist masklessly. HDMS is first deposited on GaN template to promote the adhesion of photoresist. A negative photoresist (NEB22) is then spin coated (5000 rpm, 60 s) to get a thickness of about 75 nm. A pulsed Exima laser with a wavelength of 193 nm is used as the laser source and splitted into two coherent light beams (beam 1 and 2). The realization of hole array is obtained by a first exposure of interference pattern, then the sample is rotated by 90 ° followed by a second exposure. The period of the pattern spacing is determined by the wavelength (λ) and the opening size by the beam energy dose (number of laser pulses)as shown in Figure 5.12 (a) and (b).

(4) Finally, the Si_3N_4 mask is etched by using SF_6 plasma (SF_6 15 sccm, pressure 26.6 mbar, power 50 w and time 30 s) followed by resist stripping with Acetone. We obtain a uniform patterning with a high dense regular array of circular holes of 200 nm with a pitch distance of 400 nm (see Figure 5.12 (c)).

5.2.3 The growth process study

The patterned substrate is then transferred into the MOVPE reactor for GaN nanostructures growth. The III and V precursor flow used are similar to previous SG and SAG GaN NW growths: TMGa (135 μmol/min) and NH_3 (2232 μmol/min) with a V/III ratio of 16. The carrier gas is set as pure N_2 (2000 sccm) during the whole process to avoid H_2-etching of GaN template. It has been reported that the reactor pressure and temperature has a large impact on the facet and shape formation for homoepitaxy SAG of GaN structures, thus we

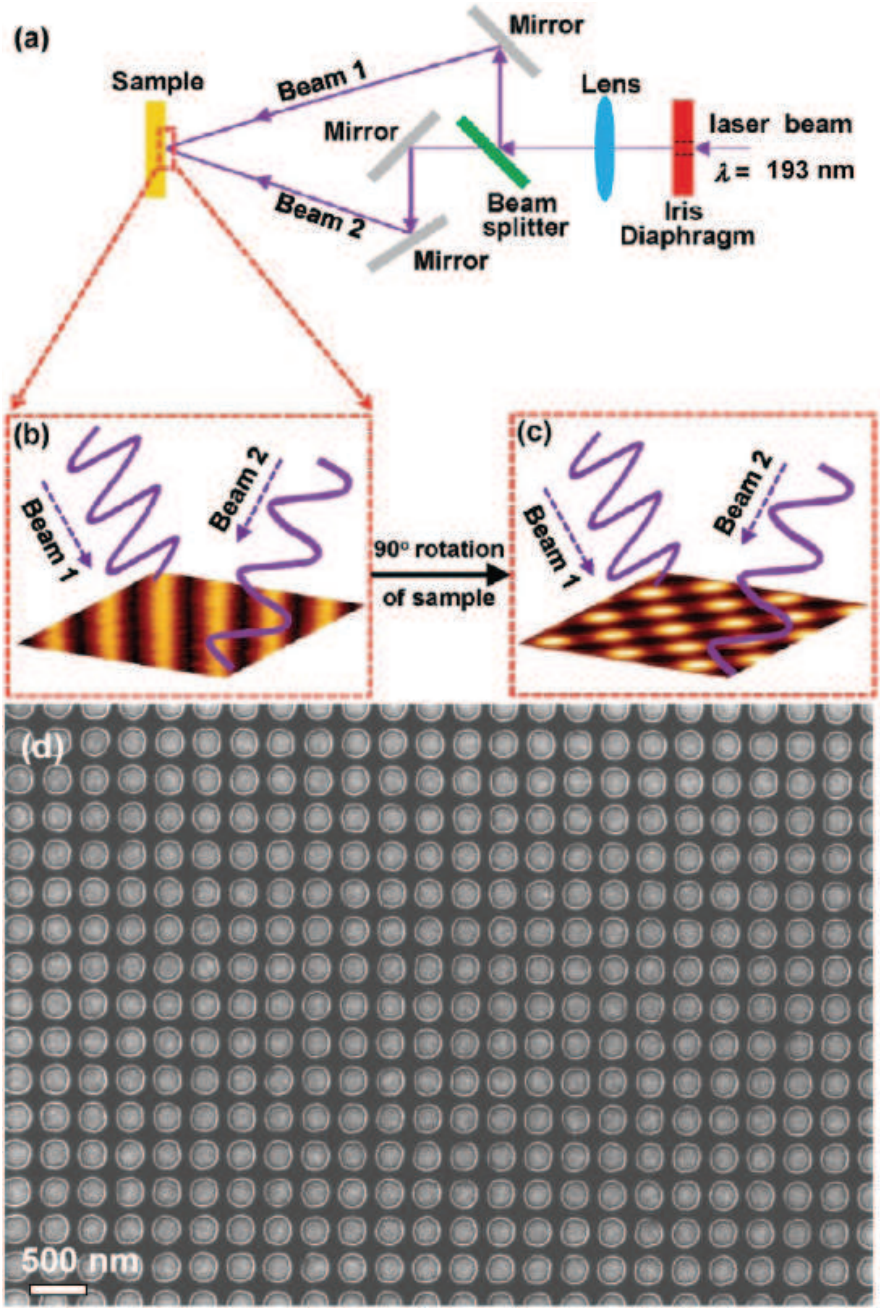

Figure 5.12: (a) The interference between beam 1 and 2 forms a grating pattern on the photoresist layer under a single laser pulse (10 ns) irradiation, (b) the sample is then rotated by 90° or by an arbitrary angle with a second exposure. The patterns of periodic arrays are formed on the photoresist layer or the substrate. (c) Top-view SEM image of the patterned substrate after resist stripping (the diameter of the opening is about 200 nm with a pitch distance of 400 nm.).

performed a series of GaN growths of 450 s using different growth pressure (200, 400 and 800 mbar) and temperature (900, 1040 and 1090 °C) while keeping the other process parameters constant (see Figure 5.13).

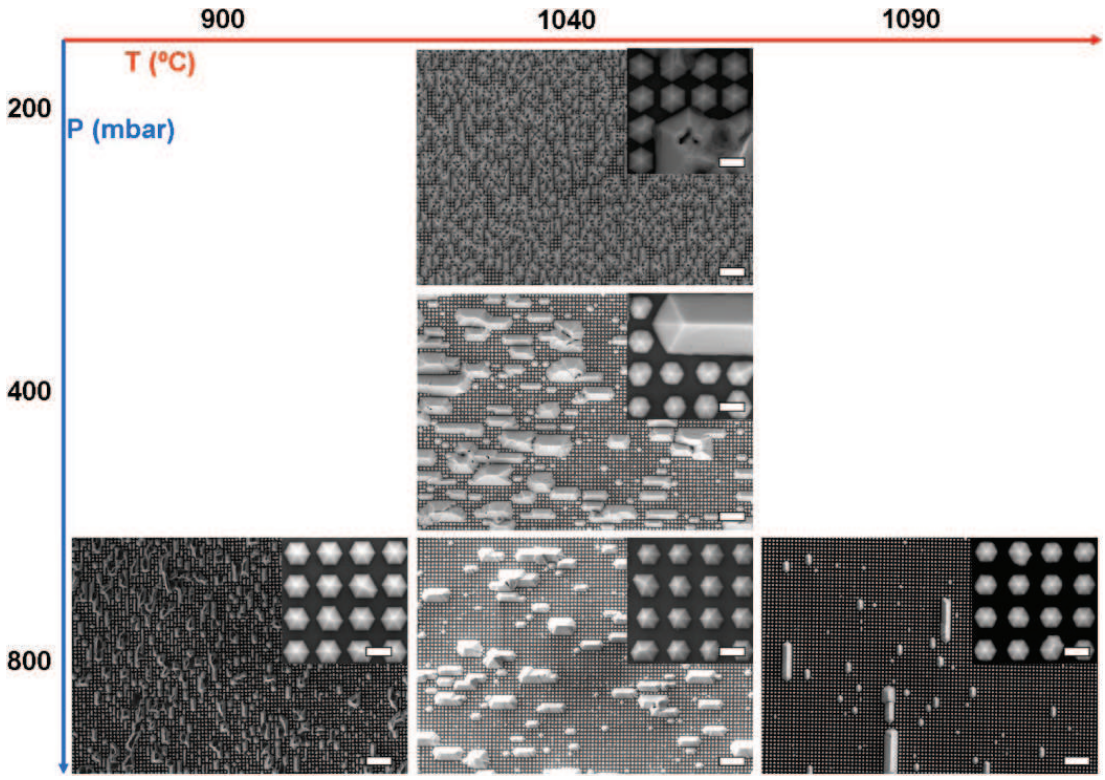

Figure 5.13: Top view SEM images of as-grown SAG GaN nanostructures on GaN template with different pressures and temperatures. The scale bars are 2 μm. The insets are enlarged SEM images showing the pyramidal geometry of the nanostructures. The scale bars for the insets are 200 nm.

It can be observed from the enlarged views (see insets of Figure 5.13) that the growth of GaN nanostructures always results in the pyramidal shape and probably from the Ga-polar crystal growth. Thus, the polarity of both the GaN nanostructure and the GaN template were determined by CBED measurements taking into account the simulation references with a sample thickness of 110 nm (see Figure 5.14). As depicted, it is shown that the GaN nanopyramids follow a growth along the Ga-polar direction (see in Figure 5.14 (b)) with a conservation of the polarity from the GaN template (see in Figure 5.14 (c)).

Concerning the selectivity homogeneity, the filling of the openings is 100 % whatever the conditions (different pressure and temperature), which maybe at-

tributed to higher sticking efficient in homoepitaxy. Moreover, the formation of big islands is clearly visible especially at lower pressure and temperature. We suppose that it is caused by a coalescence of objects. In the contrary, at higher pressure and temperature, the formation of big islands is limited probably due to a combination effects of larger adatoms diffusion length, the higher desorption rate and pre-reaction rate which may enhance the adatoms surface diffusion and avoid the coalescence.

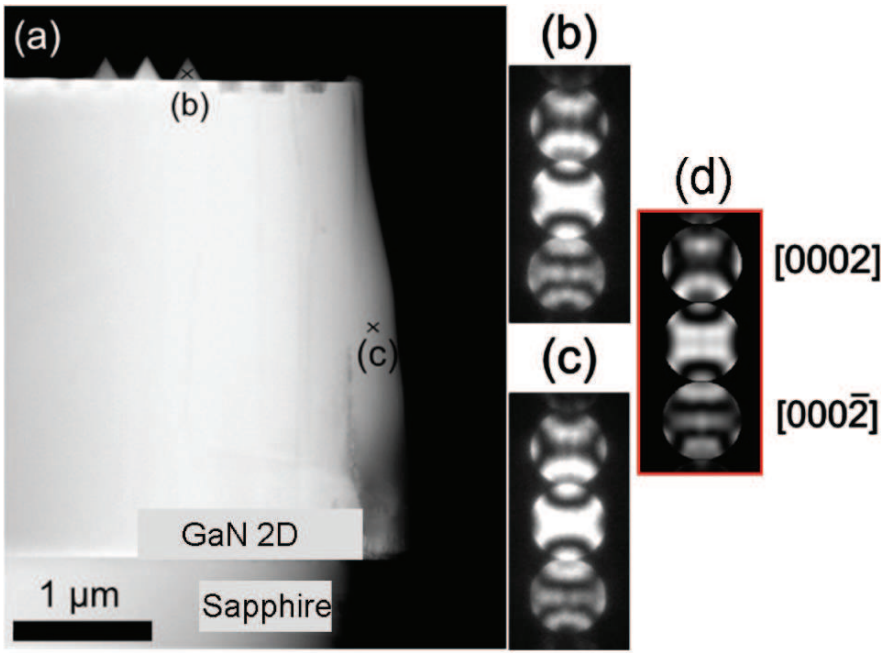

Figure 5.14: (a) STEM image of as grown SAG GaN nanostructures on GaN template. Experimental CBED patterns showing (b) Ga polarity of the GaN nanopyramid and (c) Ga polarity of the GaN template

In order to understand the growth process, we have performed a short growth (50 s) of SAG GaN nanopyramids to observe the initial nucleation stage. Figure 5.15 shows the SEM image of the as-grown sample, where the nucleation of the SAG GaN nanopyramids first appears at the contour of the circle openings. The overgrowth to form the big island already occurs in the early stage of the growth as indicated by the red rectangular in Figure 5.15. The materials deposited around the contour of the openings coalescence to form the big island. This is probably also related to the defect (non-regular shape, the residual resist ...) in the openings induced by the patterning process. The size and shape of

the big islands are determined by the number of openings involved in the initial coalescence.

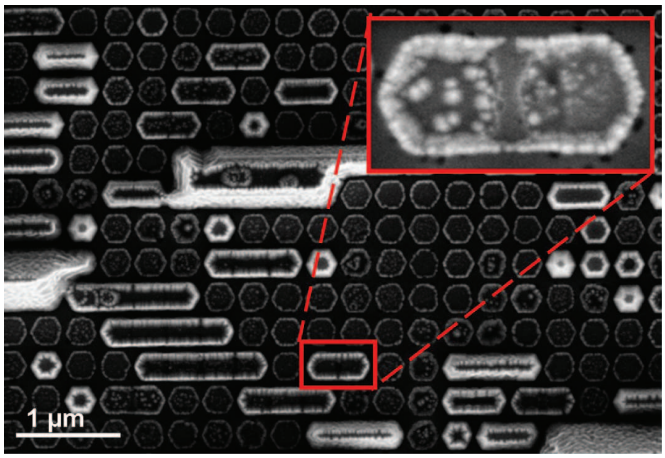

Figure 5.15: A typical top view SEM image of the initial nucleation period (50 s) of SAG GaN nanostructures on GaN template. The inset is an enlarged image showing the initial coalescence of the materials in the adjacent openings to form the big islands later.

The formation of single SAG GaN nanopyramids has been also investigated by SEM at different stage in Figure 5.16 for growth time up to 450 s. As mentioned above, the nucleation of the nanopyramids around the mask border is certainly related to an enhanced growth rate [188]. The nucleus forms hexagonal shaped ring with well-defined inclined facets in both inner and extender sides as indicated by the red arrows in Figure 5.16 (a). Meanwhile, there are also some nucleations of small pyramids inside the mask opening as indicated by the yellow arrows in Figure 5.16 (b). With the increasing growth time, the small islands which nucleate inside the opening become larger and coalescence. The hexagonal rings around the mask edge extends only toward the center of the opening with no lateral overgrowth on the mask surface and coalescences with the inner small islands. Finally, after 450 s of growth, the complete pyramid structure is formed with a tip shape and six smooth inclined $\{1\bar{1}01\}$ sidewall facets.* For clarity, the facet evolution in a cross-section view during the pyramid formation is schematically shown in Figure 5.16 (c) (the colorful lines indicates the contour

*In SAG GaN growth along the c-axis with a isotropic mask opening design like circular shape, the preferred orientation of the as-grown nanostructure (the orientation of the nanostructure is defined by vector a in Figure 5.16 (a)).

of the nanostructures inner part at different growth stage.).

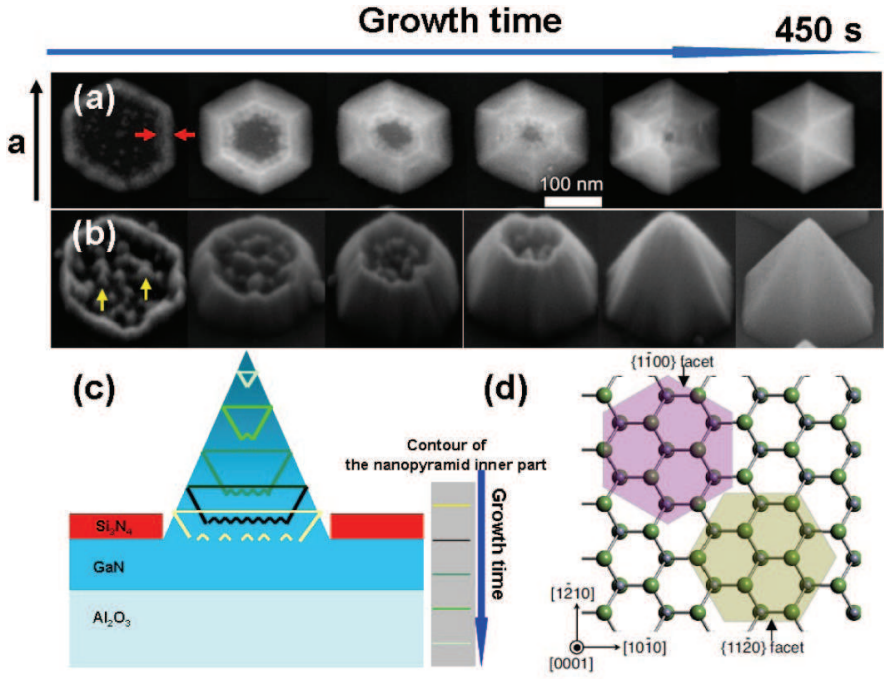

Figure 5.16: (a) Top-view, (b) 45° -tilted view SEM image and (c) the schematic drawing of the facet formation and shape evolution process of the single SAG GaN nanopyramid growth up to 450 s. (d) The atoms arrangement mapping of GaN wurzite structure on (0001) plan. The light pink and yellow hexagon represent the structure oriented along <11$\bar{2}$0> and <1$\bar{1}$00> for c-axis growth respectively.

5.2.4 The growth of InGaN Quantum dot on tip of the SAG GaN nanopyramids

5.2.4.1 Introduction

Semiconductor quantum dots (QDs) have gained huge research interest because of the three dimensional carrier confinement which can strongly localize the exciton thus making them more insensitive to the non-radiative recombination center than in quantum wells (QWs) structure [189]. This is particularly interesting for InGaN materials known for high structural defect density due to the large lattice mismatch with GaN barrier layers ($\sim$ 11 % between InN and GaN) in heteroepitaxial growth. In this regard, improved efficiencies of the LEDs has

been achieved by employing InGaN QDs as the active layer both in planar and NW-based devices [190].

Several approaches have been attempted to fabricate InGaN QDs mainly by self-assembled way through lattice mismatch Stranski-Krastanow (SK) growth mode [191], Si anti-surfactant assisted growth on AlGaN surface [192], phase segregation approach induced from In-rich clusters [193], or confined growth using patterned mask with nanometer openings [29], [194]. These methods always result in a random and inhomogeneous distribution of the QD in both distance and diameter. This limits the use of such system for emitter device applications. Site controlled growth of InGaN QDs has been obtained by deposition of InGaN/GaN QWs on the GaN micro-pyramid array grown on a patterned substrate by MOVPE, which normally leads to a InGaN QD on the tip as described in Chapter 2.3.2. The diffusion length of In adatoms is longer than Ga adatoms which probably results in a In-rich cluster on the tip of the micropyramid. However, the relative low QD density (10^6 cm^{-2}) represents a real difficulty for device applications. Obtaining a dense GaN nano-scale pyramid array naturally corresponds to an important issue. Several attempts described in Chapter 2.3.2 have illustrated the difficulties to grow such InGaN QDs on the tip of dense array of nanoscale pyramids, due to the reduced diffusion path which does not favor the formation of In-rich cluster. Thus, to date, the achievement of site-controlled InGaN QD arrays with a high density remains an issue to be well addressed.

5.2.4.2 The growth process

As depicted in the nanopyramid facet evolution (see Figure 5.16), the pyramid formation is firstly composed by a plateau surrounded by a pyramidal edge. When the growth time is increasing, the size of the plateau is reduced until the complete formation of the pyramid with a sharp tip. If the growth is stopped just before the complete formation of the pyramid, it is possible to obtain a small plateau with a concave structure (called plateau afterwards), which allows growing InGaN QD.

The SAG GaN nanopyramid was first grown for 350 s using the growth parameter depicted in Chapter 5.2.3 without silane injection. The growth time is carefully chosen to have approximately a plateau diameter of 10 nm. Then, 5×InGaN/GaN MQWs were grown on this nanopyramids array (see growth parameters in Table 4.1).

Figure 5.17 shows the top-view SEM image of the complete structure for

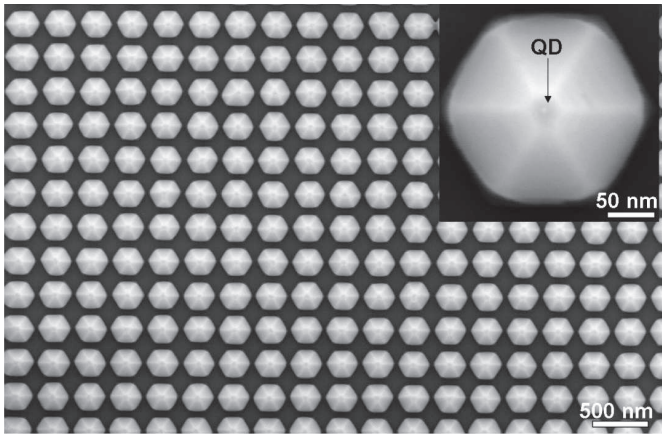

Figure 5.17: Top-view SEM image of SAG GaN nanopyramids array with 5×InGaN/GaN MQW deposition. The inset is an enlarged view for one typical nanopyramid with a InGaN QD indicated by black arrow.

350 s nanopyramid growth with the deposition of 5×InGaN/GaN MQWs. The nanostructure array is highly ordered with a density of 10^9 cm^{-2}. The inset of Figure 5.17 is an enlarged view of one typical nanopyramid. A hexagonal plateau can be easily identified on top of the nanopyramid, where a small dot is located in the middle as indicated by the black arrow. This small dot is attributed to the formation of InGaN QD. Actually, we have statistically checked by SEM and AFM observations that these QDs are homogeneously grown on each nanopyramid top with a size of about 4 nm.

5.2.4.3 The optical properties

PL experiments were conducted in collaboration with B. Gayral and D. Sam-Giao, CEA/INAC by exciting the sample with a frequency-doubled continuous wave Ar^+ laser (244 nm) and analyzing the signal by a 0.46 m focal length spectrometer. Figure 5.18 shows a typical PL spectrum of the SAG GaN nanopyramid array with InGaN QDs on tip at 5 K. In the spectrum, three dominate peaks at 3.48 , 3.35 (B) and 3.05 (A) are visible. The emission at 3.48 eV is assigned to the NBE emission from n-GaN 2D layer which is the template of the SAG.

In order to identify the origin of the peak A (3.05 eV) and B (3.35 eV), monochromatic CL mapping was perform at 5 K (in collaboration with A. L. Bavencove, CEA/LETI). Figure 5.19 (a) shows the reference SEM image of the GaN nanopyramids array with InGaN QDs. Figure 5.19 (b) and (c) are the

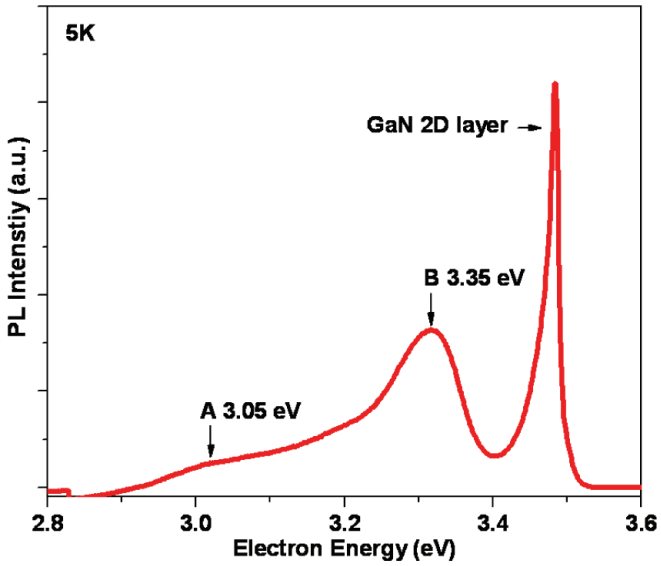

Figure 5.18: 5 K PL spectrum of SAG GaN nanopyramids array with InGaN QDs.

corresponding CL mapping images of the A (3.05 eV) and B (3.35 eV) emission energies respectively. It can be deduced that the 3.05 eV emission comes from the tip of the nanopyramids and is definitely related to the InGaN QDs structure as shown in inset of Figure 5.17. Notably, although there is still visible weak signal from the sidewall facets of the GaN nanopyramids, it is believed that such kind of luminescence is due to the free exciton diffusion resulting from the good structural properties of the nanostructure [195]. For the emission centered at 3.35 eV, it could be assigned to the InGaN MQWs homogenously deposited on the sidewall facets of the GaN nanopyramids.

A signature of the 3D carrier confinement in QDs is given by the thermal stability of the PL [196]. Figure 5.20 (a) shows the PL spectra of the as-grown sample from 5 to 300 K. As expected, we observe that the thermal quenching of the QDs (peak at $\sim$ 3.05 eV) is much lower than that of the QWs (peak at $\sim$ 3.35 eV) and the 2D layer (peak at $\sim$ 3.48 eV). The luminescence of the QDs dominates the spectra from 200 K to room temperature with the strongest intensity among the three peaks. Figure 5.20 (b) presents the integrated intensities of QD, QW and 2D layer peaks as a function of the reciprocal temperature. It is found that the 'internal quantum efficiency' (IQE defined as the ratio between the luminescence intensity at room temperature (I_{300K}) and at low temperature (I_{5K})) of the QDs is about 28 % which is much higher than the value of 4 % and 2 % for QWs and

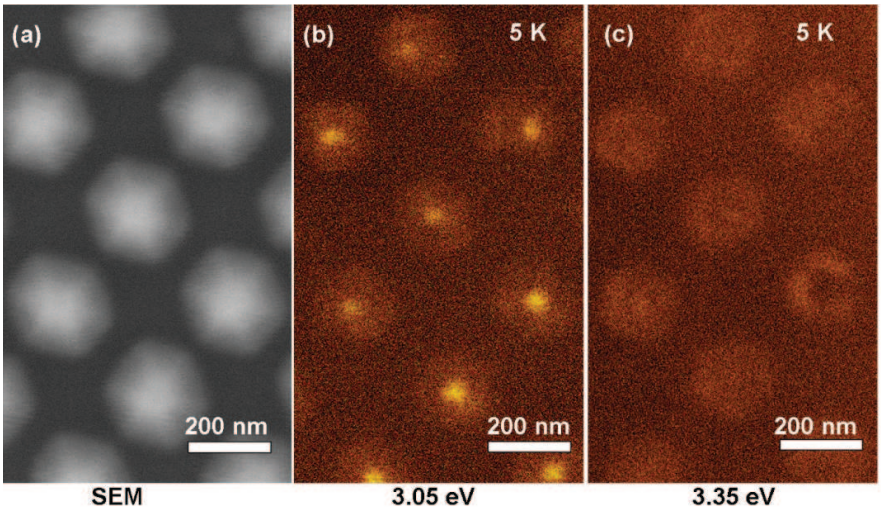

Figure 5.19: (a) Top view SEM image of an array of GaN nanopyramids with InGaN QDs on tip. 5 K cathodoluminescence (CL) mappings at (b) 3.05 eV and (c) 3.35 eV of the area shown in (a), corresponding to the QD and QW emissions respectively.

2D layer. It is believed that this IQE value (28 %) of QDs can be improved if the growth parameters are further optimized in the future.

In addition, the temperature dependent NBE emission intensity data can be fitted using the equation [197]:

$$I(T) = \frac{I_0}{1 + c\exp\frac{-E_a}{k_b T}} \tag{5.1}$$

where I(T) and I_0 are the PL intensities at temperature T and 5 K respectively, c is a constant, E_a is the associated thermal activation energy and k_b is the boltzmann constant. The fitted curve yields to the Ea value of 55, 14 and 4 meV for QD, QW and 2D layer, respectively. The larger thermal activation energy for QD further indicates the better carrier confinement. Complenmentary PL characterizations like time-resolved measurements as a function of temperature shall be carrier out to further investigate the influence of nonradiative recombination paths in the QDs structure.

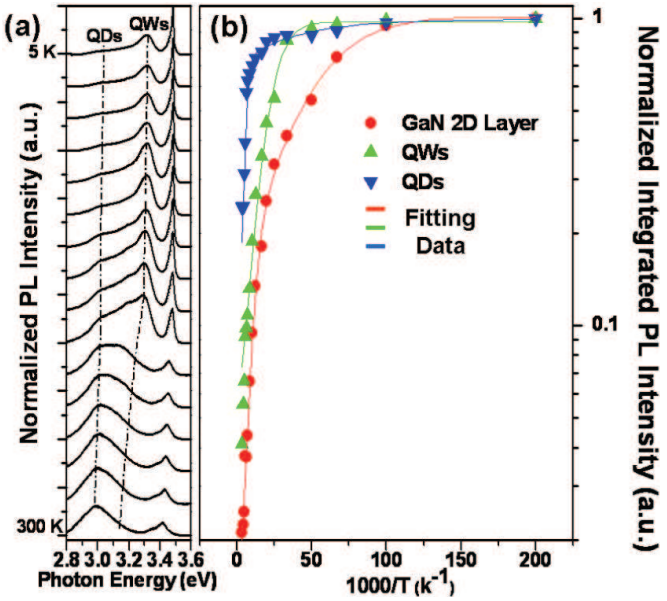

Figure 5.20: (a) Normalized PL spectra from 5 to 300 K on array of GaN nanopyramids with InGaN deposition and (b) The corresponding normalized integrated PL intensity for the GaN 2D layer, the InGaN QWs and the InGaN QDs emission peaks respectively with also the fitted curves.

5.3 Conclusions

This chapter deals with the selective area growth of GaN nanostructures on patterned substrate with Si_3N_4 as mask layer.

In the first part, it has been shown that the GaN NWs can be grown on patterned c-sapphire. The high selectivity homogeneity can be achieved by a combination of two-step temperature growth during the initial seed nucleation stage and followed by a pulsed precursor mode for NW growth period. The as grown nanostructure presents a high crystalline quality corresponding to a better optical properties with a stronger near band edge emission and the absence of the yellow band luminescence for the overgrown part on the mask surface compared to the crystal directly epitaxy on c-sapphire.

Then, the GaN nanopyramids array was successfully grown on patterned GaN template. It was demonstrated that the high selectivity homogeneity for this growth can be managed regardless of the growth conditions. The study of the facet evolution of the GaN nanopyramid opens a new approach to grow site controlled InGaN QDs array with high density (10^9 cm^{-2}). The optical properties

of such structure was characterized by CL mapping and temperature dependent PL measurements evaluating the better carrier confinement in the QD structure located on tip of the nanopyramid with higher internal quantum efficiency and thermal activation energy compared to QW and 2D layer structure.

It was also pointed out that the shape selection between wire and pyramid in SAG growth on patterned nitridated c-sapphire and GaN 2D template results from the crystal polarity control which is consistent with the observation in Chapter 4.

Chapter 6

Conclusions and Perspectives

Conclusions

My PhD thesis work focuses on the MOVPE growth of III-nitride nanostructures with both catalyst-free self-assembled technique and selective area growth approach. Two nanostructure geometries (NWs and nanopyramids) have been demonstrated as well as multiple quantum well and quantum dot heterostructure growth. The growth mechanism has been carefully studied and new growth approach and novel structure have been originally developed.

Regarding the mechanism understanding of catalyst-free self-assembled MOVPE growths of GaN NWs with *in situ* silane injection:

- (1) We have systematically studied the influence of the growth parameters on the NW geometry in terms of density, diameter and length. It has been pointed out that the higher growth temperature tends to increase the NW density and diameter due to the larger adatoms diffusion length. The carrier gas flow rate and the reactor pressure could influence the shape of NWs by mainly changing the effective TMGa/silane ratio in the gas phase: the larger the value is, the smaller the NW diameter becomes. The density of the NWs is mainly governed by the amount of provided precursor flow which could be manipulated depending on its link with different growth parameters. In particular, the smaller precursors flow rate (either TMGa or NH_3) has been presented to be a dominate factor for the reduction of the NW diameter in the V/III ratio regime, which favors the NW growth.

- (2) The necessity of the *in situ* silane injection to get wire geometry in this method has clearly been related to the surface passivation effect due to the formation of a thin SiN_x layer along the sidewalls of NWs as evidenced by secondary ions mass spectroscopy measurements. The adatom diffusion path during incorporation has also been extensively studied. The direct gas impinging into top facet and the diffusion from NW sidewall seems to play a significant role in adatoms incorporation to grow NW geometry, as shown by both experimental demonstration and fitted theoretical results.

- (3) It has also been evidenced by convergent beam electron diffraction characterization that the N-polar orientation of the GaN crystal is also a prerequirement in this method to obtain the hexagonal prismatic-shaped wire

geometry with vertical sidewall facets, whereas the Ga-polar growth always ends up with inclined facets terminating the vertical extension by a pyramidal-shaped top surface. Meanwhile, it is also shown that the crystal polarity control in order to choose the wire/pyramid geometry can be managed by the specific substrate surface treatment on sapphire or directly by the polarity GaN substrate as mentioned hereafter.

In addition, novel approaches in catalyst-free self-assembled GaN NW growth have also been developed:

- (1) By taking advantage of the understanding of polarity control, the growth method with *in situ* silane injection has been transferred to grow GaN NWs on N-polar GaN single crystal substrate, which gives a better crystalline quality from homoepitaxy and easier device integration thanks to the electrical conducting substrate.

- (2) High quality GaN NWs grown without *in situ* silane flow has also been demonstrated by a combination of employing ultra-low precursor flow and Ga-polar crystal orientation. Due to the elimination of heavily n-type doping from silane flow, the optical properties of NWs have been dramatically improved showing a shape PL spectra with an excellent typical NBE linewidth around 1-3 meV at 5 K. As expected, the Ga-polarity leads to NW with pencil-shaped geometry capped by pyramidal top (diameter as small as 5 nm approaching the tip top with the absence of any structural defects). The growth is believed to happen due to the favor of reaction-limited mechanisms rather than diffusive-limited (kinetic) transport in these low flux growth conditions. These results are summarized in Figure 6.1:

Based on the understanding of the growth mechanism for the SG GaN NWs grown with silane flow injection, we managed to develop length and position controlled novel heterostructure system with core-shell radial InGaN/GaN MQWs coated on the NW sidewall along non-polar axis. Due to the partial covering of the MQWs on the NW, it is also demonstrated that this kind of core-shell structure has advantage to be easily integrated into single NW device fabrication with a natural exposure of the n-doped part.

In the selective area growth approach, by controlling the GaN crystal polarity, two kinds of ordered nanostructure have been demonstrated using Si_3N_4 (5 nm) patterned mask:

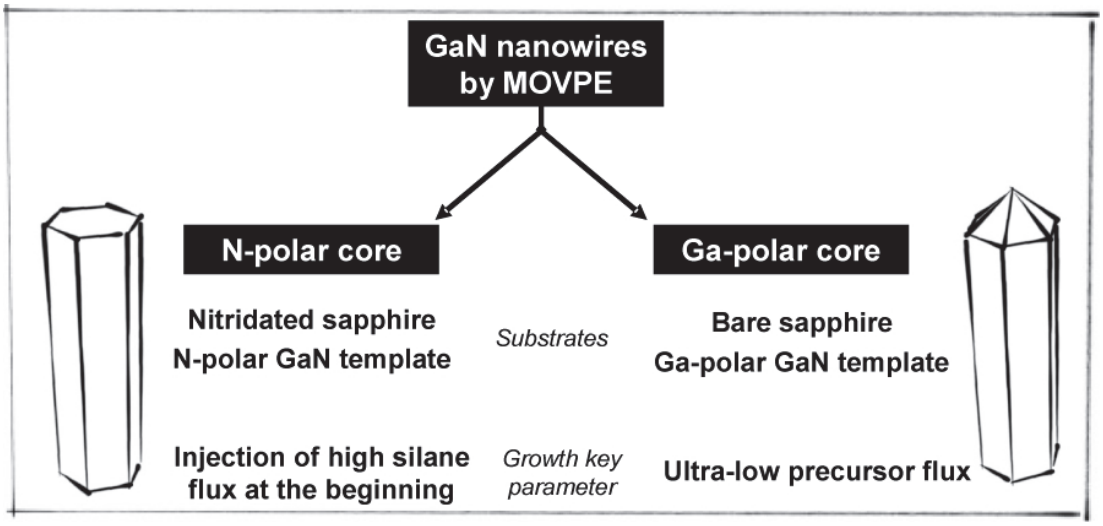

Figure 6.1: The diagram shows the crystal polarity, the substrates and the growth key parameter with the relation of getting different shaped GaN NWs by catalyst-free MOVPE approach

- (1) Hexagonal prismatic-shaped N-polar GaN NW arrays have been grown on bare c-sapphire substrate. It has been shown that the high homogeneity selectivity can be achieved with a two-step temperature for seed nucleation combined with a pulsed TMGa precursor flow growth mode during the NW growth stage. The overgrown crystal on mask surface gives better optical properties with the absence of yellow band luminescence compared to the crystal directly epitaxial on c-sapphire substrate. This observation is assigned to few defects in overgrown part characterized by TEM. Moreover, better optical properties of GaN NWs with the pulsed TMGa precursor growth mode compared to the continuous growth mode have been measured by CL mapping, which shows a more homogeneous NBE emission intensity along the NW.

- (2) Ga-polar GaN nanopyramid arrays have also been grown on Ga-polar GaN 2D template. The growth parameters have been found to have no evident influence on the geometry of the structure and the selectivity homogeneity. The facet evolution process of the single pyramid has been systematically studied as a function of growth time. It has been shown that a concave plateau can be formed on tip of the pyramid if the growth time is carefully chosen and a high density InGaN QD array ($\sim 10^9$ cm^{-2})

can be achieved for this structure. The better carrier confinement character of this QD structure has been measured by CL mapping and temperature dependent PL measurement.

Perspectives

The MOVPE catalyst-free growth of GaN nanostructures (NWs, nanopyramids and QDs) with both self-assembled and selective area growth approaches has been demonstrated in this thesis. The realization of such structure and the understanding of the growth mechanism open the opportunity in the future to address new challenge in fundamental and applied physics research fields:

For self-assembled GaN NW growth with *in situ* silane injection, the mixture of core N-polar crystal surrounded by the shell Ga-polar crystal gives the presence of an IDB as observed by STEM. This is a good candidate for high resolution CL measurement (monochromatic mapping and time resolved) to study the optical properties of the IDB by detecting the exciton recombination process around it. In addition, as discussed in the thesis, the Ga-polar crystal in single NWs ends up with an inclined facet and destroys the hexagonal symmetry and may add new contribution in the emission spectra. In the future work, to grow single N-polar crystal NWs with a perfect hexagonal shape with smooth sidewall facets is motivated in the photonic research for the study of whispering gallery mode lasing. This kind of growth could be managed by removing the SiN_x layer deposition step or to make a short interval (annealing under H_2) at high temperature between seeds nucleation and NWs growth stage.

For self-assembled GaN NW growth with low precursor flow, the ultra fine crystalline quality, the high intrinsic of the materials and the pencil-shaped top (~ 5 nm) make it an interesting template for the overgrowth of single InGaN/GaN or GaN/AlN layer aiming at the realization of single QD emitter operated at higher temperature.

In this thesis, the growth of self-assembled NW is limited to GaN material and InGaN MQW heterostructures. In principle, the extension of these methods developed in this thesis is promising to grow other III-nitride NW like ternary InGaN material with full range composition tunability, which is a good candidate for photovoltaic applications. In addition, the overgrowth of AlInN/GaN or AlGaN/GaN MQW heterostructures could be explored to get NW based LEDs emitting at UV range.

For visible LED applications, in self assembled approach, GaN NW based LED devices could be managed on low cost Si wafer regardless the large thermal and lattice mismatch (the current work of PhD student D. Salomon in the laboratory.).

In the selective area growth approach, the combination of low precursor method with patterned Ga-polar GaN 2D template shall give the possibility to get well ordered array of GaN NWs on conducting substrate. This dense NW array coated with MQW and p-capped layer is definitely promising to target on commercial LED devices with high efficiency and low cost benefiting from the NW geometry. The other peculiarity for such kind of NW based devices lies on the nanopixel level resolution for the realization of completely LED based screens display with ultra high brightness and dynamic contrast.

For heterostructures growth, the coexistence of axial and radial MQW deposition has been demonstrated in our NWs (the current work of PhD student D. Salomon in the laboratory.) This structure gives the possibility to have a directly comparison of the structural and optical properties for the MQW heterostructures grown along polar and non-polar direction. The mixture of the emission from these two structures could be used to get phosphor-free white LED based on III-nitride NWs after a careful growth optimization.

Chapter 7

Résumé en Français and Acknowledgement

7. RÉSUMÉ EN FRANÇAIS AND ACKNOWLEDGEMENT

Résumé en Français

Les nitrures (GaN, AlN et InN) et leurs alliages sont connus pour leurs propriétés remarquables d'émission de lumière de l'UV jusqu'à l'infrarouge et sont largement utilisés au quotidien principalement pour l'éclairage *via* les diodes électroluminescentes (DEL) bleues et blanches. Les nitrures sont aussi couramment employés pour la réalisation de lasers bleus à semiconducteurs, et même très récemment pour les lasers verts, pouvant atteindre de fortes puissances (1W). Par ailleurs, les nitrures vont certainement joués un rôle majeur sur le marché des transistors à forte mobilité (*High Electron Mobility Transistors*-HEMT) avec l'avènement des voitures électriques qui nécessitent de fortes puissances. On estime que ce nouveau secteur des nitrures est très prometteur puisqu'il devrait être équivalent à celui de l'éclairage dans les prochaines années. La réalisation de ces dispositifs photoniques et électroniques nécessitent de pouvoir contrôler très précisément l'épitaxie du GaN, les compositions d'alliage $Al_xIn_yGa_{1-x-y}N$, les épaisseurs à l'échelle nanométrique et les dopages n/p. La technique de MOVPE (Metal-Organic Vapor Phase Epitaxy) permet de répondre parfaitement à ces exigences et est aujourd'hui la technique utilisée par les industriels pour réaliser l'ensemble de ces dispositifs à base de nitrures. L'amélioration des performances des dispositifs a motivé depuis près de 10 ans la croissance des nanostructures de nitrures. Plusieurs types de nanostructures présentant des morphologies très variée ont été synthétisé, citons les boîtes quantiques [26], les nanopyramides [28], les nanofils [27], les nanocercles [29], les nanotubes [30], les nanoaiguilles [31], les nanopores [32] ou bien les nanoponts [33]. Depuis quelques années, la thématique des nanofils est un domaine en plein émergence dans la communauté nitrure suite à des publications phares, comme celles du groupe de Lieber (Harvard) sur la réalisation de dispositifs à fils uniques (LED et Laser à longueur d'onde variable, HEMT, Cellule Photovoltaïque) obtenus sur des fils GaN catalysé [53], [54], [114].

La voie la plus courante et la plus connue pour fabriquer des nanofils semiconducteurs est d'utiliser les nanoparticules métalliques pour obtenir un mode de croissance catalysée du type VLS (Vapeur-Liquide-Solide) [79]. Par exemple dans le cas du GaN, des nanoparticules de Ni permettent de faire croître des nanofils de GaN à section triangulaire [27], [81]. Toutefois, cette méthode reste difficile à contrôler et peut entrainer la présence d'une contamination métallique qui détériore les propriétés structurales et optiques [59], [60]. Ainsi, la croissance de fils de GaN sans catalyseur est une voie intéressante à étudier bien qu'elle soit beaucoup plus difficile à mettre en œuvre. L'épitaxie par jets moléculaire permet

de former "naturellement" des nanofils non-catalysés de GaN dans des conditions riche azote sur silicium (111) [61], [62]. Néanmoins, la croissance MOVPE de fils GaN sans catalyseur est beaucoup plus délicate à obtenir et nécessite des conditions de croissances très spécifiques comme la croissance pulsée (groupe d'Hersee, New Mexico) [63], les faibles flux de précurseur (groupe de Samuelson, Lund) ou bien un ratio spécifique N_2/H_2 des gaz vecteurs (groupe de Waag, Braunschweig) [64]. Finalement, peu d'études ont étémenées sur la croissance MOVPE de nanofils GaN non-catalysé, alors mme que la MOVPE est largement utilisée par les industriels et représente *de facto* un enjeu économique, comme en témoigne la création de la start-up GLÖ par le groupe de Lund en Suède en 2005. Notre laboratoire a développé une nouvelle méthode de croissance MOVPE de fils GaN sans catalyseur en ajoutant notamment un fort flux de silane en début de croissance pour favoriser la croissance verticale (thèse de R. Koester) [65]. Cette approche innovante en MOVPE permet d'obtenir des fils de GaN sur saphir ayant un diamètre compris entre 400 nm et 2 μm et une longueur simplement déterminée par le temps de croissance (30-100 μm/h). Bien que ces premières études démontrent la faisabilité de nanostructures filaires par MOVPE, aucune étude systématique n'a été faite pour comprendre l'influence des paramètres de croissance sur la morphologie des nanofils. En particulier, la compréhension des mécanismes de croissance mis en jeu pour la croissance de fils par MOVPE reste un champ encore totalement inexplorée. Par ailleurs, le contrôle précis en termes de position, de densité et de taille des nanostructures en utilisant des substrats nanostructurés par les techniques de lithographie est aussi un domaine qui reste à développer pour justement obtenir des propriétés optiques et structurales homogènes et pour faciliter l'intégration de ces nanostructures dans de nouveaux dispositifs.

Dans ce contexte, le but de la thèse est d'étudier la croissance par MOVPE de nanostructures de nitrures en forme de fil et de pyramide, et en particulier de décrire les mécanismes de croissance liés à ces deux types de nanostructures. De plus, ce travail de thèse a pour objectif de pouvoir mieux contrôler la taille et la densit é de ces nanostructures en développant la croissance sélective sur des substrats nanostructurés par lithographie. Dans un premier temps, un travail systématique a été entrepris pour connaître de manière quantitative l'influence des paramètres MOVPE sur la croissance des fils GaN obtenus à l'aide du silane (procédé développé au laboratoire dans la thèse de R. Koester). Nous montrons que de nombreux paramètres (température, pression, flux des précurseurs ...) ont une forte influence sur le diamètre, la longueur et la densité des fils de GaN, ce qui

donne une fenêtre de croissance relativement étroite pour obtenir des structures filaires. Néanmoins, le cœur de cette étude concerne l'influence du flux de silane qui est un des paramètres-clés dans notre procédé de croissance de fils GaN. L'étude du silane a permis de mettre en évidence la formation d'une fine couche de SiN_x sur les facettes latérales des fils quand le flux de silane est suffisamment élevé. Cette couche de passivation des flans joue le rôle d'un masque sur lequel les espèces réactives diffusent jusqu'à atteindre le sommet du fils et vont donc contribuer à la croissance verticale. La couche de SiN_x formée en surface par le fort flux de silane est essentielle puisque elle évite toute croissance latérale et forme *in fine* une structure filaire de GaN. A partir de ces observations, nous proposons un modèle de croissance qui tient compte de cette couche de passivation. Néanmoins, l'ajout de silane n'est pas la seule approche pour obtenir des nanofils de GaN sans catalyseur. En effet, nous montrons une nouvelle méthode ne nécessitant pas de silane et qui consiste à injecter les précurseurs à de très faibles flux (flux au moins dix fois plus faibles que les valeurs habituelles). Ce type de croissance permet d'obtenir des fils de GaN non-catalysés présentant d'excellentes propriétés optiques grâce à l'absence de dopage silicium.

Dans un second temps, nous avons montré que la polaritéjouait un rôle fondamental pour la croissance des nanostructures. En effet, après avoir mesuré la polarité des fils et des pyramides de GaN, nous en avons conclu que la polarité détermine la forme de la nanostructure pour des conditions de croissance identiques: polarité N (axe de croissance selon -c) pour les fils et polarité Ga (axe de croissance selon +c) pour les fil/pyramides. Ainsi, le type de nanostructures peut simplement être déterminé par la polarité en choisissant correctement l'orientation du substrat ou le traitement de surface qui favorisera telle ou telle polarité. Cette méthode a été utilisée dans le cadre des croissances sélectives à travers un masque de 5 nm de Si_3N_4 nanostructuré par lithographie (nano-impression et interférométrie laser) pour contrôler la taille et la densité des fils et des pyramides. La croissance organisée de fils a été obtenue sur substrat de saphir nitruré pour favoriser la polarité N, alors que la croissance organisée de pyramides sur une couche de GaN de polarité Ga. Notons que dans le cas des croissances de fils en faibles flux, la polarité Ga est ici nécessaire ce qui donne des fils avec une forme de pyramide au sommet (fils en forme de ≪crayon≫). Nous montrons aussi que ces nanostructures en forme de fil ou de pyramide peuvent servir à la croissance d'hétérostructures InGaN/GaN sur des plans semi-polaires (facettes des pyramides) et non-polaires (flans des fils) pour l'émission dans le visible. En particulier, une LED à nanofils uniques et la formation d'une boîte quantique au

sommet des pyramides ont été obtenues avec ce type de puits quantiques.

Ce manuscrit de thèse est organisé en 6 chapitres de la manière suivante : les chapitres 1 et 6 correspondent respectivement à l'introduction et la conclusion du travail de thèse, le chapitre 2 présente les propriétés des matériaux nitrures et donne un état de l'art sur la croissance des fils et des pyramides, le chapitre 3 présente la technique de MOVPE et montre une étude paramétrique pour optimiser la croissance de fils non-catalysés, le chapitre 4 montre des résultats importants sur l'étude du flux de silane et de la polarité pour la croissance de fils non-catalysés et propose un nouvelle approche de croissance de fils sans silane, enfin le chapitre 5 présente des résultats sur la croissance sélective de fils sur saphir et de pyramides sur GaN.

Chapitre 1: Introduction générale et objectifs

Ce chapitre correspond à l'introduction générale de la thèse. Un historique rapide du développement des nitrures est présenté en montrant deux obstacles importants qui limitent aujourd'hui les rendements de luminescence: la densité de dislocation et l'effet Stark confiné quantique sur le plan polaire orienté selon l'axe c. Les nanostructures telles que les fils et les pyramides représentent une approche alternative séduisante pour faire face aux limitations des structures planaires, en particulier en réduisant la densité de dislocations et en permettant la croissance d'hétérostructures sur les plans semi- ou non-polaires. Cette partie présente les motivations et les objectifs de ce travail de thèse et l'organisation du manuscrit.

Chapitre 2: Propriétés des semiconducteurs nitrures et croissance MOVPE des nanostructures

Après avoir rappelé les propriétés structurales et optiques singulières des nitrures (structure cristalline, structure de bandes électroniques, la polarité ...), ce chapitre dresse un état de l'art sur les croissances MOVPE des nanostructures en forme de fil et de pyramide. Dans le cas des fils, les deux types de croissance catalysée et non-catalysée sont abordées. Nous montrons aussi les différents travaux déjà réalisés sur la croissance sélective de fils et de pyramides. Enfin, une revue de la littérature concernant la croissance d'hétérostructures sur ces deux types de nanostructures montre clairement que ces nanostructures ont un réel potentiel pour des applications, principalement pour des dispositifs photoniques.

Chapitre 3: Croissance MOVPE des nitrures: étude de la croissance de fils GaN auto-assemblés

Dans ce chapitre, nous présentons la technique de MOVPE CCS et comment nous l'utilisons pour obtenir la croissance de fils GaN non-catalysés sur saphir.

Nous avons développé un procédé de croissance de fils sans-catalyseur en combinant un faible ratio V/III et l'ajout d'un flux de silane pour favoriser la croissance verticale (thèse de R. Koester). Afin d'optimiser ce procédé, nous avons réalisé une étude systématique des paramètres de croissance (température de croissance, le ratio V/III et les flux de précurseurs, le flux des gaz vecteurs et la pression) pour connaître de manière quantitative leurs influences sur la densité, le diamètre et la longueur des fils de GaN. Nous avons clairement observé que l'augmentation de la température de croissance accroit la densité et le diamètre grâce à une plus grande longueur de diffusion des espèces rèactives. La pression et le flux du gaz vecteur influencent aussi de manière significative sur la morphologie des fils car ces deux paramètres modifient le ratio TMGa/Silane dans la phase gazeuse. Par ailleurs, nous avons identifié que la réduction du flux de précurseurs III et V permet de réduire le diamètre des fils de GaN alors même que le ratio V/III est plus élevé. Ainsi, nous pouvons en conclure que la réduction de diamètre des fils n'est pas seulement contrôlée par la réduction du ratio V/III, mais aussi par la diminution des flux de précurseur.

Chapitre 4: Croissance non-catalysée de fils GaN auto-assemblé : des mécanismes de croissance avec l'injection *in situ* de silane à une nouvelle méthode à faible flux d'injection de précurseurs

La première partie de ce chapitre étudie en détail l'influence du flux de silane sur la croissance des fils de GaN. A partir d'analyses structurales fines réalisées par SIMS (*secondary ion mass spectroscopy*), nous montrons la présence d'une couche de SiN_x sur les flans des fils de GaN formée par le flux de silane. Cette couche révèle les mécanismes de croissance des fils puisque le SiN_x en surface joue le rôle d'un masque de passivation qui va empcher toute croissance latérale et favoriser la croissance verticale. Nous développons un modèle de croissance qui tient compte de ce phénomène de passivation des flans des fils où nous distinguons deux régimes de croissance différents: (1) régime transitoire (longueur du fil ¡longueur de diffusion des espèces) où toutes les espèces réactives des flans diffusent jusqu'au sommet (flux d'espèce qui augmente avec la surface latérale des fils), (2) régime linéaire (longueur du fil longueur de diffusion des espèces) où seule une partie espèces réactives des flans diffusent jusqu'au sommet (flux d'espèce contant quelque soit la longueur des fils). Nous montrons aussi que ce masque sur les flans empche toute croissance des puits quantiques InGaN/GaN tant est si bien qu'il est possible de contrôler la longueur de recouvrement des puits InGaN/GaN simplement en contrôlant l'arrt du flux de silane. Les fils de GaN recouverts au sommet de puits InGaN/GaN sont facilement intégrables pour

fabriquer des dispositifs à fils uniques puisque les contacts électriques peuvent tre pris à chaque extrémité des fils de GaN du fait du recouvrement partiel des puits InGaN/GaN. Dans une seconde partie, nous montrons que les fils de GaN présentant une facette plate au sommet sont principalement de polarité N, alors que les nanostructures de GaN de polarité Ga présentent une forme de pyramide avec des facettes inclinées. Ainsi, nous montrons que le contrôle de la polarité est un facteur déterminant pour la croissance des nanostructures du type filaire ou pyramidale. Enfin, dans une troisième partie, nous démontrons qu'il est possible de s'affranchir du silane pour la croissance de fils de GaN non-catalysé en utilisant un très faible flux de précurseurs et en favorisant cette fois une polarité Ga. Cette nouvelle approche permet d'obtenir des fils avec un diamètre de l'ordre de la centaine de nanomètre terminant par un sommet en forme de pyramide et présentant d'excellente propriétés optiques (largeur du bord de bande: 1-3 meV) grâce à l'absence de silicium.

Chapitre 5: Croissance sélective de nanostructures filaires et pyramidales de GaN

Dans ce chapitre, nous présentons les études de croissances organisées de fils et de pyramides obtenues par croissance sélective à travers un masque de Si_3N_4 nanostructuré par lithographie, et ceux dans l'objectif de contrôler la taille et la densité de ces nanostructures. Le type de nanostructure (fil/pyramide) est déterminé par la polarité (polarité N/polarité Ga). Dans une première partie, nous présentons la croissance organisée de fils sur substrat de saphir nitruré pour favoriser la polarité N. Comme la sélectivité sur saphir étant assez faible, un procédé en deux étapes avec une nucléation à basse température (950 °C) et une poursuite de la croissance à haute température (1040 °C) a permis de fortement améliorer la sélectivité sur saphir. Par ailleurs, l'utilisation d'une croissance pulsée de précurseur Ga a permis d'obtenir un réseau de fils organisés avec un taux de remplissage des ouvertures du masque entre 70 et 100 %. Dans une seconde partie, nous développons la croissance organisée de pyramides sur une surface de GaN de polarité Ga. Une étude paramétrique a permis de trouver les bonnes conditions de croissance pour réaliser un réseau organisé de nanopyramides (dimension de l'ordre de 250 nm). La croissance d'hétérostructures InGaN/GaN sur ces nanostructures pyramidales a montré un confinement quantique localisé aux sommets des pyramides lié certainement à la formation d'une boîte quantique.

Chapitre 6: Conclusions et perspectives

Ce travail de thèse a permis de révéler deux types de fils GaN non-catalysés qui ncessitent dans chacun des cas des conditions de croissance très particulires:

- (1) les fils hexagonaux de polarité N d'assez grande taille (diamètre : 400 nm-2μm, longueur supérieur 5 μm) présentant un sommet plat. L'injection d'un fort flux de silane permet d'obtenir ce type de fil grâce à la couche de passivation à condition de croitre sur une surface favorisant la polarité N (saphir nitruré ou Substrat de GaN de polarité N)

- (2) les fils hexagonaux de polarité Ga de petite taille (diamètre : 100-300 nm et de longueur ¡ 2mum) se terminant par une pyramide (fils en forme de "crayon"). Dans ce cas, il est nécessaire d'utiliser de très faibles flux de précurseur pour favoriser l'apparition des plans m à condition de croitre là aussi sur une surface favorisant la polarité Ga, comme une surface de saphir non-nitrurée.

Ce contrôle de la polarité a permis de réaliser des réseaux ordonnés de fils et de pyramides par croissances sélectives. Ce travail de fond sur la compréhension des mécanismes de croissance et sur l'influence de la polarité ouvre de nombreuses perspectives. Citons à titre d'exemple, la croissance de boîtes quantiques au sommet des fils de polarité Ga, comme nous l'avons fait dans le cas des pyramides.

Acknowledgement

Foremost I would like to express my deep and sincere gratitude to Nanoscience Foundation (RTRA) for giving me the opportunity and finical support to perform my PhD thesis in so fantastic an environment in Grenoble France.

Great respects gives to Dr. J.-M. Gérard the director of the group SP2M in INAC and Dr. H. Mariettem the group leader of NPSC who always kept an eye on my progress during my PhD thesis in the last three years.

Great appreciation goes to my supervisors Dr. J. Eymery and Dr. C. Durand who taught me everything about the MOCVD and doing research in detail from A to Z and were so patient to answer my questions, gave me advice, encouragement throughout the thesis process. Their hard working, enthusiasm, inspiration, wide knowledge left me a great impression, which is also of great value in my life. Thanks for spending so much time on revising my writing and preparing together for various presentations. I really appreciate for all of your efforts and valuable advice. This thesis can never be done without you. No word can express my thanks. Just thanks again.

The jury members, Dr. M.-A. Poisson, Dr. J.-C. Harmand, Dr. N. Grandjean and Dr. J. Cibert, I appreciate a lot for your presence at my PhD defense and the good advice you gave to improve the quality of this PhD work.

I would also show my respect and cordially acknowledge to all of the researchers in INAC group. They brought me into the world of physics and gave me sound of knowledge. Sincerely thanks to all the people who contributed to this PhD work through various collaborations.

I am indebted to my colleges and friends Robert, Sandeep, Alex, Prem, Olivier, Qiran, Claudin, Nitin, Lise, Megan, Damine, Gabriel, Myriam, Karine, Lionel, Fernando, Vincent, Aparna, Yulia, Aurelie, Immanuel, Samir, Chonglong, Irina, Dai in INAC group for all their help, important support and funny time we spent together in various respects. Especially I shall mention Robert who shared me with his experience and helped me a lot in my initial stay in France (and also now in Germany).

My Chinese friends Peng and his wife, Zheng and his wife, Lin and his girl friend, Ke, Hongxin, Hongming, thank you so much for providing a funny daily life and stimulating learning environment in which we support each other and grow together. I still remember all the happy time during the weekend and Chinese Spring Festivals. I wish you all the best for your future.

I am also thankful to the technical staff, administrative staff and secretaries

at INAC and Nanoscience foundation for assisting me in many different ways. You kept everything in order and were always available in my PhD study.

Last but not the least, I want to express my thanks to my wife Jinyi and my parents. They support me without asking anything returned. Thank you for your love and support.

Bibliography

[1] J. Wu, W. Walukiewicz, K. M. Yu, J. W. Ager, E. E. Haller, H. Lu, William J. Schaff, Y. Saito, and Y. Nanishi. **Unusual properties of the fundamental band gap of InN**. *Applied Physics Letters*, **80**(21):3967, 2002. 2

[2] V. Davydov, A. Klochikhin, V. Emtsev, D. Kurdyukov, S. Ivanov, V. Vekshin, F. Bechstedt, J. Furthmller, J. Aderhold, J. Graul, A. Mudryi, H. Harima, A. Hashimoto, A. Yamamoto, and E. Haller. **Band Gap of Hexagonal InN and InGaN Alloys**. *physica status solidi (b)*, **234**(3):787–795, 2002. 2

[3] I. Vurgaftman and J. R. Meyer. **Band parameters for nitrogen-containing semiconductors**. *Journal of Applied Physics*, **94**(6):3675, 2003. 2, 17, 18

[4] W. C. Johnson, J. B. Parson, and M. C. Crew. **Nitrogen Compounds of Gallium. III**. *Journal of Physical Chemistry*, **36**(10):2651–2654, 1932. 3

[5] H. P. Maruska and J. J. Tietjen. **The preparation and properties of vapor deposited single-crsyaline GaN**. *Applied Physics Letters*, **15**(10):327, 1969. 3

[6] W. Seifert, R. Franzheld, E. Butter, H. Sobotta, and V. Riede. **On the origin of free carriers in highconducting nGaN**. *Crystal Research and Technology*, **18**(3):383–390, 1983. 3

[7] H. Amano, I. Akasaki, K. Hiramatsu, N. Koide, and N. Sawaki. **Effects of the buffer layer in metalorganic vapour phase epitaxy of GaN on sapphire substrate**. *Thin Solid Films*, **163**:415–420, 1988. 3

[8] I. Akasaki, H. Amano, Y. Koide, K. Hiramatsu, and N. Sawaki. **Effects of ain buffer layer on crystallographic structure and on electrical and optical properties of GaN and Ga1-xAlxN (0 < x <0.4) films grown on sapphire substrate by MOVPE**. *Journal of Crystal Growth*, **98**(1-2):209–219, 1989. 3

[9] S. Nakamura, T. Mukai, M. Senoh, and N. Iwasa. **Thermal Annealing Effects on P-Type Mg-Doped GaN Films**. *Japanese Journal of Applied Physics*, **31**(Part 2, No. 2B):L139–L142, 1992. 3

[10] H. Amano, M. Kito, K. Hiramatsu, and I. Akasaki. **P-Type Conduction in Mg-Doped GaN Treated with Low-Energy Electron Beam Irradiation (LEEBI)**. *Japanese Journal of Applied Physics*, **28**(Part 2, No. 12):L2112–L2114, 1989. 3

[11] S. Nakamura, T. Mukai, and M. Senoh. **Candela-class high-brightness InGaN/AlGaN double-heterostructure blue-light-emitting diodes**. *Applied Physics Letters*, **64**(13):1687, 1994. 3

[12] L. Liu and J. H. Edgar. **Substrates for gallium nitride epitaxy**. *Materials Science and Engineering: R: Reports*, **37**(3):61–127, 2002. 4

[13] P. Gibart. **Metal organic vapour phase epitaxy of GaN and lateral overgrowth**. *Reports on Progress in Physics*, **67**(5):667–715, 2004. 4, 6

[14] P. Waltereit, O. Brandt, A. Trampert, H. T. Grahn, J. Menniger, M. Ramsteiner, M. Reiche, and K. H. Ploog. **Nitride semiconductors free of electrostatic fields for efficient white light-emitting diodes**. *Nature*, **406**(6798):865–868, 2000. 4

[15] S. F. Chichibu, A. C. Abare, M. P. Mack, M. S. Minsky, T. Deguchi, D. Cohen, P. Kozodoy, S. B. Fleischer, S. Keller, J. S. Speck, J. E. Bowers, E. Hu, U. K. Mishra, L. A. Coldren, S. P. DenBaars, K. Wada, T. Sota, and S. Nakamura. **Optical properties of InGaN quantum wells**. *Materials Science and Engineering B*, **59**(1-3):298–306, 1999. 4

[16] S. C. Ling, T. C. Lu, S. P. Chang, and J. R. Chen. **Low efficiency droop in blue-green m-plane InGaN/GaN light emitting diodes**. *Applied Physics Letters*, **96**(23). 4

[17] C. J. Sun and M. Razeghi. **Comparison of the physical properties of GaN thin films deposited on (0001) and (0112) sapphire substrates**. *Applied Physics Letters*, **63**(7):973, 1993. 5

[18] M. D. Craven, F. Wu, A. Chakraborty, B. Imer, U. K. Mishra, S. P. DenBaars, and J. S. Speck. **Microstructural evolution of a-plane GaN grown on a-plane SiC by metalorganic chemical vapor deposition**. *Applied Physics Letters*, **84**(8):1281, 2004. 5

[19] S. Stemmer, P. Pirouz, Y. Ikuhara, and R. F. Davis. **Film/Substrate Orientation Relationship in the AIN/6H-SiC Epitaxial System**. *Physical Review Letters*, **77**(9):1797, 1996. 5

[20] X. Ke. **-LiAlO2 single crystal: a novel substrate for GaN epitaxy**. *Journal of Crystal Growth*, **193**(1-2):127–132, 1998. 5

[21] X. Ni, U. Ozgur, A. A. Baski, H. Morkoc, Lin Zhou, David J. Smith, and C. A. Tran. **Epitaxial lateral overgrowth of (11-22) semipolar GaN on (1-100) m-plane sapphire by metalorganic chemical vapor deposition**. *Applied Physics Letters*, **90**(18):182109, 2007. 5

[22] R. Liu, A. Bell, F. A. Ponce, C. Q. Chen, J. W. Yang, and M. A. Khan. **Luminescence from stacking faults in gallium nitride**. *Applied Physics Letters*, **86**(2):021908, 2005. 5

[23] Z. H. Wu, A. M. Fischer, F. A. Ponce, B. Bastek, J. Christen, T. Wernicke, M. Weyers, and M. Kneissl. **Structural and optical properties of nonpolar GaN thin films**. *Applied Physics Letters*, **92**(17):171904, 2008. 5

[24] H. Teisseyre, C. Skierbiszewski, B. ucznik, G. Kamler, A. Feduniewicz, M. Siekacz, T. Suski, P. Perlin, I. Grzegory, and S. Porowski. **Free and bound excitons in GaNAlGaN homoepitaxial quantum wells grown on bulk GaN substrate along the nonpolar (11-20) direction**. *Applied Physics Letters*, **86**(16):162112, 2005. 5

[25] M. Ueda, K. Kojima, M. Funato, Y. Kawakami, Y. Narukawa, and T. Mukai. **Epitaxial growth and optical properties of semipo-**

lar (11-22) GaN and InGaNGaN quantum wells on GaN bulk substrates. *Applied Physics Letters*, **89**(21):211907, 2006. 5

[26] S. Tanaka, S. Iwai, and Y. Aoyagi. **Self-assembling GaN quantum dots on AlxGa1xN surfaces using a surfactant**. *Applied Physics Letters*, **69**(26):4096, 1996. 5, 156

[27] X. F. Duan and Charles M. Lieber. **Laser-Assisted Catalytic Growth of Single Crystal GaN Nanowires**. *Journal of the American Chemical Society*, **122**(1):188–189, 2000. 5, 22, 103, 156

[28] C. W. Liu, A. atka, Lethy K. Jagadamma, Paul R. Edwards, D. Allsopp, Robert W. Martin, P. Shields, J. Kovac, F. Uherek, and W. Wang. **Light Emission from InGaN Quantum Wells Grown on the Facets of Closely Spaced GaN Nano-Pyramids Formed by Nano-Imprinting**. *Applied Physics Express*, **2**(12):121002, 2009. 5, 29, 39, 40, 156

[29] Y. D. Wang, K. Y. Zang, S. J. Chua, Melissa S. Sander, S. Tripathy, and Clifton G. Fonstad. **High-Density Arrays of InGaN Nanorings, Nanodots, and Nanoarrows Fabricated by a Template-Assisted Approach**. *The Journal of Physical Chemistry B*, **110**(23):11081–11087, 2006. 5, 141, 156

[30] J. Q Hu, Y. Bando, J. H Zhan, F. F Xu, T. Sekiguchi, and D. Golberg. **Growth of SingleCrystalline Cubic GaN Nanotubes with Rectangular CrossSections**. *Advanced Materials*, **16**(16):1465–1468, 2004. 5, 156

[31] C. T. Lin, G. H. Yu, X. Z. Wang, M. X. Cao, H. F. Lu, H. Gong, M. Qi, and A. Z. Li. **Catalyst-Free Growth of Well Vertically Aligned GaN Needlelike Nanowire Array with Low-Field Electron Emission Properties**. *The Journal of Physical Chemistry C*, **112**(48):18821–18824, 2008. 5, 156

[32] Isaac H. Wildeson, David A. Ewoldt, R. Colby, Eric A. Stach, and Timothy D. Sands. **Controlled Growth of Ordered Nanopore Arrays in GaN**. *Nano Letters*, **11**(2):535–540, 2011. 5, 29, 156

[33] K. K. Kim, T. Henry, G. Cui, J. Han, Y. Y. Song, Arto V. Nurmikko, and H. Tang. **Epitaxial growth of aligned GaN nanowires and nanobridges**. *physica status solidi (b)*, **244**(6):1810–1814, 2007. 5, 156

[34] E. Calleja, M. A. Snchez-Garca, F. J. Snchez, F. Calle, F. B. Naranjo, E. Muoz, U. Jahn, and K. Ploog. **Luminescence properties and defects in GaN nanocolumns grown by molecular beam epitaxy**. *Physical Review B*, **62**(24):16826, 2000. 6, 24, 103

[35] O. Landr, D. Camacho, C. Bougerol, Y. M. Niquet, V. Favre-Nicolin, G. Renaud, H. Renevier, and B. Daudin. **Elastic strain relaxation in GaN/AlN nanowire superlattice**. *Physical Review B*, **81**(15):153306, 2010. 6

[36] Y. J. Hong, J. M. Jeon, M. Kim, and S. R. Jeon. **Structural and optical characteristics of GaN/ZnO coaxial nanotube heterostructure arrays for light-emitting device applications**. *New Journal of Physics*, **11**(12). 6

[37] H. W. Lin. **InGaN/GaN nanorod array white light-emitting diode**. *Applied Physics Letters*, **97**(7). 6

[38] T. Kuykendall, P. Ulrich, S. Aloni, and P. D. Yang. **Complete composition tunability of InGaN nanowires using a combinatorial approach**. *Nat Mater*, **6**(12):951–956, 2007. 6, 24

[39] T. Y. Tang, C. H. Lin, Y. S. Yung-Sheng Chen, W. Y. Shiao, W. M. Chang, C. H. Liao, K. C. Shen, C. C. Yang, M. C. Hsu, J. H. Yeh, and T. C. Hsu. **Nitride Nanocolumns for the Development of Light-Emitting Diode**. *IEEE Transactions on Electron Devices*, **57**(1):71–78, 2010. 6, 27

[40] Q. M. Li, Y. Lin, Randall J. Creighton, Jeffrey J. Figiel, and George T. Wang. **NanowireTemplated Lateral Epitaxial Growth of LowDislocation Density Nonpolar aPlane GaN on rPlane Sapphire**. *Advanced Materials*, **21**(23):2416–2420, 2009. 6, 22

[41] R. Colby, Z. W. Liang, Isaac H. Wildeson, David A. Ewoldt, Timothy D. Sands, Edwin R. Garcia, and Eric A. Stach. **Disloca-**

tion Filtering in GaN Nanostructures. *Nano Letters*, **10**(5):1568–1573, 2010. 6, 26

[42] Isaac H. Wildeson, R. Colby, David A. Ewoldt, Z. W. Liang, Dmitri N. Zakharov, Nestor J. Zaluzec, Edwin R. Garcia, Eric A. Stach, and Timothy D. Sands. **III-nitride nanopyramid light emitting diodes grown by organometallic vapor phase epitaxy**. *Journal of Applied Physics*, **108**(4):044303, 2010. 6

[43] F. Qian, S. Gradecak, Y. Li, C. Y. Wen, and Charles M. Lieber. **Core/Multishell Nanowire Heterostructures as Multicolor, High-Efficiency Light-Emitting Diodes**. *Nano Letters*, **5**(11):2287–2291, 2005. 6, 31

[44] T. Kim, J. S. Kim, M. S. Yang, S. M. Lee, Y. S. Park, U. I. Chung, and Y. H. Cho. **Highly efficient yellow photoluminescence from 11?2 InGaN multiquantum-well grown on nanoscale pyramid structure**. *Applied Physics Letters*, **97**(24):241111, 2010. 6, 39, 40

[45] Y. R. Wu, Y. Y. Lin, H. H. Huang, and J. Singh. **Electronic and optical properties of InGaN quantum dot based light emitters for solid state lighting**. *Journal of Applied Physics*, **105**:013117, 2009. 6

[46] Y. L. Chang, J. L. Wang, F. Li, and Z. Mi. **High efficiency green, yellow, and amber emission from InGaN/GaN dot-in-a-wire heterostructures on Si(111)**. *Applied Physics Letters*, **96**(1):013106, 2010. 6

[47] Justin C. Johnson, H. J. Choi, Kelly P. Knutsen, Richard D. Schaller, P. D. Yang, and Richard J. Saykally. **Single gallium nitride nanowire lasers**. *Nat Mater*, **1**(2):106–110, 2002. 7

[48] A. L. Henneghien, G. Tourbot, B. Daudin, O. Lartigue, Y. Desieres, and J. M. Gerard. **Optical anisotropy and light extraction efficiency of MBE grown GaN nanowires epilayers**. *Optics Express*, **19**(2):527–539, 2011. 7

[49] W. Lim, J. S. Wright, B. P. Gila, Jason L. Johnson, A. Ural, T. Anderson, F. Ren, and S. J. Pearton. **Room temperature hydrogen detection using Pd-coated GaN nanowires**. *Applied Physics Letters*, **93**(7):072109, 2008. 7

[50] J. Renard, R. Songmuang, C. Bougerol, B. Daudin, and B. Gayral. **Exciton and Biexciton Luminescence from Single GaN/AlN Quantum Dots in Nanowires**. *Nano Letters*, **8**(7):2092–2096, 2008. 7, 103

[51] C. W. Hsu, A. Lundskog, Fredrik K. Karlsson, U. Forsberg, E. Janzen, and Per O. Holtz. **Single Excitons in InGaN Quantum Dots on GaN Pyramid Arrays**. *Nano Letters*, **11**(6):2415–2418, 2011. 7, 38

[52] C. H. Lee, J. K. Yoo, Y. J. Hong, J. H. Cho, Y. J. Kim, S. R. Jeon, J. H. Baek, and G. C. Yi. **GaN/In(1x)Ga(x)N/GaN/ZnO nanoarchitecture light emitting diode microarrays**. *Applied Physics Letters*, **94**(21):213101, 2009. 7, 31

[53] Y. Li, J. Xiang, F. Qian, S. Gradecak, Y. Wu, H. Yan, Douglas A. Blom, and Charles M. Lieber. **Dopant-Free GaN/AlN/AlGaN Radial Nanowire Heterostructures as High Electron Mobility Transistors**. *Nano Letters*, **6**(7):1468–1473, 2006. 7, 35, 156

[54] Y. J. Dong, B. Z. Tian, Thomas J. Kempa, and Charles M. Lieber. **Coaxial Group IIINitride Nanowire Photovoltaics**. *Nano Letters*, **9**(5):2183–2187, 2009. 7, 29, 36, 95, 156

[55] L. Rigutti, M. Tchernycheva, A. De Luna Bugallo, G. Jacopin, F. H. Julien, L. F. Zagonel, K. March, O. Stephan, M. Kociak, and R. Songmuang. **Ultraviolet Photodetector Based on GaN/AlN Quantum Disks in a Single Nanowire**. *Nano Letters*, **10**(8):2939–2943, 2010. 7

[56] L. Liao, W. Bai, J, R. Cheng, Y. C. Lin, S. Jiang, Y. Q. Qu, Y. Huang, and X. F. Duan. **Sub-100 nm Channel Length Graphene Transistors**. *Nano Letters*, **10**(10):3952–3956, 2010. 7

[57] H. Sekiguchi, K. Kishino, and A. Kikuchi. **Emission color control from blue to red with nanocolumn diameter of InGaN/GaN nanocolumn arrays grown on same substrate**. *Applied Physics Letters*, **96**(23):231104, 2010. 7, 96

[58] K. Nishizuka, M. Funato, Y. Kawakami, Y. Narukawa, and T. Mukai. **Efficient rainbow color luminescence from In[sub x]Ga[sub 1x]N single quantum wells fabricated on 1122 microfacets**. *Applied Physics Letters*, **87**(23):231901, 2005. 7, 39

[59] S. Breuer, C. Pfuller, T. Flissikowski, O. Brandt, Holger T. Grahn, L. Geelhaar, and H. Riechert. **Suitability of Au- and Self-Assisted GaAs Nanowires for Optoelectronic Applications**. *Nano Letters*, **11**(3):1276–1279, 2011. 8, 156

[60] C. Chze, L. Geelhaar, O. Brandt, Walter M. Weber, H. Riechert, S. Mnch, R. Rothemund, S. Reitzenstein, A. Forchel, T. Kehagias, P. Komninou, George P. Dimitrakopulos, and T. Karakostas. **Direct comparison of catalyst-free and catalyst-induced GaN nanowires**. *Nano Research*, **3**(7):528–536, 2010. 8, 23, 156

[61] M. Tchernycheva, C. Sartel, .G Cirlin, L. Travers, G. Patriarche, J.C. Harmand, L. S. Dang, J. Renard, B. Gayral, L. Nevou, and F. Julien. **Growth of GaN free-standing nanowires by plasma-assisted molecular beam epitaxy: structural and optical characterization**. *Nanotechnology*, **18**(38):385306, 2007. 8, 157

[62] R. Songmuang, O. Landre, and B. Daudin. **From nucleation to growth of catalyst-free GaN nanowires on thin AlN buffer layer**. *Applied Physics Letters*, **91**:251902, 2007. 8, 24, 88, 157

[63] Stephen D. Hersee, X. Y. Sun, and X. Wang. **The Controlled Growth of GaN Nanowires**. *Nano Letters*, **6**(8):1808–1811, 2006. 8, 26, 27, 104, 157

[64] W. Bergbauer, M. Strassburg, C. Klper, N. Linder, C. Roder, J. Lhnemann, A. Trampert, S. Fndling, S. F. Li, H. H. Wehmann, and A. Waag. **Continuous-flux MOVPE growth of position-controlled N-face GaN nanorods and embedded InGaN quantum wells**. *Nanotechnology*, **21**(30):305201, 2010. 8, 28, 104, 128, 157

[65] R. Koester, J. S. Hwang, C. Durand, D. Le Si Dang, and J. Eymery. **Self-assembled growth of catalyst-free GaN wires by**

metalorganic vapour phase epitaxy. *Nanotechnology*, **21**(1):015602, 2010. 8, 24, 59, 60, 74, 89, 104, 107, 157

[66] M. Park, J. J. Cuomo, B. J. Rodriguez, and W. C. Yang. **Micro-Raman study of electronic properties of inversion domains in GaN-based lateral polarity heterostructures**. *Journal of Applied Physics*, **93**(12). 15

[67] F. Tuomisto, K. Saarinen, B. Lucznik, I. Grzegory, H. Teisseyre, T. Suski, S. Porowski, P. R. Hageman, and J. Likonen. **Effect of growth polarity on vacancy defect and impurity incorporation in dislocation-free GaN**. *Applied Physics Letters*, **86**(3):031915, 2005. 15, 103

[68] H. M. Ng and A. Y. Cho. **Investigation of Si doping and impurity incorporation dependence on the polarity of GaN by molecular beam epitaxy**. *Journal of Vacuum Science & Technology B: Microelectronics and Nanometer Structures*, **20**(3):1217, 2002. 15

[69] M. Losurdo. **Interplay between GaN polarity and surface reactivity towards atomic hydrogen**. *Journal of Applied Physics*, **95**(12):8408, 2004. 15

[70] M. A. Mastro, O. M. Kryliouk, T. J. Anderson, A. Davydov, and A. Shapiro. **Influence of polarity on GaN thermal stability**. *Journal of Crystal Growth*, **274**(1-2):38–46, 2005. 15

[71] F. D. Liu, R. Collazo, S. Mita, Z. Sitar, G. Duscher, and Stephen J. Pennycook. **The mechanism for polarity inversion of GaN via a thin AlN layer: Direct experimental evidence**. *Applied Physics Letters*, **91**(20):203115, 2007. 15, 97, 104, 105

[72] S. Pezzagna. **Polarity inversion of GaN(0001) by a high Mg doping**. *Journal of Crystal Growth*, **269**(2-4):249–256, 2004. 15

[73] F. Bechstedt, J. Furthmller, M. Ferhat, L. K. Teles, L. M. R. Scolfaro, J. R. Leite, V. Yu. Davydov, O. Ambacher, and R. Goldhahn. **Energy gap and optical properties of InxGa1xN**. *physica status solidi (a)*, **195**(3):628–633, 2003. 16

[74] M. Suzuki, T. Uenoyama, and A. Yanase. **First-principles calculations of effective-mass parameters of AlN and GaN**. *Physical Review B*, **52**(11):8132–8139, 1995. 16

[75] G. D. Chen, M. Smith, J. Y. Lin, H. X. Jiang, Su-Huai Wei, M. Asif Khan, and C. J. Sun. **Fundamental optical transitions in GaN**. *Applied Physics Letters*, **68**(20):2784, 1996. 16

[76] F. Bernardini and V. Fiorentini. **Nonlinear macroscopic polarization in III-V nitride alloys**. *Physical Review B*, **64**(8), 2001. 18

[77] V. Fiorentini, F. Bernardini, and O. Ambacher. **Evidence for nonlinear macroscopic polarization in IIIV nitride alloy heterostructures**. *Applied Physics Letters*, **80**(7):1204, 2002. 18

[78] T. Paskova. **Development and prospects of nitride materials and devices with nonpolar surfaces**. *physica status solidi (b)*, **245**(6):1011–1025, 2008. 20

[79] R. S. Wagner and W. C. Ellis. **Vapor-liquid-solid mechanism of single crystal growth**. *Applied Physics Letters*, **4**(5):89, 1964. 21, 156

[80] C. C. Chen. **Catalytic Growth and Characterization of Gallium Nitride Nanowires**. *Journal of the American Chemical Society*, **123**(12). 22, 103

[81] Y. Huang, X. F. Duan, Y. Cui, and Charles M. Lieber. **Gallium Nitride Nanowire Nanodevices**. *Nano Letters*, **2**(2):101–104, 2002. 22, 156

[82] Z. H. Zhong, F. Qian, D. L. Wang, and Charles M. Lieber. **Synthesis of p-Type Gallium Nitride Nanowires for Electronic and Photonic Nanodevices**. *Nano Letters*, **3**(3):343–346, 2003. 22

[83] T. Kuykendall, Peter J. Pauzauskie, Y. F. Zhang, J. Goldberger, D. Sirbuly, J. Denlinger, and P. D. Yang. **Crystallographic alignment of high-density gallium nitride nanowire arrays**. *Nature Materials*, **3**(8):524–528, 2004. 22, 23, 24

[84] Y. B. Tang, Z. H. Chen, H. S. Song, C. S. Lee, H. T. Cong, H. M. Cheng, W. J. Zhang, I. Bello, and S. T. Lee. **Vertically Aligned**

p-Type Single-Crystalline GaN Nanorod Arrays on n-Type Si for Heterojunction Photovoltaic Cells. *Nano Letters*, **8**(12):4191–4195, 2008. 22, 24, 27

[85] Q. M. Li, Randall J. Creighton, and George T. Wang. **The role of collisions in the aligned growth of vertical nanowires**. *Journal of Crystal Growth*, **310**(16):3706–3709, 2008. 22, 23, 24

[86] Q. M. Li and George T. Wang. **Improvement in aligned GaN nanowire growth using submonolayer Ni catalyst films**. *Applied Physics Letters*, **93**(4):043119, 2008. 22

[87] T. Kuykendall, P. Pauzauskie, S. Lee, Y. F. Zhang, J. Goldberger, and P. D. Yang. **Metalorganic Chemical Vapor Deposition Route to GaN Nanowires with Triangular Cross Sections**. *Nano Letters*, **3**(8):1063–1066, 2003. 23

[88] George T. Wang, Alec A. Talin, Donald J. Werder, Randall J. Creighton, E. Lai, Richard J. Anderson, and I. Arslan. **Highly aligned, template-free growth and characterization of vertical GaN nanowires on sapphire by metalorganic chemical vapour deposition**. *Nanotechnology*, **17**(23):5773–5780, 2006. 23

[89] R. Meijers, T. Richter, R. Calarco, T. Stoica, H.-P. Bochem, M. Marso, and H. Lth. **GaN-nanowhiskers: MBE-growth conditions and optical properties**. *Journal of Crystal Growth*, **289**(1):381–386, 2006. 24

[90] S. Figge, T. Aschenbrenner, C. Kruse, G. Kunert, M. Schowalter, A. Rosenauer, and D. Hommel. **A structural investigation of highly ordered catalyst- and mask-free GaN nanorods**. *Nanotechnology*, **22**(2):025603, 2011. 24

[91] O. Landre, V. Fellmann, P. Jaffrennou, C. Bougerol, H. Renevier, A. Cros, and B. Daudin. **Molecular beam epitaxy growth and optical properties of AlN nanowires**. *Applied Physics Letters*, **96**(6):061912, 2010. 24

[92] T. Stoica, Ralph J. Meijers, R. Calarco, T. Richter, E. Sutter, and H. Lth. **Photoluminescence and Intrinsic Properties of MBE-Grown InN Nanowires**. *Nano Letters*, **6**(7):1541–1547, 2006. 24

[93] T. Stoica, R. Meijers, R. Calarco, T. Richter, and H. Luth. **MBE growth optimization of InN nanowires**. *Journal of Crystal Growth*, **290**(1):241–247, 2006. 24

[94] G. Tourbot, C. Bougerol, A. Grenier, M. Den Hertog, D. Sam-Giao, D. Cooper, P. Gilet, B. Gayral, and B. Daudin. **Structural and optical properties of InGaN/GaN nanowire heterostructures grown by PA-MBE**. *Nanotechnology*, **22**:075601, 2011. 24

[95] H. M. Kim, Y. H. Cho, H. Lee, S. I. Kim, S. R. Ryu, D. Y. Kim, T. W. Kang, and K. S. Chung. **High-Brightness Light Emitting Diodes Using Dislocation-Free Indium Gallium Nitride/Gallium Nitride Multiquantum-Well Nanorod Arrays**. *Nano Letters*, **4**(6):1059–1062, 2004. 24

[96] C. Hahn, Z. Y. Zhang, A. Fu, C. H. Wu, Y. J. Hwang, Daniel J. Gargas, and P. D. Yang. **Epitaxial Growth of InGaN Nanowire Arrays for Light Emitting Diodes**. *ACS Nano*, **5**(5):3970–3976, 2011. 24

[97] B. Alloing, S. Vezian, O. Tottereau, P. Vennegues, E. Beraudo, and J. Zuniga-Perez. **On the polarity of GaN micro- and nanowires epitaxially grown on sapphire (0001) and Si(111) substrates by metal organic vapor phase epitaxy and ammonia-molecular beam epitaxy**. *Applied Physics Letters*, **98**:011914, 2011. 24

[98] H. Sekiguchi, K. Kishino, and A. Kikuchi. **Ti-mask Selective-Area Growth of GaN by RF-Plasma-Assisted Molecular-Beam Epitaxy for Fabricating Regularly Arranged InGaN/GaN Nanocolumns**. *Applied Physics Express*, **1**:124002, 2008. 25

[99] K. Kishino, H. Sekiguchi, and A. Kikuchi. **Improved Ti-mask selective-area growth (SAG) by rf-plasma-assisted molecular beam epitaxy demonstrating extremely uniform GaN nanocolumn arrays**. *Journal of Crystal Growth*, **311**(7):2063–2068, 2009. 25

[100] T. Gotschke, T. Schumann, F. Limbach, T. Stoica, and R. Calarco. **Influence of the adatom diffusion on selective growth of GaN nanowire regular arrays**. *Applied Physics Letters*, **98**(10):103102, 2011. 25, 74

[101] P. Deb, H. Y. Kim, V. Rawat, M. Oliver, S. H. Kim, M. Marshall, E. Stach, and T. Sands. **Faceted and Vertically Aligned GaN Nanorod Arrays Fabricated without Catalysts or Lithography**. *Nano Letters*, **5**(9):1847–1851, 2005. 25

[102] X. Wang, X. Y. Sun, M. Fairchild, and Stephen D. Hersee. **Fabrication of GaN nanowire arrays by confined epitaxy**. *Applied Physics Letters*, **89**(23):233115, 2006. 25, 26

[103] T. Y. Tang, W. Y. Shiao, C. H. Lin, K. C. Shen, J. J. Huang, S. Y. Ting, T. C. Liu, C. C. Yang, C. L. Yao, J. H. Yeh, T. C. Hsu, W. C. Chen, H. C. Hsu, and Li. C. Chen. **Coalescence overgrowth of GaN nanocolumns on sapphire with patterned metal organic vapor phase epitaxy**. *Journal of Applied Physics*, **105**(2):023501, 2009. 27, 29

[104] W. Bergbauer, M. Strassburg, Ch. Klper, N. Linder, C. Roder, J. Lhnemann, A. Trampert, S. Fndling, S. F. Li, and H. H. Wehmann. **N-face GaN nanorods: Continuous-flux MOVPE growth and morphological properties**. *Journal of Crystal Growth*, **315**(1):164–167, 2011. 28

[105] S. Bidnyk, B. D. Little, Y. H. Cho, J. Krasinski, J. J. Song, W. Yang, and S. A. McPherson. **Laser action in GaN pyramids grown on (111) silicon by selective lateral overgrowth**. *Applied Physics Letters*, **73**(16):2242, 1998. 29

[106] K. C. Zeng, J. Y. Lin, H. X. Jiang, and W. Yang. **Optical properties of GaN pyramids**. *Applied Physics Letters*, **74**(9):1227, 1999. 29

[107] V. Perez-Solorzano, A. Groning, M. Jetter, T. Riemann, and J. Christen. **Near-red emission from site-controlled pyramidal InGaN quantum dots**. *Applied Physics Letters*, **87**(16):163121, 2005. 29, 37, 38

[108] W. H. Goh, G. Patriarche, P. L. Bonanno, S. Gautier, T. Moudakir, M. Abid, G. Orsal, A. A. Sirenko, Z. H. Cai, and A. Martinez. **Structural and optical properties of nanodots, nanowires, and multi-quantum wells of III-nitride grown**

by MOVPE nano-selective area growth. *Journal of Crystal Growth*, **315**(1):160–163, 2011. 29, 40

[109] F. Shahedipour-Sandvik, J. Grandusky, A. Alizadeh, C. Keimel, S. P. Ganti, S. T. Taylor, S. F. LeBoeuf, and P. Sharma. **Strain dependent facet stabilization in selective-area heteroepitaxial growth of GaN nanostructures**. *Applied Physics Letters*, **87**(23):233108, 2005. 30

[110] K. Hiramatsu, K. Nishiyama, A. Motogaito, H. Miyake, Y. Iyechika, and T. Maeda. **Recent Progress in Selective Area Growth and Epitaxial Lateral Overgrowth of IIINitrides: Effects of Reactor Pressure in MOVPE Growth**. *physica status solidi (a)*, **176**(1):535–543, November 1999. 30

[111] S. Kim, Jeremy L. Schroeder, and Timothy D. Sands. **Pulsed selective epitaxial growth of hexagonal GaN microprisms**. *Journal of Crystal Growth*, **310**(6):1107–1111, 2008. 30

[112] D. Y. Song, A. Chandolu, N. Stojanovic, S. A. Nikishin, and M. Holtz. **Effect of impurity incorporation on emission wavelength in cathodoluminescence spectrum image study of GaN pyramids grown by selective area epitaxy**. *Journal of Applied Physics*, **104**(6):064309, 2008. 30, 130

[113] Y. J. Hong, C. H. Lee, A. Yoon, M. Y. Kim, H. K. Seong, H. J. Chung, C. Sone, Y. J. Park, and G. C. Yi. **Visible-Color-Tunable Light-Emitting Diodes**. *Advanced Materials*, **23**(29):3284–3288, 2011. 32

[114] F. Qian, Y. Li, S. Gradeak, H. G. Park, Y. J. Dong, Y. Ding, Z. L. Wang, and Charles M. Lieber. **Multi-quantum-well nanowire heterostructures for wavelength-controlled lasers**. *Nature Materials*, **7**(9):701–706, 2008. 33, 156

[115] P. R. Edwards, R. W. Martin, I. M. Watson, C. Liu, R. A. Taylor, J. H. Rice, J. H. Na, J. W. Robinson, and J. D. Smith. **Quantum dot emission from site-controlled InGaNGaN micropyramid arrays**. *Applied Physics Letters*, **85**(19):4281, 2004. 38, 96

[116] F. Widmann, B. Daudin, G. Feuillet, Y. Samson, J. L. Rouviere, and N. Pelekanos. **Growth kinetics and optical properties of self-organized GaN quantum dots**. *Journal of Applied Physics*, **83**(12):7618, 1998. 39

[117] B. Neubert, P. Bruckner, F. Habel, F. Scholz, T. Riemann, J. Christen, M. Beer, and J. Zweck. **GaInN quantum wells grown on facets of selectively grown GaN stripes**. *Applied Physics Letters*, **87**(18):182111, 2005. 39

[118] D. H. Reep. **Deposition of GaAs Epitaxial Layers by Organometallic CVD**. *Journal of The Electrochemical Society*, **130**(3):675, 1983. 44

[119] David W. Jenkins, John D. Dow, and M. H. Tsai. **N vacancies in AlxGa1xN**. *Journal of Applied Physics*, **72**(9):4130, 1992. 47

[120] C. Martin, M. Dauelsberg, H. Protzmann, A. Boyd, E. Thrush, M. Heuken, R. Talalaev, E. Yakovlev, and A. Kondratyev. **Modelling of group-III nitride MOVPE in the closed coupled showerhead reactor and Planetary Reactor**. *Journal of Crystal Growth*, **303**(1):318–322, 2007. 57

[121] M. Dauelsberg, C. Martin, H. Protzmann, A. Boyd, E. Thrush, J. Kappeler, M. Heuken, R. Talalaev, E. Yakovlev, and A. Kondratyev. **Modeling and process design of III-nitride MOVPE at near-atmospheric pressure in close coupled showerhead and planetary reactors**. *Journal of Crystal Growth*, **298**:418–424, 2007. 57, 58

[122] K. Dovidenko, S. Oktyabrsky, J. Narayan, and M. Razeghi. **Aluminum nitride films on different orientations of sapphire and silicon**. *Journal of Applied Physics*, **79**(5):2439, 1996. 57

[123] K. S. Kim, C. S. Oh, K. J. Lee, G. M. Yang, C. H. Hong, K. Y. Lim, H. J. Lee, and A. Yoshikawa. **Effects of growth rate of a GaN buffer layer on the properties of GaN on a sapphire substrate**. *Journal of Applied Physics*, **85**(12):8441, 1999. 59

[124] T. Yang, K. Uchida, T. Mishima, J. Kasai, and J. Gotoh. **Control of Initial Nucleation by Reducing the V/III Ratio during the**

Early Stages of GaN Growth. *physica status solidi (a)*, **180**(1):45–50, 2000. 59

[125] J. Chen, S. M. Zhang, B. S. Zhang, J. J. Zhu, G. Feng, X. M. Shen, Y. T. Wang, H. Yang, and W. C. Zheng. **Effects of reactor pressure on GaN nucleation layers and subsequent GaN epilayers grown on sapphire substrate**. *Journal of Crystal Growth*, **254**(3-4):348–352, 2003. 59

[126] D. D. Koleske, A. J. Fischer, A. A. Allerman, C. C. Mitchell, K. C. Cross, S. R. Kurtz, J. J. Figiel, K. W. Fullmer, and W. G. Breiland. **Improved brightness of 380 nm GaN light emitting diodes through intentional delay of the nucleation island coalescence**. *Applied Physics Letters*, **81**(11):1940, 2002. 63

[127] Ann I. Persson, Magnus W. Larsson, S. Stenstrom, Jonas B. Ohlsson, L. Samuelson, and Reine L. Wallenberg. **Solid-phase diffusion mechanism for GaAs nanowire growth**. *Nat Mater*, **3**(10):677–681, 2004. 74

[128] Leonardo C. Campos, M. Tonezzer, Andre S. Ferlauto, V. Grillo, R. Magalhes-Paniago, S. Oliveira, Luiz O. Ladeira, and Rodrigo G. Lacerda. **VaporSolidSolid Growth Mechanism Driven by Epitaxial Match between Solid AuZn Alloy Catalyst Particles and ZnO Nanowires at Low Temperatures**. *Advanced Materials*, **20**(8):1499–1504, 2008. 74

[129] Z. L. Wang. **Zinc oxide nanostructures: growth, properties and applications**. *Journal of Physics: Condensed Matter*, **16**(25):R829–R858, 2004. 74

[130] W. S. Shi, Y. F. Zheng, N. Wang, C. S. Lee, and S. T. Lee. **Oxide-assisted growth and optical characterization of gallium-arsenide nanowires**. *Applied Physics Letters*, **78**(21):3304, 2001. 74

[131] Timothy J. Trentler, Kathleen M. Hickman, Subhash C. Goel, Ann M. Viano, Patrick C. Gibbons, and William E. Buhro. **Solution-Liquid-Solid Growth of Crystalline III-V Semiconductors: An Analogy to Vapor-Liquid-Solid Growth**. *Science*, **270**(5243):1791 –1794, 1995. 74

[132] M. J. Bierman, Y. K. A. Lau, A. V. Kvit, A. L. Schmitt, and S. Jin. **Dislocation-Driven Nanowire Growth and Eshelby Twist**. *Science*, **320**(5879):1060–1063, 2008. 74

[133] J. Zhu, H. L. Peng, A. F. Marshall, D. M. Barnett, W. D. Nix, and Y. Cui. **Formation of chiral branched nanowires by the Eshelby Twist**. *Nature Nanotechnology*, **3**(8):477–481, 2008. 74

[134] Linus E. Jensen, Mikael T. Bjrk, Sren Jeppesen, Ann I. Persson, Jonas B. Ohlsson, and L. Samuelson. **Role of Surface Diffusion in Chemical Beam Epitaxy of InAs Nanowires**. *Nano Letters*, **4**(10):1961–1964, 2004. 74, 124

[135] Magnus T. Borgstrm, G. Immink, B. Ketelaars, R. Algra, and E. P.A.M. Bakkers. **Synergetic nanowire growth**. *Nature Nanotechnology*, **2**(9):541–544, 2007. 74

[136] E. Givargizov. **Fundamental aspects of VLS growth**. *Journal of Crystal Growth*, **31**:20–30, 1975. 74

[137] J. Johansson, C. Svensson, Patrik T., T. Mrtensson, L. Samuelson, and W. Seifert. **Mass Transport Model for Semiconductor Nanowire Growth**. *The Journal of Physical Chemistry B*, **109**(28):13567–13571, 2005. 74

[138] V. Dubrovskii, G. Cirlin, I. Soshnikov, A. Tonkikh, N. Sibirev, Yu. Samsonenko, and V. Ustinov. **Diffusion-induced growth of GaAs nanowhiskers during molecular beam epitaxy: Theory and experiment**. *Physical Review B*, **71**(20), 2005. 74

[139] V. Dubrovskii, N. Sibirev, G. Cirlin, A. Bouravleuv, Yu. Samsonenko, D. Dheeraj, H. Zhou, C. Sartel, J. Harmand, G. Patriarche, and F. Glas. **Role of nonlinear effects in nanowire growth and crystal phase**. *Physical Review B*, **80**(20), 2009. 74

[140] Daniel E. Perea, Eric R. Hemesath, Edwin J. Schwalbach, Jessica L. Lensch-Falk, Peter W. Voorhees, and Lincoln J. Lauhon. **Direct measurement of dopant distribution in an individual vapourliquidsolid nanowire**. *Nature Nanotechnology*, **4**(5):315–319, 2009. 78

[141] Erik C. Garnett, Y. C. Tseng, Devesh R. Khanal, J. Q. Wu, J. Bokor, and P. D. Yang. **Dopant profiling and surface analysis of silicon nanowires using capacitancevoltage measurements**. *Nature Nanotechnology*, **4**(5):311–314, 2009. 78

[142] S. Haffouz, H. Lahreche, P. Vennegues, P. de Mierry, B. Beaumont, F. Omnes, and P. Gibart. **The effect of the Si/N treatment of a nitridated sapphire surface on the growth mode of GaN in low-pressure metalorganic vapor phase epitaxy**. *Applied Physics Letters*, **73**(9):1278, 1998. 79

[143] De Luna A. Bugallo, L. Rigutti, G. Jacopin, F. H. Julien, C. Durand, X. J. Chen, D. Salomon, J. Eymery, and M. Tchernycheva. **Single-wire photodetectors based on InGaN/GaN radial quantum wells in GaN wires grown by catalyst-free metal-organic vapor phase epitaxy**. *Applied Physics Letters*, **98**(23):233107, 2011. 79

[144] Shadi A. Dayeh, Edward T. Yu, and D. L. Wang. **Surface Diffusion and SubstrateNanowire Adatom Exchange in InAs Nanowire Growth**. *Nano Letters*, **9**(5):1967–1972, 2009. 83

[145] W. Seifert, M. Borgstrom, K. Deppert, K. Dick, J. Johansson, M. Larsson, T. Martensson, N. Skold, C. Patriktsvensson, and B. Wacaser. **Growth of one-dimensional nanostructures in MOVPE**. *Journal of Crystal Growth*, **272**(1-4):211–220, 2004. 83

[146] D. Dalacu, A. Kam, D. Guy Austing, X. H. Wu, J. Lapointe, Geof C. Aers, and Philip J. Poole. **Selective-area vapourliquid-solid growth of InP nanowires**. *Nanotechnology*, **20**(39):395602, 2009. 83, 86

[147] V. Ruth and J. P. Hirth. **Kinetics of Diffusion-Controlled Whisker Growth**. *The Journal of Chemical Physics*, **41**(10):3139, 1964. 83, 84, 85, 123

[148] Alec M. Fischer, Z. H. Wu, K. W. Sun, Q. Y. Wei, Y. Huang, R. Senda, D. Iida, M. Iwaya, H. Amano, and Fernando A. Ponce. **Misfit Strain Relaxation by Stacking Fault Generation in InGaN**

Quantum Wells Grown on m -Plane GaN. *Applied Physics Express*, **2**:041002, 2009. 93

[149] O. Hayden, A. B. Greytak, and D. C. Bell. **Core-Shell Nanowire Light-Emitting Diodes**. *Advanced Materials*, **17**(6):701–704, 2005. 95

[150] K. Tachibana, T. Someya, S. Ishida, and Y. Arakawa. **Selective growth of InGaN quantum dot structures and their microphotoluminescence at room temperature**. *Applied Physics Letters*, **76**(22):3212, 2000. 96

[151] M. Aoki, H. Yamane, M. Shimada, T. Kajiwara, S. Sarayama, and Francis J. DiSalvo. **Morphology and Polarity of GaN Single Crystals Synthesized by the Na Flux Method**. *Crystal Growth & Design*, **2**(1):55–58, 2002. 96

[152] D. Cherns, L. Meshi, I. Griffiths, S. Khongphetsak, S. V. Novikov, N. Farley, R. P. Campion, and C. T. Foxon. **Defect reduction in GaN/(0001)sapphire films grown by molecular beam epitaxy using nanocolumn intermediate layers**. *Applied Physics Letters*, **92**(12):121902, 2008. 96

[153] S. H. Lee, T. Minegishi, J. S. Park, S. H. Park, J. S. Ha, and H. J. Lee. **Ordered Arrays of ZnO Nanorods Grown on Periodically Polarity-Inverted Surfaces**. *Nano Letters*, **8**(8). 96

[154] V. Ramachandran, R. M. Feenstra, W. L. Sarney, L. Salamanca-Riba, J. E. Northrup, L. T. Romano, and D. W. Greve. **Inversion of wurtzite GaN(0001) by exposure to magnesium**. *Applied Physics Letters*, **75**(6):808, 1999. 98

[155] V. Jindal and F. Shahedipour-Sandvik. **Theoretical prediction of GaN nanostructure equilibrium and nonequilibrium shapes**. *Journal of Applied Physics*, **106**(8):083115, 2009. 101, 106, 110, 123

[156] M. C. Liu, Y. J. Cheng, J. R. Chang, S. C. Hsu, and C. Y. Chang. **Optical properties of self assembled GaN polarity inversion domain boundary**. *Applied Physics Letters*, **99**(2):021103, 2011. 103

[157] K. A. Bertness, N. A. Sanford, J. M. Barker, J. B. Schlager, A. Roshko, A. V. Davydov, and I. Levin. **Catalyst-free growth of**

GaN nanowires. *Journal of Electronic Materials*, **35**(4):576–580, 2006. 103

[158] F. Glas. **Critical dimensions for the plastic relaxation of strained axial heterostructures in free-standing nanowires**. *Physical Review B*, **74**(12), 2006. 103

[159] J. Y. Yoo, Y. J. Hong, S. J. An, G. C. Yi, B. H. Chon, T. H. Joo, J. W. Kim, and J. S. Lee. **Photoluminescent characteristics of Ni-catalyzed GaN nanowires**. *Applied Physics Letters*, **89**(4):043124, 2006. 103

[160] F. Furtmayr, M. Vielemeyer, M. Stutzmann, A. Laufer, Bruno K. Meyer, and M. Eickhoff. **Optical properties of Si- and Mg-doped gallium nitride nanowires grown by plasma-assisted molecular beam epitaxy**. *Journal of Applied Physics*, **104**(7):074309, 2008. 103

[161] O. Brandt, C. Pfller, C. Chze, L. Geelhaar, and H. Riechert. **Sub-meV linewidth of excitonic luminescence in single GaN nanowires: Direct evidence for surface excitons**. *Physical Review B*, **81**(4), 2010. 103, 108, 109

[162] P. Fini, L. Zhao, B. Moran, M. Hansen, H. Marchand, J. P. Ibbetson, S. P. DenBaars, U. K. Mishra, and J. S. Speck. **High-quality coalescence of laterally overgrown GaN stripes on GaN/sapphire seed layers**. *Applied Physics Letters*, **75**(12):1706, 1999. 104

[163] X. J. Chen, G. Perillat-Merceroz, D. Sam-Giao, C. Durand, and J. Eymery. **Homoepitaxial growth of catalyst-free GaN wires on N-polar substrates**. *Applied Physics Letters*, **97**(15):151909, 2010. 104, 123

[164] M. Jetter, V. Perez-Solorzano, A. Groening, M. Ubl, H. Graebeldinger, and H. Schweizer. **Selective growth of GaInN quantum dot structures**. *Journal of Crystal Growth*, **272**(1-4):204–210, 2004. 106

[165] J. Eymery, F. Rieutord, V. Favre-Nicolin, O. Robach, Y. M. Niquet, L. Frberg, T. Mrtensson, and L. Samuelson. **Strain and Shape of Epitaxial InAs/InP Nanowire Superlattice Measured by Grazing Incidence X-ray Techniques**. *Nano Letters*, **7**(9):2596–2601, 2007. 108

[166] Michael E. Coltrin and Christine C. Mitchell. **Mass transport and kinetic limitations in MOCVD selective-area growth**. *Journal of Crystal Growth*, **254**(1-2):35–45, 2003. 110

[167] T. Akasaka, Y. Kobayashi, S. Ando, N. Kobayashi, and M. Kumagai. **Selective MOVPE of GaN and AlxGa1-xN with smooth vertical facets**. *Journal of Crystal Growth*, **189-190**:72–77, 1998. 111

[168] T. Leveder, S. Landis, L. Davoust, and N. Chaix. **Optimization of demolding temperature for throughput improvement of nanoimprint lithography**. *Microelectronic Engineering*, **84**(5-8):953–957, 2007. 118

[169] X. Zhang, P. D. Dapkus, and D. H. Rich. **Lateral epitaxy overgrowth of GaN with NH[sub 3] flow rate modulation**. *Applied Physics Letters*, **77**(10):1496, 2000. 121, 126

[170] K. Kawasaki. **Formation of GaN nanopillars by selective area growth using ammonia gas source molecular beam epitaxy**. *Journal of Crystal Growth*, **243**(1):129–133, 2002. 123

[171] T. Tanaka, K. Uchida, A. Watanabe, and S. Minagawa. **Selective growth of gallium nitride layers with a rectangular cross-sectional shape and stimulated emission from the optical waveguides observed by photopumping**. *Applied Physics Letters*, **68**(7):976, 1996. 123

[172] S. C. Jain, M. Willander, J. Narayan, and Van R. Overstraeten. **IIInitrides: Growth, characterization, and properties**. *Journal of Applied Physics*, **87**(3):965, 2000. 123

[173] Y. Sakata and K. Komatsu. **Migration effect on semiconductor surface for narrow-stripe selective MOVPE**. *Journal of Electronic Materials*, **29**(1):37–41, 2000. 123

[174] W. Feng, V. V. Kuryatkov, A. Chandolu, D. Y. Song, M. Pandikunta, S. A. Nikishin, and M. Holtz. **Green light emission from InGaN multiple quantum wells grown on GaN pyramidal stripes using selective area epitaxy**. *Journal of Applied Physics*, **104**(10):103530, 2008. 123

[175] A. I. Persson, L. E. Froberg, S. Jeppesen, M. T. Bjork, and L. Samuelson. **Surface diffusion effects on growth of nanowires by chemical beam epitaxy**. *Journal of Applied Physics*, **101**(3):034313, 2007. 123

[176] A. Vajpeyi, A. Georgakilas, G. Tsiakatouras, K. Tsagaraki, M. Androulidaki, S. Chua, and S. Tripathy. **Effect of substrate temperature on spontaneous GaN nanowire growth and optoelectronic properties**. *Physica E: Low-dimensional Systems and Nanostructures*, **41**(3):427–430, 2009. 123, 124

[177] M. Hiroki and N. Kobayashi. **Flat Surfaces and Interfaces in AlN/GaN Heterostructures and Superlattices Grown by Flow-Rate Modulation Epitaxy**. *Japanese Journal of Applied Physics*, **42**(Part 1, No. 4B):2305–2308, 2003. 126

[178] L. Polenta, A. Castaldini, and A. Cavallini. **Defect characterization in GaN: Possible influence of dislocations in the yellow-band features**. *Journal of Applied Physics*, **102**(6):063702, 2007. 130, 134

[179] M. Sumiya, K. Yoshimura, T. Ito, K. Ohtsuka, S. Fuke, K. Mizuno, M. Yoshimoto, H. Koinuma, A. Ohtomo, and M. Kawasaki. **Growth mode and surface morphology of a GaN film deposited along the N-face polar direction on c-plane sapphire substrate**. *Journal of Applied Physics*, **88**(2):1158, 2000. 130

[180] P. R. Tavernier, T. Margalith, J. Williams, D. S. Green, S. Keller, S. P. DenBaars, U. K. Mishra, S. Nakamura, and D. R. Clarke. **The growth of N-face GaN by MOCVD: effect of Mg, Si, and In**. *Journal of Crystal Growth*, **264**(1-3):150–158, 2004. 130

[181] V. Kirilyuk, A. R. A. Zauner, P. C. M. Christianen, J. L. Weyher, P. R. Hageman, and P. K. Larsen. **Exciton-related photolu-**

minescence in homoepitaxial GaN of Ga and N polarities. *Applied Physics Letters*, **76**(17):2355, 2000. 130

[182] D. G. Zhao, S. J. Xu, M. H. Xie, S. Y. Tong, and H. Yang. **Stress and its effect on optical properties of GaN epilayers grown on Si(111), 6H-SiC(0001), and c-plane sapphire**. *Applied Physics Letters*, **83**(4):677, 2003. 130

[183] M. Yoshikawa, M. Kunzer, J. Wagner, H. Obloh, P. Schlotter, R. Schmidt, N. Herres, and U. Kaufmann. **Band-gap renormalization and band filling in Si-doped GaN films studied by photoluminescence spectroscopy**. *Journal of Applied Physics*, **86**(8):4400, 1999. 130, 131

[184] L. Tian, N. Stojanovic, D. Y. Song, A. A. Bernussi, J. M. Berg, and M. Holtz. **Influence of photonic nanotexture on the light extraction efficiency of GaN**. *Applied Physics Letters*, **91**(10):103115, 2007. 131

[185] D. S. Jiang. **Electrical properties and photoluminescence of Te-doped GaAs grown by molecular beam epitaxy**. *Journal of Applied Physics*, **53**(2):999, 1982. 131

[186] M. Leroux, B. Beaumont, N. Grandjean, P. Lorenzini, S. Haffouz, P. Vennegues, J. Massies, and P. Gibart. **Luminescence and reflectivity studies of undoped, n- and p-doped GaN on (0001) sapphire**. *Materials Science and Engineering B*, **50**(1-3):97–104, 1997. 131

[187] J. L. Lyons, A. Janotti, and C. G. Van de Walle. **Carbon impurities and the yellow luminescence in GaN**. *Applied Physics Letters*, **97**(15):152108, 2010. 134

[188] W. C. Hou and Franklin C. N. Hong. **Controlled surface diffusion in plasma-enhanced chemical vapor deposition of GaN nanowires**. *Nanotechnology*, **20**(5):055606, 2009. 139

[189] J. M. Gerard, O. Cabrol, and B. Sermage. **InAs quantum boxes: Highly efficient radiative traps for light emitting devices on Si**. *Applied Physics Letters*, **68**(22):3123, 1996. 140

[190] M. Zhang, P. Bhattacharya, and W. Guo. **InGaN/GaN self-organized quantum dot green light emitting diodes with reduced efficiency droop**. *Applied Physics Letters*, **97**(1):011103, 2010. 141

[191] K. Tachibana, T. Someya, and Y. Arakawa. **Nanometer-scale InGaN self-assembled quantum dots grown by metalorganic chemical vapor deposition**. *Applied Physics Letters*, **74**(3):383, 1999. 141

[192] H. Hirayama, S. Tanaka, P. Ramvall, and Y. Aoyagi. **Intense photoluminescence from self-assembling InGaN quantum dots artificially fabricated on AlGaN surfaces**. *Applied Physics Letters*, **72**(14):1736, 1998. 141

[193] K. O'Donnell, R. Martin, and P. Middleton. **Origin of Luminescence from InGaN Diodes**. *Physical Review Letters*, **82**(1):237–240, 1999. 141

[194] G. Y. Liu, H. P. Zhao, J. Zhang, J. Park, L. J. Mawst, and N. Tansu. **Selective area epitaxy of ultra-high density InGaN quantum dots by diblock copolymer lithography**. *Nanoscale Research Letters*, **6**(1):342, 2011. 141

[195] J. Y. Yoo, G. S. Yi, and L. S. Dang. **Probing Exciton Diffusion in Semiconductors Using SemiconductorNanorod Quantum Structures**. *Small*, **4**(4):467–470, 2008. 143

[196] D. I. Lubyshev, P. P. Gonzalez-Borrero, E. Marega, E. Petitprez, N. La Scala, and P. Basmaji. **Exciton localization and temperature stability in self-organized InAs quantum dots**. *Applied Physics Letters*, **68**(2):205, 1996. 143

[197] M. Leroux, N. Grandjean, B. Beaumont, G. Nataf, F. Semond, J. Massies, and P. Gibart. **Temperature quenching of photoluminescence intensities in undoped and doped GaN**. *Journal of Applied Physics*, **86**(7):3721, 1999. 144